UNIVERSITY OF SOUTHAMPTON

FACULTY OF SCIENCE, ENGINEERING AND MATHEMATICS

School of Ocean and Earth Sciences

Physical controls on spring bloom dynamics in the Irminger Basin, North Atlantic

by

Stephanie Anne Henson

Thesis for the degree of Doctor of Philosophy

September 2005

UNIVERISTY OF SOUTHAMPTON
ABSTRACT
FACULTY OF ENGINEERING, SCIENCE AND MATHEMATICS
SCHOOL OF OCEAN AND EARTH SCIENCES
Doctor of Philosophy

PHYSICAL CONTROLS ON SPRING BLOOM DYNAMICS IN THE IRMINGER BASIN, NORTH ATLANTIC

by Stephanie Anne Henson

Much of the primary production in northern latitudes is associated with the relatively short spring phytoplankton bloom. Quantifying the bloom is essential to understanding export production and energy transfer to higher trophic levels. This study focuses on the physical forcing controlling the spring bloom in the Irminger Basin (IB), situated between Greenland and Iceland. *In situ* data are available from four cruises to the region carried out under the UK Marine Productivity programme. This data set is extended with six years of SeaWiFS satellite chlorophyll-a concentration (chl-a) data, together with the corresponding model net heat flux (NCEP reanalysis) and satellite measured wind speed (QuikSCAT), sea surface temperature (SST; AVHRR) and photosynthetically available radiation (PAR; SeaWiFS). The remotely sensed data are complemented by a 1-D vertical mixing model and temperature and salinity profiles from Argo drifting profilers.

The seasonality in temperature-nutrient (TN) relationships is investigated and the TN relationships are improved by including chlorophyll in the regressions. Basin-wide, daily estimates of nitrate, phosphate and silicate are made from satellite SST and chl-a.

The study focuses on three biogeographical zones determined by cluster and Empirical Orthogonal Function analysis of SeaWiFS chl-a data. The three areas have distinct chl-a signatures and cover the East Greenland shelf, the Reykjanes Ridge and the Central Basin.

An ANOVA analysis reveals that significant interannual variability is occurring in chlorophyll-a. An objective method for determining the start day of the spring bloom is described. Interannual variability in the timing of the initiation of the bloom and its magnitude and duration is discussed.

The influence of the prevailing meteorology on chl-a in different seasons are investigated using generalized linear modelling. Whilst net heat flux and PAR are the dominating factors in spring, wind speed and SST become increasingly influential during summer and autumn. A method for estimating time series of Sverdrup's critical depth from remotely sensed PAR and attenuation coefficient data is outlined. It is found that the spring bloom never begins before the mixed layer depth becomes shallower than the critical depth, and there is a delay of ~10 days. Specific criteria for the start of the bloom in terms of net heat flux and PAR are determined. The effect of nutrient depletion on the decline of the bloom is discussed.

The East Greenland coastal zone is used as an example of the lasting impact that anomalous meteorological conditions can have on the following spring's bloom. In 2002 the East Greenland region experienced anomalously low chl-a concentrations. Strong easterly winds, associated with the tip-jet phenomena, occurred throughout winter and spring and net heat flux was anomalously low in 2002. The spring bloom in the Irminger Basin can be affected by large scale climatic events, such as shifts in the North Atlantic Oscillation.

Finally, the timing of nutrient depletion and its impact on community succession is considered. The possibility of iron limitation in the basin is discussed. A lower bound estimate of export production is made based on the timing of silica availability, and hence diatom dominance, of the spring bloom. The contributions to export production by diatoms and non-diatoms are estimated.

TABLE OF CONTENTS

LIST OF TABLES

LIST OF FIGURES

DECLARATION OF AUTHORSHIP

I, STEPHANIE ANNE HENSON declare that the thesis entitled

PHYSICAL CONTROLS ON SPRING BLOOM DYNAMICS IN THE IRMINGER BASIN, NORTH ATLANTIC

and the work presented in it are my own. I confirm that:

- this work was done wholly or mainly while in candidature for a research degree at this University;
- where any part of this thesis has previously been submitted for a degree or any other qualification at this University or any other institution, this has been clearly stated;
- where I have consulted the published work of others, this is always clearly attributed;
- where I have quoted from the work of others, the source is always given. With the exception of such quotations, this thesis is entirely my own work;
- I have acknowledged all main sources of help;
- where the thesis is based on work done by myself jointly with others, I have made clear exactly what was done by others and what I have contributed myself;
- parts of this work have been published as:

Henson, S. A., R. Sanders, J. T. Allen, I. S. Robinson and L. Brown (2003), Seasonal constraints on the estimation of new production from space using temperature-nitrate relationships, *Geophysical Research Letters*, **30**(17), 1912; doi:10.1029/2003GL017982 – attached as Appendix 1

Signed: ………………………………………………………………………..

Date:……………………………………………………………………………

ACKNOWLEDGEMENTS:

Firstly, thank you to Ian and John for supporting and encouraging me throughout my PhD. And apologies to John who never did get his FISHES data analysed! At SOC (or should that be NOC,S now?) there have been many people who have helped me with data, modelling, programming and just good old ideas: Dave Poulter, Peter Challenor, Graham Quartly, Paolo Cipollini, Steve Alderson, Raymond Pollard, Penny Holliday and Louise Brown and thanks to all of the staff and students of George Deacon Division. Thanks to all the other MarProdders, both at SOC and elsewhere, for many interesting discussions and one very enjoyable cruise.

Three people deserve an extra-big thank you: Joanna Waniek for supplying me with the 1-D model used in this thesis; Claire Holeton for teaching me more biology than I ever thought I wanted to know; and Richard Sanders for his support and enthusiasm – and atrocious handwriting!

And then there are the many good friends I have at SOC, without whom the last three years would have been far more stressful and infinitely less fun. Thanks to Jacqui, Kate and Chris for being fantastic house-mates and friends – long live Cromwell Road; to Stuart and Sandy for being brilliant office-mates and putting up with all my dumb biology questions; to Naoise and Chris for understanding the importance of coffee and biscuits; to Alex for all the cooking and never missing a Friday night and to Anna for being a wonderful friend and for really dancin'. And thanks to all the other Friday-nighters: Aggie, the Andys and Dan, Calum, Donna, Emma, Jenny, Jo, Pete and all the other people I can't remember right now (probably thanks to alcohol-induced amnesia!)

Special thanks and a lot of love to Tim for being my best friend, my partner and so much more. Finally, to my family who have been incredibly supportive through my many long years of study. Thanks to Oma for providing a peaceful haven in Alabama and for all the retail therapy; to Grandma for all those Sunday lunches; and to my sister Kirsten – I still love you despite it all. Thanks to my father David and my mother Barbara, who never stopped believing that I could do it – I love you both very much.

This thesis is dedicated to the memory of my two grandfathers: Helmuth and Eric.

GRADUATE SCHOOL OF THE NATIONAL OCEANOGRAPHY
CENTRE, SOUTHAMPTON

This PhD thesis by
Stephanie Anne Henson
has been produced under supervision of the following persons:

Supervisors:

Prof Ian Robinson
Dr John Allen

Chair of the Advisory Panel:

Prof Patrick Holligan

1. OVERVIEW:

This overview introduces the rationale behind the project in terms of the importance of understanding variability in the biogeochemical carbon cycle and the contribution of the spring bloom to the biological pump. A list of objectives and an overview of the thesis structure are also included.

1.1. RATIONALE:

A major route for the transfer of carbon from the atmosphere to the ocean is through the uptake of CO_2 by phytoplankton and its subsequent removal from surface waters – the biological pump. As well as driving this biological pump, primary production forms the base of the marine food web and thus affects all trophic levels, including commercial fishing. Estimating the magnitude, seasonality and variability of primary production is therefore central to understanding the controls over, and the strength of, the carbon pump.

In many parts of the world oceans the cycle of primary production is dominated by the annual phytoplankton spring bloom. The bloom is characterised by pronounced increases in plankton biomass and the removal of dissolved nutrients in surface waters. In terms of the global carbon cycle only a fraction of this total production is available for transfer to deep waters or higher trophic levels and so contributes to the carbon pump.

The Irminger Basin, the focus of this study, is believed to be a highly productive region and supports several major fisheries. It may also be a site for deep open ocean convection and its meteorological conditions are likely to be affected by the state of the North Atlantic Oscillation. Four cruises were undertaken to the region in successive seasons – a relative novelty in cruise programmes. This unique facet of the Marine Productivity programme allows the seasonal variability in biological and physical parameters to be assessed.

In order to understand the variability in the timing and magnitude of spring blooms, an understanding of the underlying physical forcing is first required. Perturbations to the forcing may be reflected in the biological response, but to quantify the perturbations and their impact, knowledge of the ‘normal’ state of the system is necessary. For this a long time series of data at high spatial and temporal resolution is essential. Only satellite data are able to provide synoptic snapshots at a sufficiently high resolution to address this question. Satellite data however are limited by the parameters that can be sensed remotely and because they provide only a surface measurement. Combining satellite data with modelled data and *in situ* data from cruises and profiling floats allows novel measurements to be made and extends the capabilities of all the data sources.

1.2. OBJECTIVES:

This thesis aims to define the physical controls on spring bloom characteristics and their interannual and spatial variability in the Irminger Basin. The study seeks to demonstrate that by combining satellite, *in situ* and model data new insights into the interactions between physical and biological processes can be gained. The specific aims of this thesis are to:

- Demonstrate that nitrate, phosphate and silicate can be estimated from remotely sensed SST and chlorophyll-a, and characterise the seasonality in the relationships.
- Divide the Irminger Basin into a series of biogeographical zones on the basis of satellite chlorophyll-a concentration.
- Quantify the interannual variability in spring bloom characteristics – magnitude, duration and timing of the start and end of the bloom.
- Assess the impact of meteorology on chlorophyll concentration in pre- and post-bloom periods.

- Calculate Sverdrup's critical depth and compare to modelled mixed layer depth.
- Investigate the influence of net heat flux and PAR on the timing of the start of the bloom.
- Determine the factors controlling the decline of the spring bloom.
- Characterise the unique bloom conditions and causes of interannual variability on the East Greenland coast.
- Estimate the timing of nutrient depletion and its impact on community succession and export production.

1.3. OVERVIEW OF THESIS STRUCTURE:

An introduction to the concept of the spring bloom and the controls on interannual variability is presented in Chapter 2, which also provides a review of the current knowledge of the physical and biological oceanography of the Irminger Basin.

In Chapter 3 details of the data collection and processing are given, for both *in situ* and satellite data, including a discussion of the possible sources of error and limitations of the SeaWiFS chlorophyll-a concentration.

The derivation of temperature-nutrient relationships and an analysis of, and a correction for, the seasonality in the relationships is outlined in Chapter 4. The chapter only presents the data and regressions, with the results and implications for the spring bloom integrated into later chapters. Parts of the chapter have been previously published as Henson et al. (2003), 'Seasonal constraints on the estimation of new production from space using temperature-nitrate relationships', Geophysical Research Letters 30(17), 1912, which is included as Appendix 1. The chapter however introduces additional data and further analysis not included in the published paper.

In Chapter 5 the Irminger Basin is divided into biogeographical zones on the basis of SeaWiFS chlorophyll-a concentration using two methods: cluster analysis and Empirical Orthogonal Function analysis. The analysis is presented here as the results justify the definition of the three zones used in later chapters to characterise the interannual variability of the spring bloom in the basin. The cluster analysis is relevant only to defining the zones, but the Empirical Orthogonal Function analysis is referred to again in later chapters.

In Chapter 6 the interannual variability in spring bloom characteristics is explored graphically and statistically. Variability in the timing, magnitude and duration of the bloom is discussed.

The physical controls on the spring bloom are considered in Chapter 7. The influence of sea surface temperature, net heat flux, photosynthetically available radiation and wind speed on the chlorophyll concentration in both the pre- and post-bloom period is analysed with Generalised Linear Modelling. Sverdrup's critical depth is estimated and compared to mixed layer depth calculated from Argo float profiles. The influence of net heat flux and photosynthetically available radiation on the timing of the bloom is discussed. The factors contributing to the decline of the bloom are explored, with a focus on nutrient depletion. The chapter concludes by examining the particular bloom conditions and causes of interannual variability in the East Greenland coast region, which differs markedly from the rest of the Irminger Basin.

Chapter 8 discusses the role of nutrient depletion in the timing of community succession and export production in the basin. A discussion on possible iron limitation of the Irminger Basin is followed by a calculation of a lower bound estimate of export production and the relative contribution by diatoms is assessed.

Finally, Chapter 9 presents a summary of conclusions, a reflection on the data sources used and a discussion of future work and the study's farther-reaching implications.

2. INTRODUCTION:

One of the routes for carbon transfer to the ocean is via CO_2 uptake by phytoplankton and its subsequent removal from surface waters – the biological pump (Eppley and Peterson, 1979). In the global ocean primary production arises from photosynthesis carried out by phytoplankton. Photosynthesis requires light and nutrients (principally the macronutrients nitrate, phosphate and silicate). Thus the spatial and temporal distribution of these factors often dictates patterns of biological productivity. Quantifying the variability of these parameters is therefore necessary for understanding the variability in primary production.

2.1. THE SPRING BLOOM:

2.1.1. TRADITIONAL VIEW OF THE SPRING BLOOM:

In many parts of the world's oceans the annual cycle of phytoplankton growth is dominated by a rapid, intense population explosion – the spring bloom (Falkowski et al., 2000). In the North Atlantic the spring bloom is seen in satellite images as a mass greening extending over scales of more than 2000 km which can propagate northwards at up to 20 km day^{-1} (Siegel et al., 2002). During winter in northern latitudes phytoplankton growth is principally limited by low light levels (see Figure 2.1). Strong winds and net heat loss from the ocean result in convective overturning due to buoyancy loss. Although nutrient concentrations are uniformly high throughout the water column, the deep mixed layer ensures that phytoplankton are only in the sunlit surface layers for a short period of time before being mixed down into deeper, darker water. As spring approaches the combined effects of longer, warmer days and reduced wind speeds leads to formation of a thermally stratified surface layer. The stability of this layer traps the phytoplankton, and the nutrients they require for growth, in the sunlit upper water column. Under these conditions phytoplankton grow very quickly, rapidly diminishing the stock of nutrients in the surface layer. Additionally, zooplankton begin reproducing rapidly as the bloom starts and grazing reduces phytoplankton biomass after a short time. During summer, although there is sufficient light, the stratified layer prevents new nutrients from reaching the upper water column, restricting growth. Production is limited to that which can be sustained by recycled nitrogen and a small amount of nutrients diffused across the thermocline. Zooplankton may also consume the phytoplankton biomass almost as soon as it is produced. As autumn approaches and solar heating declines the stratified layer can no longer be maintained. The deepening of the thermocline can allow new nutrients into the surface waters and, in regions where there is still adequate light, a small autumn bloom may occur. The return to winter conditions signals the end of the growth period – until next spring.

This idealised description of the annual spring bloom was formalised by Gran and Braarud (1935) and Sverdrup (1953). Sverdrup's critical depth hypothesis states that net growth will only occur when stratification traps phytoplankton near the surface, where sufficient light is available to allow the production of organic matter by photosynthesis to exceed its destruction by respiration. He defined a critical depth at which production integrated over the water column is equal to losses by metabolic processes and sinking (Figure 2.2). If the mixed layer is deeper than the critical depth light becomes limiting as the phytoplankton are mixed out of the euphotic zone for too long to allow net growth. Sverdrup's theory maintains that the spring bloom will be initiated when the mixed layer depth becomes shallower than the critical depth. The irradiance at the critical depth is termed the critical irradiance and has been defined empirically by Riley (1957). If the ocean mixed layer depth is shallower than the critical depth, community production outstrips community losses and net phytoplankton growth occurs.

2.1.2. CONTROLS ON TIMING OF THE BLOOM:

Considering Sverdrup's critical depth model (SCDM) it is clear that a combination of increased ocean heating and light levels are required to initiate a spring bloom. The light field decreases exponentially (and rapidly) with depth in the ocean, dependent on the clarity of the water, time of day and time of year. Net heat gain by the ocean depends on the elevation of the sun, day length and cloudiness. Provided sufficient nutrients are available and grazing does not outstrip phytoplankton growth, a spring bloom should occur when heating has shallowed the mixed layer to less than the critical depth. This theory has been tested repeatedly since its conception in 1953. In the original study Sverdrup (1953) examined observations of mixed layer depth (MLD) and phytoplankton and zooplankton concentrations taken from March to May 1949 at Ocean Weather Ship ‘M’ located at 66°N, 2°E. His results proved his hypothesis with the concentration of both phytoplankton and zooplankton increasing rapidly as the MLD became shallower than the calculated critical depth in mid May.

In more recent times the advent of improved monitoring systems, both shipboard and satellite-based, and increased computing capability have allowed a more detailed examination of Sverdrup’s theory. For example, modelling studies such as Ebert et al. (2001), who developed a model in which the local light intensity determines the reproductive rate of phytoplankton and phytoplankton are transported by turbulent diffusion. They concluded that the critical depth and compensation depth adequately captured the conditions necessary for a phytoplankton bloom. Morin et al. (1991) developed a simple model of critical depth taking into account the evolution of the global solar irradiance and the depth of the mixed layer which permitted prediction of the initiation of phytoplankton development on the Armorican shelf (Northwest Europe).

Recent observational studies include that by Walsby et al. (2003) carried out at Lake Kinneret, Israel. From a database of measurements of sea surface temperature (SST), light attenuation and irradiance covering 1994-2000 they successfully predicted the period of growth for a common species of cyanobacteria. Similarly Stal and Walsby (2000) concluded that in the Baltic Sea growth of cyanobacteria populations could only occur in the summer months when the MLD was shallower than the critical depth. From an extensive set of *in situ* measurements Labry et al. (2001) determined that if the MLD was shallower than the critical depth, and therefore that the phytoplankton were receiving at least the critical irradiance, a winter bloom could be triggered in the Gironde plume (Bay of Biscay). Whilst SCDM does hold for these specific localities, other studies have questioned the universal validity of SCDM.

2.1.3. RETHINKING SVERDRUP:

Both heat flux and light intensity, the key driving factors in SCDM, are heavily dependent on latitude. A poleward progression of the spring bloom, which keeps pace with the movement of the region of mixed layer shallowing, is therefore expected. However, Colebrook (1979 and 1982) showed that variation in the timing of the onset of the spring bloom in the North Atlantic is uncorrelated with annual differences in the timing of surface warming or the development of the seasonal thermocline. The advent of undulating towed sensors in the 1980's allowed higher horizontal resolution than was possible with traditional 'bottle' stations. Strass and Woods (1988 and 1991) reported on a series of transects from the Azores towards Greenland. They concluded that the horizontal migration of the surface chlorophyll maximum did not match the northward movement of the shallowing mixed layer, but instead followed the propagation of the 12°C isotherm outcrop (Figure 2.3). This suggests that in addition to stable stratification, there may also be a temperature limitation on bloom processes. Temperature is believed to control the enzyme-mediated rates of photosynthesis. Although the response varies between species, laboratory experiments have shown that phytoplankton photosynthetic rates increase with temperature up to an optimal temperature, after which they decrease (e.g. Eppley, 1972; Yoder, 1979).

A CZCS ocean colour data study (Obata et al., 1996) and a modelling study by Follows and Dutckiewicz (2002), both concluded that across the north Atlantic the MLD is generally shallower than the critical depth at the start of the bloom – but only in the sub-polar regions. Follows and Dutkiewicz (2002) and Dutkiewicz et al. (2001) combined an ecosystem model with SeaWiFS chlorophyll-a data to define a non-dimensional parameter h_c/h_m, the ratio of the local critical depth to the end of winter MLD. On the basis of this the North

Atlantic is divided into a region approximately north of 35°N where (roughly speaking) SCDM applies, and an area south of 35°N where it does not (Figure 2.4). Obata et al. (1996) used Coastal Zone Colour Scanner (CZCS) chlorophyll-a data along with Levitus (1982) derived MLD and critical depth estimated from cloud cover and light attenuation data. They demonstrated that Sverdrup's model holds for the sub-polar North Atlantic and NW Pacific, but fails in other regions, principally oligotrophic regions. In these areas, principally found in sub-tropical regions, low wind speeds and strong year-round heating lead to almost continuous stratification and the MLD is almost permanently shallower than the critical depth. Light is not limiting for longer than a few hours during the night, or a stormy day and under these conditions the surface layer quickly becomes depleted of nutrients. Because of this no single, pronounced, annual bloom is observed in oligotrophic regions and SCDM cannot account for variability in biomass (e.g. Dugdale and Wilkerson, 1998; Boyd and Harrison, 1999; Strom et al., 2000; Le Borgne et al., 2002).

In a study conducted in the Southern Ocean around the island of South Georgia, Korb and Whitehouse (2004) observed two different biomass provinces to the north-east and north-west of the island. Despite both areas having a MLD shallower than the critical depth and similar light conditions, the NW region had much higher biomass than the NE region. The authors conclude that another factor must be influencing the distribution of biomass around the island, and suggest iron limitation as a possible cause. In other words, a shallow MLD alone is not sufficient to start a bloom – other conditions, such as sufficient nutrients, must also be met. In sub-tropical regions and the Southern Ocean low biomass has been ascribed to limiting concentrations of iron and dramatic increases in chlorophyll concentration has followed iron fertilisation experiments (see Boyd (2002) for a review). Limiting concentrations of other nutrients can prevent a bloom starting under otherwise favourable conditions, e.g. silica in the equatorial Pacific upwelling (Dugdale and Wilkerson, 1998) or manganese in the Ross Sea (Sedwick et al., 2000).

In some cases it seems that not even a shallow ML is necessary for a bloom to start. Durbin et al. (2003) found that in the Gulf of Maine an early winter bloom can occur prior to thermal stratification becoming established. At the time of the survey elevated chlorophyll levels were associated with a MLD deeper than the critical depth. They hypothesised that the transient presence of a cell of low salinity water was able to provide the necessary stability for a bloom to start, without the hydrographic conditions satisfying SCDM.

Spring phytoplankton bloom conditions for the southeastern Bering Sea were simulated with a coupled phytoplankton-nutrient-detritus model by Eslinger and Iverson (2001). They conclude that a shallow mixed layer is not necessary to trigger a bloom and instead merely a cessation of convective mixing during a period of increased air temperature and low wind speed is required.

During research cruises to the Gulf of Maine in 1990 and 1992 Townsend et al. (1992) observed a spring bloom occurring in the absence of vertical stratification (Figure 2.5). They suggest that the deepening penetration of light in the clear winter waters in concert with weak wind mixing could be sufficient to maintain growth rates that exceed the vertical excursion rates. Once begun a bloom may enhance the warming of the surface waters through the light scattering and absorption properties of phytoplankton. They conclude that in some instances the development of the thermocline is not a prerequisite for the spring bloom, but rather that its development is initiated by increasing phytoplankton stocks. In a follow-up model study Townsend et al. (1994) demonstrated that spring blooms can begin following winter deep convection and prior to the development of thermal stratification, provided that the wind speed is below a predictable threshold.

Finally Sverdrup's theory does not account for the survival of the over-wintering stock of phytoplankton. Intuitively we know that a phytoplankton population, however small, must survive the deep mixing of the winter and provide a seed for the following year's spring bloom. Studies in the sub-arctic North Atlantic by Backhaus et al. (2003) concluded that a winter population can be maintained, even under conditions of deep mixing, because overturning within convection cells repeatedly brings phytoplankton to the surface where, over the long term, they are exposed to uniform levels of irradiance. In addition Huisman et al. (1999) argue that turbulent mixing may maintain phytoplankton with low sinking velocities above the critical depth. Below a threshold value of turbulence phytoplankton can remain in the illuminated upper layers of the water column for sufficiently long for growth to outstrip the rate of diffusion by turbulent mixing.

These studies have questioned the universal validity of Sverdrup's critical depth model, suggesting that the critical depth criterion may be a necessary, *but not sufficient*, condition for the initiation of a phytoplankton bloom.

2.1.4. INTERANNUAL VARIABILITY IN BLOOMS:

It is clear that many factors can influence the timing and magnitude of the bloom and that it may not always be easy to determine the controlling forcing. It may be possible to deduce these controls by studying the interannual variability of a spring bloom and comparing it to variability in potential forcing factors.

Water mass change, and the concomitant nutrient concentration change, will have an impact on the magnitude and duration of a spring bloom. SeaWiFS derived chlorophyll-a images of the southern Adriatic Sea for 1998-2000 in Santoleri et al. (2003) show differences in bloom onset, duration and intensity. The relationship between atmospheric forcing and variability of bloom timing was investigated using a coupled physical-biological model. They conclude that local winter climatic conditions (essentially the maximum convective depth) alone cannot explain changes in the bloom, and that nutrient concentration differences due to changing water masses have the greatest influence.

Despite no large interannual variability in meteorological forcing (SST and wind stress) at the ESTOC site, north of the Canary Islands, both observed and modelled biogeochemical processes displayed significant variability (Pätsch et al., 2002). The authors note the sensitivity of the local ecosystem to nutrient availability, and conclude that the magnitude of the bloom depends on small changes in winter weather which dictate whether the MLD reaches the nutricline.

At the Biotrans site (47°N, 20°W) Koeve (2001) concluded that from 1988 – 1990 there was no significant interannual variation in winter-time nutrient concentrations. However in 1992, following an anomalously warm winter nitrate was found to be much lower than average. He concluded that changes in maximum MLD reached would impact on the following spring's bloom via reduced/enhanced nutrient supply.

Between 1990 and 2000 at a fixed station in the Irminger Basin Olafsson (2003) observed no correlation between winter (February) MLD and nitrate or phosphate concentration, although in the neighbouring Iceland Sea highly significant correlations were found (Figure 2.6). He suggests that for the Iceland Sea convective mixing reached into subsurface water of relatively constant composition, whilst in the Irminger Sea, where mixing extends to greater depths, there were significant variations in the subsurface water.

Thomas, Townsend and Weatherbee (2003), using 4 years of SeaWiFS data covering the Gulf of Maine, found pronounced interannual variability in bloom timing and overall chlorophyll concentrations. They concluded that cold anomalies in the sea surface temperature (SST) field, linked to dominant water mass changes were responsible. They were however surprised to observe no clear relationship between local wind forcing and the variability, as ten years previously Townsend et al.'s (1994) modelling study of the Gulf of Maine concluded that variations in the timing of the bloom are related to the incident radiation and wind mixing. This reasoning again has its basis in the critical depth model. They argue that in early spring, following the winter deep convective mixing and prior to surface waters warming up, there is a period when the average air-sea net heat flux is zero. The water column is then neutrally stable from the surface to the depth of winter convective mixing. Aside from night-time convective mixing the only source of energy for vertical mixing is the wind, and if it is not capable of mixing the water column to a depth deeper than the critical depth, phytoplankton growth can occur. So a period of sunny, calm weather in early spring, whilst not sufficient to establish the seasonal thermocline, may prompt a bloom. Therefore interannual variations in wind speed and incident light may be reflected in the bloom timing.

A study of SeaWiFS chlorophyll-a concentration for 1997-2001 in the Santa Monica Basin off Southern California revealed that chlorophyll biomass was significantly correlated with air temperature and wind stress (Nezlin and Li, 2003). An increase in biomass followed 5-6 days after an increase in wind stress accompanied by a simultaneous decrease in air temperature. They concluded that an intensification of phytoplankton growth resulted from the mixing of the water column by wind stress and subsequent entrainment of nutrients in to the euphotic layer.

Skliris et al. (2001) employed a 1-D vertical, coupled hydrodynamic-biological model of the Bay of Calvi (Corsica) to study the spring evolution of plankton communities. The model was validated with *in situ* physical, chemical and biological measurements taken on cruises in 1986 and 1988. Their results showed that once the seasonal thermocline was in place, and after the peak of the bloom had died back, increases in phytoplankton followed wind events. These events introduce new nutrients into the euphotic zone through deepening of the mixed layer and provide the only possible stimulation of new production during the summer months. An increase in biomass occurred ~3 days after a suitable wind event, defined as either a few hours at high wind speed (>11 ms^{-1}) or 1-2 days at speeds of 7-11 ms^{-1}.

A somewhat different phytoplankton response to wind events was observed at a fixed station occupied for one month in May 1995 in the North-western Mediterranean (Anderson and Prieur, 2000). A decrease in phytoplankton was observed after a sharp wind event, despite an increase in nutrients in the surface waters. Ten days later however a lower speed and longer duration event led to an increase in biomass. The authors suggest that the phytoplankton response to the second event would not have occurred if the nitracline and pycnocline had not been brought to the same depth by the previous wind event. In this region, during the post-bloom period, wind-induced mixing would not appear sufficient alone to enhance primary production and more complex successive processes are needed.

Wind events were found to interrupt the springtime shoaling of the mixed layer in a modelling study initialised for the Biotrans site at 47°N, 20°W over the period 1989-1997 (Waniek et al., 2002; Waniek, 2003). The frequency and intensity of events was found to vary from year to year due to shifts in storm tracks or modes of atmospheric circulation. The model simulations suggested that these events are important for the development of the phytoplankton population. In years where the transition from winter to spring is a smooth process and the spring is calm and warm the bloom was relatively short-lived with high biomass but low primary production (Figure 2.7). In contrast if the transition period and the spring itself experience many storms, and therefore the spring bloom is frequently interrupted, the bloom has lower amplitude and biomass, but the primary and export production are higher. Meteorological factors were found to be responsible for controlling the timing of the spring bloom and also the type of bloom i.e. a continuous, intense event, or a more protracted bloom with a slow increase to maximum chlorophyll values. Waniek (2003) concludes that the key factor in controlling the timing of the initiation of the bloom is net heat flux. In the model experiments the bloom begins during the first period of positive net heat flux (i.e. into the ocean) following the last cold storm event.

Net heat flux was also determined to be the controlling factor in the initiation of the bloom by Azumaya et al. (2001) who used a 3-D ecosystem model to examine the annual cycle of phytoplankton biomass in Funka Bay, Japan. The incident light intensity at the sea surface was sufficient even in January for a bloom to begin, but it wasn't until the net heat flux changed from negative to positive in March that the rapid spring diatom bloom began.

Dutkiewicz et al. (2001) employed a simple two-layer ecosystem model to study the effects of changes in boundary-layer mixing rates on phytoplankton abundances across the North Atlantic. For regions with deep winter time mixing, such as the sub-polar gyre, the competition between supply of extra nutrients and the length of time phytoplankton spend above the critical depth is crucial. They concluded that in these regions increased spring time mixing decreases surface chlorophyll concentrations. However, when they compared the model output to *in situ* data from Ocean Weather Station 'India' and CZCS ocean colour data the results were inconclusive.

In their follow-up study Follows and Dutkiewicz (2002) again used Ocean Weather Station data, this time combined with SeaWiFS chlorophyll-a concentration data, to examine the relationships between changes in intensity of the spring bloom and changes in weather patterns (for 1998-2000). In the sub-polar regime local interannual changes are found to be small relative to regional variations. However, the authors divided the region into 5° x 5° bins, and at high latitudes one would expect the variations between one box and the next to be significant. Although the sub-polar bloom occurs in a period of restratification, the data does not show a clear and consistent trend between the interannual variation of the bloom and wind forcing or heat flux (Figure 2.8). They infer that other factors, such as changes in incident PAR due to cloud cover, local mesoscale variability, lateral advections, top-down control on the ecosystem or poor data coverage at high latitudes due to cloudiness, introduce sources of variability uncorrelated with upper ocean mixing.

This introduction demonstrates that interannual variability in spring bloom timing and magnitude can come from a number of sources. Often it is not one factor working alone, but rather the interaction of heat flux, PAR, wind events, nutrient concentration, grazing etc., that controls the bloom. In the next section the specific conditions in the Irminger Basin and current knowledge of the physical and biological characteristics are described.

2.2. THE IRMINGER BASIN:

2.2.1. PHYSICAL OCEANOGRAPHY:

The Irminger Basin (IB) is situated between Greenland and Iceland in the North Atlantic sub-polar gyre (see Figure 2.9). Parts of the basin reach to 4000 m depth, with rapid shoaling along the Greenland and Iceland coasts. The Reykjanes Ridge, stretching south-west from Iceland, separates the IB from the Iceland Basin. The mean circulation of the IB, both at the surface and at depth, is cyclonic (Lavender et al., 2000; Reverdin et al., 2003). The recirculation is relatively strong (~5 cms^{-1}), narrow (~300 km) and transports approximately 2-5 Sv (Pickart et al., 2002). In the east the surface circulation is dominated by the northward flowing Irminger Current – a branch of the North Atlantic Current (see Figure 2.10). The majority of the Irminger Current turns west and returns southwards as part of the East Greenland Current (EGC), whilst a small part continues northwards to the west of Iceland. The Irminger Current transports salty and warm (compared to the interior of the basin) Modified North Atlantic Water (MNAW) cyclonically around the basin (Krauss, 1995). Part of the MNAW leaves the IB by flowing northward through the Denmark Strait and part joins the EGC, which travels southwards along the edge of the Greenland continental shelf, also taking with it surface Arctic water (Orvik and Niiler, 2002). Below the East Greenland Current the deep western boundary current carries cold fresh Denmark Strait Overflow Water towards the Labrador Sea. Cold fresh water originating from the Labrador Sea spreads across the subpolar gyre and reaches the central IB. Several varieties of subpolar mode water are found east of the Irminger Current. These consist of thick homogenous layers formed over the Reykjanes Ridge and in the Iceland Basin. Fresh Labrador Sea Water dominates the intermediate, interior layers of the IB. The edges of the basin are influenced by overflow water that enters the North Atlantic over the sills between Iceland and Scotland (Bacon, 1997; Pollard et al., 2004). A comprehensive study of the water masses of the region can be found in Read (2001).

The interior of the IB is relatively quiescent, although some small eddies (20 to 40 km diameter) develop at the front between the EGC and the Irminger Current (Eden and Böning, 2002), and a few large eddies (diameters up to 70 km) are occasionally observed in the interior of the basin (Krauss, 1995). High values of surface eddy kinetic energy are observed along the Greenland continental shelf (Frantantoni, 2001). In the neighbouring Labrador Sea the associated eddy fluxes are thought to enhance the restratification process after intense winter cooling has overturned the water masses to create Labrador Sea Water (LSW, e.g. Dickson et al., 1996). LSW is found in the IB typically below 1000 m and until recently the Labrador Sea was regarded as the only site of formation of LSW. It is formed by deep convection, the process which exposes cold, saline water, normally held below the permanent thermocline to the sea surface and which drives the abyssal limb of the North Atlantic meridional overturning circulation. Deep convection has previously thought to only occur in the Greenland, Labrador, Mediterranean and Weddell Seas (e.g. Marshall and Schott, 1999). However, modelling studies (Pickart et al., 2003a; Straneo et al., 2003) suggest that the transit time for LSW from the Labrador Sea into the IB is up to two years - much longer than the six months which would be required to match the distribution of LSW, assuming that no LSW was formed in the IB (Sy et al., 1997). Thus the idea, formulated by Nansen (1912) and long since discarded, that LSW can be formed by deep convection in the IB, needed to be revisited.

The basin-scale circulation is driven by a local, seasonally variable, wind stress curl that reaches maximum intensity in February (Figure 2.11; Spall and Pickart, 2003). This phenomenon, known as the Greenland tip jet (Doyle and Shapiro, 1999), develops periodically in the lee of Cape Farewell (the southern tip of Greenland). It forms when high-level northwesterly winds are accelerated, due to the Bernoulli effect, over the steep topography of the eastern (leeward) side of Greenland, drawing very cold air over the southern IB. February tends to experience the most tip-jet events, although there is little variation throughout the winter months (December – March). Additional events often also occur in late autumn and early spring (Pickart et al., 2003b). The tip-jet is capable of locally enhancing surface heat losses for short periods, and thus has the potential to induce convection. In addition, the vertical scale of circulation is much larger than the mean depth of the basin, due to generally weak stratification and steeply sloping bathymetry at the boundaries of the basin. The circulation is maintained in an approximately steady state by the existence of slow topographic Rossby waves (Spall and Pickart, 2003). The cyclonic circulation in the basin causes upward doming of isopycnal surfaces, suggesting that, provided buoyancy fluxes are large enough to produce convective overturning, these domed regions are sites where water mass transformation could most easily occur (Pickart et al., 2003b).

The response of the IB to tip-jet events was investigated with a primitive equation model by Pickart et al. (2003b). The model produced a region of increased surface density and deep mixed layers, approximately 200 km in diameter, to the east of Cape Farewell. The deepest mixed layers, which took up to 2.5 months to develop, were 2000 m deep (Figure 2.12). Indirect support for deep convection in the IB came from Pickart et al. (2003a) who compared wintertime heat flux, wind stress curl and potential vorticity conditions in the IB to those in the Labrador Sea. The authors reasoned that as the meteorological and hydrographic properties were similar in both regions then the deep convection seen in the Labrador Sea could also be expected in the IB. They supported this argument with results from an advective-diffusive model which predicted a mixed layer depth of ~1800 m.

In situ studies of potential deep convection in the IB have had mixed results. Hydrographic sections, combined with Argo drifting float data, showed evidence of convection to 700-1000 m in March 1997 to the southwest of the tip of Greenland (Figure 2.13; Bacon et al., 2003). However an atlas of hydrographic sections published by Grant (1968) showed mixing down to only 400-500 m. More recently, data collected from Argo floats between 1994 and 2003 in the IB suggested that the typical mixed layer depth at the end of winter is ~400 m, with maximum values of ~850 m occasionally observed. (Centurioni and Gould, 2004). These estimates agree with two *in situ* studies by Lavender et al. (2000) and Lavender (2002) and also with the results from three 1-D mixed layer models all of which recorded an average winter mixed layer depth of 400 m. It should be noted that whilst Pickart et al. (2003b) initialised their model with a cast from a late summer cruise in a high NAO year, Centurioni and Gould (2004) used a mean profile of March and April conditions from 1994 to 2003. On the other hand Argo floats take a profile only every 10 days and so are not ideally suited to investigating highly localized convective events, possibly associated with horizontal scales of ~10 km (Clarke and Gascard, 1983).

All the studies described above emphasise the importance to deep convection of pre-conditioning - the weakening of stratification by buoyancy fluxes. As tip-jet events are triggered by storms passing to the northeast of Cape Farewell, so they are influenced by the phase of the North Atlantic Oscillation (NAO). A positive index is associated with a more northeasterly storm track, and so a greater number of storms will pass near Greenland (Rogers, 1990). Both modelling studies by Pickart et al. (2003a, b) found that convection reached to only ~700 m when the initial density profile was representative of stratification during low NAO periods. This suggests that overturning is unlikely to occur during low NAO years, or in the first winter of strong forcing following a low NAO period. Centurioni and Gould (2004) point out that between 1997 and 2003, when no or little indication of deep convection was seen, the NAO was generally low.

Even without the tip-jet events the Irminger Basin experiences severe meteorological conditions. In winter some of the strongest wind stress curl anywhere in the world ocean is found in the vicinity of Greenland (~ 10^{-6} Nm^{-3}), often an order of magnitude greater than over the rest of the subpolar North Atlantic (Milliff and Morzel, 2001). In addition to tip-jet events as defined by Pickart et al. (2003b), reverse tip-jet events have also been observed (Moore, 2003). These high speed wind events generally occur in winter and are characterised by easterly flow i.e. in the opposite direction to the tip-jet. Analysis by Moore (2003) suggests that the reverse tip-jet events are almost as common as tip-jet events, and, in contrast to the tip-jets, are more likely to occur in a negative NAO winter. He concludes that tip-jet events tend to occur when the cyclone centre is to the northeast of Cape Farewell, while reverse tip-jets occur when the cyclone centre is south of Cape Farewell (Figure 2.14).

During winter the Irminger Basin also experiences large negative (i.e. out of the ocean) net air-sea heat fluxes. Surface heat fluxes are regularly around -300 Wm^{-2} but during a tip-jet event surface heat fluxes can become as large as approximately -800 Wm^{-2} for a day or two (Doyle and Shapiro, 1999). The net heat flux becomes positive (i.e. into the ocean) around early April, reaches a maximum of ~150 Wm^{-2} during June and July and becomes predominantly negative again in September, although storms can cause short spells of negative heat flux during an otherwise warm period (Waniek and Holliday, 2005). Mean surface temperatures between January and March are ~4-5 °C throughout most of the basin, with the Reykjanes Ridge area a couple of degrees warmer and the Greenland coast region a little cooler (Centurioni and Gould, 2004). In summer (June – September) the surface temperature reaches ~9-11 °C, again with the Reykjanes Ridge a little warmer and the Greenland coastal region cooler (Holliday et al., 2005).

2.2.2. BIOLOGICAL CHARACTERISTICS:

The northern North Atlantic is regarded as a very productive region of the world ocean. Certainly several major fisheries are located in this region, principally based in Iceland and western Scotland. Although, for the Irminger Basin, few direct measurements of primary productivity exist, satellite chlorophyll-derived estimates suggest that new production is at least ~100-150 $gCm^{-2}yr^{-1}$ (Laws et al., 2000; Falkowski et al., 1998) and total production may be as high as ~250 $gCm^{-2}yr^{-1}$ (Platt et al., 1991a). Such a contribution to the biological carbon pump would certainly be significant.

The Irminger Basin lies within the Atlantic Arctic province of Longhurst (1998) which extends from the Greenland shelf towards the Iceland Basin and is bounded in the south by the Polar Front. He notes (from CZCS ocean colour images) that the spring bloom in the region occurs simultaneously and patchily, rather then following the northward progression of the shoaling seasonal pycnocline. The IB was further sub-divided into six zones by Holliday et al.

(2005). The zones were defined based on surface and shallow water types and chlorophyll-a profiles. The regions are the Central Irminger Sea, the Irminger Current (sub-divided into Northern and Southern zones), the East Greenland Current (sub-divided into a cold and fresh Polar zone and a warm Atlantic region) and the Reykjanes Ridge (Figure 2.15). Each region experiences different hydrographic conditions and the phytoplankton response varies accordingly. In the northern North Atlantic the widely accepted picture of the typical seasonal cycle in phytoplankton is expected to follow the classic Sverdrup theory (see Section 2.1.1; Sverdrup, 1953). The following data describing a typical seasonal cycle were mainly collected during a series of cruises to the Irminger Basin (Marine Productivity programme) in November/December 2001, April/May 2002, July/August 2002 and November/December 2002.

Winter chlorophyll concentrations in the Irminger Basin are very low – typically <0.1 mgm^{-3} (Holliday et al., 2005). Concentrations of the major inorganic nutrients are high with nitrate at 12-14 μmol l^{-1}, silica of 5-8 μmol l^{-1} and phosphate of 1.1-1.3 μmol l^{-1} (Sanders et al., 2005). As expected in the poor light and deep mixing conditions in winter, primary production was estimated in December 2002 (using the C^{14} method) to be low, at 0.01-0.27 mgCm^{-3}h^{-1} (Astoreca, 2003).

The principal mesozooplankter found in the Irminger Basin is the copepod *Calanus finmarchicus* (Heath et al., 2000). During winter *C. finmarchicus* enter a diapause state (Hirche, 1996) and, in the IB, descend to a depth of ~1000 m (Heath et al., 2004). In the late summer and autumn development is arrested during moulting stages IV and V and the *C. finmarchicus* descend to (it is assumed) a neutral buoyancy depth. The arousal from diapause, transition to stage VI (full maturity) and migration to the surface to spawn does not take place until late winter-early spring of the following year (Heath, 1999; Gislason and Astthorsson, 2000). The timing of the arousal from diapause needs to coincide with the start of the phytoplankton spring bloom to ensure sufficient food exists for reproduction. *C. finmarchicus* can produce eggs before the bloom starts, but the resulting nauplii are only able to recruit to copepodites if egg production is coincident with the phytoplankton bloom (Niehoff et al., 1999; Hirche et al., 2001). As it takes ~37 days to develop from an egg into a feeding form of *C. finmarchicus* the timing of the end of diapause is clearly crucial to the zooplankton's continuing survival, however the mechanism by which *C. finmarchicus* time their ascent is unknown (Mayor et al., 2004).

When spring arrives with its increasing light levels and milder weather a phytoplankton population explosion occurs. The mechanism behind the North Atlantic spring bloom is explained in Section 2.1.1 and so will not be revisited here. The bloom in the IB does not progress neatly northwards as Sverdrup's theory would suggest. Instead it is expected to begin earliest around the coasts of Greenland and Iceland in late April/early May, reaching the central IB in late May (Longhurst, 1998). Peak chlorophyll concentrations are found around the coastal regions and can reach 10 mgm^{-3} (Holliday et al., 2005). During the Marine Productivity cruises in 2002, flagellates and ciliates dominated the early stages of the bloom in the central Irminger Basin (Figure 2.16), whilst along the Reykjanes Ridge diatoms formed a large part of the phytoplankton population (although note that these stations were occupied ~20 days later than those in the central basin; Holeton et al., 2004). Along the Greenland coast a massive *Phaeocystis sp.* bloom was observed in mid-May, prompted by an influx of freshwater from spring melting of sea ice (Waniek et al., 2005). The input of freshwater promotes a sufficiently stratified surface layer that small phytoplankton can begin to grow. At the surface, nitrate becomes quickly depleted, whilst silica remains close to winter levels, so silicious phytoplankton i.e. diatoms, are apparently not able to so easily exploit the early freshwater-induced stratification.

The Marine Productivity cruises in July/August 2002 found that nitrate concentrations do not reach levels likely to be limiting to growth anywhere in the basin at anytime during the year. Silica however is depleted by the summer along the Greenland coast (Sanders et al., 2005). Surface chlorophyll concentrations were generally <1 mgm^{-3}, although at some stations a chlorophyll maxima was observed at the base of the mixed layer (Holliday et al., 2005). Although the very high values of the peak of the bloom are no longer seen the chlorophyll concentration is still 10 times that of winter and primary production is capable of being sustained at a rate of 0.02-1.57 $mgCm^{-3}h^{-1}$ (Astoreca, 2003). The concentration of diatoms was again relatively low, with flagellates and picoplankton dominating the phytoplankton population (Figure 2.16; Holeton et al., 2004).

Estimates of new production in the IB have been made on the basis of nitrate drawdown and temperature-nitrate relationships. Henson et al. (2003) used a relationship between SST and nitrate, combined with estimates of spring and summer mixed layer depth from Argo floats, to estimate annual new production of ~60 $gCm^{-2}yr^{-1}$. An estimate based on nitrate drawdown between the spring and summer cruises, including terms for nitrate flux across the thermocline and atmospheric deposition, put new production at ~36 $gCm^{-2}yr^{-1}$ (Sanders et al., 2005). Waniek et al. (2005) estimated the annual new production on the Greenland shelf to be 76 $gCm^{-2}yr^{-1}$, again based on nitrate drawdown and a productive period of 6 months. However, results from a 1-D model (Waniek and Holliday, 2005) put the figure close to between 36 $gCm^{-2}yr^{-1}$ for the East Greenland coast and 46 $gCm^{-2}yr^{-1}$ for the northern Irminger Basin.

2.3. SUMMARY:

This introduction has demonstrated the lack of consensus in the literature on the conditions necessary for a spring bloom to be initiated. The Irminger Basin itself is rarely visited by research vessels, and so the Marine Productivity data set offers a unique opportunity to investigate the seasonal characteristics of the region. But only by combining the *in situ* data with satellite data can the necessary spatial and temporal context be determined.

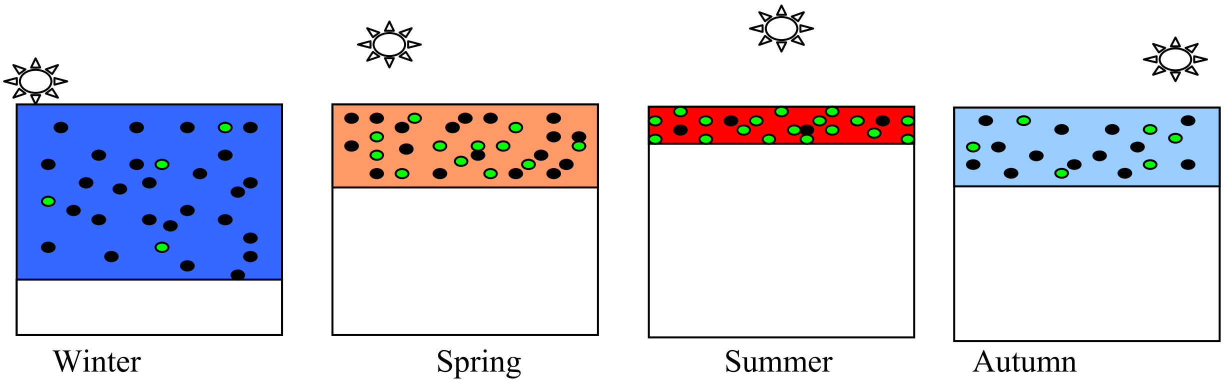

Figure 2.1: Sketch of annual cycle of mixed layer depth and nutrient and phytoplankton concentrations. Black dots represent nutrients and green dots represent phytoplankton. Winter conditions: deep mixed layer, cold surface waters, low light levels, high nutrient concentrations, low phytoplankton concentration. Spring conditions: shallowing mixed layer, increasing surface temperature and light levels, rapidly increasing phytoplankton and decreasing nutrient concentrations. Summer conditions: shallow mixed layer, warm surface temperature, high light levels, high phytoplankton but very low nutrient concentrations. Autumn conditions: Deepening mixed layer, cooling surface temperature, decreasing light levels, increasing nutrient and decreasing phytoplankton concentrations.

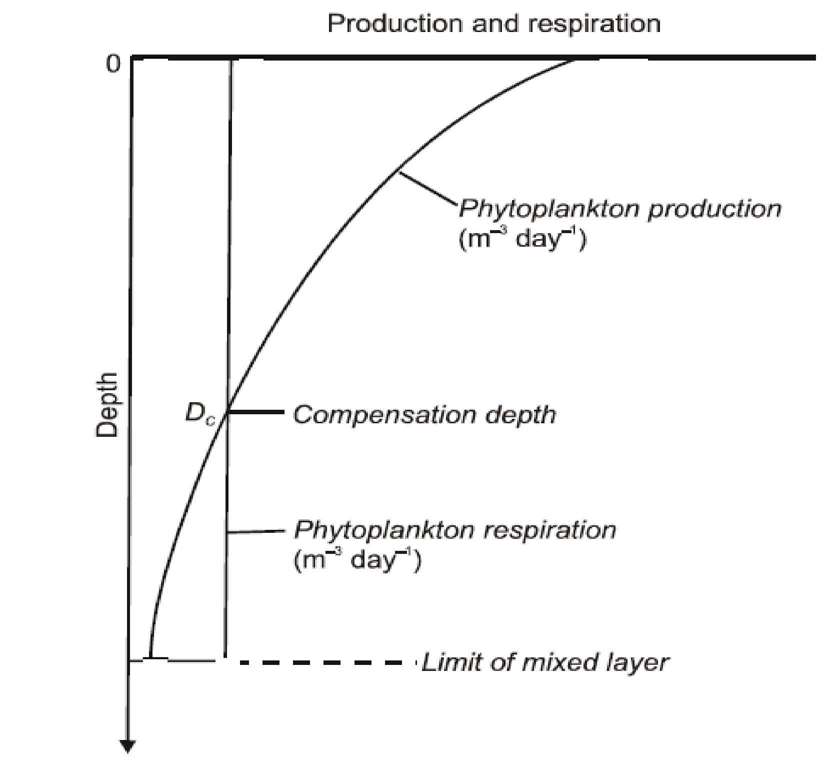

Figure 2.2: Diagram illustrating theoretical distribution of phytoplankton production and respiration. Redrawn from Mann and Lazier (1996), after Sverdrup (1953). The compensation depth is defined as the depth at which the daily rate of photosynthesis equals the daily rate of respiration. The compensation depth is generally taken to be the 1% (of surface irradiance) light depth. The critical depth is the depth at which the water column integrated production is equal to the integrated respiration. In order for *net* growth to occur the mixed layer depth must be shallower than the critical depth.

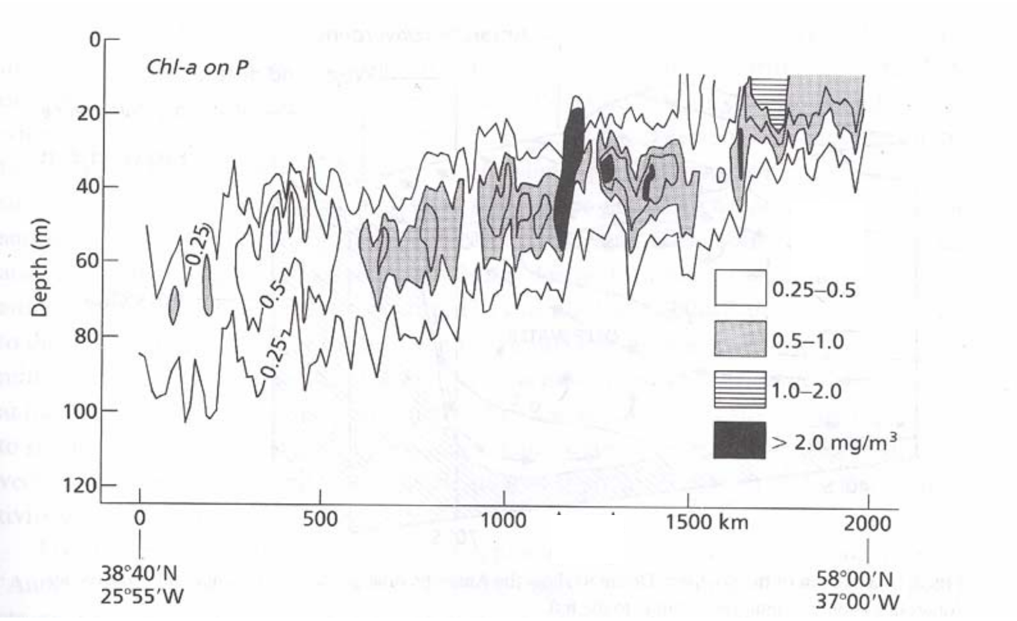

Figure 2.3: Vertical distribution of chlorophyll on a transect between the Azores and Greenland in late summer. Note that the zone of maximum chlorophyll gets progressively more shallow towards the north. From Strass and Woods (1998).

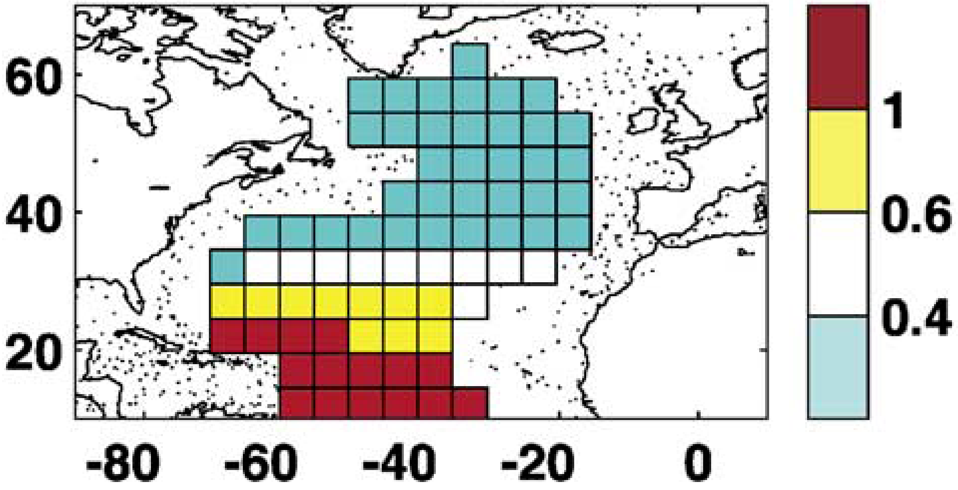

Figure 2.4: Map of climatological ratio of h_c/h_m, the spring critical layer depth (m) over end of winter mixed layer depth (m). Where h_c/h_m is low (subpolar regions) the depth of mixing can become shallower than the critical depth and Sverdrup's critical depth model can be expected to hold. In regions of high h_c/h_m (subtropical regions) phytoplankton are mixed to depths similar to the critical depth. From Follows and Dutkiewicz (2002).

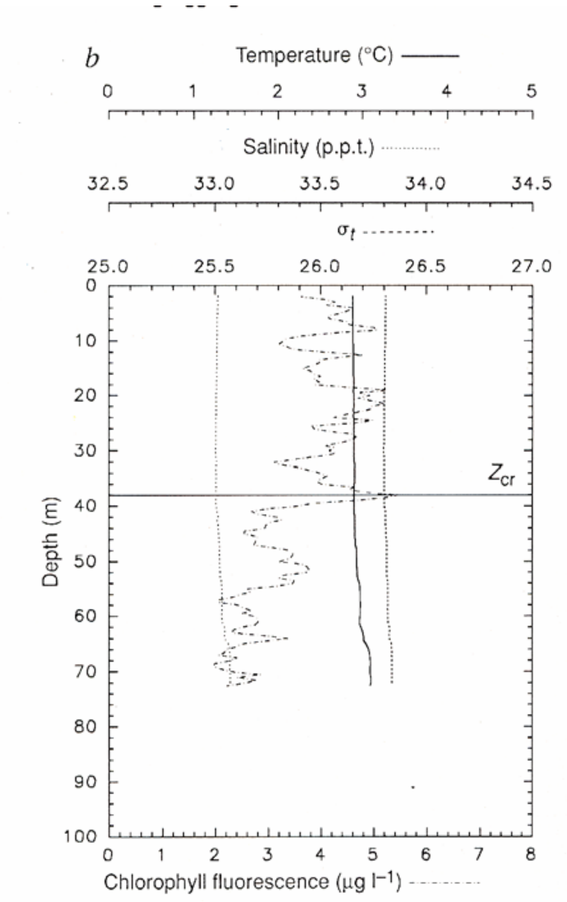

Figure 2.5: Vertical profiles of chlorophyll fluorescence, temperature, salinity and density measured in Massachusetts Bay, western Gulf of Maine, in March. Note that a bloom of chlorophyll is occurring in the absence of vertical stratification. A critical depth (Z_{CR}) of 38m is marked. From Townsend et al. (1992).

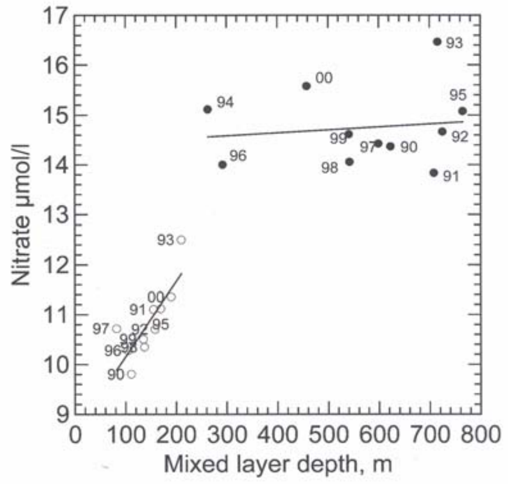

Figure 2.6: Surface nitrate concentration against winter (February) mixed layer depth from fixed stations in the Iceland (open circles) and Irminger Basins (filled circles) for 1990-2000. Numbered symbols indicate years. Whilst a statistically strong relationship is seen in the Iceland Basin, there is no correlation in the Irminger Basin. From Olafsson (2003).

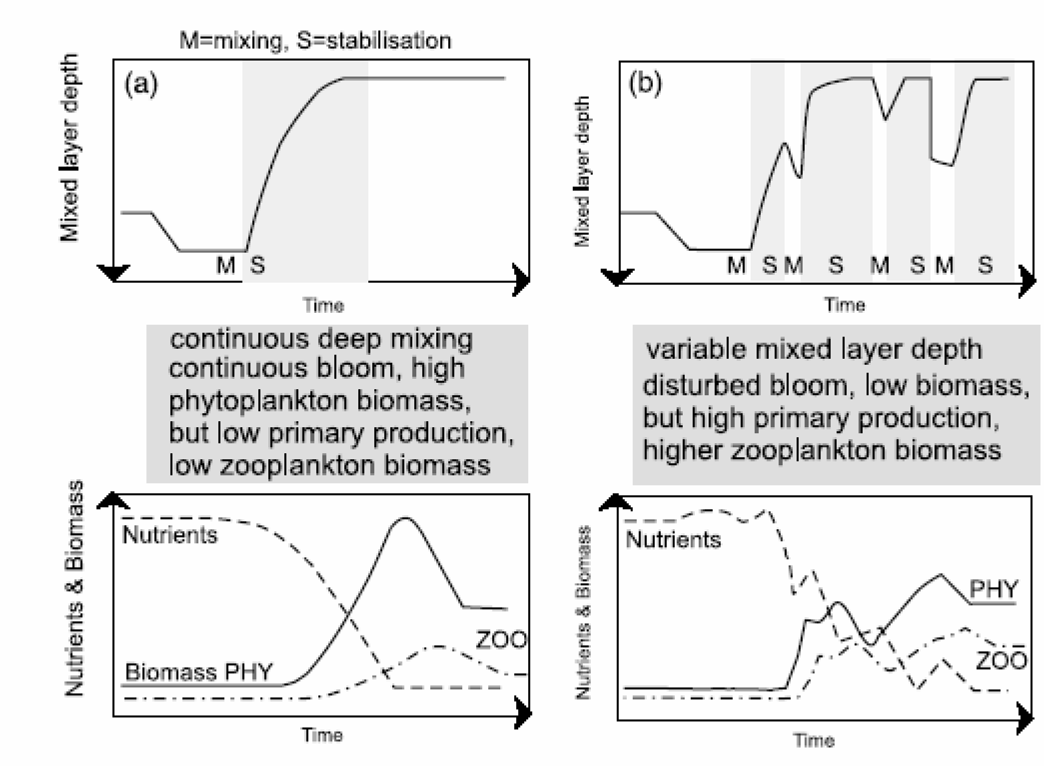

Figure 2.7: Sketches of bloom characteristics: (a) continuous bloom with the typical mixed layer distribution and the associated development of the biomass and nutrient concentrations, (b) disturbed bloom and its characteristics. The periods of mixing (M) and stabilisation (S) of the water column are indicated. From Waniek (2003).

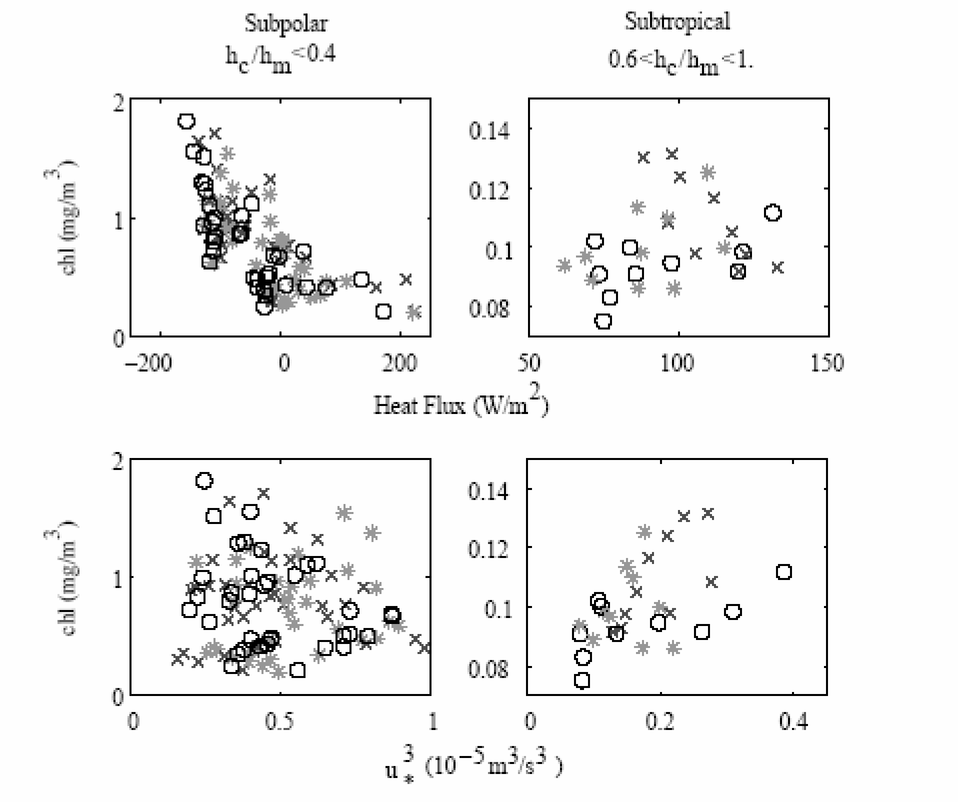

Figure 2.8: SeaWiFS chlorophyll (mg m^{-3}) for each of three bloom periods (circles: 1998, crosses: 1999 and asterisks: 2000) plotted against (top panel) heat flux (W m^{-2}) and (lower panel) friction velocity, u^3_* (x 10^{-5} m^3 s^{-3}). Low (subpolar) and high (subtropical) h_c/h_m (ratio of critical depth to winter mixed layer depth) regimes are shown (see also Figure 2.4). Data are averaged over the bloom period and for five degree bins. Note that for the subpolar region there is no clear trend between the chlorophyll concentration and the heat flux or wind forcing. From Follows and Dutkiewicz (2002).

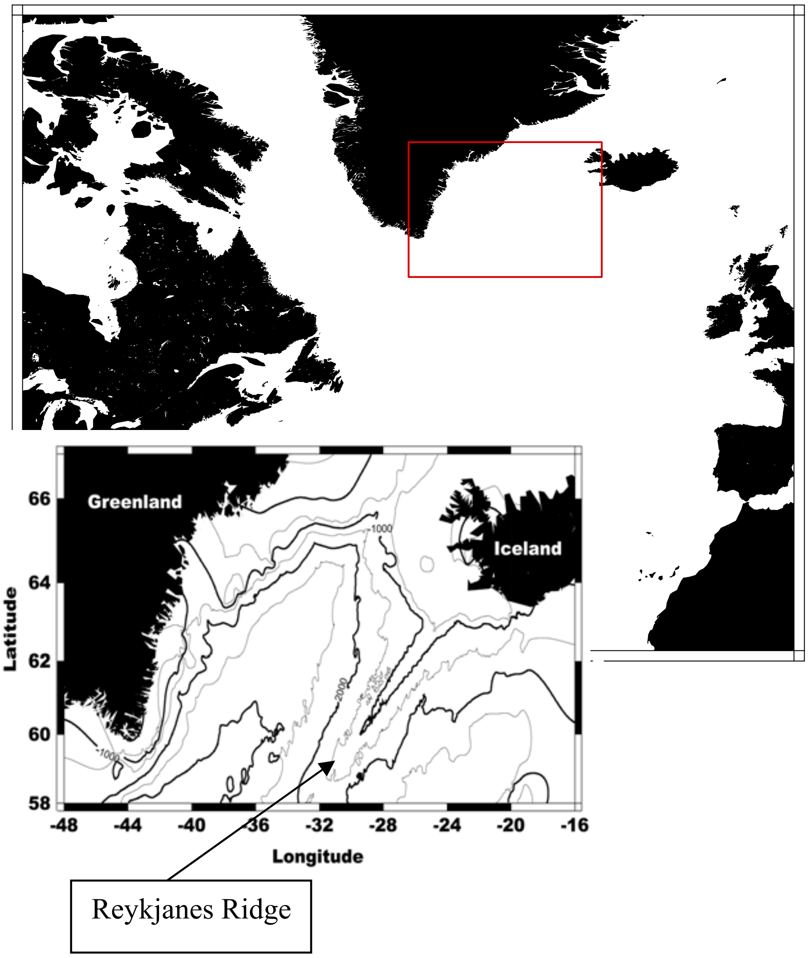

Figure 2.9: Map showing the location of the Irminger Basin (inset) in relation to the North Atlantic. Small map shows the bathymetry of the basin and location of Iceland and Greenland.

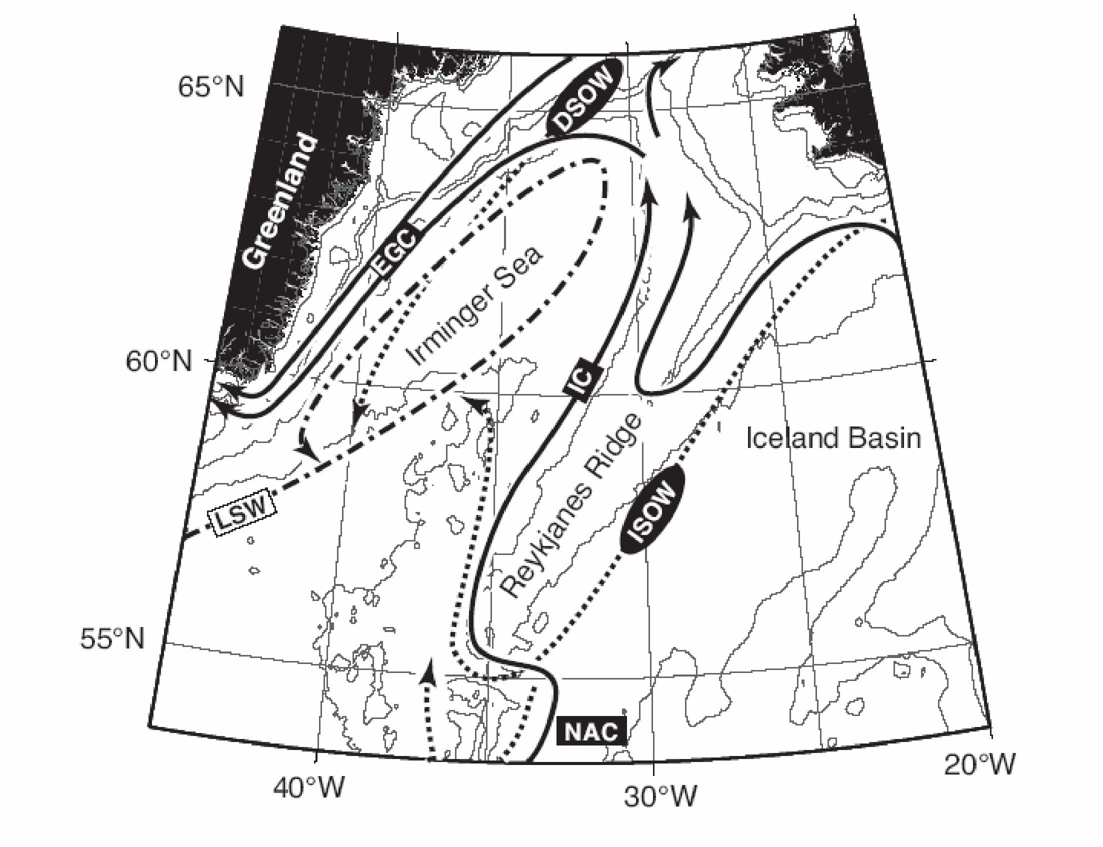

Figure 2.10: Schematic showing the main circulation features of the Irminger Basin. Surface currents are shown by solid lines (NAC: North Atlantic Current, IC: Irminger Current, EGC: East Greenland Current). Mid-depth currents are shown by the dot-dash line (LSW: Labrador Sea Water). Deep currents are shown by dotted lines (ISOW: Iceland-Scotland Overflow Water, DSOW: Denmark Strait Overflow Water). Depth contours are 0, 500, 1000, 2000, 3000 and 4000 m. From Holliday et al. (2005).

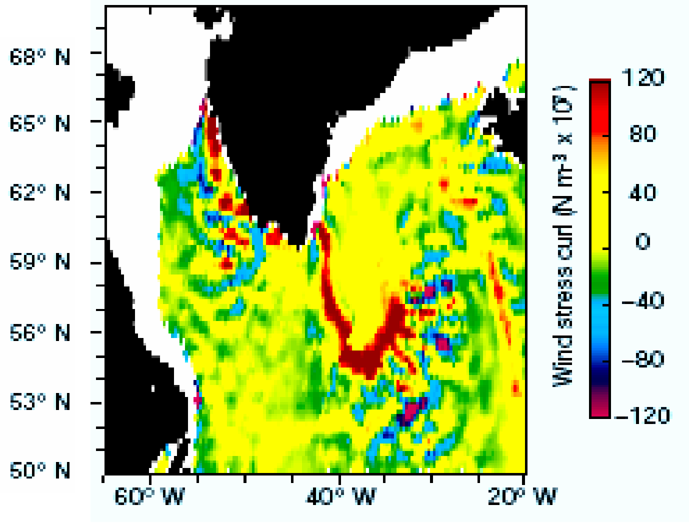

Figure 2.11: Wind stress curl during a tip-jet event on the 12th January 2001. Note the high wind stress off the southern tip of Greenland. Image from the radar scatterometer aboard the QuikSCAT satellite. From Dickson (2003).

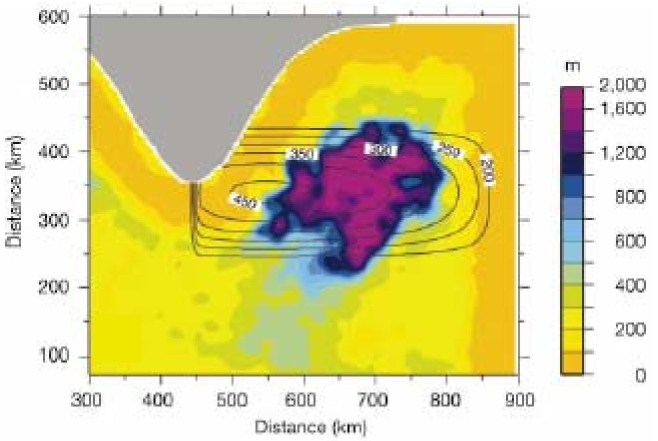

Figure 2.12: Tip-jet event as seen in a regional numerical model. Mixed layer depth in winter (coloured contours) overlaid by the idealised tip-jet heat flux forcing (line contours in W m^{-2}). The grey mass at the top of the figure represents Greenland. From Pickart et al. (2003).

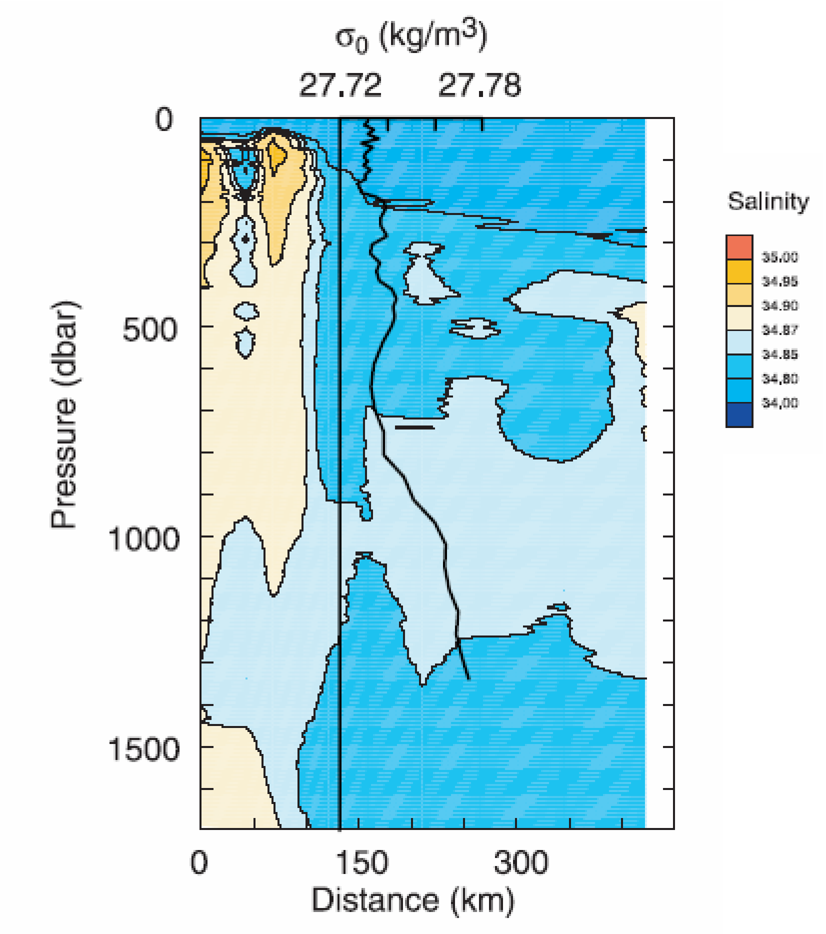

Figure 2.13: Colour contours are salinity data from a CTD transect taken due east away from the Greenland coast at ~ 60°N in July 1997. The overlying black line is a potential density profile from an Argo float taken on 16th March 1997. The vertical axis at σ_0 = 27.2 kgm^{-3} shows the float location relative to the section. From Bacon et al. (2003).

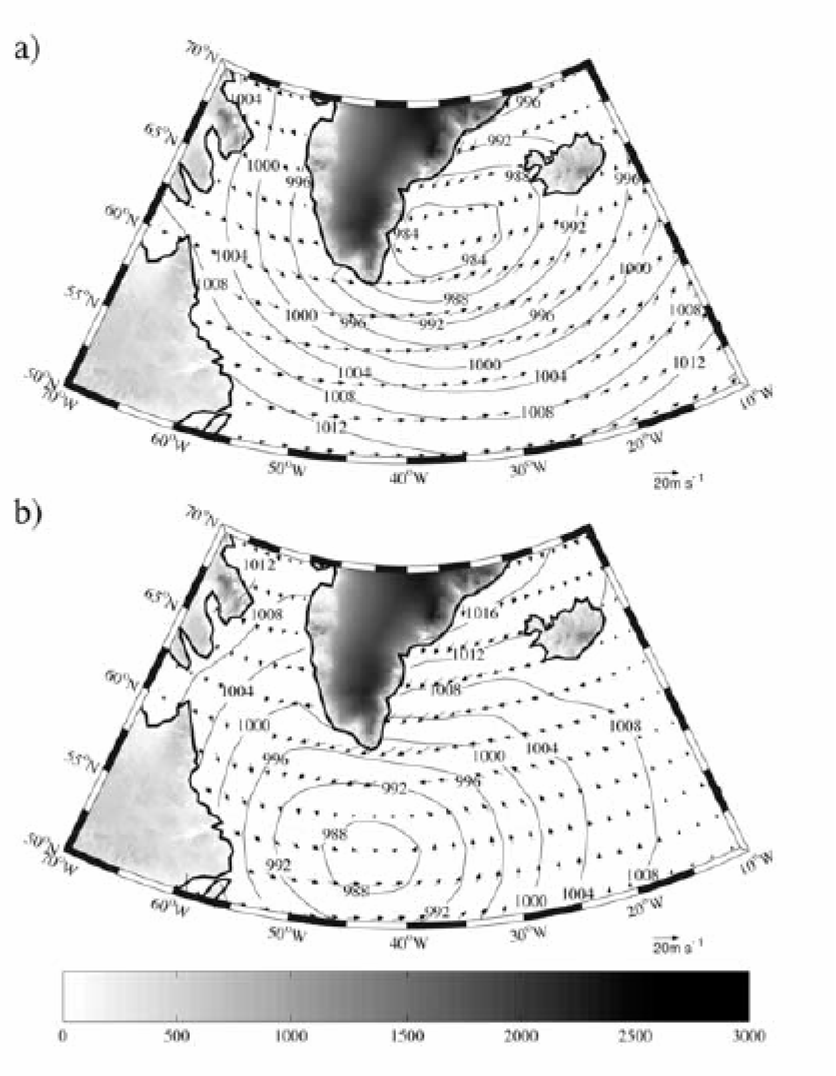

Figure 2.14: Composite sea-level pressure (mb - contours) and 10 m winds (ms^{-1} - vectors) for a) tip-jet events and b) reverse tip-jet events over the Irminger Sea during the winter months 1948-2000 (data from the NCEP reanalysis project). Topography (m) is indicated by shading. From Moore (2003).

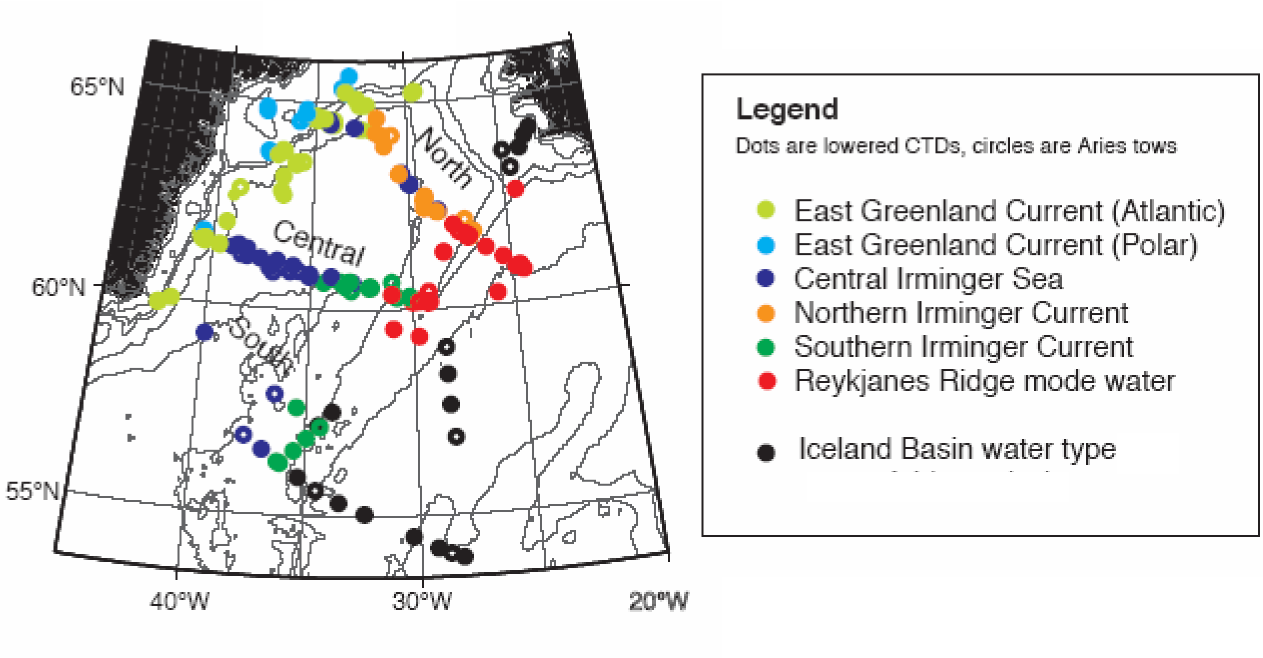

Figure 2.15: The zones in the Irminger Basin on the basis of hydrographic data from the four Marine productivity cruises. Solid circles indicate full-depth lowered CTD stations, open circles denote Aries CTD stations (tows). Depth contours are 0, 500, 1000, 2000, 3000 and 4000 m. From Holliday et al. (2005).

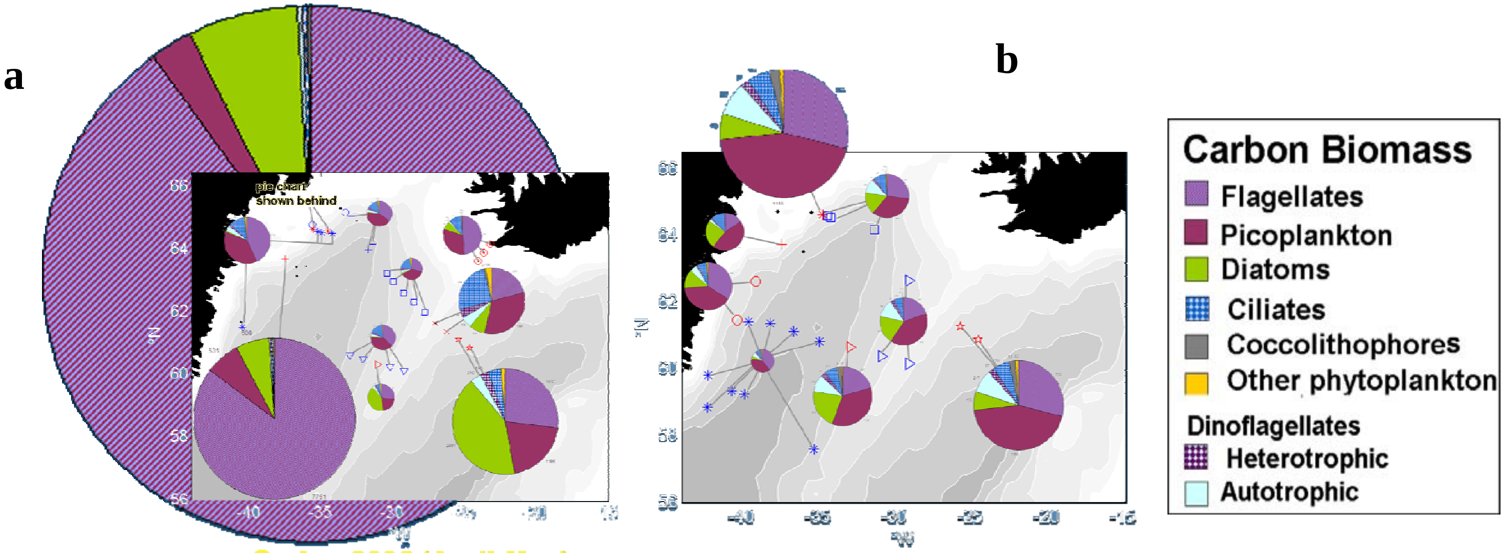

Figure 2.16: Distribution and taxonomic/species composition of depth-integrated carbon during Marine Productivity cruises (a) D262 (spring) and (b) D264 (summer). Size of the pies indicate the integrated carbon biomass of the total community from phytoplankton counts. Pies represent the averages of location with similar community structure (grouping shown by marker type; samples not included in the pie charts are shown by black dots). The large pie chart behind (a) shows a dense bloom of *Phaeocystis sp.* From Holeton et al. (2004).

3. DATA:

This study uses several different sources of satellite data, as well as a 1-D vertical mixing model and *in situ* data. The collection and processing of the *in situ* data, both electronic and water sample data, is described in the next section 3.1. The various satellite data are described in Sections 3.2 to 3.6, including a discussion on the limitations of SeaWiFS-derived chlorophyll-a concentration in Section 3.2.2. Details of processing data from the NCEP reanalysis model for net heat flux can be found in Section 3.7, and Section 3.8 discusses the Argo float profiles and estimating mixed layer depth. Finally Section 3.9 contains details of the 1-D vertical mixing model used in this study.

3.1. IN SITU DATA:

The multi-institute and multi-disciplinary Marine Productivity (or MarProd) programme is a NERC (Natural Environment Research Council) sponsored thematic programme set within the wider context of the international Global Ocean Ecosystem Dynamics (GLOBEC) project. The primary aim of the MarProd programme was to characterise the physical controls on zooplankton distribution in the Irminger Basin. As part of the programme four interdisciplinary cruises were undertaken aboard the RVS *Discovery* in early winter 2001 from 1st November to 18th December (D258), spring 2002 from 18th April to 27th May (D262), summer 2002 from 25th July to 28th August (D264) and early winter 2002 from 5th November to 20th December (D267). An extensive range of physical, chemical and biological measurements were taken, the full details of which can be found in the cruise reports (Pollard and Hay et al., 2002; Richards et al., 2002; Brierley et al., 2003; Allen et al., 2004).

3.1.1. UNDERWAY SURFACE SAMPLES:

Underway surface meteorological and thermosalinograph (TSG) measurements were made by the RSU (Research Ships Unit) Surfmet system throughout all four cruises. The inlet for the TSG system is at approximately 5m below the sea surface. The measurements made include temperature, conductivity and fluorescence recorded every second. The raw data stream from Surfmet was read into Pstar format and initial processing was done aboard ship. (Pstar is a Fortran based suite of scripts written specifically for the processing of oceanographic data - see http://www.soc.soton.ac.uk/JRD/PEXEC for documentation). Further Pstar processing ensured that absent data values were set to –999. Navigation files with the *Discovery*'s best determined position from an Ashtech G12 positioning system were merged with the TSG files. Two-minute averages of the underway data were created and merged with the vessel's heading and attitude data from the ship's ultra short baseline 3D GPS Ashtech ADU2 navigation system.

In order to calibrate the underway salinity and fluorescence measurements, water samples were taken every four hours from either the TSG sample tap or the non-toxic supply as it left the FRRF (Fast Repetition Rate Fluorometer), depending on the available water pressure. Two Guildline Autosal salinometers were installed in the *Discovery*'s chemistry laboratory. The conductivity of the discrete samples was calculated using the housing temperature and zero pressure and compared to the Surfmet conductivities. The calibration equation was applied to the Surfmet conductivities and all salinities were recalculated (accuracy ± 0.002 psu).

Samples for chlorophyll analysis were decanted into two 300ml aliquots and filtered through 25mm Whatman GF/F filters using a positive pressure filtration unit. The filters were then placed in amber glass vials containing 10ml 90% acetone and immediately stored in the dark at 5°C for 24 hours to extract the chlorophyll. Samples were warmed to room temperature before the fluorescence was measured using a Turner Designs fluorometer (TD700). Chlorophyll standard solutions (from Sigma-Aldrich Inc.) covering the expected chlorophyll range were used for calibration of the fluorometer before each set of samples was analysed. The chlorophyll concentrations were calculated from the absorbance measured at 750, 664, 647 and 630 nm in a Cecil Spectrophotometer, using the equations of Jeffrey and Humphrey (1975). Chlorophyll concentrations from the discrete samples were compared to the underway fluorescence. A single calibration was applied to the entire raw fluorescence stream.

Underway nutrient samples were taken on cruises D262, D264 and D267 concurrently with the salinity and chlorophyll samples. Concentrations of the dissolved inorganic nutrients (nitrate, phosphate and silicate) were measured in unfiltered water samples on a Skalar SanPlus segmented flow autoanalyser following the method outlined in Kirkwood (1995) and Sanders and Jickells (2000). Water was drawn into brand new 40ml diluvials and immediately refrigerated at 4°C until analysis, which commenced within 12 hours of sampling. Nutrient concentrations were calculated using calibration curves obtained from dilutions of the working standards used on the first MarProd cruise. Throughout each sample run, wash and drift standards were run every 10-15 minutes to enable baseline and drift corrections. The performance of the auto-analyser was monitored throughout the cruises and duplicates of at least three samples per station ensured the consistency of the nutrient measurements. After completion of each run data were processed using Skalar Flow Access v1.4 software and saved in both Flow Access runfile and Excel format. Overall the precision of the data from individual cruises are estimated to be better than ± 0.18 μmol/l for nitrate, ± 0.02 μmol/l for phosphate and ± 0.15 μmol/l for silicate (1% of top standard for nitrate and phosphate and 0.5% for silicate). Consistency of the data between cruises was ensured by the analysis of commercial nutrient standards (Ocean Scientific International) at regular intervals on each cruise and by the comparison of deep water nutrient concentrations.

A Fast Repetition Rate Fluorometer (FRRF) was attached to RRS *Discovery*'s non-toxic supply. The instrument can be used to make rapid, non-destructive, *in vivo* measurements of phytoplankton physiological status. Power was provided by a standard Chelsea Instruments deck unit. Data were recorded internally and downloaded every 24 hours to a PC laptop. The optical chamber was cleaned every two days using a soft white tissue and little finger. The FRRF settings induced variable fluorescence using a flash protocol of 100 saturation flashes per sequence with a flash duration of 4 μs. There were 20 flashes per relaxation sequence with a flash duration of 4 μs, a relaxation interflash delay of 61 μs and a 10 s sleeptime between acquisition pairs. Acquisition pairs were averaged in groups of 32 to reduce noise in the data. F_v/F_m and σ_{PSII} were calculated by fitting the measured saturation curves to the biophysical model of Kolber et al. (1998) using Matlab code based on software provided by S. Laney ('v4'; Laney, 2003). Only data collected during the night time were used in the analysis in order to minimise physiological effects associated with daylight.

3.1.2. CTD DATA:

The CTD (Conductivity, Temperature, Depth) package used on all four cruises consisted of a frame with 24 x 10-litre sample collection bottles, two Temperature-Conductivity pairs, an oxygen sensor, fluorometer, transmissometer and ADCP (Acoustic Doppler Current Profiler). On the summer (D264) and second winter cruise (D267) a FRRF was also attached to the CTD frame for short vertical casts to determine the light profile before each primary productivity CTD cast. A map of the study region showing the location of CTD stations is displayed in Figure 3.1. Raw full-rate data recorded from the CTD casts were initially processed using Pstar to de-spike the data, average over 1 second and calculate density from the temperature and salinity measurements. From full profile CTDs samples were taken in the following order: oxygen, nutrients, salinities and chlorophyll. The standard bottle firing depths were (wire out in metres): 5(x2), 10, 25, 50, 75, 100, 125, 150, 200, 300, 400, 600, 800, 1000, 1250, 1500, 1750, 2000, 2250, 2500, 2750, bottom. Chlorophyll samples were drawn from the top six rosette bottles for chlorophyll-a and other pigment studies and size fractionation. The chlorophyll-a samples were analysed fluorometrically as outlined above and used to calibrate the CTD fluorometer. Calibration was carried out on a cruise-by-cruise basis by calculating a linear fit (least squares regression) between all the bottle samples and CTD fluorescence (after initial SeaBird calibration from volts to mgm^{-3}). No correction was made for quenching. Standard deviations of residuals were 0.05 mgm^{-3} for D258, 0.2 mgm^{-3} for D262, 0.14 mgm^{-3} for D264 and 0.016 mgm^{-3} for D267 (Holliday et al., 2005). Similarly salinity samples were analysed as above and used to calibrate the conductivity sensor. A single Pstar format file containing the CTD instrument data plus the bottle sample measurements (e.g. nutrients, chl-a etc.) was created for each CTD cast.

Phytoplankton samples for species identification analysis were taken at the surface, the chlorophyll maximum and at 100 m depth. Duplicates of 100 ml samples at each depth were preserved with 1% Lugol's solution and 2 % buffered formalin. Taxa counts were performed by inverted microscopy. Biovolume was calculated for each protist plankton species (Kovala and Larrance, 1966) then converted to carbon biomass following carbon to biovolume relationships described for diatoms (Menden Deuer and Lessard, 2000) and non-diatom protist plankton (Strathman, 1967). Picoplankton samples were enumerated with a LEICA DMIRB microscope with a 1000x magnification.

3.2. SEAWIFS CHLOROPHYLL-A:

The principle that particulate and dissolved substances suspended in water will interact with incident light forms the basis of ocean colour remote sensing. In conditions typical for the open ocean, where concentrations of particulate matter and dissolved substances are low, water molecules scatter light in a way similar to the atmosphere, producing a characteristic deep blue colour. The scattering of light by particulates and the absorption of light by dissolved substances will alter this colour. Chlorophyll, the photosynthetic pigment found in phytoplankton, absorbs strongly in the red and blue regions of the visible light spectrum, but not in the green. Therefore as the concentration of phytoplankton increases, the colour of the water will appear increasingly green. The absorption of light can be quantified to determine the concentration of chlorophyll in the water, allowing estimation of phytoplankton abundance in a given area (McClain et al., 2000).

The SeaWiFS instrument, carried aboard the SeaStar satellite, began acquiring data on the 16th September 1997 and is still operational. The project's purpose is to obtain global ocean colour data and to process that data, in conjunction with ancillary data, into meaningful biological parameters (Hooker et al., 1992). The value of satellite-measured ocean colour to biological oceanography was proved by the Coastal Zone Colour Scanner (CZCS) instrument, whose demise in 1986 prompted the development of SeaWiFS. Whilst CZCS was envisioned as a proof-of-concept sensor, SeaWiFS was specifically designed to study ocean colour. The instrument has six visible wavelength wavebands and two high-sensitivity near-infrared wavebands (Table 3.1). Selection of the SeaWiFS wavebands was based on consideration of the spectral absorption characteristics of common in-water optical constituents, mean extra-terrestrial irradiance and spectral transmittance of atmospheric constituents.

3.2.1. DATA PROCESSING:

SeaWiFS data are freely available for scientific research purposes subject to prior approval by the SeaWiFS project and with a two-week embargo period. Level 1A Local Area Coverage (LAC) 1km resolution data were downloaded from the password protected Distributed Active Archive Center (DAAC) site at http://daac.gsfc.nasa.gov/data/dataset/SEAWIFS/. L1 data consists of at-spacecraft raw radiance counts with calibration and navigation information available separately in the data file. All satellite passes available from the HRPT (High Resolution Picture Transmission) station HDUN (Dundee University) between March and October 1997-2003 were ordered. Data prior to March and after October were very cloud-contaminated and the low incidence angle of solar radiation masked large parts of the study region. In addition the ancillary data files containing TOVS and EPTOMS ozone measurements and NCEP meteorology data were downloaded. The data were ordered in 2-weekly blocks, limited by size constraints on the NASA ftp site (maximum 2GB per order) and file storage space at NOCS. After a delay of approximately 6 hours the data were available to download from the NASA ftp site (ftp:\\daac.gsfc.nasa.gov) as Hierarchical Data Format (.hdf) files.

NASA provide IDL-based software, SeaDAS, which enables users to process and display Level 1 to 3 SeaWiFS data (http://seadas.gsfc.nasa.gov). SeaDAS v4.0 has an interactive user-interface and allows the user to generate a Level 2 product from the Level 1 files supplied from the DAAC. L2 data consists of five normalized water-leaving radiances and seven geophysical parameters (including chlorophyll-a concentration: chl-a) derived from the radiance data. Processing to L2 with the SeaDAS software also outputs the L2 flags, which mark areas where confidence in the chl-a product is low. Each flag has a code denoting why the pixel has been flagged. The reasons for low confidence cover a wide range of atmospheric and geophysical effects, such as sun glint, too high a wind speed, ice and coccolithophore blooms. At this stage in the processing the ozone and meteorological data files are used to correct for atmospheric effects, such as light scattering and sun angles differing from the nadir. The calculation of chl-a uses the NASA OC4 algorithm:

$$R = \log((Rrs443 > Rrs490 > Rrs510)/Rrs555)$$
$$C = 10^{(a0 + a1*R + a2*R^2 + a3*R^3)} + a4$$

where *Rrs* is the remote sensing reflectance at a particular wavelength, *C* is the derived chlorophyll-a and *a0* to *a4* are constants calibrated to the SeaBASS *in situ* chl-a dataset (see Section 3.2.2 for a discussion of SeaBASS). In the multi-band technique the maximum ratio between the three wavebands at 443, 490 and 510 nm is used as the numerator in the above equation. This method should improve estimation of chl-a at low concentrations and prevent saturation at concentrations of chl-a > 1.5 mgm^{-3} (O'Reilly et al., 1998).

The next stage is to project the L2 product onto a suitable reference grid. The navigation data are included so that land masks may be correctly placed. For this dataset a cylindrical projection was chosen and the region bounded by 55N-

66N, 44W-20W was extracted into an image 1000 x 1000 pixels, so that each pixel covered an area ~1km^2. To carry out this procedure using the SeaDAS interface for the ~1000 images downloaded would have been extremely time consuming. In response Dave Poulter (Laboratory for Satellite Oceanography, NOCS) wrote an IDL script, SeaPiCK, which allowed the user to batch process L1 files to L2 projected files. This increased the efficiency of processing immensely and allowed each 2 week long batch of data to be processed in ~12 hours without any further input from the user.

The resulting hdf files contain mapped chl-a and L2 flag data, each a single swath from every satellite pass that was within range of the Dundee University receiving station. For each day up to 3 images were available, each covering a different part of the study region. Daily and 3-day composites of the data were created from the swaths. A further IDL script written by Dave Poulter created the composites by calculating the median, for each pixel, across all images where data for that pixel were available. 3-day means were only created if at least two out of the three days contained data. The script outputs a bitmap file with pixels on a digital colour scale from 0 (black) to 255 (white) with the land masses overlaid. To convert from digital number to chl-a the following equation must be applied:

$$C = \frac{(\exp(D * 0.035))}{100}$$

where D = digital number and C = chl-a concentration.

A script was written to read the bitmap files into Matlab. The script allows the user to specify the latitude and longitude of the study region and the averaging interval required (e.g. into 0.5° x 0.5° boxes). The resulting images were found to be rather ‘speckled’ – that is they contained isolated pixels of unreasonably high chl-a values, probably due to cloud contamination. In an attempt to remove these spurious values pixels which lay outside 2 standard deviations of the mean chl-a value were set to NaNs (Not a Number – the Matlab designation for missing data). The data are then split into squares of size specified by the user and a mean value for that box is calculated. Where sufficient data were available the chl-a data were interpolated – this bridged small data gaps, but could not fill in large areas affected by cloud. This script outputs a 3-D matrix of chl-a for each year of data. The matrix size is ((lat_start-lat_end)/size of box, (lon_start-lon_end)/size of box, number of weeks) e.g. for 55N-66N and 44W-20W split into 0.5° boxes for 365 days the matrix will be of size (22 x 48 x 365). This format allows easy manipulation and plotting of the data and comparison with other datasets. Monthly means were also created from the daily files for March to October for 1998 – 2003.

3.2.2. LIMITATIONS OF SEAWIFS CHLOROPHYLL-A DATA:

The SeaWiFS instrument purports to achieve radiometric accuracy to $\pm$ 5% and retrieved chlorophyll-a concentration to an accuracy of $\pm$ 30%. The difference in achievable accuracies between the measured water-leaving radiance and the chlorophyll-a product indicates that accurately retrieving biological information from ocean colour measurements is not a straightforward task.

Even before algorithms to estimate chl-a from ocean colour are considered, a key difficulty lies in the small range of radiances measured by the satellite. Figure 3.2 shows results from a model which simulates a high latitude ocean with a typical, cloud-free atmosphere (Hooker et al., 1992). Note that virtually the entire range of oceanic chlorophyll (from 0.01 to 10 mgm^{-3}) is contained within a very narrow band of at-satellite radiances, requiring a highly stable and sensitive instrument with precise corrections for atmospheric radiances.

The optical signal reaching SeaWiFS contains information not just about the surface layer, it also contains contributions from deeper within the water column (Platt and Sathyendranath, 1988). However, the signal is strongly damped by the attenuation between the surface and at depth. This damping reduces the contributions from deeper than one attenuation length to negligible levels. The attenuation depends on the viewing wavelength and the optical properties of the water, which in turn are determined by the amount and nature of particulate material in the water column (Gordon and McCluney, 1975). Even above the attenuation depth the signal is heavily weighted towards the surface because of the exponential decay of the light as it travels through the water column (Sathyendranath, 1986). The attenuation length does not encompass all depths where photosynthesis takes place i.e. the photic zone, which is typically ~4 attenuation lengths (Gordon and Clark, 1980). Vertical profiles of phytoplankton also rarely show an homogeneous distribution, which can result in errors in the satellite-derived estimation of pigment concentration (Ballestero, 1999). *In situ* profiles often show a subsurface maximum in chlorophyll concentration, which usually occurs within the photic zone but below the one attenuation length and therefore may be partially or completely invisible to a satellite sensor (Platt and Sathyendranath 1988). The chl-a concentration that SeaWiFS measures is therefore not purely a surface value, but a weighted average over the attenuation depth, which may also not be representative of the average chl-a concentration throughout the euphotic zone. In the central Irminger Basin the water is generally very clear and free from particulate matter. In winter the attenuation depth is approximately 25m and is reduced to around 10m in spring. SeaWiFS is therefore actually measuring a weighted distribution of the chl-a over a few metres depth. In comparison, *in situ* samples for chlorophyll fluorescence on the Marine Productivity cruises were discrete samples taken from the ship's non-toxic supply, which draws water from ~5m depth.

The derivation of chl-a concentration from radiance relies on the fact that chlorophyll-a absorbs relatively more blue and red light than green, and the spectrum of backscattered sunlight progressively shifts from deep blue to green as the concentration of phytoplankton increases (e.g. Yentsch, 1960). The chlorophyll-a absorption spectrum (Figure 3.3) displays a double peak, with absorption maxima at wavelengths of 430nm (blue) and 662nm (red). However chl-a is not the only pigment in seawater which absorbs light in this range. Chlorophyll-b and c spectra are different to, but overlap with, chl-a and in addition there are many accessory pigments and degradation products associated with phytoplankton which absorb in the optical wavelengths. Separating the signal associated with chl-a from that of other pigments is attempted through the maximum band ratio method (see preceding Section 3.2.1). The empirical relationship employed by this method was derived by comparing *in situ* radiance and pigment measurements with SeaWiFS derived chl-a.

The SeaBASS dataset (http://seabass.gsfc.nasa.gov/) archives measurements of apparent and inherent optical properties, phytoplankton pigment concentrations, and other related oceanographic and atmospheric data, such as water temperature, salinity, wind speed, and aerosol optical thickness from world-wide cruises undertaken between 1975 and the present. The archive contains data from over 1,100 field campaigns, however some regions of the world ocean have very poor coverage (Werdell et al., 2003). For example, there are only 48 data points for the Irminger Basin (IB), none of which lie in the central basin (Figure 3.4). If the IB is typical of other high latitude regions, i.e. has similar bio-optical properties, this lack of *in situ* validation data should not present any major difficulties. However, the Greenland, Iceland and Norwegian (GIN) Seas have been found to have atypical relative concentrations of chl-a and b (Trees et al., 1992). Chl-a is ~75% of the global average, whilst chl-b is double the global average. In addition, relative to chl-a, there are substantially more carotenoids in the GIN seas than anywhere else. Only in this region are they the major pigment group and exceed the fraction for chl-a (Aiken et al., 1995). Chl-b absorbs more strongly at its peak absorbance (at wavelength 490 nm) than chl-a at its peak wavelength of 443 nm (see Figure 3.3). A higher proportion of chl-b in the phytoplankton population will result in a reduced chl-a signal, as detected by SeaWiFS.

The SeaBASS dataset, used to calibrate the SeaWiFS chl-a algorithm, contains chl-a and other pigment measurements from both fluorescence and HPLC (High Performance Liquid Chromatography) methods. Both of these techniques have inherent errors, particularly the fluorometric method where inaccuracies are introduced when chlorophylls b and c and phaeopigments are present (e.g. Bianchi et al., 1995). HPLC minimizes these interferences, since the pigments are physically separated on a column and individually quantified by absorption and fluorescence detectors (JGOFS, 1991). As an example, Moore et al. (2005) found that in the Iceland Basin the chl-a concentration measured by HPLC was 50% of that from fluorometry. In regions with little input to the SeaBASS dataset, and particularly those where only fluorometric measurements of chl-a are available, the SeaWiFS algorithm may contain significant errors.

The bio-optical properties of high latitude regions are recognised to be significantly different from lower latitude ecosystems (Mitchell, 1992). High-latitude plankton are often larger and are acclimated to low temperature and light regimes (Mitchell and Holm-Hansen, 1991) with low light adapted phytoplankton containing a reduced proportion of carotenoid pigments (Mitchell and Kiefer, 1988). Chlorophyll-specific absorption is lower than in temperate latitude phytoplankton due to packaging effects (Holm-Hansen and Mitchell, 1991), that is, the reduction in absorption efficiency of a substance enclosed in a particle in comparison with the absorption efficiency of the same substance in solution (Duysens, 1956; Kirk, 1994). In phytoplankton, the packaging effect is a function of the diameter of the cell and the intracellular concentration of pigments (Morel & Bricaud 1981; Sathyendranath et al. 1987). Nonpigmented particle absorption (i.e. by suspended particulate matter or gelbstoff) is also relatively low in high latitudes (Cota et al., 2003). Combined, these factors can result in a higher reflectance in the blue part of the spectrum and a reduced reflectance in the green compared to lower latitude ecosystems (Dierssen and Smith, 2000; Stramska et al., 2003). This will result in an apparent reduced chl-a concentration, as measured by SeaWiFS.

The North Atlantic spring bloom is believed to consist primarily of diatoms in the early stages with a progression to smaller plankton species, such as prymnesiophytes and dinoflagellates, once the diatoms have depleted the surface silica reserves (e.g. Mitchell, 1992; Barlow et al., 1993; Gregg et al., 2003; Moore et al., 2005). Chl-a cell concentration is known to vary between different phytoplankton species (Chan, 1978; Jeffrey and Vesk, 1997) and in the same species under different growth conditions (Goericke and Montoya, 1998; Marra, 1997). Therefore a typical North Atlantic bloom might appear in the SeaWiFS chl-a product as a peak early in the spring when the bloom is dominated by chl-a rich diatoms, then, as the diatom population falls back and the bloom becomes dominated by chl-a poor flagellates, the SeaWiFS chl-a concentration will also drop, leading to a bias in the satellite measured signal. The SeaWiFS chl-a product is strongly influenced by the species present in the water and their relative concentrations of chl-a.

The SeaWiFS sensor has a spatial resolution of 1km – that is it measures the total radiance of a patch of water over an area $1km^2$. The distribution of phytoplankton in surface waters is affected by turbulence and any biological patchiness which occurs on a scale of around, or less than, 1km will not be resolved by SeaWiFS. *In situ* measurements of chlorophyll are point measurements, often widely spaced, and as such are also not able to adequately represent the small-scale variability in phytoplankton distribution. Sub-pixel clouds can also contaminate the signal, leading to spuriously high chl-a values, and are characterised by speckles on an image. This patchiness can lead to uncertainties in the comparison of *in situ* measurements with satellite data.

Importantly, the SeaWiFS chl-a concentration does not equate to biomass. There are many problems with associating chl-a concentration with biomass: (a) chlorophyll concentration per cell is species specific, (b) older cells have fewer pigments, (c) pigment composition and concentration is affected not only by nutrients, but also by light intensity and spectral quality, (d) usually only chl-a is measured, although other pigments and accessories may be present and (e) chlorophyll concentration and cell size are not always correlated (Clark, 1997).

All of the above factors contribute to uncertainties in the SeaWiFS chl-a product, including in the Irminger Basin. When using the chl-a concentration in this region it is important to consider the potential sources of error and to bear in mind that the accuracy of the chl-a signal may have been compromised. Bias can easily be introduced into a dataset such as this, which is affected by cloud cover and does not have a simple biological regime. The match-up of *in situ* chlorophyll-a measurements against SeaWiFS chl-a is demonstrated in Figure 3.5. The fluorometrically measured chlorophyll-a concentration taken *in situ* during the four Marine Productivity cruises is plotted against the coincident (same day, within 0.25° in latitude and longitude) SeaWiFS chl-a. The SeaWiFS chl-a is generally an underestimate of the *in situ* chlorophyll concentration. A linear regression has a correlation of $r^2 = 0.23$, rmse = 0.32 mg m^{-3}, $p < 0.01$, $n = 266$ and the equation $Chl_{in\ situ} = 0.57 + 0.61 * Chl_{SeaWiFS}$.

Despite the uncertainties in satellite-derived chlorophyll concentrations, satellite remote sensing is the only method which provides sufficient spatial and temporal resolution to study many phenomena, including interannual variability of the spring bloom. *In situ* measurements of chlorophyll concentration also have errors associated with them, some of which are quite considerable. In conclusion, satellite measurements are the only feasible option for studying large-scale, or long time-scale, processes. Although errors exist in the derivation of chlorophyll-a from ocean colour, as with *in situ* measurements errors do not invalidate the data, provided careful consideration of the sources of the inaccuracies are considered when drawing conclusions.

3.3. AVHRR SEA SURFACE TEMPERATURE:

The Advanced Very High Resolution Radiometer (AVHRR) is a broad-band, four or five channel (depending on the model) scanner, sensing in the visible, near-infrared, and thermal infrared portions of the electromagnetic spectrum. This sensor is carried on National Oceanic and Atmospheric Administration's (NOAA's) Polar Orbiting Environmental Satellites (POES), beginning with TIROS-N in 1978 and providing a continuous source of global Sea Surface Temperature (SST) data since then (Hastings, 2001). The history of SST computation from AVHRR radiances is discussed at length by McClain et al. (1985). Briefly, radiative transfer theory is used to correct for the effects of the atmosphere on the observations by utilizing ‘windows’ of the electromagnetic spectrum where little or no atmospheric absorption occurs. Channel radiances are transformed (through the use of the Planck function) to units of temperature, then compared to *a priori* temperatures measured at the surface. This comparison yields coefficients which, when applied to the global AVHRR data, give estimates of surface temperature which are nominally accurate to $\pm$ 0.3°C (Vazquez, 1999).

AVHRR SST data were ordered through the NASA JPL Physical Oceanography Distributed Active Archive Center (PODAAC) POET GUI tool (http://podaac-esip.jpl.nasa.gov/poet/). The AVHRR data are available at 0.5° resolution as a daily product. All data from 1st January 1998 to 31st December 2003 for the region 55N–66N, 20W–44W were ordered as latitude-longitude maps in ASCII format. The data were instantly available to download from the JPL ftp site (ftp:\\podaac.jpl.nasa.gov). A script was written to import the daily ASCII files into Matlab and create three day averages from the daily data. Linear interpolation allowed small gaps in the data due to cloud cover to be filled.

3.4. WIND SPEED AND DIRECTION:

Radar scatterometers are able to measure winds over the ocean from space. A scatterometer transmits pulses of microwave energy and the energy in the returned echo depends on the electrical properties and roughness of the surface. Over the ocean the roughness is a function of the near-surface vector wind which generates ocean waves. With measurements made from multiple azimuth directions, the wind at approximately 10m above the sea surface can be estimated from the radar measurements.

Scatterometers aboard two different satellites are used in this study. Wind data pre June-1999 was from the Active Microwave Instrument aboard ERS-2. After this time, data from the SeaWinds instrument aboard the QuikBird satellite (commonly called QuikScat) was used.

ERS-2 was launched by the European Space Agency in April 1995 and is still operating. The platform carries several instruments including the Active Microwave Instrument (AMI) which combines the functions of a Synthetic Aperture Radar and a wind scatterometer. The wind scatterometer uses three sideways looking antennae; one pointing normal to the satellite flight path, one pointing 45° forward and the third pointing 45° backward. These antenna beams continuously illuminate a swath 500 km wide as the satellite advances along its orbit and each provide measurements of radar backscatter from the sea surface for overlapping 50 km resolution cells using a 25 km grid spacing. The accuracy of the derived wind speed is $\pm$ 2ms^{-1} for wind speed and $\pm$ 40° for wind direction (http://earth.esa.int/ers/eeo4.144/).

ERS-2 wind speed data were ordered through the NASA JPL Physical Oceanography Distributed Active Archive Center (PODAAC) website (http://podaac-esip.jpl.nasa.gov/poet/). The ERS-2 data are available at 1° resolution as a weekly averaged product. All data from 1st January 1998 to mid-July 1999 for the region 55N – 66N, 20W – 44W were ordered as latitude-longitude maps in ASCII format. The data are instantly available to download from the JPL ftp site (ftp:\\podaac.jpl.nasa.gov). A Matlab script was written to import the ASCII files into Matlab. As the other satellite data were at a resolution of 0.5° a linear interpolation was carried out to extrapolate the data from 1° to 0.5° resolution.

The QuikScat scatterometer is a microwave radar designed specifically to measure ocean near-surface wind speed and direction. The SeaWinds mission was a "quick recovery" mission to fill the gap created by the loss of data from the NASA Scatterometer (NSCAT), when the satellite it was flying on lost power in June 1997. It uses a rotating dish antenna with two spot beams that sweep in a circular pattern to collect data in a continuous, 1,800-kilometer-wide swath with a wind vector resolution of 25 km. The wind speed and direction are derived from the satellite-received backscatter intensity using the Ku-2001 algorithm based on Liu and Tang (1996). Wind speed and direction daily data is available from July 19th 1999 and is accurate to $\pm$ 0.5ms^{-1} and $\pm$ 20° respectively (http://winds.jpl.nasa.gov/missions/quikscat/index.cfm).

QuikScat data is available free of charge through Remote Sensing Systems Inc. (http://www.remss.com/). The data is provided at 0.25° resolution as a daily product in gridded binary data files from the RSS ftp site (ftp:\\ftp.ssmi.com). These files contain wind speed and wind direction data and a rain flag (rain is known to reduce the accuracy of the wind measurements). All daily data files from 19th July 1999 to 31st December 2003 were downloaded. Basic routines to read the data files into Matlab are provided by RSS. These were adapted to extract only the relevant region from the global data set (55N-66N, 44W-20W) and to resample the data to a 0.5° grid to match the other satellite data. To convert from digital number (*DN*) to wind speed and direction, the following scalings were applied:

$$speed = DN * 0.2; \qquad direction = DN * 1.5$$

3.5. SEAWIFS PHOTOSYNTHETICALLY AVAILABLE RADIATION:

The amount and intensity of light reaching the ocean surface is a crucial variable affecting the production of carbon by phytoplankton. Photosynthetically Available Radiation (PAR) is the incident quantum flux in the wavelength range 400 to 700 nm (the range in which photosynthetic pigments efficiently absorb light), i.e. the number of photons available for photosynthesis. The primary environmental factor affecting the amount of light reaching the sea surface is atmospheric cloud cover. Contributing factors that affect the solar irradiance are the type of cloud cover, the presence of atmospheric aerosols, and the solar zenith angle (i.e. low latitudes receive more solar irradiance than high latitudes). The solar irradiance products produced for SeaWiFS use data on cloud and ice cover, albedo, cloud optical thickness etc. from the International Satellite Cloud Climatology Project (ISCCP). Atmospheric, cloud, and surface data from ISCCP are used as input with a fast scheme for computing clear-sky irradiance from the solar zenith angle, air properties, and surface reflectance. The scheme then uses simple cloud properties (cloud fraction, cloud optical thickness, and diffuse albedo) to produce daily-averaged total and photosynthetically active solar irradiance fields. Descriptions of the algorithm used, algorithm verification, and results of global data analysis can be found in Bishop and Rossow (1991) and Bishop, Rossow and Dutton (1997). The SeaWiFS PAR product is accurate to within ± 15 % (Frouin et al., 2003).

Global, daily, 9km resolution PAR data is available in hdf format to approved SeaWiFS users from ftp://samoa.gsfc.nasa.gov. All data from March 1998 to October 2003 were downloaded. Data from November to January are absent due to the low sun angle at this time of year. A Matlab script was written to read in the hdf files, select the data in the study region (55N-66N, 44W-20W), resample the data to 0.5° resolution using a linear interpolation scheme and create three day composites, in order to be on the same spatial and temporal scale as the other satellite data. To convert from digital number (*DN*) to PAR the following scaling was applied:

$$PAR = 0.3 * DN$$

The PAR is expressed in Einsteins m^{-2} day^{-1}, equivalent to mol photons m^{-2} day^{-1}. Conversion to W m^{-2} is by (Smith and Morel, 1974):

$$\text{PAR (Watts)} = \frac{\text{PAR (Einsteins)} \,.\, 6\text{x}10^{23}}{86400 \,.\, 2.77\text{x}10^{18}}$$

3.6. SEAWIFS DIFFUSE ATTENUATION COEFFICIENT:

K490, the diffuse attenuation coefficient, represents the rate at which light at a wavelength of 490 nm is attenuated with depth. Gordon and McCluney (1975) showed that ~90% of remotely sensed ocean colour is reflected from the upper layer, the depth of which is the inverse of K490. The SeaWiFS K490 algorithm uses the water-leaving radiances at wavelengths 490 nm and 555 nm and constants derived from the SeaBASS data archive (see Section 3.2.2 on SeaWiFS data). The algorithm is expected to work well in open ocean waters, but less well in turbid, coastal waters. Full details of the algorithm and its verification can be found in O’Reilly et al. (2000). The SeaWiFS K490 product has an accuracy of ± 25% (Mueller, 2000).

8-day composites at global 9km resolution are available in hdf format to approved SeaWiFS users from ftp:\\samoa.gsfc.nasa.gov. All data from March 1998 to October 2003 were downloaded. Data from November and February are absent due to the low sun angle at this time of year. A Matlab script was written to read in the hdf files, select the study region (55N-66N, 44W-20W) and to resample the data to 0.5°, daily resolution using a linear interpolation scheme in order to be on the same spatial scale as the other satellite data. To convert from digital number (DN) to K490 the following scaling equation was applied:

$$K490 = 10^{((0.01*DN)-2)}$$

3.7. NCEP NET HEAT FLUX:

The net air-sea heat flux defines whether the ocean surface is being heated or cooling down. The balance of fluxes is:

$$Q_{net} = Q_B + Q_L + Q_S + Q_I$$

where Q_B is the net upward flux of long-wave radiation, Q_L is the upward latent heat flux, Q_S is the upward sensible heat flux, Q_I is the net flux of solar radiation and Q_{net}, the net heat flux, is negative out of the ocean and positive into the ocean. The heat flux is a measure of the stability of the water column and also reflects cloudiness.

The NCEP/NCAR (National Centers for Environmental Prediction/ National Center for Atmospheric Research) Reanalysis Project is an effort to reanalyze historical land and marine surface meteorological data using coupled models. The project uses a state-of-the-art analysis/forecast system to perform data assimilation using past data from 1948 to the present. The model includes parameterizations of all major physical processes, i.e. convection, large scale precipitation, shallow convection, gravity wave drag, radiation with diurnal cycle and interaction with clouds, boundary layer physics, an interactive surface hydrology, and vertical and horizontal diffusion processes. Details of the model dynamics and physics can be found in Kanamitsu (1989) and Kanamitsu et al. (1991). 6-hourly, daily and monthly data of a suite of atmospheric variables, such as humidity, wind speed, soil moisture, precipitation etc. are available at various pressure levels from 10m to 1000m above sea-level.

NCEP/NCAR reanalysis products are freely available to download from their website (http://www.cdc.noaa.gov/cdc/data.ncep.reanalysis.html). Daily, surface, Gaussian-gridded data at 2° resolution (the highest resolution available) from 1st January 1998 to 31st December 2003 in NetCDF format were downloaded from the NCEP/NCAR ftp site (ftp:\\ftp.cdc.noaa.gov). As net heat flux is not available as a product, variables for net upward flux of long-wave radiation, upward latent heat flux, upward sensible heat flux and net flux of short-wave solar radiation were downloaded (NCEP variables nlwrs.sfc, lhtfl.sfc, shtfl.sfc and nswrs.sfc respectively). In order for Matlab to read NetCDF files a specific toolbox had to be installed. This toolbox software is written, maintained and supported by Dr. Charles R. Denham, U.S. Geological Survey, Woods Hole and is freely available to download from http://woodshole.er.usgs.gov/staffpages/ cdenham/public_html/MexCDF/nc4ml5.html.

A Matlab script was written to read in the daily NetCDF files for all the variables, select the study region (55N-66N, 44W-20W) calculate the net heat flux, make 3 day averages and extrapolate the data to 0.5° resolution using a nearest neighbour interpolation scheme. To convert from digital number (DN) to the heat flux components the following scaling equations were applied:

$$
\begin{aligned}
Q_I &= 0.100000001490116 * \mathrm{DN} + 1876.5 \\
Q_S &= 0.100000001490116 * \mathrm{DN} + 2176.5 \\
Q_L &= 0.100000001490116 * \mathrm{DN} + 856.5 \\
Q_B &= 0.100000001490116 * \mathrm{DN} + 3176.5
\end{aligned}
$$

where Q_I, Q_S, Q_L and Q_B are as above and *DN* is the digital number. The net heat flux has errors that vary seasonally and regionally, but the mean error is $\pm$ 30 Wm^{-2} (Josey et al., 1999).

3.8. ARGO FLOAT TEMPERATURE AND SALINITY PROFILES:

Argo floats are a global array of temperature/salinity profiling floats (http://argo.jcommops.org/). The first Argo deployment began in 2000 and the network has now grown to over 1000 operational floats worldwide. The Argo programme builds on a previous float deployment programme, PALACE, which deployed seven floats in the Irminger Basin in 1996, four with temperature and salinity sensors, the others measuring temperature only. The floats cycle to 2000 m depth every ten days, with a 4-5 year lifetime for individual instruments. As the floats resurface the T/S profiles are transmitted via satellite to regional data centres and are publicly available within a few hours (Roemmich et al., 2001). The temperature sensors are accurate to $\pm$ 0.005°C (Turton, 2002). The salinity sensors are initially accurate to $\pm$ 0.01 psu (Wong et al., 2003) but as the floats age the accuracy of the measurements are susceptible to drift. The degradation of the quality of the data, often due to biofouling, is ~0.0009 psu per month (Bacon et al., 2001). The salinity measurements are consistent between floats to ~0.006 psu (Centurioni and Gould, 2004).

Argo and PALACE float profiles are freely available to download from the IFREMER Coriolis project website (http://www.ifremer.fr/coriolis/cdc/ default.htm). All available temperature and/or salinity profiles from 1st January 1998 to 31st December 2003 in the study region (55N-66N, 44W-20W) were downloaded in NetCDF format and imported into Matlab (details of the NetCDF toolbox can be found in Section 3.7).

3.8.1. MIXED LAYER DEPTH:

Density profiles were calculated from the salinity and temperature data using the UNESCO 1983 equation of state, excluding the bulk secant modulus term (Gill, 1982). However, on examining the density profiles some dubious features were seen, which were traced back to the salinity profiles. A difference of up to 1 psu between two floats in similar locations was found. In addition floats prior to ~2001 were equipped with temperature sensors only. The mixed (ML) depth is therefore calculated from the temperature profiles alone. Several different methods for calculating ML depth are available (Thomson and Fine, 2003). The threshold method is the simplest and is the one applied here. The depth of the surface mixed layer is defined as the depth z at which the temperature difference $\Delta T(z) = T(z) - T(z_0)$ in the upper ocean exceeds a specified threshold value. Values of ΔT range in the literature from 0.01 to 0.15 °C, however most authors agree on a threshold value of $\Delta\sigma_\theta$ (potential density difference) of ~0.01 kgm^{-3} (see Thomson and Fine, 2003 for a review). To determine a suitable value for ΔT in the study region the *in situ* CTD profiles were examined. A potential density difference of 0.01 kgm^{-3} was found to be equivalent to a temperature difference of ~0.07 °C between the surface and the mixed layer. The ML depth of each profile was calculated using this method. As a further check the ML depth was also estimated from the maximum value of the Brunt-Väisälä frequency, calculated as:

$$N^2 = -\frac{g}{\rho}.\frac{d\rho}{dz}$$

where g is the gravitational acceleration constant (= 9.81 ms^{-2}), ρ is the density and z is the depth. The density was calculated using the UNESCO formula mentioned previously with the suspect salinity profiles removed. In addition the minimum value of $d\rho/dz$ was also calculated. The ML depths estimated by each method were not statistically different. In all the following work ML depth from Argo float profiles has been estimated using the temperature threshold method (where $\Delta T = 0.07$ °C).

3.9. 1-D PHYSICAL MODEL:

For parts of this study a 1-D vertical mixing model, which uses a Kraus and Turner (1967) mixing scheme, developed by Stefan Rahmstorf (Institut für Meereskunde, Kiel) is used to estimate mixed layer depth. The fine details of the model can be found in Rahmstorf (1991) and only a brief outline is given here. The version of the model used in this study was supplied as a Matlab script by Joanna Waniek (NOCS) and is as described in Waniek (2003).

The model represents four physical processes which redistribute heat through the water column: wind mixing, convection, upwelling and turbulent diffusion. Its key feature is that the mixed layer depth is not prescribed, but rather calculated from integrated kinetic and thermal energy budgets. The energy budget of the mixed layer is defined as:

$$\frac{g}{2\rho_0}h^2\frac{d\rho}{dt}+\frac{g}{\rho_0}hw_e\Delta\rho=-mU^3-\frac{1-n}{2}hB \qquad \text{[Eqn 3.1]}$$

where g is the acceleration due to gravity (= 9.81 $\mathrm{ms^{-1}}$), ρ_0 is density at the surface, ρ is density, h is mixed layer depth, m is the wind mixing efficiency, U is the wind speed, w_e is the entrainment velocity, where:

$$w_e=\begin{cases} dh/dt & dh/dt>0 \\ 0 & dh/dt\le 0 \end{cases}$$

and $B = (g\alpha/c_p\rho_0)Q$, where Q is the surface heat flux, α is the thermal expansion coefficient of seawater and c_p is the heat capacity of seawater. Lastly if B is positive (i.e. heating), n = 1; if B is negative (cooling) potential energy is released, a fraction of which, f, can be used for further entrainment, so that:

$$n=\begin{cases} 1 & B>0 \\ f & B<0 \end{cases}$$

The left-hand side of Equation 3.1 is then the rate of change of potential energy in the water column. The first term on the right-hand side is the wind input to the potential energy and, for cooling ($B < 0$), the final term is the rate of decrease of potential energy due to dissipation of convective energy.

The mixed layer model described above is embedded in an upwelling-diffusion model of the whole water column, described by:

$$\frac{\partial T}{\partial t} = K\frac{\partial^2 T}{\partial z^2} - w\frac{\partial T}{\partial z}$$

where K is the turbulent diffusion coefficient, w is the upward vertical velocity and T is the ocean temperature at depth z.

The model takes as its input the wind speed (in ms^{-1}), air temperature at 2 m (in Kelvin), net shortwave radiation at the surface (in Wm^{-2}), relative humidity at the surface (as a % of water per unit of air) and cloud cover (as a percentage from 0 to 100 %). Wind speed was taken from the ERS or QuikSCAT satellites as described in Section 3.4. The other variables were downloaded from the NCEP/NCAR Reanalysis Project (NCEP variables: air.2m, nswrs.sfc, rhum.sig995 and tcdc.eatm respectively; see Section 3.7 for description of NetCDF processing). The model parameters and their values or formulae are listed in Table 3.2.

The model is initialised with temperature and salinity from CTD profiles measured on the winter 2001 MarProd cruise. For the Central Irminger Sea zone (see Chapter 5 for definition of zones) CTD 14239 was used, in the Reykjanes Ridge region, CTD 14295 and on the East Greenland coast CTD 14249 was used (details of the CTD profile locations, dates and measurements can be found in the cruise report: Richards et al., 2002). The model is implemented with a finite difference scheme at 2 m vertical resolution to a depth of 800 m, then at a resolution of 50 m to the bottom (determined by the maximum depth of the CTD profile). The time step is 1 day. The model outputs daily profiles of temperature, salinity, density and heat distribution. Mixed layer depth is estimated using the same criteria as for the Argo float data ($\Delta T = 0.07$ °C; see Section 3.8.1).

Band	Centre Wavelength	Bandwidth	Colour	Primary use
1	412 nm	20 nm	Violet	Gelbstoff
2	443 nm	20 nm	Blue	Chlorophyll absorption
3	490 nm	20 nm	Blue-green	Pigment absorption (case 2), turbidity
4	510 nm	20 nm	Blue-green	Chlorophyll absorption
5	555 nm	20 nm	Green	Pigments, optical properties, sediments
6	670 nm	20 nm	Red	Atmospheric correction (CZCS heritage)
7	765 nm	40 nm	Near-infrared	Atmospheric correction, aerosol radiance
8	865 nm	40 nm	Near-infrared	Atmospheric correction, aerosol radiance

Table 3.1: SeaWiFS wavelength bands and primary uses. Note: Case 2 in the third line of the table refers to generally coastal, highly productive, turbid waters.

Parameter	**Formula/Symbol**	**Value**
Vertical turbulent diffusion coefficient	K	1.2 cm^2 s^{-1}
Vertical velocity	W	1.27 x 10^{-7} ms^{-1}
Longwave radiation, W m^{-2}	$Q_B = -\varepsilon\sigma T_S^4(1-0.6m_w^2).(0.39-0.05\sqrt{e_a})$	
Black body correction	ε	0.985
Stefan-Boltzmann constant	Σ	5.73 x 10^{-8} W m^{-2} K^{-4}
Vapour pressure for water and air, mbar	$e_{a,s} = r \text{ x } 6.11 \text{ x } 10^{\frac{7.5T}{T+237.3}}$	
Cloud cover factor	m_w	
Sensible heat flux, W m^{-2}	$Q_H = c_p \text{ x } C_H \text{ x } \rho_a(T_a - T_s)U_{10}$	
Air and water temperature in K	T_a, T_s	
Wind speed, ms^{-1}	U_{10}	
Specific heat capacity of seawater, at constant pressure	$c_p = 4150$	4150 J kg^{-1} K^{-1}
Stanton number	C_H	1.1 x 10^{-3}
Latent heat flux, W m^{-2}	$Q_L = \rho_a \text{ x } C_L \text{ x } U_{10} \text{ x } 0.622p^{-1}(e_a - e_s)$	
Air pressure, Pa	P	
Air density	ρ_a	1.2 kg m^{-3}
Dalton number	C_L	1.5 x 10^{-3}
Relative humidity, %	R	
Wind mixing efficiency	$m = 2.5 \text{ x } 10^{-3} \exp(-h/50)\rho_a\kappa$	
Mixed layer depth, m	H	
Drag coefficient	κ	1.2 x 10^{-3}
Acceleration constant	G	9.81 m s^{-1}
Attenuation coefficient of seawater	c_w	0.04 m^{-1}

Table 3.2: Parameters and their symbols and formulae or values used in the vertical mixing model.

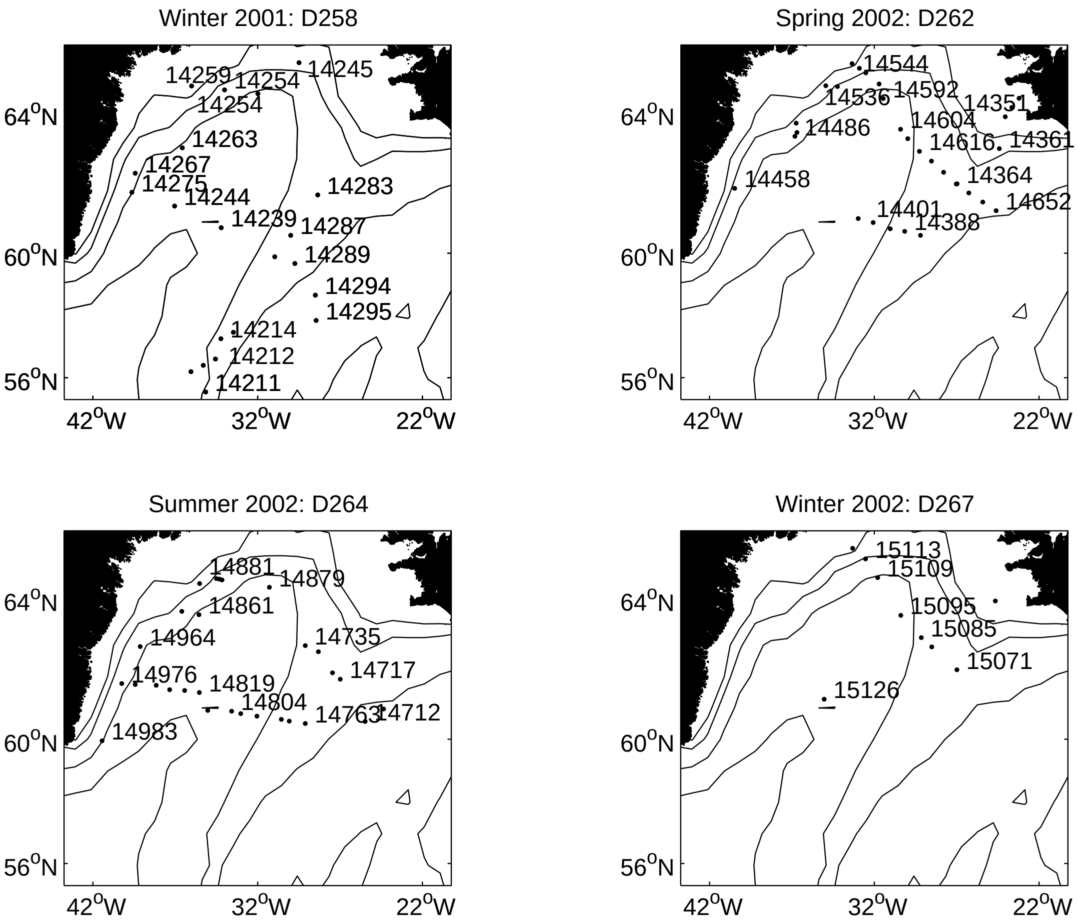

Figure 3.1: Maps of study area showing location of CTD stations and selected station numbers for each of the four Marine Productivity cruises.

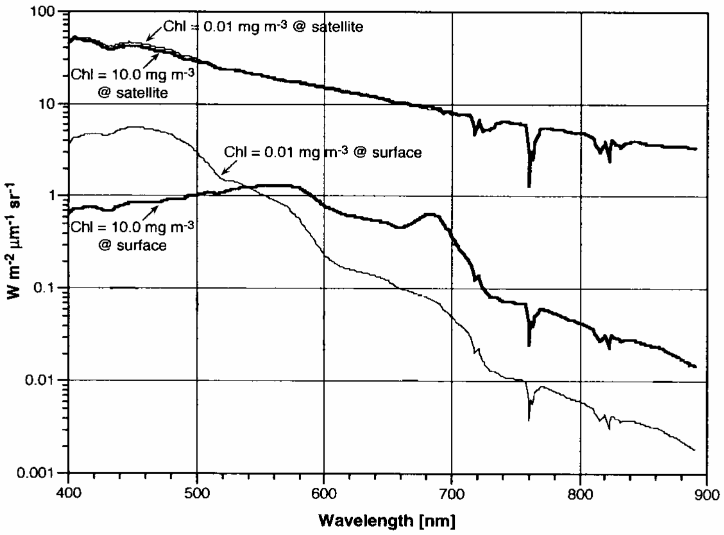

Figure 3.2: Comparison of radiances measured at satellite and water leaving radiances for chlorophyll concentrations of 0.01 and 10 mgm^{-3}. Note the small difference in at-satellite radiances between low and high chlorophyll concentrations. From model results over cloud-free oceans by H. Gordon in Hooker et al. (1992).

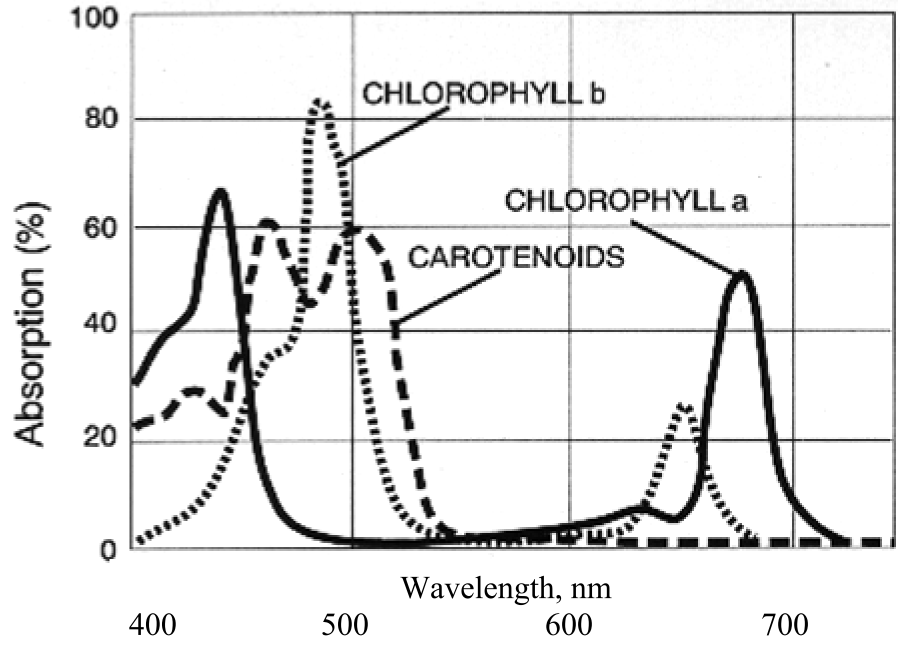

Figure 3.3: Relative absorption spectra of phytoplankton pigments chlorophyll-a, chlorophyll-b and carotenoids. From http://www.life.uiuc.edu/govindjee/paper/fig5.gif

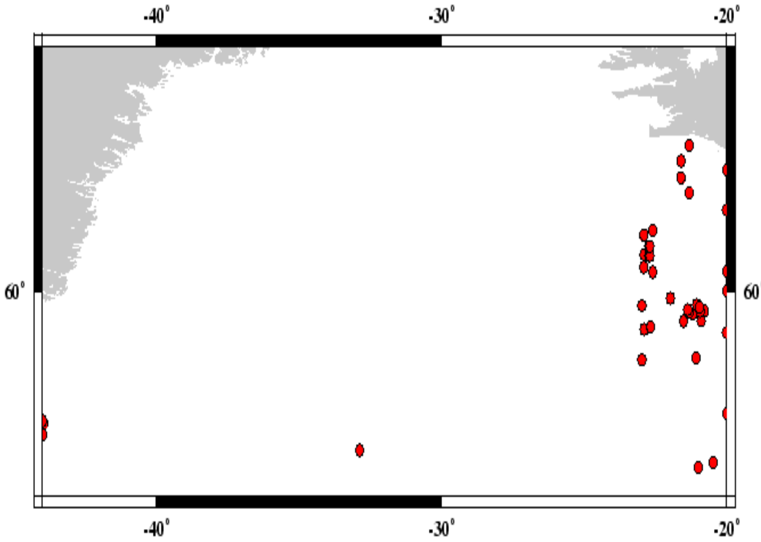

Figure 3.4: Map showing *in situ* chl-a measurements (red dots) made in the Irminger Basin region contained in the SeaBASS database which is used to calibrate the SeaWiFS chl-a algorithm. SeaBASS map drawing tool available at http://seabass.gsfc.nasa.gov/

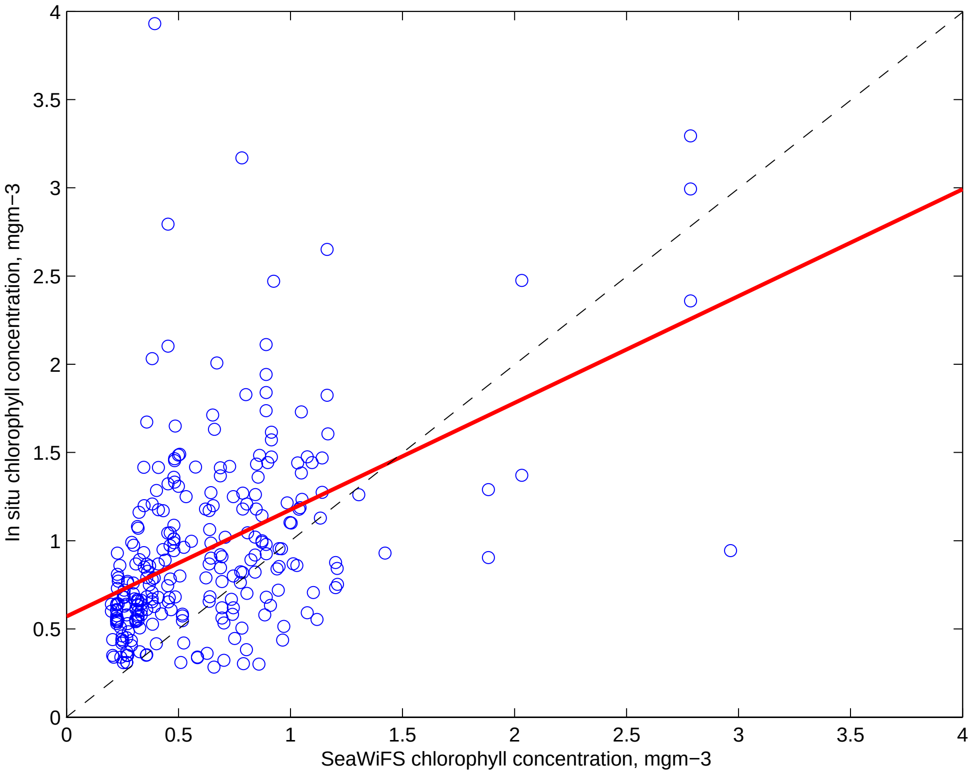

Figure 3.5: *In situ* fluorometrically measured chlorophyll-a concentration taken on the four Marine Productivity cruises against coincident SeaWiFS chl-a. Black dotted line is 1:1 line. Red line shows linear regression best fit: $Chl_{in\ situ} = 0.57 + 0.61*Chl_{SeaWiFS}$, $r^2 = 0.23$, rmse = 0.32 mg m^{-3}, $p < 0.01$, $n = 266$.

4. TEMPERATURE-NUTRIENT RELATIONSHIPS:

This chapter examines the possibility of estimating the nutrients nitrate, phosphate and silicate from remotely sensed sea surface temperature (SST) and chlorophyll-a concentration. The seasonality in the temperature-nutrient relationships are examined and the implications discussed. Parts of this chapter have been previously published as Henson et al. (2003), 'Seasonal constraints on the estimation of new production from space using temperature-nitrate relationships', Geophysical Research Letters 30(17), 1912, which is included as Appendix 1.

4.1. THE NEED FOR REMOTELY SENSED NUTRIENT ESTIMATES:

Supply and depletion of nutrients in surface waters controls phytoplankton populations. Without the major inorganic nutrients (nitrate, silicate and phosphate) and some minor ones (e.g. iron, manganese) phytoplankton are unable to bloom. The end of the North Atlantic spring bloom is often associated with nutrient depletion, although occasional new growth in the autumn has been linked to storms which can re-stock the surface waters with nutrients (see Section 2.1.1 for a discussion).

Estimating nutrient concentrations is key to understanding planktonic ecosystems, but traditional shipboard measurements are not able to sample over wide areas or long time periods. The possibility of estimating nutrient concentration from remotely sensed parameters is therefore alluring. Inverse relationships between sea surface temperature and the major inorganic nutrients (particularly nitrate) have been determined with the aim of estimating surface nutrient concentration from remotely sensed SST. Correlations have been found in regions as diverse as the California Coast (Dugdale et al., 1997), the Northwest Iberian upwelling (Álvarez-Salgado et al., 2002), the tropical Pacific (Chavez et al., 1996) and the Ushant tidal front in the Bay of Biscay (Morin et al., 1993).

Each of the above studies resulted in a different temperature-nitrate (TN) relationship: so they are expected to vary spatially, but can they vary temporally too?

The vast majority of work on temperature-nutrient relationships has concentrated on nitrate (rather than phosphate or silicate). Historically there are more nitrate measurements available for analysis than for phosphate or silicate. Additionally the drawdown of nitrate during the spring bloom can be used to estimate new production. As defined by Dugdale and Goering (1967) new production is that portion of total production driven by 'newly available nitrogen' that is supplied through convective mixing, mesoscale activity or atmospheric input. In terms of the global carbon cycle it is only the new production fraction of total production that is available for export to deep waters or higher trophic levels (Eppley and Peterson, 1979). The amount of nitrate consumed by phytoplankton over the spring growth period can be converted into an estimate of new production via the Redfield ratio (Redfield et al., 1963). Following Dugdale and Goering's (1967) definition of new production most published studies estimate it from the drawdown of nitrate. More recently however the definition of new production has been re-stated as the drawdown of the *limiting* nutrient over the growth period (Aufdenkampe et al., 2002). This may be nitrate, or it may be silicate or even iron. Nevertheless, several studies have been published which estimate new production from nitrate drawdown, either on a local or global scale (Sathyendranath et al., 1991; Minas and Minas, 1992; Longhurst et al., 1995; Hernàndez-de-la-Torre et al., 2003).

4.2. TEMPERATURE-NITRATE RELATIONSHIPS:

The studies of TN relationships mentioned above were generally conducted in upwelling regions where cold, nutrient rich water is being regularly supplied. As the water moves offshore it becomes warmer and at the same time phytoplankton consume the nutrients – in this situation a monotonic relationship between temperature and nitrate may be expected. But does a simple linear temperature-nitrate regression apply in the Irminger Basin, a region with deep winter mixing and no nitrate limitation?

The Marine Productivity data set has the advantage of four successive cruises across one whole year. Any seasonality in the TN relationship in the Irminger Basin can therefore be explored. The possibility of seasonality in the TN relationship has been acknowledged (Pastuszak et al., 1982; Gong et al., 1995), but the data were inadequate to explore the causes and consequences of variability.

This chapter discusses the seasonality and interannual variability in temperature-nutrient relationships and a method for mitigating the biological dependence in these relationships. It does not discuss the impacts of nutrient concentration and limitation on the spring bloom. This will be returned to in Chapter 7.3.

4.2.1. SEASONALITY IN THE TEMPERATURE-NITRATE RELATIONSHIP:

Underway surface samples of nitrate were collected on three of the four MarProd cruises. For the winter 2001 cruise, when no underway nutrient samples were taken, the nutrient concentration measured from the surface bottle of each of the CTD stations was used. The coincident sea surface temperature for all nutrient measurements was taken from the ship's Surfmet system (see Section 3.1.1 for details of data collection and processing). A total of 468 good quality temperature-nitrate pairs were used to create the nitrate against temperature scatter plot in Figure 4.1. A linear least-squares regression was carried out and a moderately good fit was obtained ($r^2 = 0.7$; rmse = 2.2 μmol l^{-1}), but the degree of correlation is disappointing when compared to other studies.

Previously published studies have tended to aggregate all available cruise data in a study region, regardless of season. However, as the MarProd dataset was collected over four successive seasons it offered the opportunity to investigate the seasonal variability of the relationship. Plots of SST against nitrate were produced separately for each cruise (Figure 4.2). The spring and summer cruise plots display no correlation ($r^2 = 0.02$ and 0.24 respectively), whilst both winter cruises have strong correlations of r^2 greater than 0.8. Note that the ‘winter’ cruises actually took place in November/December when surface cooling was beginning to mix the water column, entraining new nutrients which the phytoplankton were not able to exploit due to limiting light levels. Although a linear TN relationship in winter is likely (and physically plausible because both heat and nutrients are conserved), in spring and summer the biological utilisation of nitrate occurs at a different rate to the warming of the sea surface. The seasonality evident in Figure 4.2 suggests that TN relationships can only be derived with confidence from early winter data.

Why might a linear relationship between temperature and nutrients be expected? Models of the annual cycle in nutrient and chlorophyll concentrations all display a strong seasonality at high latitudes, characterized by a short lived burst of phytoplankton growth during the spring bloom. At the end of winter the classic model of the annual nutrient cycle with wind-driven cooling and deep convective mixing results in low surface temperatures but high surface nutrient levels (see Figure 2.1). Biological utilization of nitrate is minimal due to low light levels and continual mixing until, in spring, increasing light levels and re-stratification due to increased surface heating and reduced wind stress result in the onset of renewed biological production and rapid consumption of nutrients. The water is subsequently warmed through solar heating and depleted of nutrients following the onset of the phytoplankton growth season; however, during this time nitrate does not behave conservatively. It is consumed and excreted by biological activity. In post-bloom summer nutrients have been stripped by phytoplankton from surface waters and the SST is at its peak. As solar heating declines through autumn and early winter overturning commences, cold nutrient-rich water is brought to the surface but phytoplankton are not able to utilize it. Therefore winter is the only time of the year when nitrate and temperature are conserved and a linear TN relationship can be expected. At all other times of the year biological consumption of nutrients and/or solar heating invalidates the assumption that SST varies linearly with surface nitrate.

A conceptual model of the seasonal variability of the TN relationship is shown in Figure 4.3. Point A represents post-bloom summer, with high temperatures and low nitrate concentrations. Point B is the late winter/pre-bloom spring before large-scale nutrient uptake begins and is associated with low temperatures and high nitrate concentrations. Points A and B represent the end-members of the mixing due to convective overturning that takes place during autumn and winter. The return path from point B to A takes place during the growth season and can follow one of two routes. If biological utilization of nitrate occurs at a faster rate than an increase in SST through solar heating, path 1 is taken. Alternatively, if the increase in SST occurs more rapidly than biological uptake of nitrate, path 2 will be followed.

In Figure 4.4 data from all four cruises are plotted together. The spring and summer data stand out as ‘blobs’ of data at either end of the linear winter data. The spring cruise took place in April/May 2002, before the spring bloom had been initiated in large parts of the basin. The spring data is clustered around point B in the high nitrate, low temperature regime. A few scattered points have lower nitrate values – these measurements were taken along the Iceland and Greenland coast where the spring bloom had already begun. The summer data are clustered around point A in the low nitrate, high temperature regime and are indicative of the post-bloom state in July/August 2002 at the time of the summer cruise. The data fit the conceptual model in Figure 4.3 well. Most of the spring and summer data falls below the winter line, suggesting that the spring bloom in 2002 followed path 1. Therefore in the Irminger Basin biological utilisation of nitrate occurs at a faster rate than SST increases due to surface heating. The winter 2002 data follows on from Point B, consistent with the transition from a high temperature, low nitrate regime back to a low temperature, high nitrate pre-bloom regime.

As well as seasonal variability, interannual variability is also evident in the data. Figure 4.5 shows TN plots for winter 2001 and winter 2002 on the same axes. The slopes of the two linear best fit lines are clearly different. The nitrate depletion temperature (NDT; i.e. the temperature at which nitrate goes to zero) is ~16 °C for winter 2001 and ~19 °C for winter 2002 – a difference of 3° in just one year. Additionally the maximum nitrate observed in winter 2001 is ~16 μmol l^{-1}, but in winter 2002 it is just ~12 μmol l^{-1}. The difference may be attributable to changes in the composition of sub-mixed layer water masses, although it is more likely due to a difference in mixed layer depth at the time of the two cruises. Winter 2002 has a shallower slope than winter 2001 implying that the 2002 early winter mixed layer at the time of the cruise was shallower and therefore that less nitrate had been mixed into surface waters. Visual inspection of the cruise CTD data for both winters confirms that at the time of D258 (winter 2001) convective mixing was well underway and the mixed layer (ML) depth was ~300 m. During D267 (winter 2002) the ML depth was shallower and little evidence of winter mixing was observed. Wintertime meteorological conditions can affect the depth of the winter ML and thus nutrient concentrations. A stormy winter may lead to a deeper winter ML and an increased nutrient stock the following spring. It must be remembered however that the 'winter' cruises took place in November/ December, and whilst the deepening of the ML may have been delayed in 2002 relative to 2001, by the following spring it is possible that nutrient concentrations at the start of the bloom were the same for both years.

The seasonal and interannual variability observed in the TN relationship in the Irminger Basin sounds a note of caution about aggregating data compiled from several different seasons and years in order to estimate nitrate from remotely sensed SST. More positively, there is a seasonal time range during which a mechanistic link between temperature and nitrate exists, and therefore when TN relationships can be used with confidence.

4.2.2. REDUCING SEASONALITY IN THE TEMPERATURE-NITRATE RELATIONSHIP:

As explained in the previous section a linear TN relationship cannot be relied upon during the phytoplankton growth season due to the biological utilisation of nitrate. If the effects of biological uptake of nitrate can be mitigated, the estimation of nitrate during the growth season may be improved. Goes et al. (1999 and 2000) suggested including chlorophyll a (chl-a) in the regression to increase the predictive power of the TN relationship.

For the Irminger Basin surface chl-a measurements were taken underway every four hours from the ship's non-toxic supply and analysed fluorometrically (see Section 3.1.1 for details of the method). A multiple regression for nitrate against SST and chl-a was performed for the entire dataset. A plot of the predicted nitrate and the measured nitrate is shown in Figure 4.6. The r^2 statistic is now 0.80, with rmse of 1.77 μmol l^{-1} (c.f. $r^2 = 0.71$, rmse = 2.2 μmol l^{-1} without chl-a), with $p < 0.001$ and $n = 468$. The regression equation is:

$$N = 25.33 - 1.78T - 1.84C$$

The addition of chl-a to the regression has corrected the seasonality in the T-N relationship, resulting in a highly linear and physically realistic model. Armed with a statistically sound regression equation surface nitrate can be estimated from satellite images of SST and chlorophyll-a at high spatial and temporal resolution. In this study the satellite data resolution is 0.5° spatially and up to daily temporally – something that would be impossible with traditional ship board measurements.

4.3. TEMPERATURE-PHOSPHATE RELATIONSHIP:

Figure 4.7 shows temperature against phosphate for all *in situ* underway and surface bottle CTD measurements separated by season. A linear regression performed on all the data, regardless of season, results in an $r^2 = 0.73$ and rmse = 0.14 μmol l^{-1}. Although less pronounced there is a seasonality in the data similar to that seen in the TN plots with clusters of data in spring and summer and linear data in both winters. Including chlorophyll-a in the regression improves the r^2 statistic to 0.80 and rmse to 0.11 μmol l^{-1} (Figure 4.8), with $p < 0.001$ and $n = 406$. The regression equation is:

$$P = 1.72 - 0.12T - 0.11C$$

Phosphate potentially has an important role in global biogeochemical cycling. There are two views of how primary production in the world's ocean is regulated, depending on the timescale in which the question is posed. On a seasonal time scale nitrate is likely to be the first nutrient to be consumed to limiting concentrations and so limits seasonal phytoplankton blooms (Falkowski, 1997). On a geological timescale nitrogen is released through phytoplankton mortality and grazing and returns to the water column in the form of ammonium and nitrate. Nitrogen is also supplied through atmospheric deposition, and so is constantly being recycled in the upper ocean. There is no atmospheric reservoir of phosphorus, however and no alternative source once phosphate runs out (Tyrell, 1999). Phosphate has been found to be limiting in lake systems (Hecky and Kilham, 1988) and in the Sargasso Sea (Wu et al., 2000), but nitrate is, in practice, the most limiting nutrient in surface waters.

4.4. TEMPERATURE-SILICATE RELATIONSHIP:

Figure 4.9 shows temperature against silicate for all *in situ* underway and surface bottle CTD measurements separated by season. A linear regression performed on all the data, regardless of season, results in an $r^2 = 0.78$ and rmse = 1.38 μmol l^{-1}. The seasonality seen in the temperature-nitrate plots is not as evident in the temperature-silicate data. Spring silica concentrations are consistently ~ 8 μmol l^{-1} at all temperatures, with the exception of a few outliers, whilst the summer silica concentrations are ~ < 2 μmol l^{-1} at all temperatures. During the spring cruise the shallowness of the T-S slope is a consequence of geographical differences in surface temperature alone, with higher temperatures found towards the east of the basin. In the North Atlantic the first species to bloom and the primary contributor to the huge increases in biomass observed during a spring bloom are expected to be diatoms, which require silica to form their frustules (Savidge et al., 1995). The lack of silica consumption during the spring cruise suggests that the measurements were taken before the spring bloom had begun (this point will be discussed further in Chapter 8.1).

By the time of the summer cruise, at temperatures above ~9 °C, silica is consistently below < 2 μmol l^{-1}. At these concentrations diatoms are out-competed by other non-siliceous species (Egge and Aksnes, 1992; Brown et al., 2003). By the time of the summer cruise the diatom bloom has ended and little silica is being consumed. The dominant phytoplankton species are likely to be small flagellates and picoplankton, which do not require silica for growth (this will also be discussed further in Chapter 8.1).

Including chl-a in the regression of silica and temperature results in an increase of r^2 to 0.83 and rmse to 1.32 μmol l^{-1} (Figure 4.10), with $p < 0.001$ and $n = 468$. The regression equation is:

$$S = 15.66 - 1.33T - 0.59C$$

The summer silica concentration is relatively insensitive to the inclusion of chl-a, although the addition of the chl-a term to the regression improves the linearity in the other seasons. The nature of the regression equation implies that if SST and chl-a are decreasing, silica is expected to increase – however this is not occurring in summer, hence the overestimation in predicted silica. There appears to be no response in silica concentration to decreasing SST and chl-a, suggesting that during events which mix up cold water, silica is being consumed before it reaches the surface waters, indicating the possible presence of a sub-surface siliceous plankton community. The same issue does not arise in the T-N relationship because nitrate remains at relatively high concentrations throughout the year, and non-siliceous plankton can continue to flourish in the well-lit surface waters. Despite this only approximately 15 % of the predicted summertime silica concentrations fall outside two standard deviations from the regression best fit line.

4.5. CHAPTER SUMMARY:

The relationships derived above between sea surface temperature and nitrate, phosphate and silicate allow estimates of nutrient concentration and limitation throughout the basin at high spatial and temporal resolution. These will be vital to filling in the gaps in the *in situ* record and will allow a better understanding of the influence of nutrients on the interannual and spatial variability in the spring bloom.

- A seasonal dependence is evident in the temperature-nitrate relationship for the Irminger Basin.
- A linear T-N relationship is valid only in early winter, when surface cooling is beginning to mix the water column, entraining new nutrients which the phytoplankton are not able to exploit due to limiting light levels.
- An idealised T-N cycle is suggested and confirmed by the *in situ* data.
- Including chl-a in the regression improves the predictive power of the relationship.
- Similarly for phosphate and silicate: seasonality is observed in the data, but the relationship with SST is improved if chl-a is included in the regression.

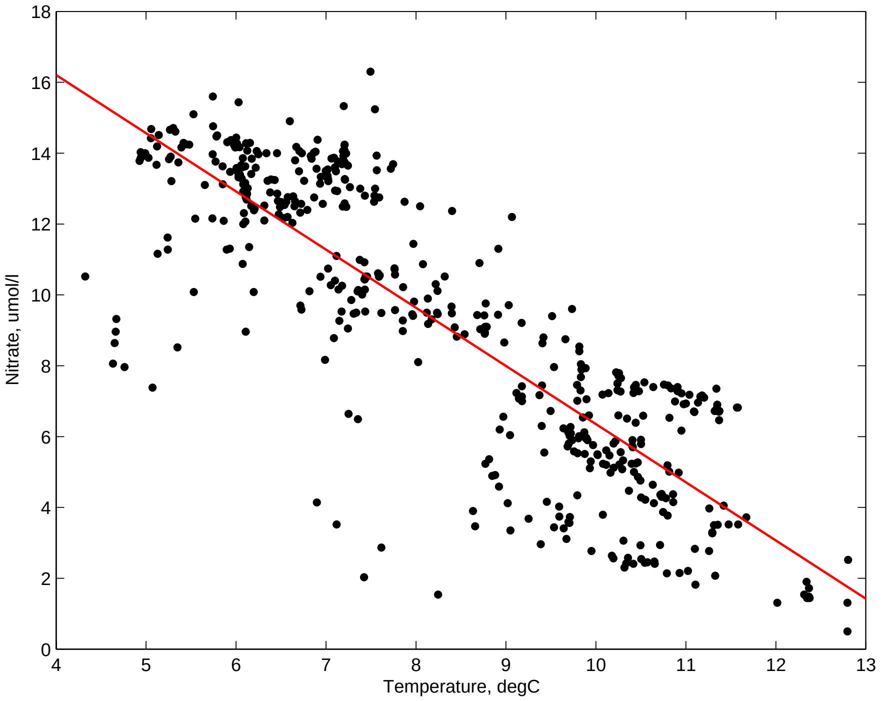

Figure 4.1: All surface temperature and nitrate data from all four cruises. The linear regression equation is N = 23 - 1.6T (red line) and has an $r^2 = 0.70$, rmse = 2.2 μmol l^{-1}, $p < 0.001$, $n = 468$. Higher order regressions result in no improvement to the r^2 statistic.

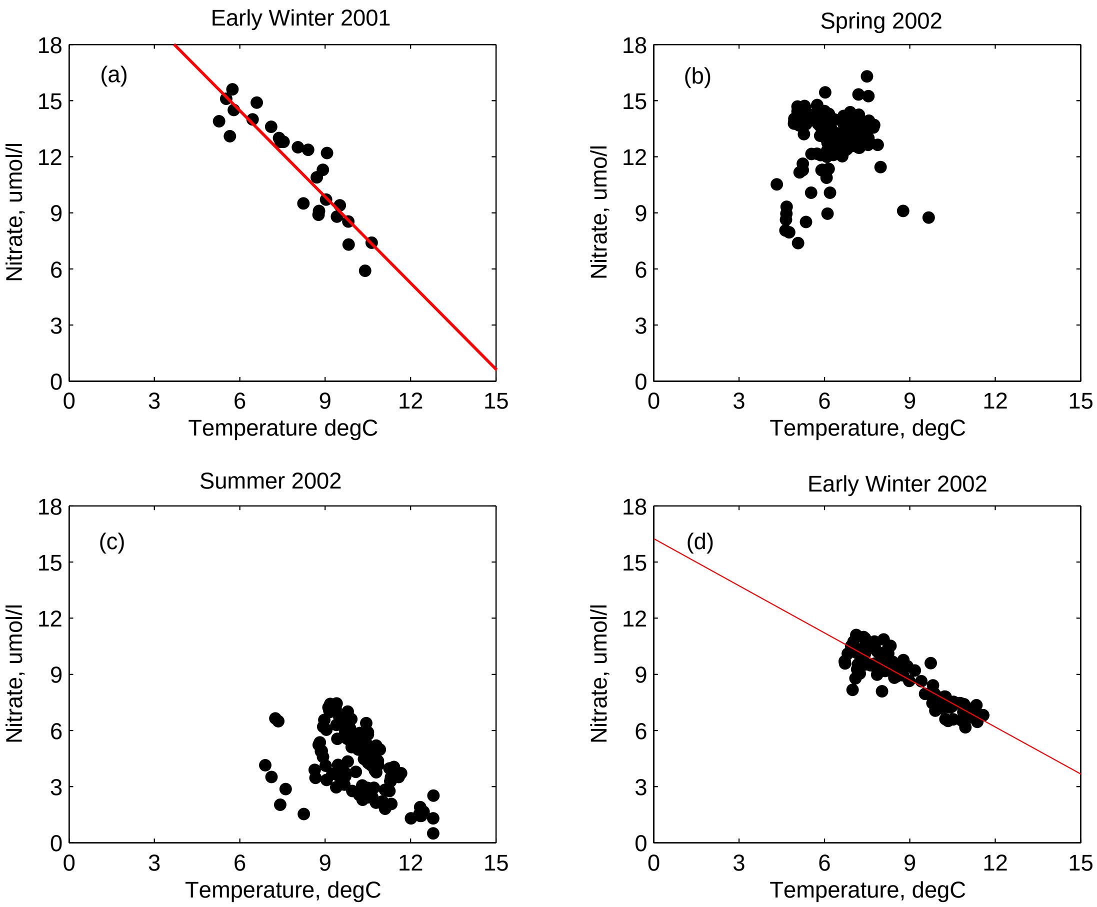

Figure 4.2: Temperature-nitrate plots for (a) Early winter 2001 (cruise D258, November/December), N = 24 – 1.5T, $r^2 = 0.82$, $p < 0.001$, n = 26; (b) Spring 2002 (cruise D262, April/May) and (c) Summer 2002 (cruise D264, July/August) regression lines not shown because statistically insignificant; (d) Early winter 2002 (cruise D267, November/December), N = 16 – 0.84T, $r^2 = 0.83$, $p < 0.001$, n = 122.

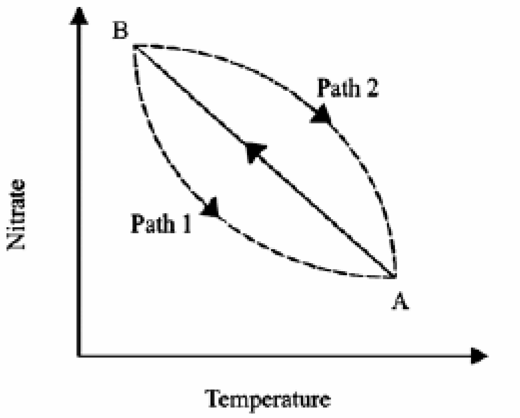

Figure 4.3: Idealised representation of the annual temperature-nitrate cycle. Point A represents post-bloom summer and Point B pre-bloom spring. Two alternative spring bloom scenarios are represented by Paths 1 and 2.

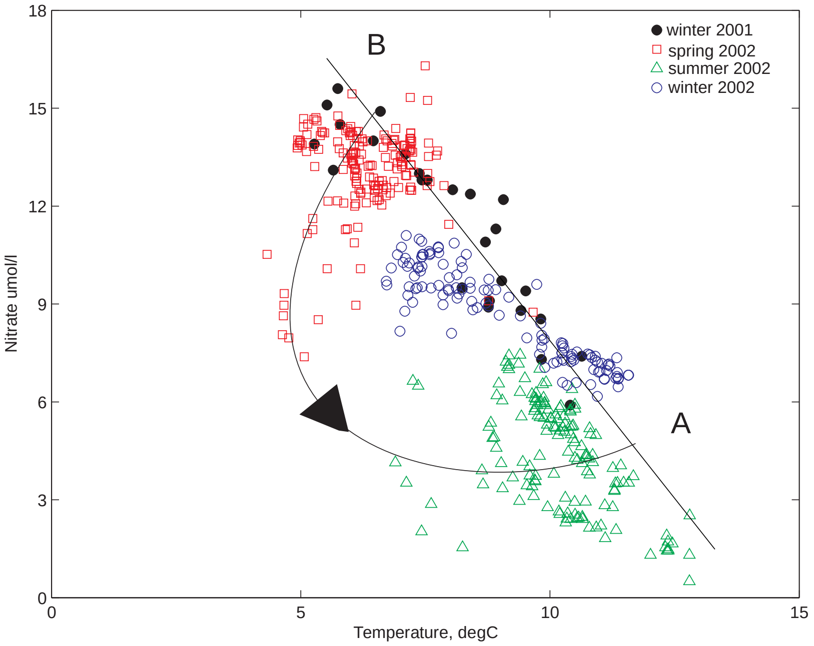

Figure 4.4: Temperature against nitrate for all four cruises. Winter 2001 (black solid dots), spring 2002 (red squares), summer 2002 (green triangles) and winter 2002 (blue open circles). The straight line is the winter 2001 mixing line and the curved line is the return path from point B (pre-bloom spring) to A (post-bloom summer).

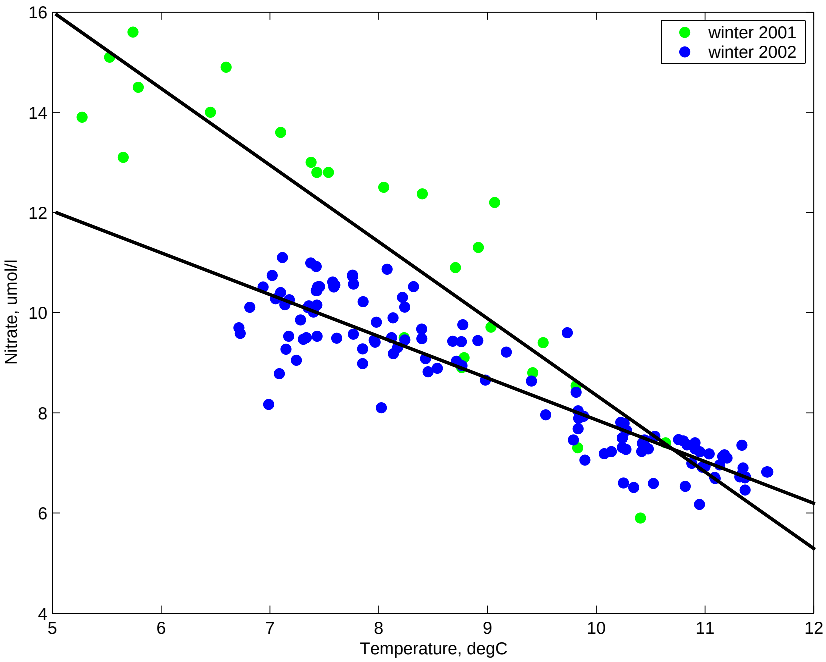

Figure 4.5: Temperature against nitrate for winter 2001 (green dots) and winter 2002 (blue dots). The individual best fit lines for both winters are also plotted.

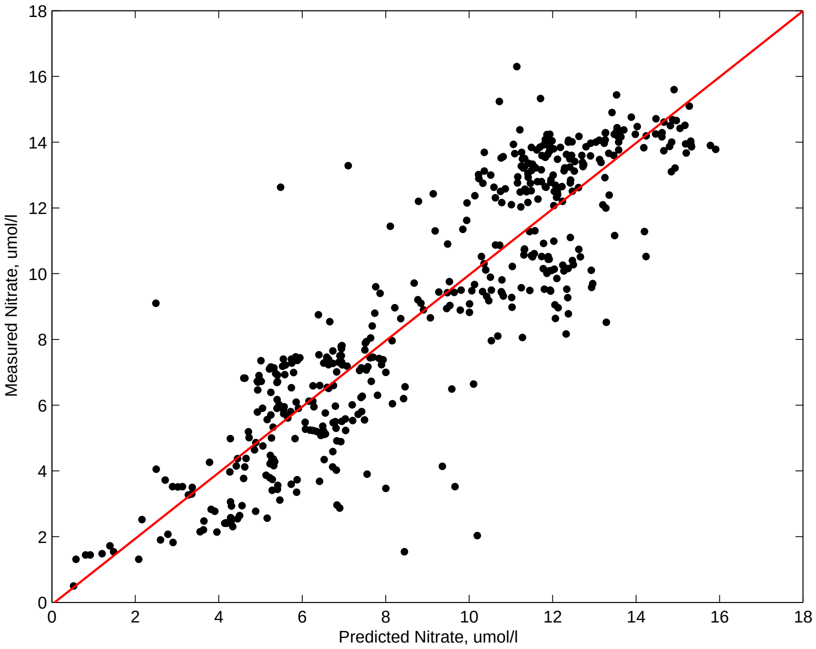

Figure 4.6: Nitrate measured *in situ* against nitrate predicted from a multiple regression of SST and chlorophyll against nitrate, N = 25.33 – 1.78T – 1.84C, $r^2 = 0.80$, rmse = 1.77 μmol l^{-1}, $p < 0.001$, $n = 468$. Higher order regressions make no improvement to the r^2 statistic.

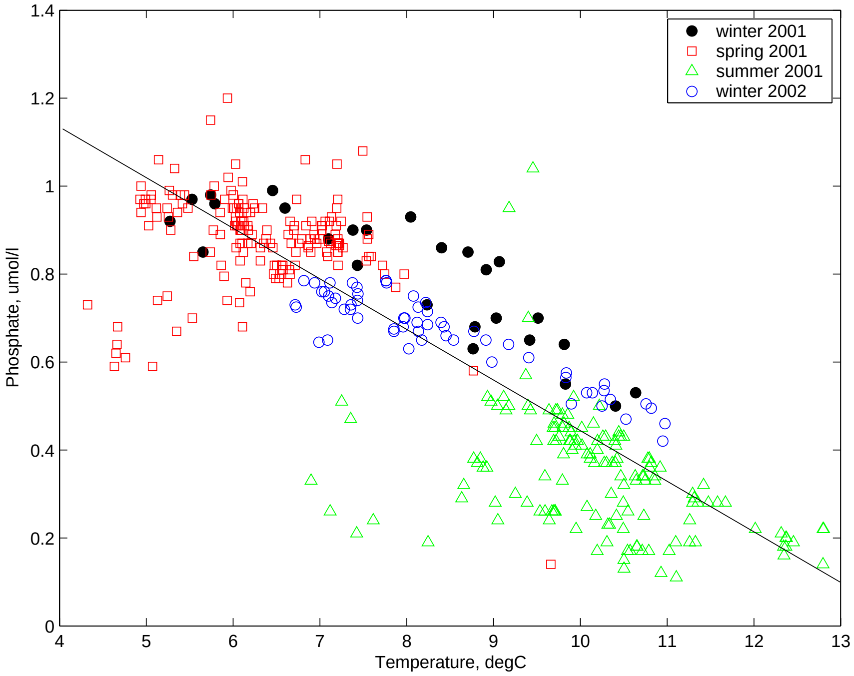

Figure 4.7: Temperature against phosphate for all four cruises. The regression line is shown in black, $P = 1.6 - 0.11T$, $r^2 = 0.73$, rmse = 0.14 µmol l^{-1}, $p < 0.001$, $n = 406$. Higher order regressions result in no improvement to the r^2 statistic.

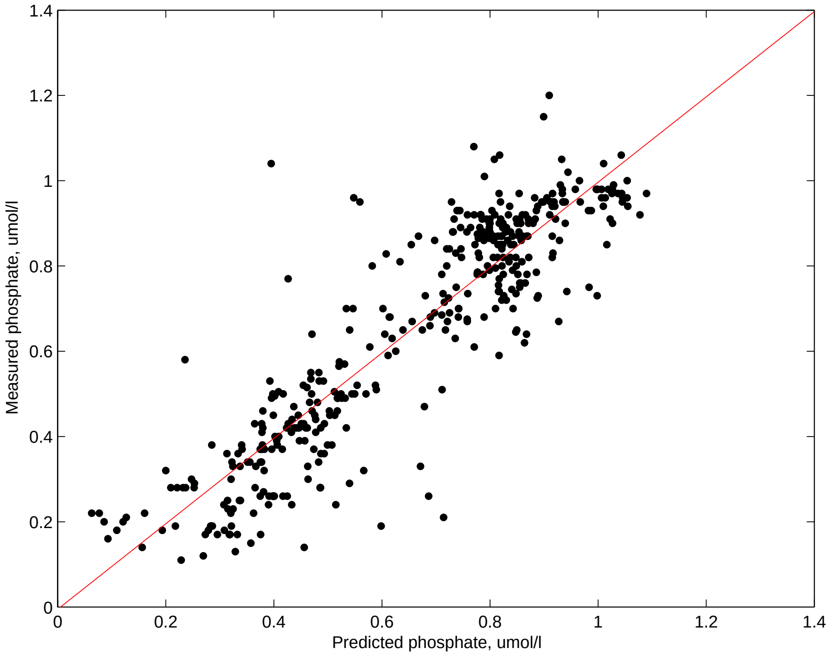

Figure 4.8: Phosphate measured *in situ* against phosphate predicted from a multiple regression of SST and chlorophyll against phosphate, $P = 1.72 - 0.12T - 0.11C$, $r^2 = 0.80$, rmse = 0.11 µmol l^{-1}, $p < 0.001$, $n = 406$. Higher order regressions make no improvement to the r^2 statistic.

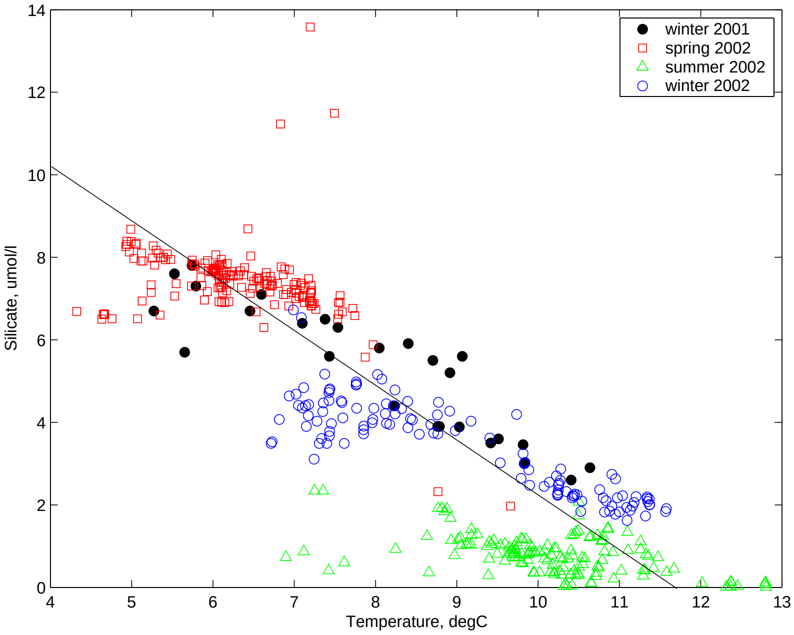

Figure 4.9: Temperature against silicate for all four cruises. The regression line is shown in black, $S = 15 - 1.3T$, $r^2 = 0.78$, rmse = 1.38 μmol l^{-1}, $p < 0.001$, $n = 468$. Higher order regressions result in no improvement to the r^2 statistic. The points which show very high silica concentrations in spring were measured on the northeast Greenland coast.

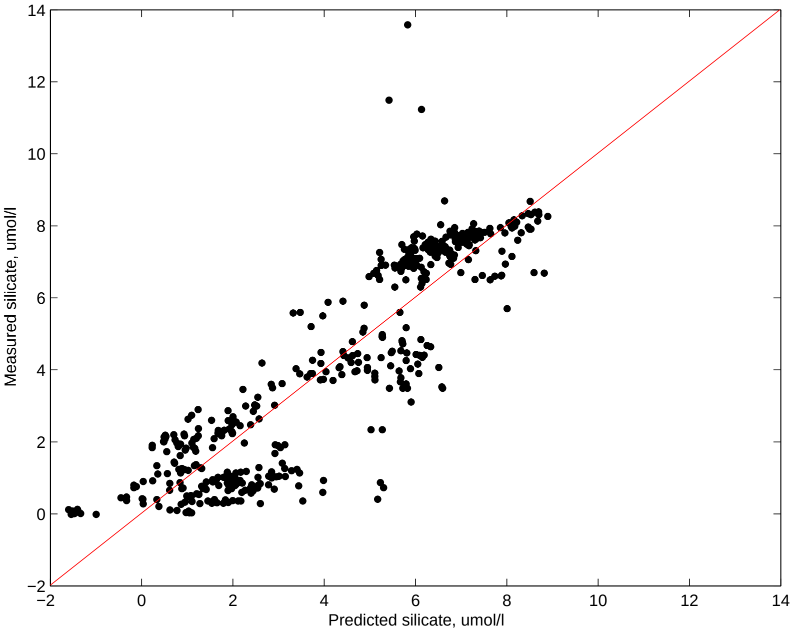

Figure 4.10: Silicate measured *in situ* against silicate predicted from a multiple regression of SST and chl against silicate, $S = 15.66 - 1.33T - 0.59C$, $r^2 = 0.80$, rmse = 1.32 μmol l^{-1}, $p < 0.001$, $n = 468$. Higher order regressions make no improvement to the r^2 statistic.

5. BIOGEOGRAPHICAL ZONES OF THE IRMINGER BASIN:

The Irminger Basin is divided into biogeographical zones on the basis of SeaWiFS chl-a in this chapter. Two methods are explored: cluster analysis and Empirical Orthogonal Function analysis. The zones defined here will be used in the subsequent chapters to represent the spatial variability in chl-a characteristics in the basin.

5.1. THE NEED FOR BIOGEOGRAPHICAL ZONES:

When confronted with a large dataset of daily satellite data for several parameters spanning six years and covering an area some 3 x 10^{10} km^2 (as in this study) it is not feasible to examine every data point or time series. Instead the technique of biogeographical zonation is a convenient way to divide up a large area into several regions, within each of which ecological characteristics are expected to stay reasonably homogenous. Such zonation seeks to define regions where the observed parameters (in this case SeaWiFS chl-a) display similar magnitude and temporal variability. A large dataset can thus be reduced to a few zones whose characteristics are representative of the areas they cover, yet are distinct from each other. Zonation not only reduces the complexity of a dataset but also reduces noise: because the features of each data series within a zone are similar, a typical mean signal can be determined.

The concept of biogeographic zones dates back to the early days of terrestrial ecology. However, the division of the oceans into biogeographic zones was rather more difficult than for the land, as so few observations existed. The advent of ocean colour satellite measurements in 1979 (the Coastal Zone Colour Scanner, CZCS) allowed estimates of chlorophyll concentration with far finer spatial and temporal resolution than could ever be obtained with ship board measurements. Although small scale regional zones had been described, or whole basins divided purely latitudinally, it was not until 1998 that Alan Longhurst published the first comprehensive atlas of biogeographic zones throughout the world's oceans (Longhurst, 1998). The Irminger Basin (IB) falls wholly within Longhurst's (1998) Atlantic Arctic Province which extends from the Greenland shelf towards the Iceland Basin and is bounded in the south by the Polar Front. However, a single province is much too large to be of help in a regional study such as this one. Holliday et al. (2005) used the Marine Productivity dataset (see Section 3.1 for a description) to further sub-divide the IB into six zones, on the basis of shallow (0-500 m) water types distinguished by their temperature, salinity and nutrient concentration– i.e. their physical hydrographic properties (see Figure 2.15 and Chapter 2.2.1). This study's primary focus however is the characteristics of the chlorophyll-a distribution. As the *in situ* chlorophyll and phytoplankton taxonomic data collected during the MarProd programme are insufficient to define biological zones, in this study the SeaWiFS chlorophyll-a product is used to divide the IB into zones.

In Figure 5.1 mean monthly composites of six years (1998-2003) of SeaWiFS chlorophyll-a concentration (chl-a) data are presented. The spring bloom in the Irminger Basin does not progress smoothly northwards during the course of spring, but rather begins in April on the Iceland shelf and in early May along the east Greenland coast. The monthly composites tend to blur the finer details of the bloom progression, but this is remedied in Figure 5.2 which presents mean (from 1998 – 2003) weekly composites from 8th April to 7th October. Chl-a remains consistently high (~2 mg m^{-3}) on the Iceland shelf from April until October, whilst on the Greenland coast the chl-a levels have dropped back from ~2 mg m^{-3} in mid-May to ~0.5 mg m^{-3} by mid-June. In the central basin (deeper than ~2000 m) chl-a is seen to increase to ~1 mg m^{-3} from mid-May but soon returns to low levels (~0.5 mg m^{-3}) by mid-June, although a brief increase to ~0.8 mg m^{-3} is observed in late August. Further east over the Reykjanes Ridge, the area shallower than ~1000 m that stretches southwest from Iceland, chl-a slowly increases throughout May with the area closest to Iceland experiencing chl-a up to ~2 mg m^{-3} and further offshore concentrations reach ~1 mg m^{-3}. Chl-a remains at ~0.7 mg m^{-3} throughout June and July then increases again to ~1 mg m^{-3} in early August before decreasing again during September. In winter very few SeaWiFS chl-a images are available in the Irminger Basin due to cloud cover and low incident sun angle, and therefore they are not presented here. The first image presented, from the 8th to 14th April, shows uniform chl-a of ~0.3 mg m^{-3} across the basin.

Examination of the composites reveals that the Irminger Basin spring bloom has different characteristics in different parts of the basin. This suggests that dividing the basin into zones on the basis of chl-a could be successful. Two quantitative, objective methods for defining the zones are described. Firstly, cluster analysis is used to determine regions which have similar chl-a magnitudes on a seasonal time scale. Then a more complex method for dividing the basin, Empirical Orthogonal Function analysis, is described.

5.2. CLUSTER ANALYSIS:

Cluster analysis is a technique which aids in organising large datasets into meaningful structures. It is a multivariate statistical classification for discovering whether the individuals of a population fall into different groups by making quantitative comparisons of characteristics. As an exploratory data analysis tool it aims to sort objects into different groups in such a way that the degree of association between two objects is maximal if they belong to the same group and minimal otherwise. Cluster analysis can be used to highlight patterns in data, although it cannot provide an explanation or interpretation for why they exist.

K-means clustering is a method suitable for clustering large data sets, which uses the actual observations of objects or individuals in the data. For n objects, each having p variables k-means clustering treats each observation in the data as an object having a location in p-space – this is illustrated for a two-variable ($p = 2$) example in Figure 5.3. K-means clustering assesses the distance (as shown in Figure 5.3) between each object and every other object in the dataset. The distance measure is the squared Euclidean, so that the distance, d, between object i and object j is:

$$d_{ij} = \sum_{n=1}^{n=p} (x_{in} - x_{jn})^2 \qquad \text{[Eqn 5.1]}$$

where x is the variable to be clustered. It then finds a partition in which objects within each cluster are as close to each other as possible and as distant from objects in other clusters as possible. Each cluster in the partition is defined by its member objects and by its centre or centroid. The centroid for each cluster is the point to which the sum of distances from all objects in that cluster is minimized – this is illustrated for a two-variable (p = 2), three cluster (k = 3) example in Figure 5.4. K-means clustering uses an iterative algorithm that minimizes the sum of distances from each object to its cluster centroid, over all clusters. The cluster centroids are initially placed at random in the variable space. Each object is assigned to the centroid to which it is closest, creating the initial clusters. The position of the centroid is then recalculated and objects are re-assigned to the closest centroid. This continues until reassigning any single object to a different cluster increases the total sum of distances, i.e. k-means clustering attempts to minimise the function J:

$$J = \sum_{j=1}^{k} \sum_{i=1}^{n} \left| x_{ij} - C_j \right|^2 \qquad \text{[Eqn 5.2]}$$

where k is the number of clusters, n is the number of objects, x is the position of the variable and C is the position of the centroid. The result is a set of clusters that are as compact and well-separated as possible. The disadvantage of k-means clustering is that the user must decide how many clusters should be generated prior to the analysis. Fortunately there are objective ways of deciding the optimum number of clusters. The simplest way to judge how many clusters are required to accurately represent the data is to consider the silhouette values. The silhouette value for each point is a measure of how similar that point is to points in its own cluster compared to points in other clusters, and ranges from -1 to +1. A value of +1 indicates that points are very distant from neighbouring clusters, zero indicates points that are not distinctly in one cluster or another and -1 indicates points that are probably assigned to the wrong cluster. Ordinary significance tests, such as analysis-of-variance F tests, are not valid for testing differences between clusters. Since clustering methods attempt to maximize the separation between clusters, the assumptions of the usual significance tests are violated (Hawkins et al., 1982).

For the purposes of this analysis the chl-a data were divided into five 'seasons'. Winter is from 1st January to 10th April (day of year 1 to 100), early spring is from 11th April to 30th May (days 100 to 150), the late spring period is from 31st May to 19th July (days 150 to 200), summer is from 20th July to 7th September (days 200 to 250) and autumn is from 8th September to 16th December (days 250 to 350). The data are divided into seasons, rather than months, to smooth out some of the variability in the data which can make it hard for the k-means clustering solution to converge. The seasonal means of chl-a (Figure 5.5) still capture the key features of the seasonal progression of chlorophyll concentration.

An average chl-a value for each pixel during each season over six years was calculated. A matrix was formed such that each row was a chl-a measurement (i.e. object) and each column was one of the five seasons (i.e. $p = 5$). The k-means analysis is thus attempting to define clusters of chl-a magnitude in five-season space. The Matlab function *kmeans* was used to perform the analysis with the distance measure (that is, the method of measuring the distance between points that *kmeans* attempts to minimise) set to squared Euclidean (as in Equation 5.1). The *kmeans* function does not permit NaNs (Not a Number, the Matlab term for missing or invalid data), so the NaNs in the seasonal means (which exist only for pixels flagged as land) were removed. The *kmeans* function uses a two-phase iterative algorithm. In the first phase each iteration consists of reassigning objects to their nearest cluster centroid, all at once, followed by recalculation of centroids. This phase provides a fast but potentially only approximate solution as a starting point for the second phase in which objects are individually reassigned if doing so will reduce the sum of distances. Cluster centroids are recomputed after each reassignment. Each iteration during this second phase consists of one pass though all the objects. The *kmeans* function converges to a local optimum i.e. a partition of objects in which moving any single object to a different cluster increases the total sum of distances. To determine the optimum number of clusters the *kmeans* function was executed for the number of clusters set at between four and seven. The mean of the silhouette values was greatest for five clusters (mean silhouette value = 0.60), indicating that maximum separation of clusters occurs when the data is divided into five zones (i.e. $k = 5$).

The resulting clusters are displayed in Figure 5.6. Areas on the figure that have the same colour are clusters which represent regions within which the chl-a magnitude varies seasonally in a similar manner. The colours themselves are arbitrary and simply represent a cluster number, $k = 1,2\ldots5$. The five zones resolved by the cluster analysis are approximately: dark red – the central basin; green – Reykjanes Ridge; dark blue – east Greenland coast; light blue and orange – Iceland shelf. Ignoring the Iceland shelf zones (light blue and orange), which account for only 9% of the total area, cluster analysis suggests that the basin can be divided into three regions within which the chl-a characteristics can be expected to be similar.

Comparing these regions to the zonation based on hydrographic properties proposed by Holliday et al. (2005) the central basin region corresponds to their Central Irminger Sea and parts of the Northern Irminger Current regions (see Figure 2.15, Section 2.2.1). The Reykjanes Ridge zone of the cluster analysis encompasses Holliday et al.'s Reykjanes Ridge Mode Water and parts of the Iceland Basin and Southern Irminger Current regions. The east Greenland shelf zone in the cluster analysis is equivalent to Holliday et al.'s East Greenland Current (Atlantic) and East Greenland Current (Polar). Thus the biological zones and physical zones generally correspond, although the biological zones are larger than the physical ones.

This analysis is useful as a first step, but is restricted to grouping data solely by their values, and only takes account of the seasonally-varying component of the chl-a signal. In addition it is based on a six-year average chl-a, divided into seasons – can we be confident that the zones will be valid on shorter timescales and throughout the six years of the dataset? A more complex method for partitioning data is Empirical Orthogonal Function analysis.

5.3. EMPIRCAL ORTHOGONAL FUNCTION ANALYSIS:

Empirical Orthogonal Function (EOF) analysis is a method for analysing the variability of a field which consists of only one scalar variable (e.g. sea surface temperature, wind speed). The method allows the identification of the principal modes of variability, whether spatial or temporal, in the dataset. The technique is widely used in studies which employ satellite data or climate model outputs, as there is often a huge quantity of complex data. The EOF method can sometimes help to pick out the patterns in these large datasets. An EOF analysis will return maps of the spatial patterns of variability (modes), the time variation of the modes and a measure of the amount of variability explained by each mode.

There are many thorough texts that explain the matrix algebra of EOF analysis (e.g. Preisendorfer, 1988; von Storch and Zwiers, 1999), so here only a brief overview of the mathematics of the method is given and instead the focus is on the interpretation of the results of an EOF analysis – a topic which is sometimes glossed over by the more mathematical texts (but see Venegas, 2001). Note that only analysis of real-valued fields is discussed, so that the patterns produced by the EOF analysis represent only standing oscillations, and not propagating patterns (as in the analysis of complex EOFs).

5.3.1. FORMAL DESCRIPTION:

Suppose in the dataset under analysis there are measurements of some variable at several locations, $x_1, x_{2\dots} x_p$ taken at times $t_1, t_2 \dots t_n$. At each time the measurements can be visualised as a map. The measurements must be in a matrix **F** which has n maps, each of which consist of p points, so the matrix is n rows by *p* columns (see Figure 5.7). This way of arranging the data is referred to as S-mode (spatial) analysis and will be the only method discussed here.

The data must first be detrended so that each column of data has zero mean. Then **R**, the covariance matrix of **F** is formed by calculating:

$$\mathbf{R} = \mathbf{F}^{t} \, . \, \mathbf{F} \qquad \text{[Eqn 5.3]}$$

and then the eigenvalue problem is solved such that:

$$\mathbf{RC} = \mathbf{C\Lambda} \qquad \text{[Eqn 5.4]}$$

where **Λ** is a diagonal matrix containing the eigenvalues λ_i of **R**. The column vectors c_i of **C** are the eigenvectors of **R** corresponding to the eigenvalues λ_i.

In other words we have decomposed the original matrix into a series of eigenvectors (which are the EOFs) each of which ‘explains’ a decreasing proportion of the variability in the dataset. The EOFs can be plotted as maps, each of which represents a mode of variability – a standing oscillation in the data. The percentage of variance explained by each mode can be found by dividing λ_i by the sum of all the other eigenvalues.

The time series of an EOF mode shows how the spatial pattern varies with time and is calculated as:

$$\vec{a}_i = \vec{c}_i \; . \, \mathbf{F} \qquad \text{[Eqn 5.5]}$$

The mathematics of performing an EOF analysis is relatively straightforward, but often upon completing an EOF analysis, it can be difficult to successfully interpret the results.

5.3.2. INTERPRETING EOFS:

Imagine that every row in the matrix **F** is plotted as a position vector in p-dimensional space. If the observations are totally random the resulting plot will look like a large mass of data points. If however there are any patterns or regularities in the data these will be seen as clusters of points in particular regions (or directions) of the plot. The aim of EOF analysis is to define a new coordinate system where the axes of the graphs are rotated, so that they pass through the centre of a particular cluster (see Figure 5.8 for an illustration of a case where $p = 2$). By doing this a pattern (or mode of variability) in the data is picked out and the resulting EOF describes the spatial distribution of the mode. The first EOF is the projection of the original measurements onto the new coordinate system which maximises the variance explained. An analysis often reveals that just the first few EOF modes explain a large proportion of the variance. This is exactly what is hoped for: the EOF analysis has reduced the large and complex dataset to a few modes of variability.

The difficulty now comes in trying to interpret the physical basis behind the EOF patterns. The first issue is that there is not necessarily any link between the patterns and a 'real-world' physical mechanism. The EOFs are purely statistical entities and there is no *a priori* reason why they should reflect dynamical processes. Indeed a single physical process can be spread over several modes, or alternatively more than one process may contribute to a single EOF mode.

The most important factor in being able to successfully interpret EOF modes is a thorough understanding and familiarity with the data to be analysed. An EOF analysis should not be embarked upon until the data has been investigated using more simple methods, such as identification of anomalies, time series at certain grid points, correlation analyses etc. In addition knowledge of the physical processes which might be observed is vital. In oceanography these may be, for example, upwelling events, El Niño or topographically forced processes.

Secondly, the maps of the modes of variability need to be presented in a way that will aid interpretation. The EOF patterns themselves are dimensionless and interpreting them in terms of useful quantities is not always easy. Instead an homogenous correlation map, which is the correlation between the time series of the EOF mode and the time series of the original data at each point, can be created. This map highlights the ‘centres of action’ of the mode and in addition, the square of the correlations is a measure of the percentage of the variance explained locally by each mode (Houghton and Tourre, 1992).

Finally the physical interpretation of the EOF patterns is greatly helped by studying the time series of the EOF modes. Generally an inter-annual (or possibly inter-decadal if a longer time series is available) signal will be easily recognisable in the time series, although often a running mean filter is applied to remove some of the noise. The time series will usually oscillate between positive and negative values. Where the time series is negative (positive) this corresponds to areas of negative (positive) correlation in the EOF spatial maps.

One difficulty with interpreting EOFs often arises from the fact that the modes are constrained to be orthogonal. There is usually no reason in climate studies to expect that the data were generated by orthogonal modes of variability. Richman (1986) suggests that rotating the EOFs may yield more insight into the physical processes behind them. The general concept is to replace the EOF spatial patterns in **C** (from Equation 5.4) with patterns $\mathbf{C}^{\mathbf{R}}$ that satisfy:

$$\mathbf{C}^{\mathbf{R}} = \mathbf{C}.\mathbf{R} \qquad \text{[Eqn 5.6]}$$

where the matrix **R** is chosen such that the resulting rotated patterns, $\mathbf{C}^{\mathbf{R}}$, maximise a simplicity function. There are several different rotations, each with its own simplicity function, but the ‘varimax’ rotation is the most commonly used. The varimax rotation finds a linear combination of the original EOF spatial patterns such that the variance of the time series (or loadings) is maximised. The function to be maximised is:

$$V = \sum_j \left(\frac{1}{t} \sum_i a_{ij}^4 - \left(\frac{1}{t} \sum_i a_{ij}^2 \right)^2 \right) \qquad \text{[Eqn 5.7]}$$

where t is the number of observations (see Figure 5.7) and a are the time series of Equation 5.5 (Richman, 1986). An orthogonal rotation, such as varimax, will find a new orthogonal basis, but, unlike the unrotated case, the time series in the rotated frame will not be uncorrelated. There is much debate on whether to rotate or not to rotate, but the general consensus is that if rotation aids interpretation it should be carried out (Jolliffe, 1989). More details on the mathematics and pros and cons of rotation can be found in Preisendorfer (1988) and von Storch and Navarra (1999).

In conclusion, the correlation maps and the time series of the EOF modes together, combined with a good understanding of the physical processes under study, should yield a sensible interpretation of the results. A note of caution though from von Storch and Navarra (1999): ‘[advanced statistical] methods are often needed to find a signal in a vast noisy phase space, i.e. the needle in the haystack. But after having the needle in our hand, we should be able to identify the needle by simply looking at it.’

5.3.3. EOF ANALYSIS OF IRMINGER BASIN SEAWIFS CHLOROPHYLL DATA:

All six years of daily SeaWiFS chl-a data were concatenated into a matrix of n rows (time) by p columns (space). Any interannual trend was removed from the data before further analysis. The Matlab function *eig* was used to find the eigenvalues and eigenvectors of the data covariance matrix. The *eig* function first reduces the covariance matrix **R** to upper Hessenberg form **H**, which is zero below the first subdiagonal. The reduction may be written as **R** = **QHQ’** where **Q** is orthogonal. The upper Hessenberg matrix **H** is then reduced to Schur form **T**, where **H** = **STS’**, where **S** is orthogonal. The eigenvalues are on the diagonal of

T. Eigenvectors of **R** are then computed by solving a triangular system of equations taken from **T** and multiplying by **S** (Demmel, 1997). As the *eig* function cannot handle NaNs, only data from days 50 to 300 (19th February to 27th October) were included in the analysis, as outside of this range data were consistently absent (primarily due to low incident sun angle). In addition the stationary NaNs, due to land masses, were removed from the dataset before analysis. The matrix was therefore ~ 1500 (time – 250 days by 6 years) by 800 (space – number of non-land pixels). After the *eig* function had been executed the time series of the EOFs were calculated and the spatial maps of the EOF modes were reconstructed by replacing the land pixels. When the analysis was complete the EOF maps failed to reveal the 'needle in the haystack', so a rotation, as discussed in Section 5.3.2, was undertaken, as there were no grounds to believe that the modes of variability in the chl-a dataset would be orthogonal.

When rotation of eigenvectors is performed usually only some of the eigenvectors (and corresponding time series) from the original analysis are used in order to reduce computational time. The eigenvalues of each mode were therefore examined to determine which modes to keep for rotation and which to discard, as below a certain limit the signal is essentially noise and not useful to the analysis. If two EOF modes have similar eigenvalues than the likelihood is that the EOFs are degenerate and their patterns will not describe separate modes of variability. To determine how many modes to keep, North's 'rule of thumb' was employed (North et al., 1982). To apply North's rule an estimate of the number of *independent* samples is needed. For many geophysical parameters the number of independent samples will be less than the actual number of samples. This is due to auto-correlation within a time series i.e. the parameter has 'memory' and a measurement made today is not completely independent of a measurement made yesterday. Equally a measurement made at a particular location may not be independent of a measurement made at a neighbouring location. The number of independent samples, the 'effective sample size', *N'*, can be estimated from knowledge of the first auto-correlation coefficient (Dawdy and Matalas, 1964):

$$N' = N\frac{1-r_1}{1+r_1} \qquad \text{[Eqn 5.8]}$$

where N is the sample size and r_1 is the first autocorrelation coefficient (from the covariance matrix **R** in equation 5.3). For the chl-a dataset under consideration here r_1 ~0.5, which reduces the sample size from 1500 to 500 independent samples.

North's rule of thumb states that if the error of an eigenvalue is comparable to the difference between the eigenvalue and its nearest neighbour then the corresponding EOFs are effectively degenerate. The error of an eigenvalue λ_k is:

$$\Delta\lambda_k \approx \sqrt{\frac{2}{N'}}\lambda_k \qquad \text{[Eqn 5.9]}$$

If $\Delta\lambda_k$ is comparable to $\lambda_k - \lambda_j$ (where λ_j is the neighbouring eigenvalue) then the pair should be discarded. For the chl-a dataset North's rule of thumb suggested that the first four EOF modes should be kept. The modes explain in total 44.2% of the variance, with mode 1 explaining 28.8%, mode 2: 6.5%, mode 3: 5.0% and mode 4: 3.9%.

A varimax rotation was performed on the first four EOF modes (see Section 5.3.2 for description). The Matlab script used to process the data was based on one written by David Kaplan (University of California; http://erizo.ucdavis.edu/~dmk/ software). A new set of eigenvectors and spatial EOFs are produced from the truncated EOFs supplied to the script. Homogenous correlation maps (that is the correlation, at each pixel, between the time series of the original data and the time series of the EOF) for each of the rotated modes were produced (Figure 5.9). Only those points for which the correlation is significant ($p < 0.01$) are plotted. For completeness the corresponding time series of the modes are plotted in Figure 5.10. They will not be discussed here, but will be returned to in Chapters 6 and 7.

The correlation maps reveal four distinct 'centres of action'. The Mode 1 centre is located to the southwest of Iceland, Mode 2 is on the east coast of

Greenland, Mode 3 is centred over the Reykjanes Ridge, and Mode 4 is in the centre of the basin. Comparing these zones to those of Holliday et al. (2005) Mode 1 corresponds to their Iceland shelf region and parts of the Northern Irminger Current. Mode 2 covers the East Greenland Current (Atlantic and Polar) regions, whilst Mode 3 encompasses Holliday et al.'s Iceland Basin, Southern Irminger Current and Reykjanes Ridge zones. Mode 4 corresponds to the Central Irminger Sea zone. These zones are similar to those seen in the cluster analysis, although the inner and outer Iceland shelf zones have been combined in the EOFs. As EOF analysis also considers the time-varying component of the chl-a signal we can be confident that the zones are not only valid on a seasonal time scale, or for one particular year, but throughout the six years of the dataset.

In the following chapters just three of the four zones revealed by the cluster and EOF analysis will be considered: the east Greenland coast, the Reykjanes Ridge and the central basin. The Iceland shelf is a region which displays very little seasonal variability (see Figure 5.1). A 'spring bloom' in the classical sense does not occur, as chl-a remains high throughout the year due to shallow waters and terrigenous input of nutrients. As this study focuses on the physical forcing of the spring bloom this zone is not relevant to the analysis.

In this chapter the EOF analysis has only been used to study the partitioning of the data into zones. The spatial EOF maps and the corresponding time series contain more information than this however, and will be returned to in Chapters 6 and 7.

5.4. CHAPTER SUMMARY:

Handling a large dataset is made easier by the definition of biogeographical regions within which bloom characteristics are expected to be similar. Two objective methods for determining the zones on the basis of SeaWiFS chl-a have been presented: cluster analysis and EOF analysis. The locations of the zones resulting from both methods are notably similar.

- Four biological zones have been identified within which chl-a can be expected to have similar characteristics. The characteristics of the zones will be explored in Chapter 6.
- The four zones are: the Iceland Shelf, the Reykjanes Ridge, the East Greenland coast and the Central Irminger Sea. The Iceland Shelf region, however, will not be discussed further, as it does not experience a distinct spring bloom and as such its characteristics are outside the subject area of this thesis.

In the following chapters the three zones chosen for closer inspection will be referred to as examples of spatial variability in the Irminger Basin.

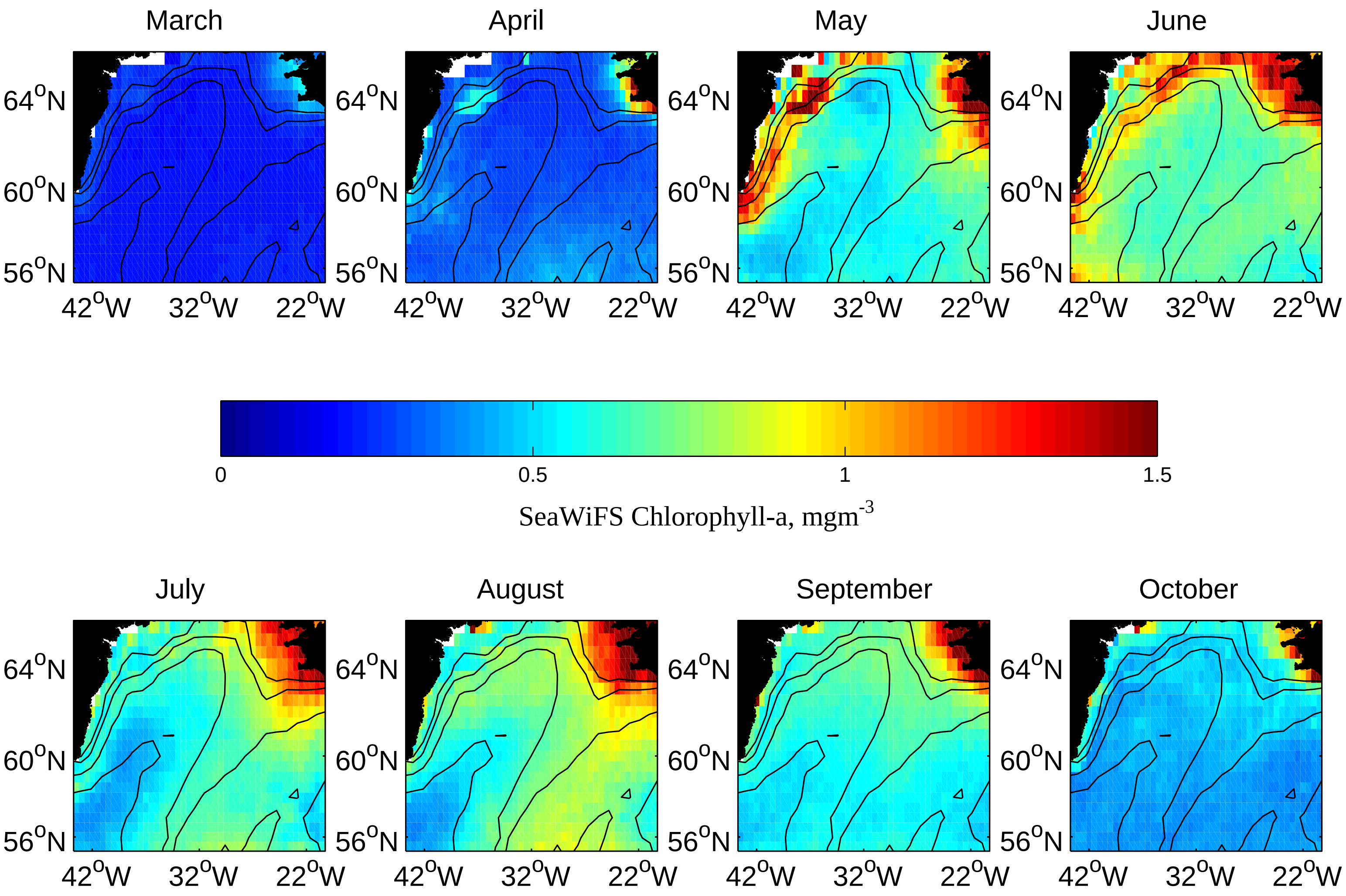

Figure 5.1: Monthly mean over six years (1998 – 2003) of SeaWiFS daily chl-a. This figure and all subsequent figures with land masses plotted were created using the m_map toolbox for Matlab plotting (Rich Pawlowick; University of British Columbia; http://www2.ocgy.ubc.ca/~rich/map.html).

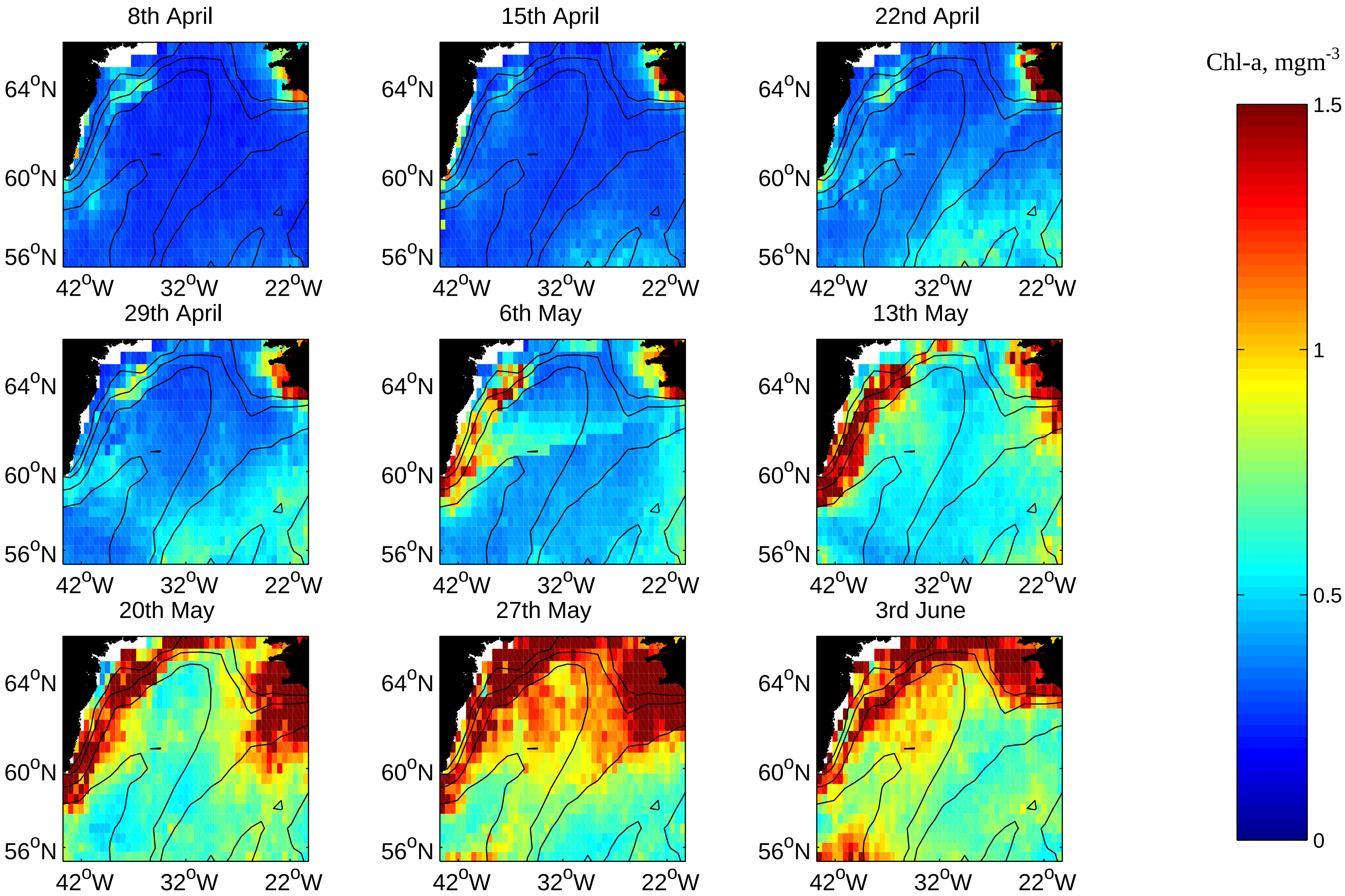

Figure 5.2: Weekly composites over six years (1998 – 2003) of SeaWiFS daily chl-a. Dates above images are the start date of the 7-day composite.

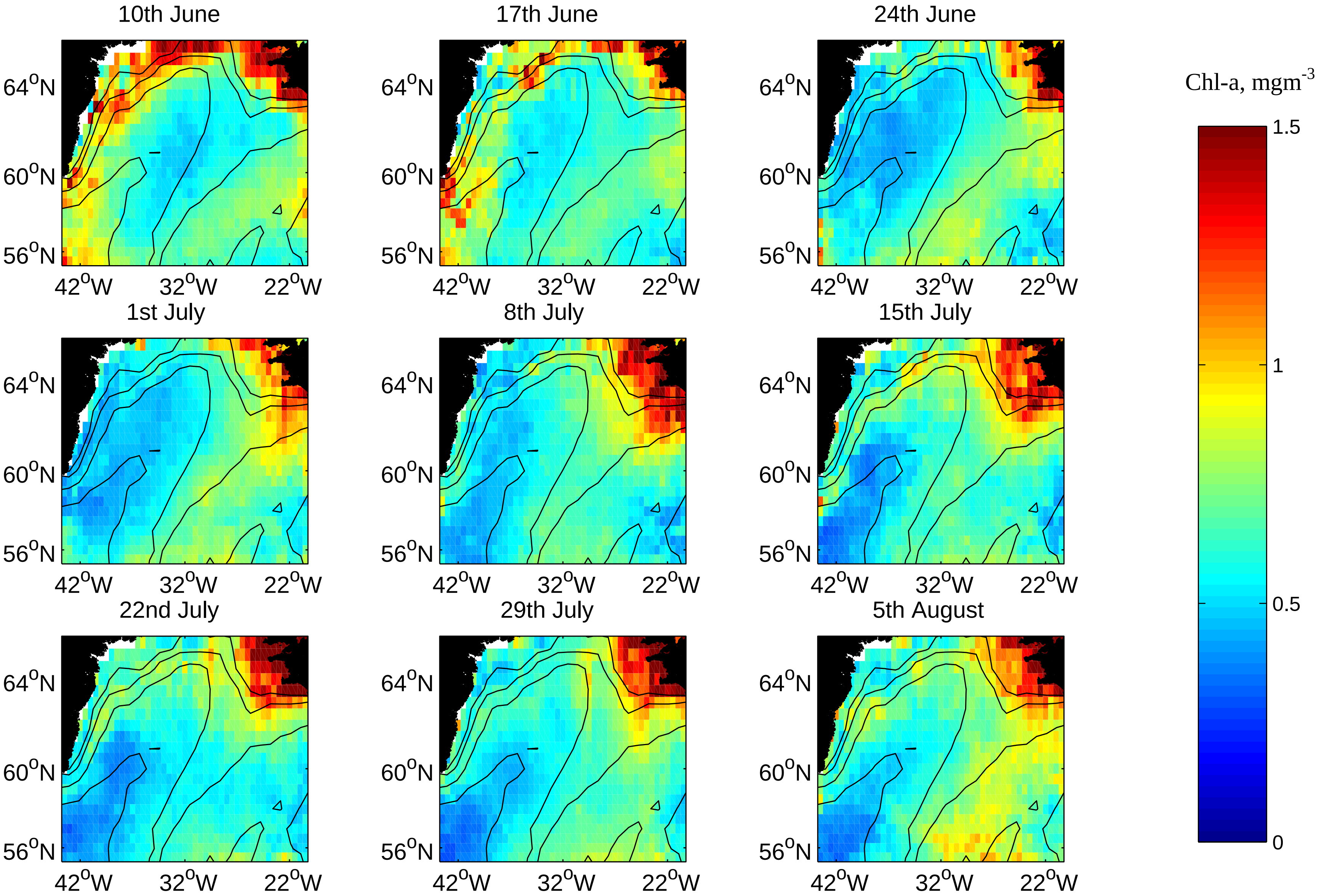

Figure 5.2 continued

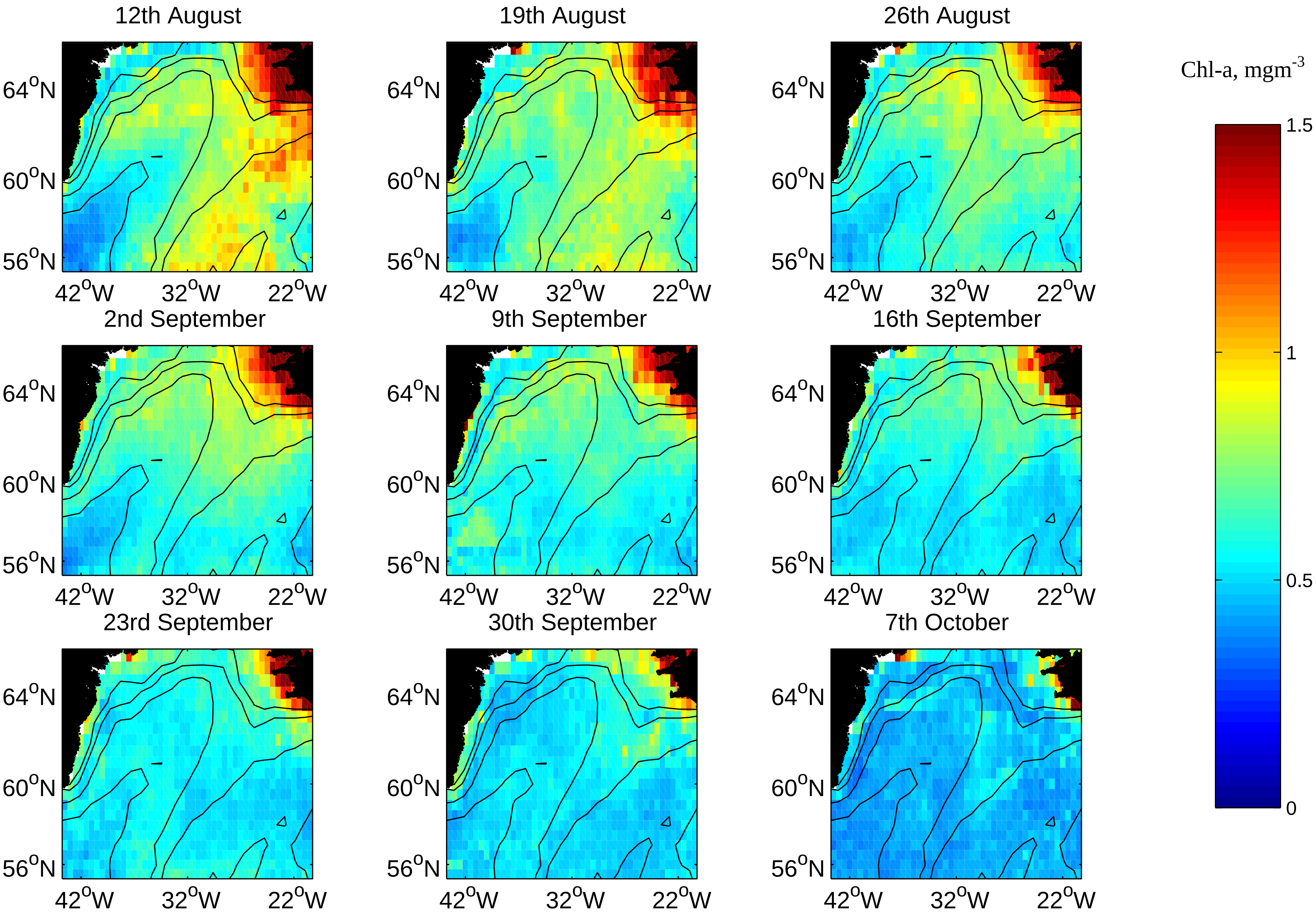

Figure 5.2 continued

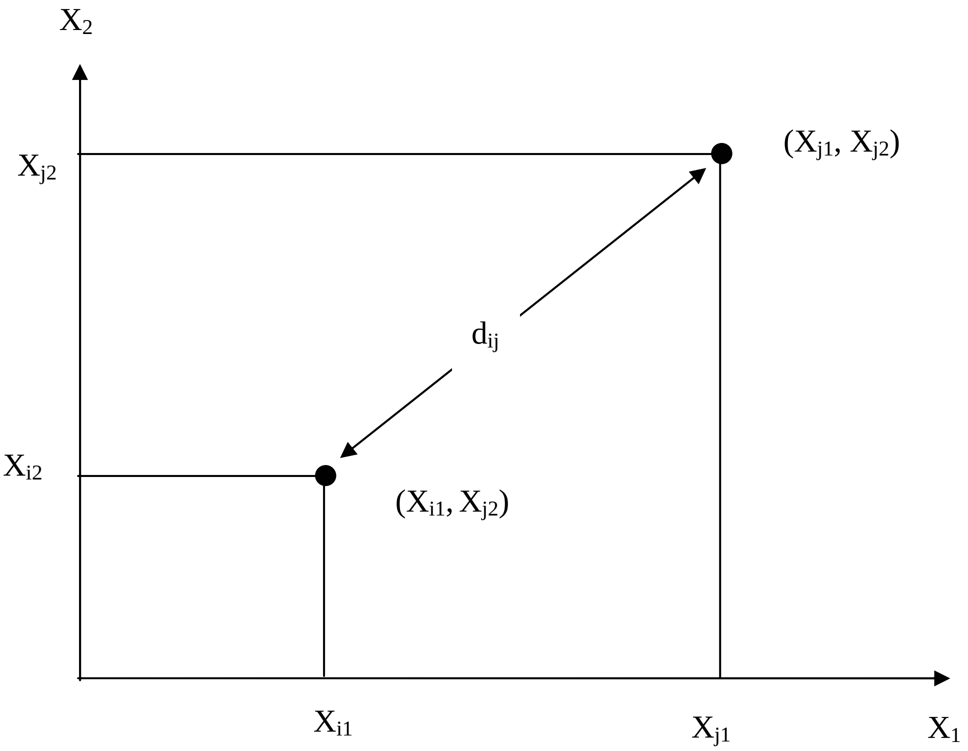

Figure 5.3: Illustration of the distance, d_{ij}, between two objects, i and j, in the case where number of variables, p = 2.

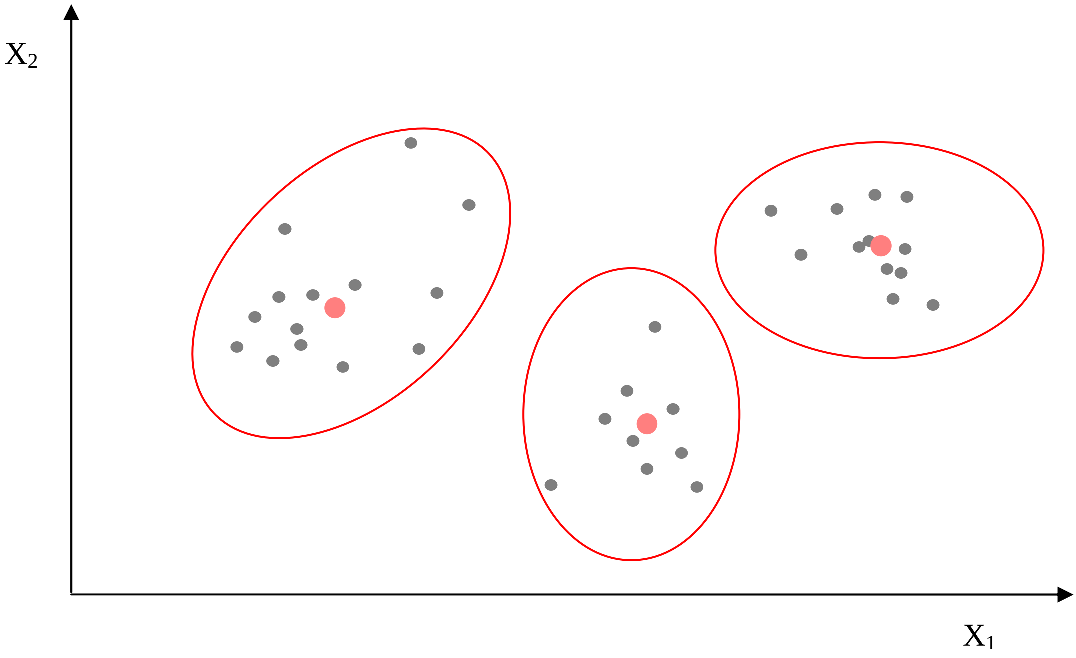

Figure 5.4: Illustration of clustering in the case where p = 2. The black dots represent objects and the red dots represent the centroid for each cluster i.e. the point to which the sum of distances from all objects in that cluster is minimized. The red ovals represent the three clusters (k = 3).

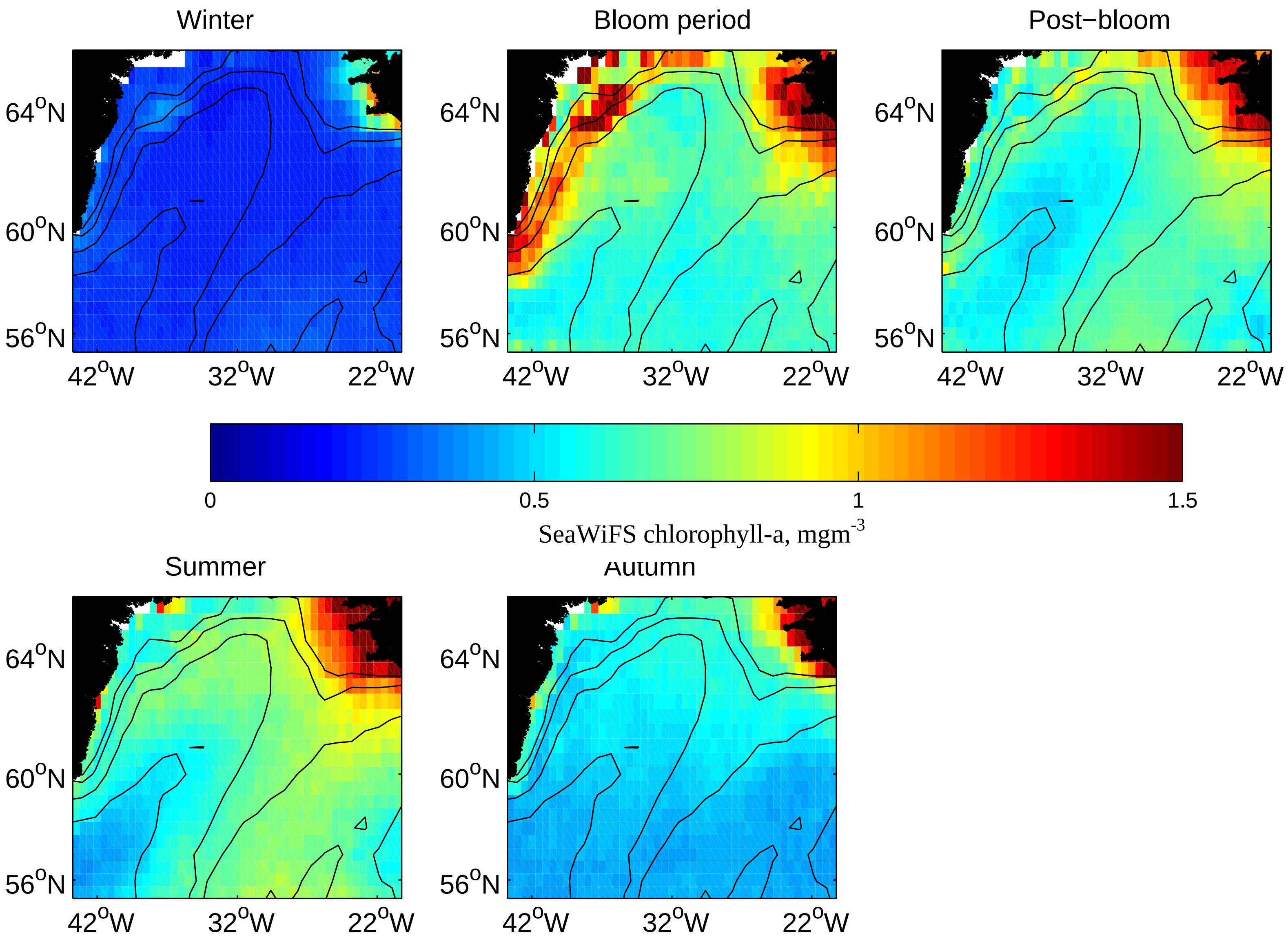

Figure 5.5: Seasonal means of chl-a from SeaWiFS daily data. For definition of seasons see Section 5.2.

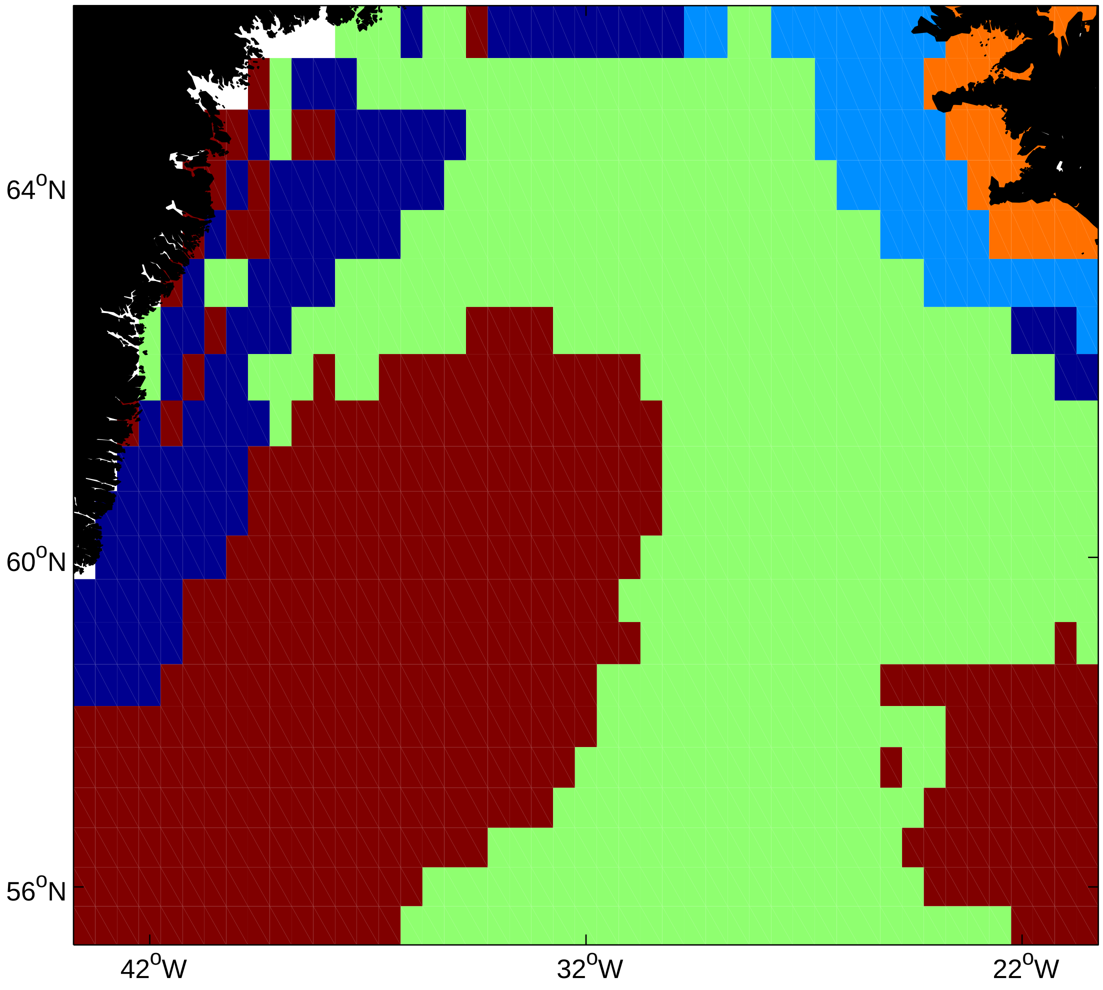

Figure 5.6: Clusters resulting from a k-means analysis of seasonal means of chl-a data (k = 5, p = 5). Colours are arbitrary. Areas with the same colours represent regions within which the chl-a magnitude varies seasonally in a similar manner.

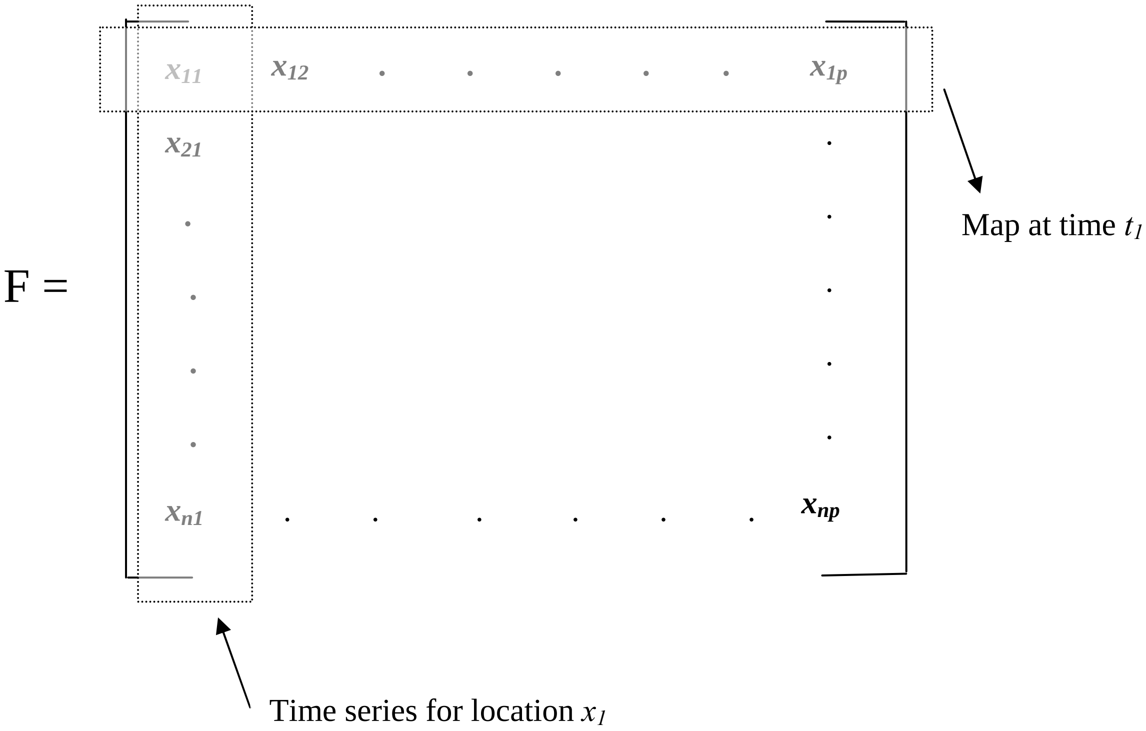

Figure 5.7: The matrix **F**, where each row is one map at locations x_1 to x_p at a given time and each column is a time series of observations x_1 to x_n.

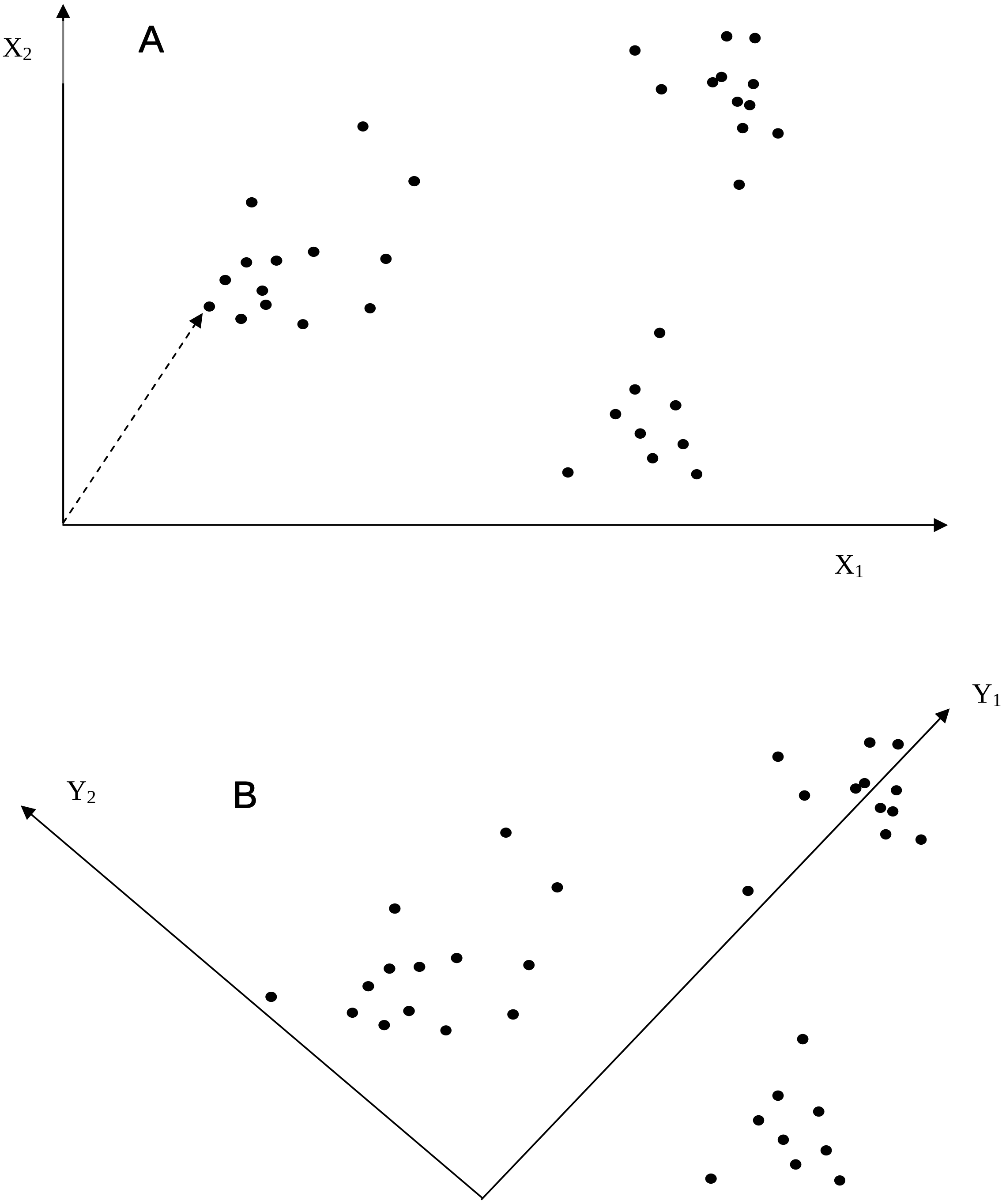

Figure 5.8: Illustrations showing A) objects in *p*-dimensional space (p = 2) whose coordinates are the variables x_1, x_2. The position vector for one object is shown as a dashed arrow. B) Axes have been rotated to pass through the centre of a cluster of data. In this example the axes are constrained to be orthogonal.

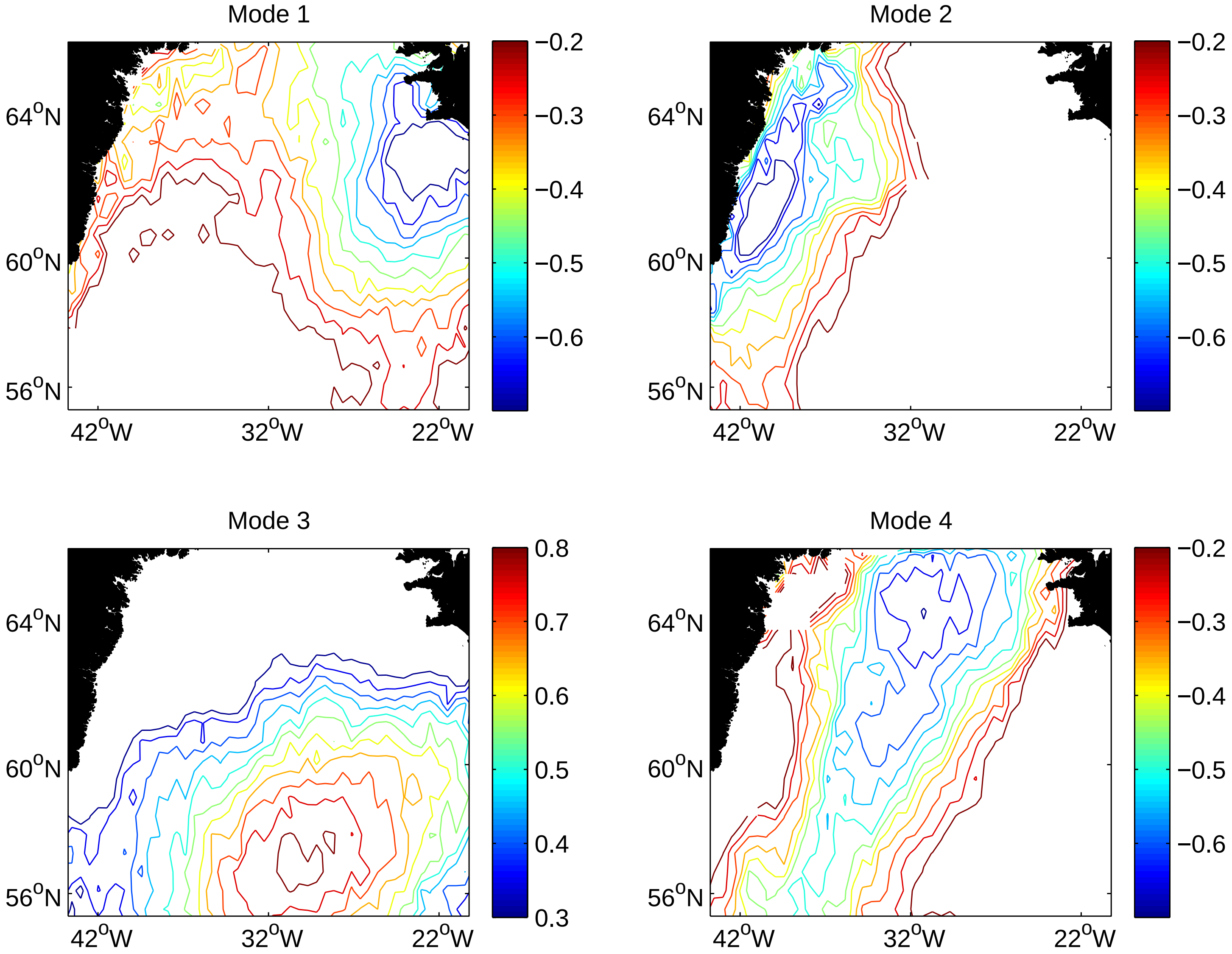

Figure 5.9: Homogenous correlation maps of the first four EOF modes of SeaWiFS chl-a daily data after varimax rotation. Only regions for which the data is statistically significant ($p < 0.01$) are plotted. Note that the colour scale is different for Mode 3.

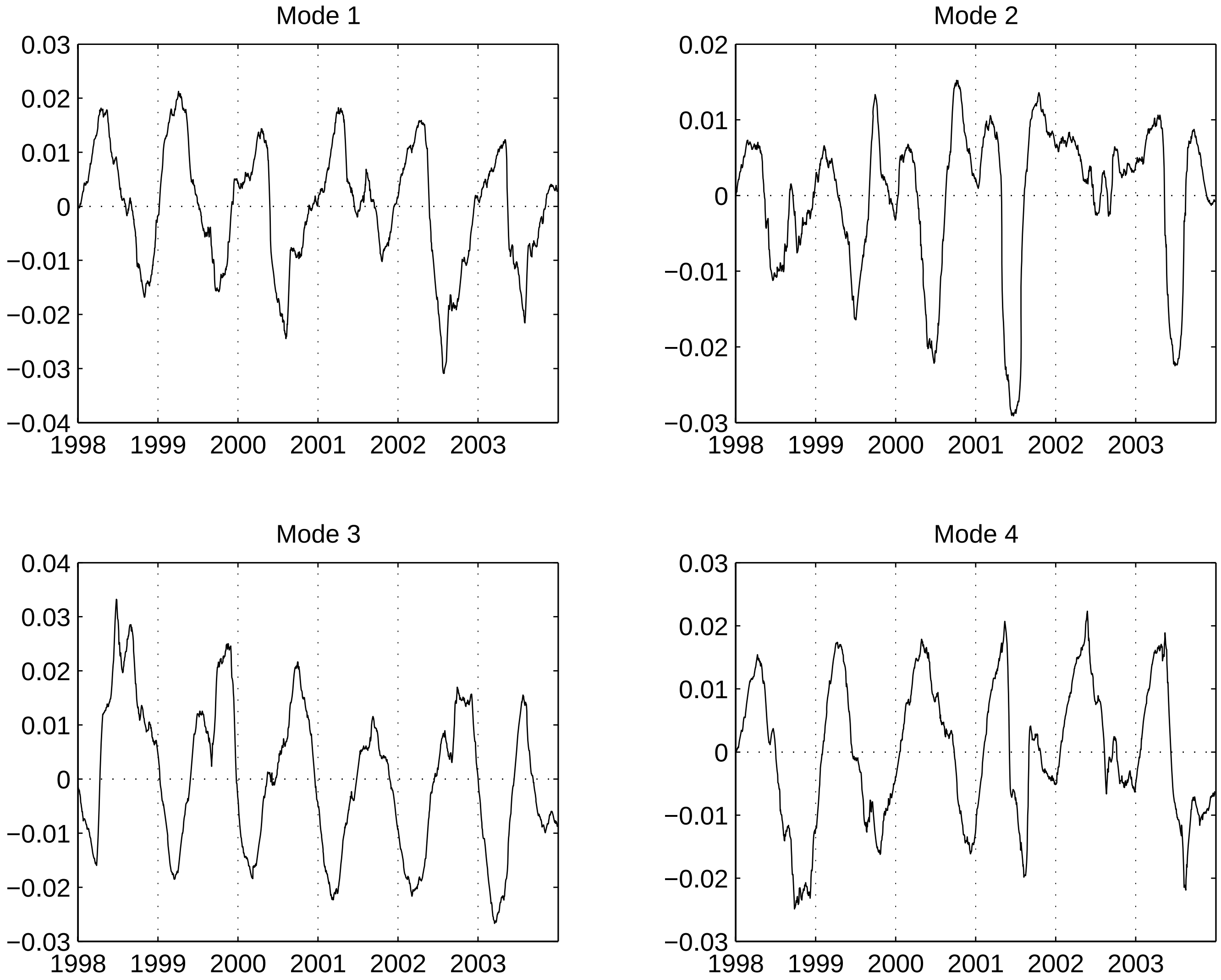

Figure 5.10: Time series of the first four EOF modes for SeaWiFS chl-a daily data after varimax rotation. Note that the data run from February to October, not over one entire year. A two month running mean has been applied.

6. INTERANNUAL VARIABILITY IN THE SPRING BLOOM:

In the northern North Atlantic much of the annual export production occurs during the spring bloom. Export production is the flux of biogenic material from surface waters to the ocean interior and to higher trophic levels – the biological pump. Defining the extent of interannual variability in the spring bloom may elucidate the variability in the biological pump, but quantifying interannual variability first requires knowledge of what is ‘normal’. To do this a long time series of measurements is ideally required. However this is rarely available in oceanography, particularly for biological measurements. In this study, six years (1998 – 2003) of SeaWiFS chlorophyll-a concentration (chl-a) data are used, along with the corresponding meteorological data. Although this is not a particularly long time series it is at high spatial and temporal resolution and so will allow some estimation of the interannual variability in the spring bloom.

This chapter presents the results of analysis of the six year chl-a record to identify the characteristics of the interannual variability in the spring bloom. This chapter is intended to ‘set the scene’ for the following chapter, which will discuss the effect of variability in the meteorological forcing on the bloom, with reference to the results shown here.

6.1. QUANTIFYING INTERANNUAL VARIABILITY:

In Chapter 5 the reasoning behind focusing on three representative zones of the Irminger Basin (IB) was discussed. In this section each zone will be represented by a 1° x 1° box over which the data have been averaged. These boxes were chosen to be close to the centres of the zones as defined in both the cluster and EOF analyses presented in Chapter 5. In Figure 6.1 the East Greenland (EG; centred on 62 °N 40 °W), Central Irminger Sea (CIS, after Holliday et al., 2005, centred on 60 °N 36 °W) and Reykjanes Ridge (RR; centred on 58.5 °N 32.5 °W) regions are shown. The data were averaged from the daily images into 3-day means. Only 3-day periods for which there are at least two data points are included (for more details on data processing see Section 3.2.1). Data are available from March to October. Outside of this period data are of very poor quality due to cloud cover, or completely absent due to low incident sun angle.

The mean (1998 – 2003) annual cycle of chl-a at 3-day resolution for each region is shown in Figure 6.2. In all regions winter chl-a is ~0.2 mg m^{-3} until mid-April. Throughout April chl-a increases slowly and is of similar magnitude in all regions. In the East Greenland (EG) region in mid-May chl-a increases suddenly to a maximum of ~1.8 mg m^{-3} but by mid-June levels have returned to ~0.5 mg m^{-3}. From mid-July to early September chl-a remains at between ~0.5 and ~0.7 mg m^{-3}. In the Reykjanes Ridge (RR) and Central Irminger Sea (CIS) zones the chl-a signals are fairly similar until mid-May. From winter values, chl-a increases throughout April with a sharper increase at the end of May. The RR has a somewhat lower chl-a maximum than CIS, but both are ~1 mg m^{-3}. It is in summer and autumn that the major differences between the RR and CIS occur. In the RR chl-a remains at ~0.7 mg m^{-3}, almost as high as during the spring peak. In the CIS chl-a only achieves a maximum of ~0.5 mg m^{-3} during summer. From early September all three zones again have similar signatures, with chl-a dropping rapidly back to winter levels. Certain times of the year are more likely to exhibit interannual variability, as shown in Figure 6.3 which displays the standard deviations about the 6-year mean for each zone. In winter and late autumn there is little interannual variability whilst in spring the standard deviation is large, particularly for the EG region. In summer and early autumn in the CIS and EG regions the variability is reduced, but in the RR the standard deviation is almost the same as in spring.

To illustrate the interannual variability in the spring bloom Figures 6.4 to 6.6 show the chl-a during each year for the CIS, RR and EG regions respectively. In the CIS (Figure 6.4) values of chl-a are low throughout March (~0.2 mg m^{-3}) in all years. The bloom starts between mid-April and mid-May and there is considerable variability in the timing of the peak of the bloom which occurs in late May to early June. The magnitude of the peak of the bloom varies from ~0.8 to 1.8 mg m^{-3}. During summer and autumn there is considerable interannual variability in the chl-a, with some years experiencing chl-a at almost as high a concentration as during the peak of the bloom. In all years chl-a levels begin to decrease again towards winter levels during September.

The Reykjanes Ridge zone also has winter chl-a levels in all years of ~0.2 mg m^{-3} (Figure 6.5). The timing of the start of the bloom is highly variable, occurring between mid-April and mid-May. The maximum chl-a reached in each year is similar, but the timing of the peak is highly variable. During autumn there is a great deal of variability in the level of activity from one year to the next with some years experiencing chl-a concentrations at least as high as during the spring peak. Again during September chl-a begins to drop towards winter levels in all years.

In the East Greenland area winter chl-a levels are ~0.2 mgm^{-3} (Figure 6.6; note that a different scale is used for the EG zone). The start of the bloom begins around mid-May with less variability in the timing than in the other zones. The bloom dies back in all years in mid-June and, as in the other zones, there is a high degree of variability in autumn chl-a levels.

6.1.1. ANALYSIS OF VARIANCE:

For a more quantitative view of the interannual variability a one-way ANOVA (Analysis of Variance) was carried out. The purpose of one-way ANOVA is to find out whether data from several groups have a common mean i.e. to determine whether the groups are actually different in the measured characteristic. The null hypothesis to be tested is that all samples in a dataset are drawn from the same population (or from different populations with the same mean). ANOVA assumes that the data are normally distributed. To ensure that the chl-a data were close to a normal distribution the data were treated with a Box-Cox transformation. This is a procedure for estimating the best transformation to normality within a family of power transformations:

$$Y' = \frac{(Y^{\lambda} - 1)}{\lambda} \qquad \text{[Eqn 6.1]}$$

where Y is the original data, Y' is the transformed data and λ is a value which maximises the log-likelihood function (this function and further information on the Box-Cox transformation can be found in Sokal and Rohlf, 1995). As the function has to be solved iteratively a specific computer program is required. There is not a standard function to perform a Box-Cox transformation available in Matlab, but it is included in a statistical toolbox published online by Richard Strauss (Texas Tech University; http://www.biol.ttu.edu/Strauss/Matlab /Matlab.htm).

For the SeaWiFS daily chl-a data presented here the Box-Cox transformation returns $\lambda = 0.0065$. A λ of 0 is equivalent to a log transformation, so the chl-a data is close to a lognormal distribution, as is expected for chl-a (Campbell, 1995). A Lilliefors test (for goodness of fit to a normal distribution) confirmed that the transformed data were approximately normally distributed.

An ANOVA analysis separates the variability in a data set into two parts: the first describes the variability between groups (i.e. differences between column means), and the second is the variability within groups (i.e. the difference between the data in each column and the column mean, or 'error' in the data). The standard Matlab function *anova1* was used to perform the analysis on the transformed chl-a data. The function returns the F-statistic, the ratio between the variability within groups (i.e. years in this study) to the variability between groups, and a p-value derived from the cumulative distribution function of F. As F increases, the p-value decreases. If the p-value is near zero, this suggests that the null hypothesis may be in doubt and that at least one sample mean is significantly different from the other sample means. A statistically significant p-value is defined here as < 0.01.

Whilst a small p-value is indicative of a statistical difference in the mean chl-a for each year, the ANOVA itself contains no information on which years are different from each other. To distinguish the years which have different means to other years, the 99% confidence interval of each year's mean is calculated. If the intervals of two years do not overlap they are considered to be significantly different, and vice versa. In Table 6.1 the years are divided into five seasons (as defined in Section 5.1) and the ANOVA analysis performed separately for each time period for the CIS region.

In the CIS region 1998 seems to be the 'most different' year as it occurs in every season, except winter. Summer is the most variable season, whilst winter and early spring are the least variable. The analysis is repeated for the RR and EG regions and is reported in Tables 6.2 and 6.3 respectively. In the RR region, 1998 is again the most different year and most variability occurs in the summer season. In the EG zone no year stands out as being very different from the others and again summer is the most variable season. For all three regions interannual variability in the chl-a is occurring throughout the year.

6.1.2. CHLOROPHYLL-A ANOMALY MAPS:

Although the ANOVA analysis is useful for demonstrating that interannual variability is occurring it does not tell us what form the variability takes. It can also only be performed on time series at specific places. To assess the larger-scale variability, maps of the seasonal anomalies were generated. The mean chl-a for each season was presented in Figure 5.5. Anomaly maps for early spring, late spring and summer for each year are presented in Figures 6.7 to 6.9 respectively. In winter and autumn there is very little variability in the chl-a values across the basin, so these images are not presented.

The main features of the early spring anomaly maps (Figure 6.7) are a strong positive anomaly (i.e. more chl-a than average) across the Reykjanes Ridge area in 1998 and a region of high variability along the East Greenland coast. In 2002 the EG region stands out as having particularly low chl-a levels, whilst in 2000 and 2001 the same region displays anomalously high chl-a values. In the late spring anomaly maps (Figure 6.8) 1998 has high chl-a levels across the southern part of the basin, whilst in 2000 low chl-a values are seen in the southeastern corner of the study region. In 2001 anomalously low chl-a is found over the eastern part of the Reykjanes Ridge and this same region experiences high chl-a levels in 2002. In 2003 the whole of the central region of the basin shows anomalously high chl-a values. In summer (Figure 6.9) 1998 and 1999 have higher than average chl-a throughout the basin, whilst in 2001 and 2003 chl-a is generally lower across the region.

The chl-a anomalies in Figures 6.7 to 6.9 are also seen in the results of the Empirical Orthogonal Function analysis described in Chapter 5.3.3. The time series of the modes (Figure 5.10) displays considerable variability from year to year. For Mode 2, which captures the variability of the East Greenland zone, negative values in the time series correspond to a strong signal in the EOF pattern (Figure 5.9 and 5.10) i.e. around April/May a strong chl-a signal is expected off the east coast of Greenland. The signal is relatively weak in 1998, increasing to a maximum in 2001, but is entirely absent in 2002, returning in 2003. This corresponds to the area of strong variability along the Greenland coast in the early spring anomaly plot (Figure 6.7). In Mode 3, centred on the Reykjanes Ridge, positive values in the time series correspond to a strong signal in the EOF pattern (Figure 5.9 and 5.10). The peak signal occurs in July/August and is greatest in 1998, decreasing to a minimum in 2001 and increasing again slightly in 2002 and 2003. For Mode 4, which represents the Central Irminger Sea, negative values in the time series correspond to a strong signal in the EOF pattern (Figure 5.9 and 5.10). The peak signal occurs in August, is strongest in 1998, but almost completely absent in 2002, with the remaining years displaying similar strength signals. The EOF analysis has the advantage over the anomaly plots of being continuous in time, rather than based on seasonal means, within which the finer details can be lost. The EOF time series and maps demonstrate that interannual variability in the dominant chl-a patterns is occurring. The most striking example, that of the East Greenland region in Mode 2, will be discussed in more detail in Chapter 7.4.

Interannual variability in chl-a concentration is clearly occurring, but what about the attributes of the spring bloom itself, such as start date, duration or magnitude? In the next sections the spatial and interannual variability in these characteristics is examined.

6.2. START OF THE SPRING BLOOM:

The timing of the initiation of the spring bloom is expected to be affected by meteorological conditions – both those of the preceding winter and during early spring. In the North Atlantic, where winter conditions lead to extensive mixing, re-stratification of the water column in spring is expected to be key to prompting phytoplankton growth. Interannual variability in meteorological forcing may be reflected in differences in the timing of the spring bloom. We might also expect to see a northward progression of the date of bloom initiation (for reasons explained in Section 2.1).

A bloom is defined by Longhurst (1998) as a large increase in biomass above normal conditions. Additionally the increase should persist over at least a few days as transient events, such as mesoscale eddies or spring storms, may result in a brief increase in chl-a which quickly drops away again because conditions are not yet right for a full spring bloom to develop. Siegel et al. (2002) define a bloom as the day when chl-a first rises 5 % above the annual median value, with no requirement that the increased chl-a levels persist. Estimation of the start of the bloom was initially made using Siegel et al.'s (2002) method. Visual inspection of chl-a time series at randomly selected pixels in the basin suggested that this method placed the start of the bloom too early. The method detected brief pulses of increased chl-a which occurred prior to the massive increase in biomass indicative of a bloom (these pulses will be discussed again in Chapter 7.2.2). A requirement that the elevated chl-a levels must persist for at least three days was found to correctly detect the start of the main spring bloom. The start of the spring bloom occurred approximately two weeks later using a persistence of three days than in Siegel et al.'s (2002) method with no persistence.

To estimate the start day of the bloom the annual median value for the daily chl-a data was calculated separately for each year and each pixel. Each pixel is then examined to find the day when the chl-a first rises 5 % above the median and remains elevated for at least three consecutive days. Different threshold values, from 1 % to 15 % above the median, were tried but had little effect on the results. The estimation of the start of the bloom by this method was checked by visually inspecting plots of chl-a against time at selected pixels. Maps of the day of the year (DY) at which the bloom is initiated are presented in Figure 6.10. In general the maps show that the bloom starts earliest around the coasts of Iceland and Greenland (~ day 100 ≈ mid April) and then spreads towards the centre of the basin. The bloom starts latest in the north central basin at ~ day 140 (≈ mid May). The maps also give the impression that the start date of the bloom gets later each year from 1998 to 2002, then becomes a little earlier again in 2003. The range in start dates for each pixel (i.e. latest start date – earliest start date) is shown in Figure 6.11. In some areas, such as the northeast of the basin there is little variability in the bloom start date, but in other areas the range can be 35 – 40 days. In fact the mean range of bloom start dates for the whole basin is almost 30 days across just six years of data. Interannual variability in the timing of the initiation of the spring bloom is clearly occurring in the Irminger Basin but are these differences reflected in the intensity or length of the bloom?

6.3. MAGNITUDE AND DURATION OF THE BLOOM:

If a delay in establishing stratification leads to a delay in the start of the spring bloom is it possible that the ‘window’ when light and grazing are at optimum levels for phytoplankton growth is missed and therefore that the bloom might be reduced in magnitude or duration? One way of assessing the magnitude of the bloom is by studying the maximum chl-a reached. Figure 6.12 shows maps of the maximum chlorophyll-a concentration for each pixel, calculated from the SeaWiFS daily data. Maximum chl-a ranges from ~1-2 mg m^{-3} in the central basin to > 6 mg m^{-3} around Iceland and along the Greenland coast. Whilst the bloom start date appears to get later from 1998 to 2002, there is no similar trend in the maximum chl-a. In specific areas, such as along the Greenland coast, there are similar levels of maximum chl-a in 2000 and 2003, although the bloom start dates are ~30 days earlier in 2000 than 2003. Thus there is no indication that the interannual variability seen in the start date of the bloom is reflected in the maximum chl-a value.

However, the magnitude of the bloom is not fully described by the maximum chl-a reached. A better measure might be the summed chl-a during the bloom period. To define the bloom period a definition of the end of the bloom is first required. Here this is defined as the slump in chl-a that occurs after the peak of the bloom, but prior to any autumn activity. This is illustrated in Figure 6.13, a schematic of a typical annual chl-a signature in the study region. Quantitatively the end of the bloom is best defined as the first day after the start of the bloom that chl-a sinks to below one-third of the maximum chl-a and remains there for at least two days. The summed chl-a is then the sum of all chlorophyll values between the start and the end of the bloom minus the average pre-bloom chl-a (the shaded area in Figure 6.13). This calculation does not account for the life-span of a single phytoplankter, which is of the order of a couple of days (Lalli and Parsons, 1997). Maps of the summed chl-a over the bloom period for each year are presented in Figure 6.14. Generally the summed chl-a is between ~2 and 5 mg m^{-3}, with patches of ~10 to 15 mg m^{-3}. However, there does not seem to be a connection between timing of the start of the bloom and magnitude of the bloom.

Finally, the duration of the bloom was defined as the number of days between the start of the bloom and the end of the bloom, as estimated above. Figure 6.15 shows the duration of the bloom for each year. The duration ranges from a few days to ~40 days, principally in the coastal regions, but again there is little indication of any link between when the bloom starts and how long it lasts.

The lack of a link between the start date of the spring bloom and its magnitude or duration suggests that the ‘window’ for optimum phytoplankton growth is rather longer than might be expected in a high latitude region. A later bloom start does not appear to have a detrimental effect on the magnitude and duration of the subsequent bloom. It indicates that light levels are not limiting to growth during a long period of the spring and summer. This will be returned to in Chapter 7.3.

6.4. CHAPTER SUMMARY:

Interannual variability in chlorophyll concentration is occurring throughout the Irminger Basin. The start day of the bloom varies by ~30 days over the six years of data for most locations in the basin. The variability in the bloom start date doesn't appear to affect the duration or magnitude of the spring bloom.

- Statistically significant interannual variability in chl-a occurs across the basin.
- Estimates of the start day of the bloom can be made by calculating the day when chl-a rises 5 % above the yearly median and stays elevated for at least three days.
- Estimates of the end of the bloom can be made by calculating the day when the chl-a drops to one-third of the maximum value and remains lower than this for at least two days.
- The magnitude and duration of the bloom are not correlated with the start day of the bloom.
- There is a long window of opportunity for phytoplankton growth during the spring and summer.

Season	**p-value**	**Year**	**is different from Year**
All days	< 0.01	1998	1999, 2001, 2002, 2003
		1999	1998
		2000	1998
		2001	1998
		2002	1998
		2003	1998
Winter 1 Jan to 10 Apr	> 0.01 (not significant)	2002	2003
		2003	2002
Early spring 11 Apr to 30 May	< 0.01	1998	2002
		2002	1998
Late spring 31 May to 19 July	< 0.01	1998	2000, 2001
		2000	1998, 2003
		2001	1998
		2003	2000
Summer 20 July to 7 Sept	< 0.01	1998	2000, 2001, 2002, 2003
		1999	2001, 2003
		2000	1998, 2001, 2003
		2001	1998, 1999, 2000
		2002	1998, 2003
		2003	1998, 1999, 2000, 2002
Autumn 8 Sept to 16 Dec	< 0.01	1998	1999, 2001
		2000	2001
		2001	1998, 2000

Table 6.1: p-values and a listing of which years are different from which other years from an ANOVA analysis of daily SeaWiFS chl-a data for the CIS zone. The table shows the results for each year as a whole, and then separated into seasons.

Season	**p-value**	**Year**	**is different from Year**
All days	< 0.01	1998	1999, 2000, 2001, 2002, 2003
		1999	1998
		2000	1998
		2001	1998
		2002	1998
		2003	1998
Winter 1 Jan to 10 Apr	< 0.01	1998	2003
		1999	2003
		2000	2003
		2002	2003
		2003	1998, 1999, 2000, 2002
Early spring 11 Apr to 30 May	< 0.01	1998	1999, 2000, 2001, 2002, 2003
		1999	1998, 2002
		2000	1998, 2002
		2001	1998
		2002	1998, 1999, 2000
		2003	1998
Late spring 31 May to 19 July	< 0.01	1998	1999, 2000, 2001, 2002
		1999	1998
		2000	1998, 2003
		2001	1998
		2002	1998
		2003	1998, 2000
Summer 20 July to 7 Sept	< 0.01	1998	2001, 2003
		1999	2001, 2002, 2003
		2000	2001, 2003
		2001	1998, 1999, 2000
		2002	1999
		2003	1998, 1999, 2000
Autumn 8 Sept to 16 Dec	< 0.01	1998	2001
		2001	1998, 2002
		2002	2001

Table 6.2: p-values and a listing of which years are different from which other years from an ANOVA analysis of daily SeaWiFS chl-a data for the RR zone. The table shows the results for each year as a whole, and then separated into seasons.

Season	**p-value**	**Year**	**is different from Year**
All days	< 0.01	1998 2001 2003	2001, 2003 1998 1998
Winter 1 Jan to 10 Apr	< 0.01	1999 2002 2003	2003 2003 1999, 2002
Early spring 11 Apr to 30 May	< 0.01	1998 2000 2001 2002 2003	2002 2002, 2003 2002 1998, 2000, 2001 2000
Late spring 31 May to 19 July	< 0.01	1998 1999 2001 2003	1999, 2001, 2003 1998 1998 1998
Summer 20 July to 7 Sept	< 0.01	1998 1999 2000 2001 2002 2003	2000, 2001 2000, 2001 1998, 1999, 2002, 2003 1998, 1999, 2002, 2003 2000, 2001 2000, 2001
Autumn 8 Sept to 16 Dec	< 0.01	1998 1999 2000 2001 2003	2001 2001 2001 1998, 1999, 2000, 2003 2001

Table 6.3: p-values and a listing of which years are different from which other years from an ANOVA analysis of daily SeaWiFS chl-a data for the EG zone. The table shows the results for each year as a whole, and then separated into seasons.

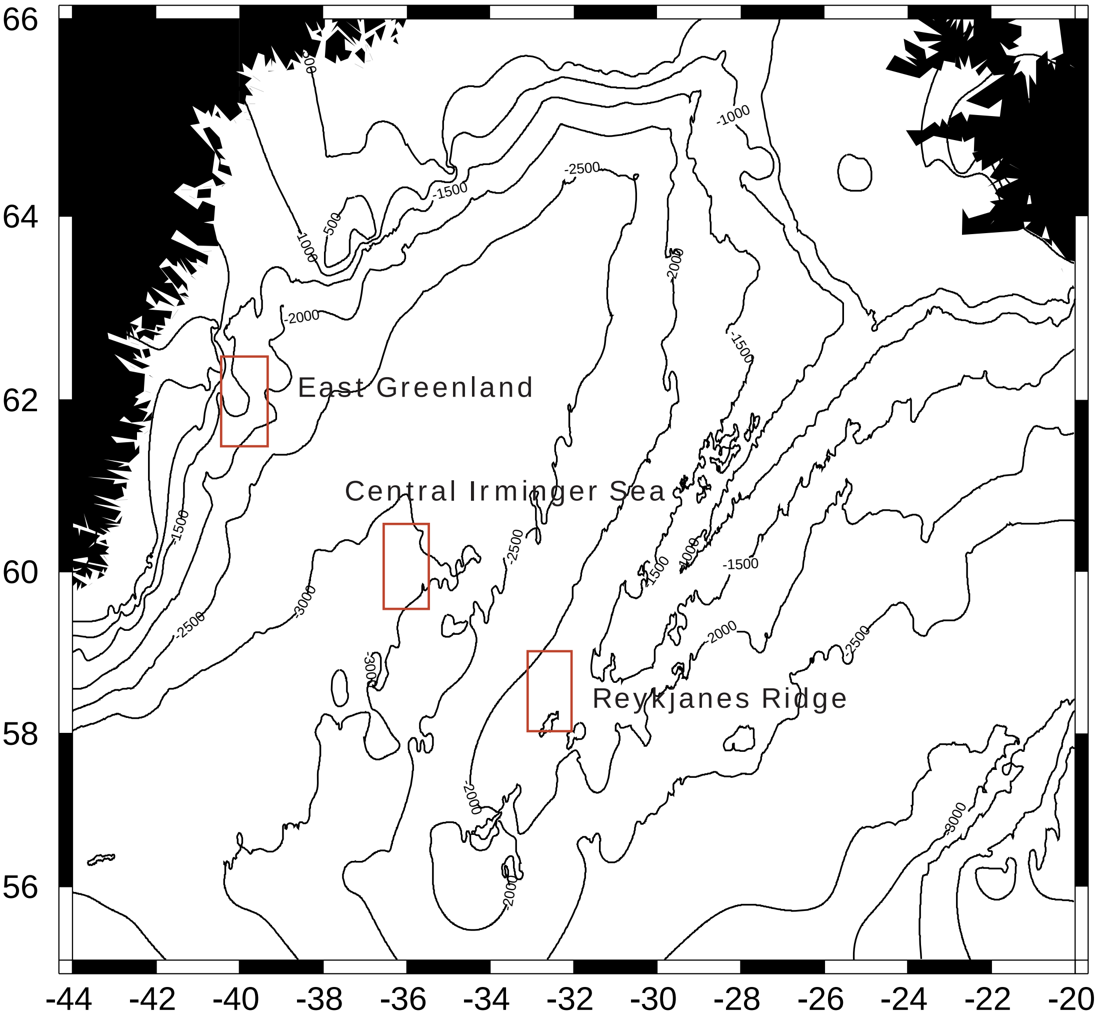

Figure 6.1: Map of the study region and bathymetry with the 1° x 1° boxes used to define the East Greenland, Central Irminger Sea and Reykjanes Ridge regions outlined in red.

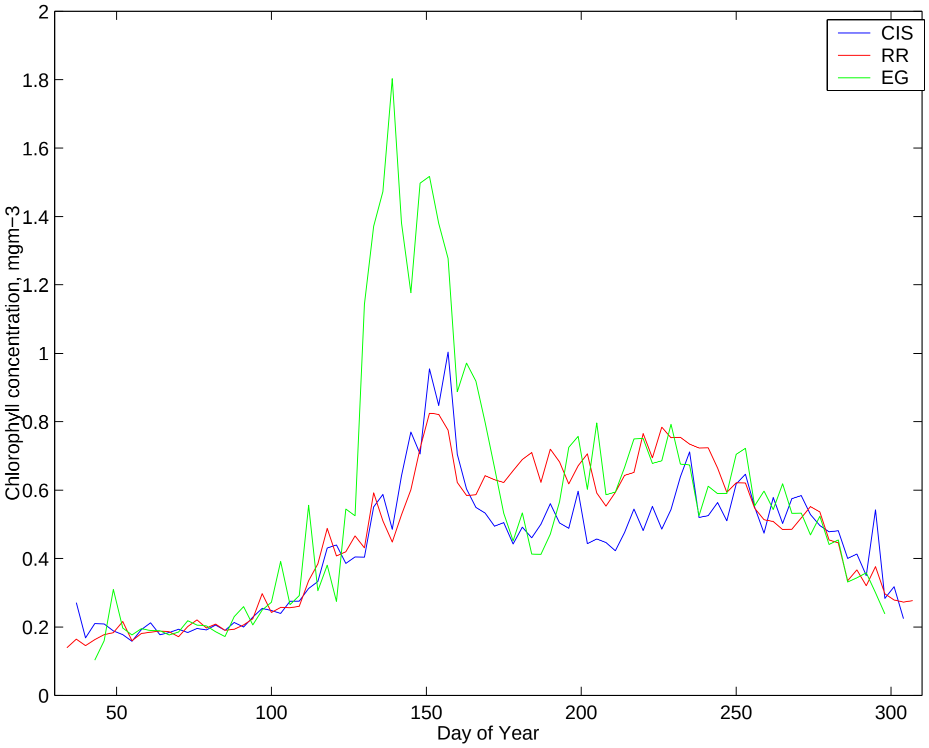

Figure 6.2: Mean annual cycle of SeaWiFS chl-a (3-day average) for the Central Irminger Sea (blue), Reykjanes Ridge (red) and East Greenland (green) regions.

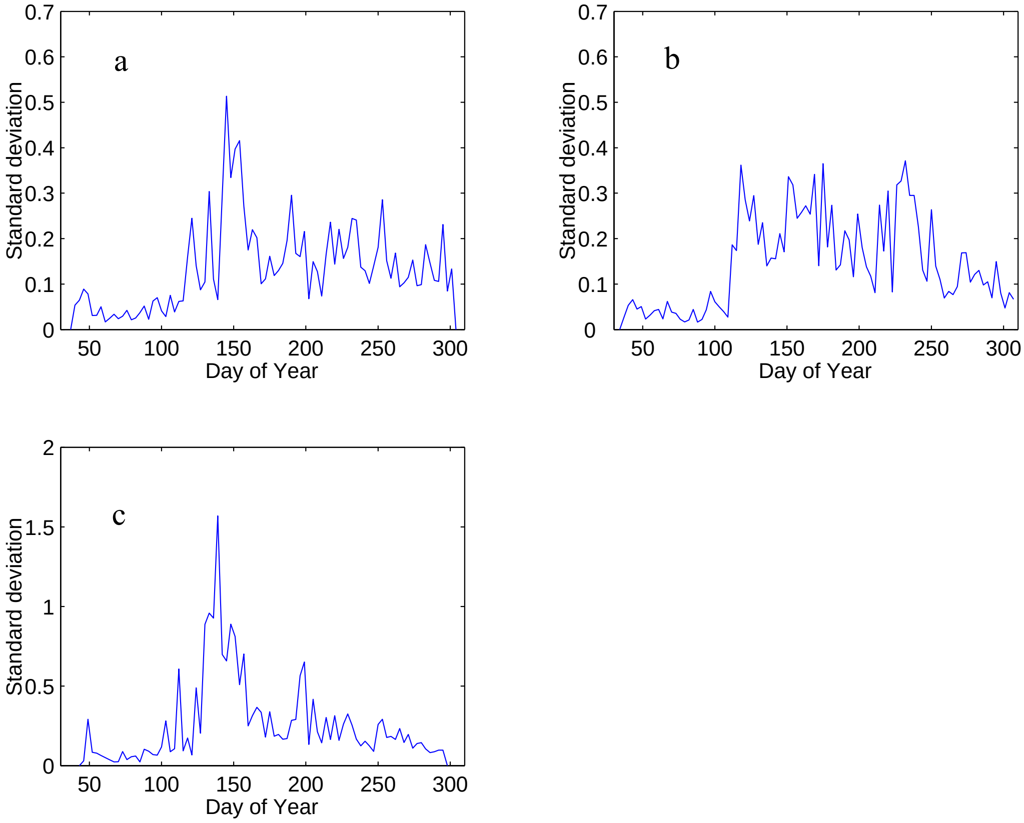

Figure 6.3: Mean annual standard deviation for a) Central Irminger Sea, b) Reykjanes Ridge and c) East Greenland regions. Note that the scale is different in c).

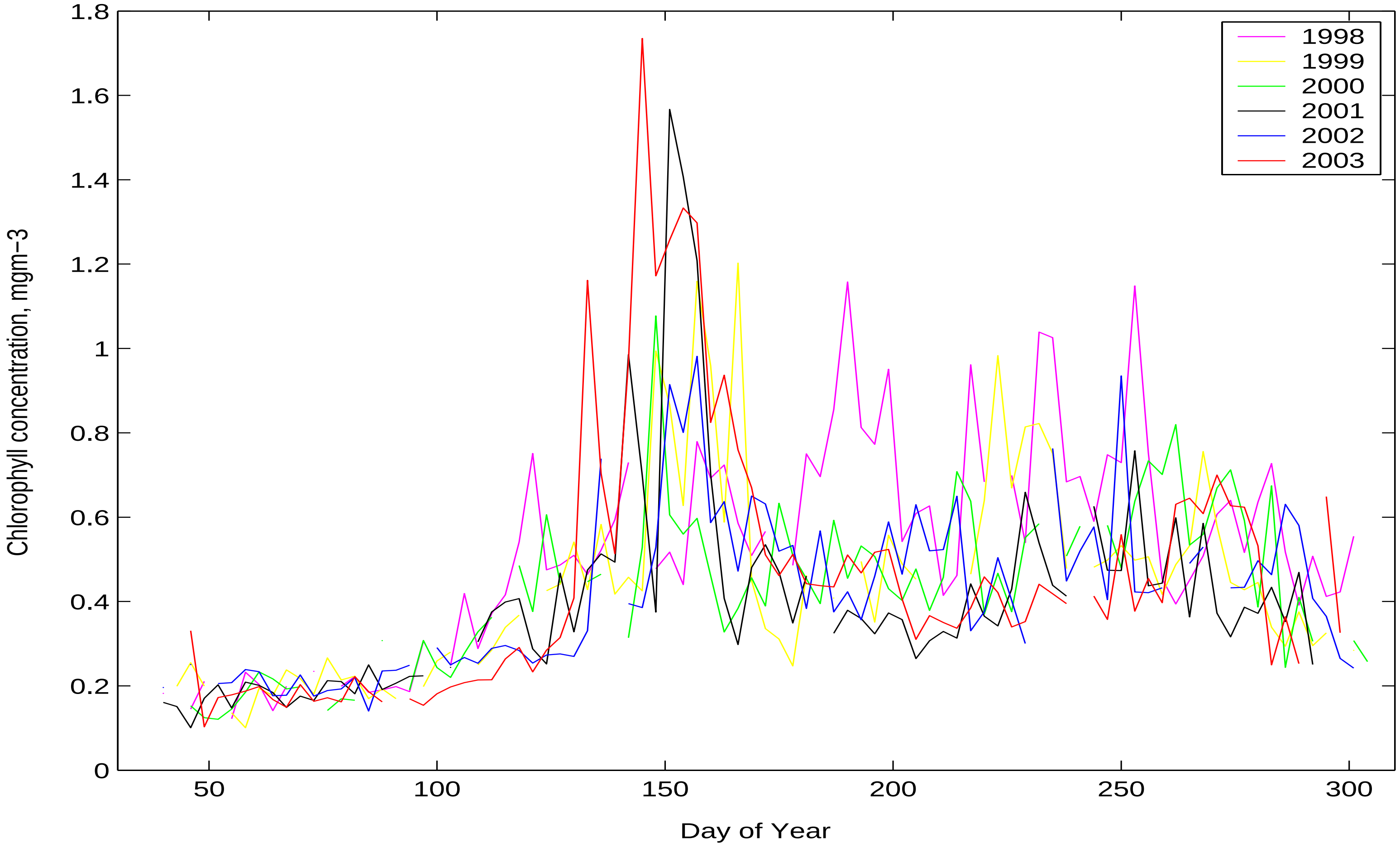

Figure 6.4: 3-day mean SeaWiFS chl-a for the Central Irminger Sea region for 1998 (magenta), 1999 (yellow), 2000 (green), 2001 (black), 2002 (blue) and 2003 (red). Note that the data run from mid-February to the end of October.

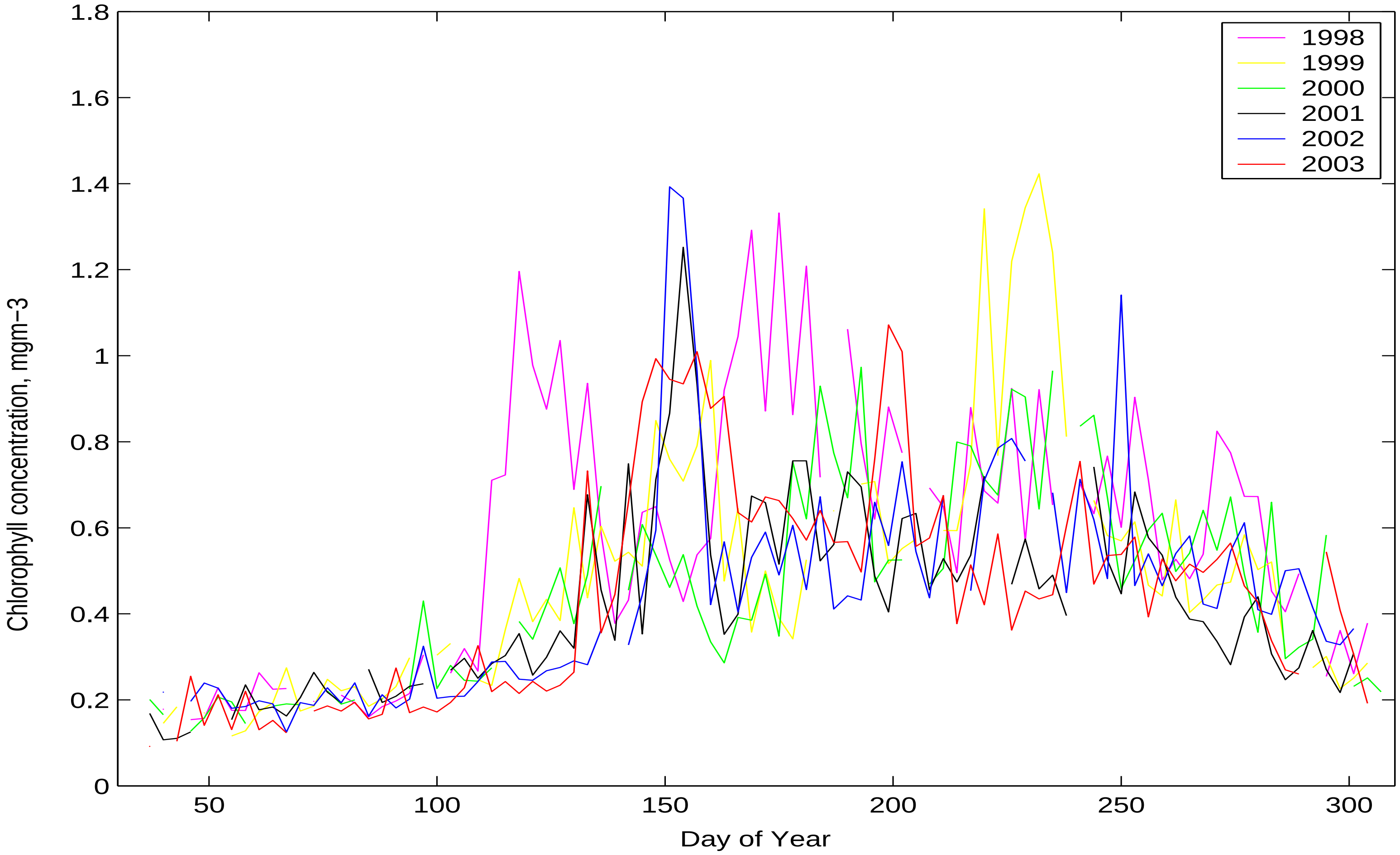

Figure 6.5: 3-day mean SeaWiFS chl-a for the Reykjanes Ridge region for 1998 (magenta), 1999 (yellow), 2000 (green), 2001 (black), 2002 (blue) and 2003 (red). Note that the data run from mid-February to the end of October.

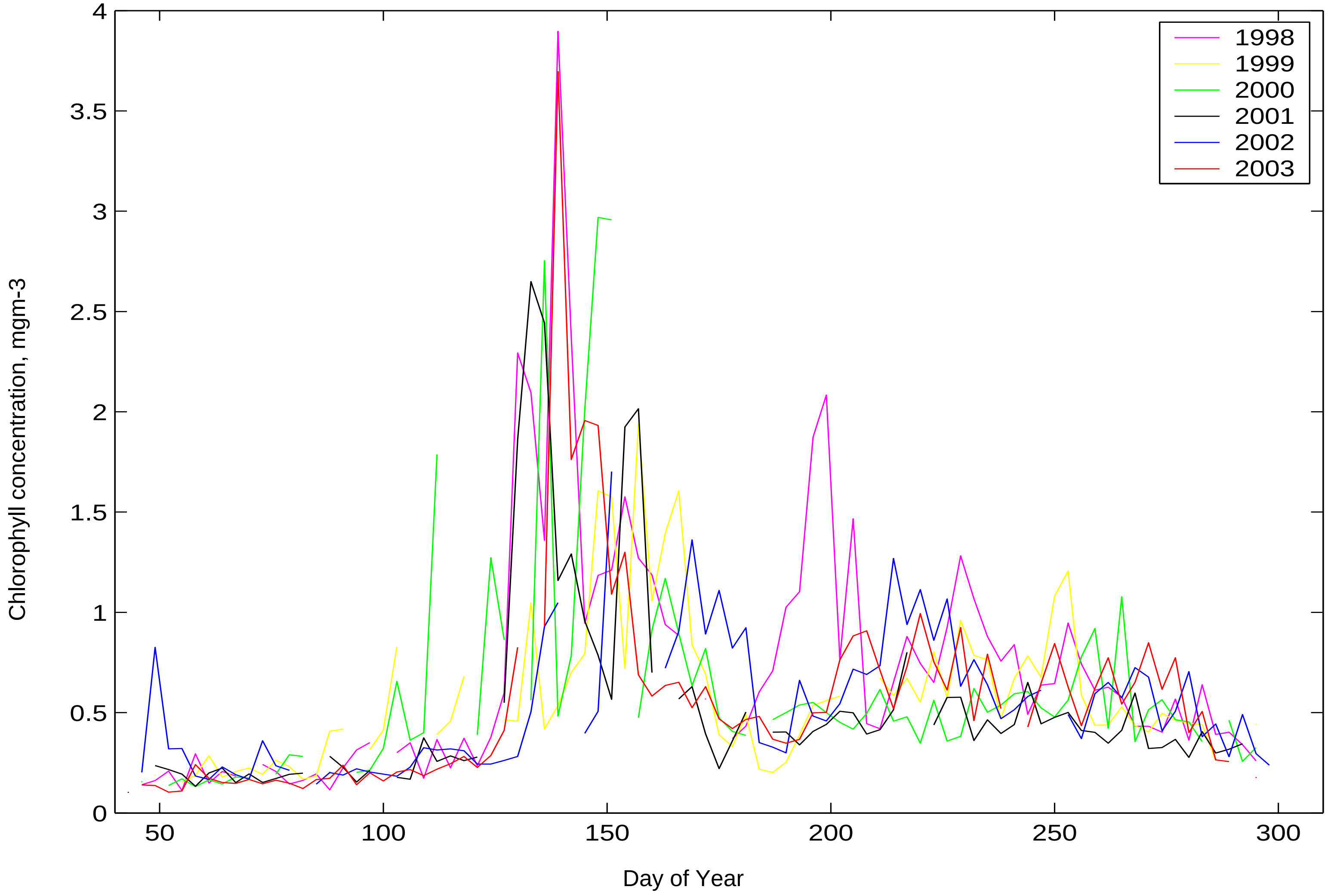

Figure 6.6: 3-day mean SeaWiFS chl-a for the East Greenland region for 1998 (magenta), 1999 (yellow), 2000 (green), 2001 (black), 2002 (blue) and 2003 (red). Note that the data run from mid-February to the end of October.

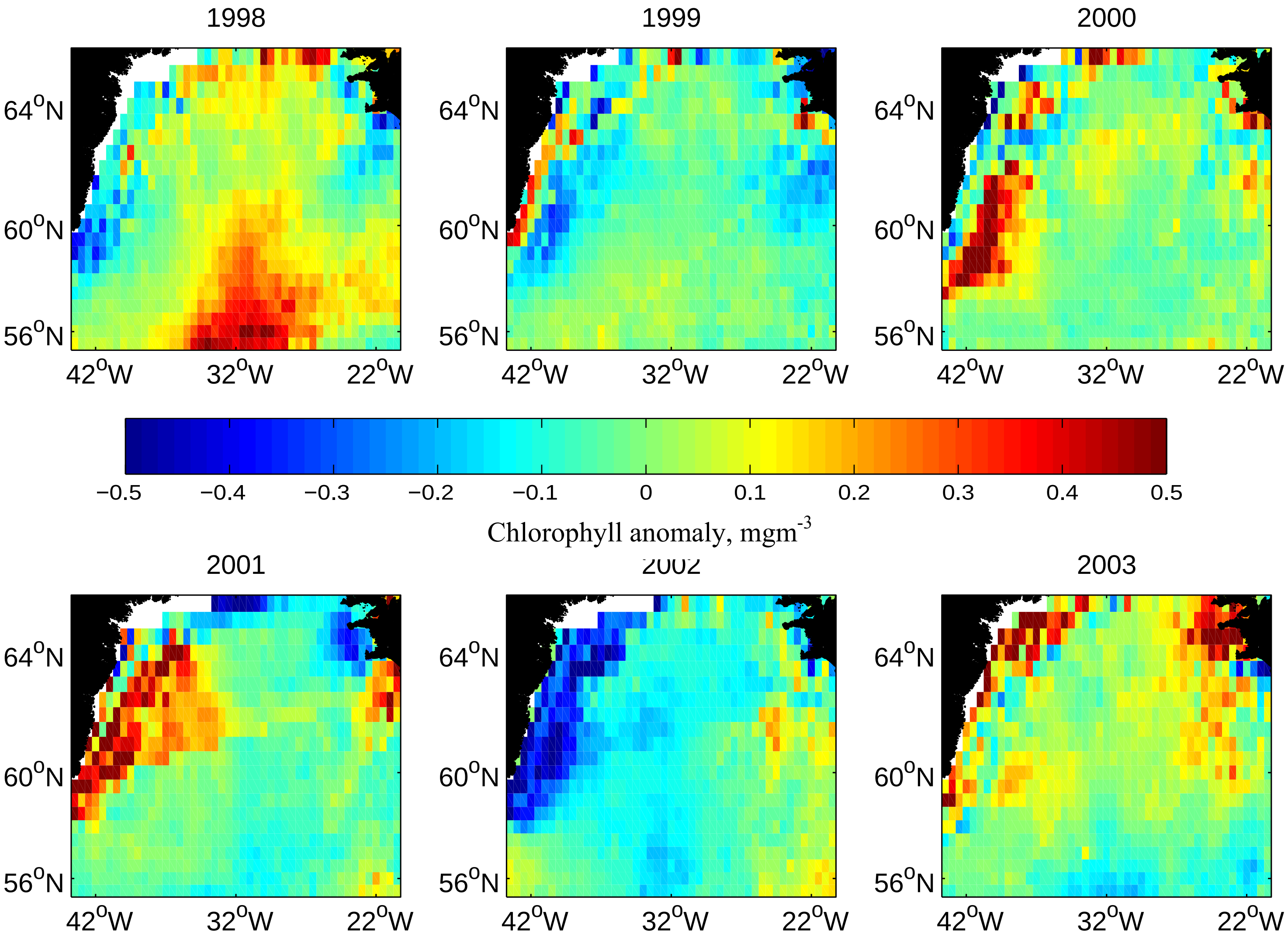

Figure 6.7: Anomalies from the seasonal mean for early spring (11th April to 30th May) for each year. Warm colours indicate a positive anomaly i.e. more chl-a than the mean, and cold colours indicate a negative anomaly. The seasonal mean (calculated from 1998 – 2003) for early spring is in Figure 5.5.

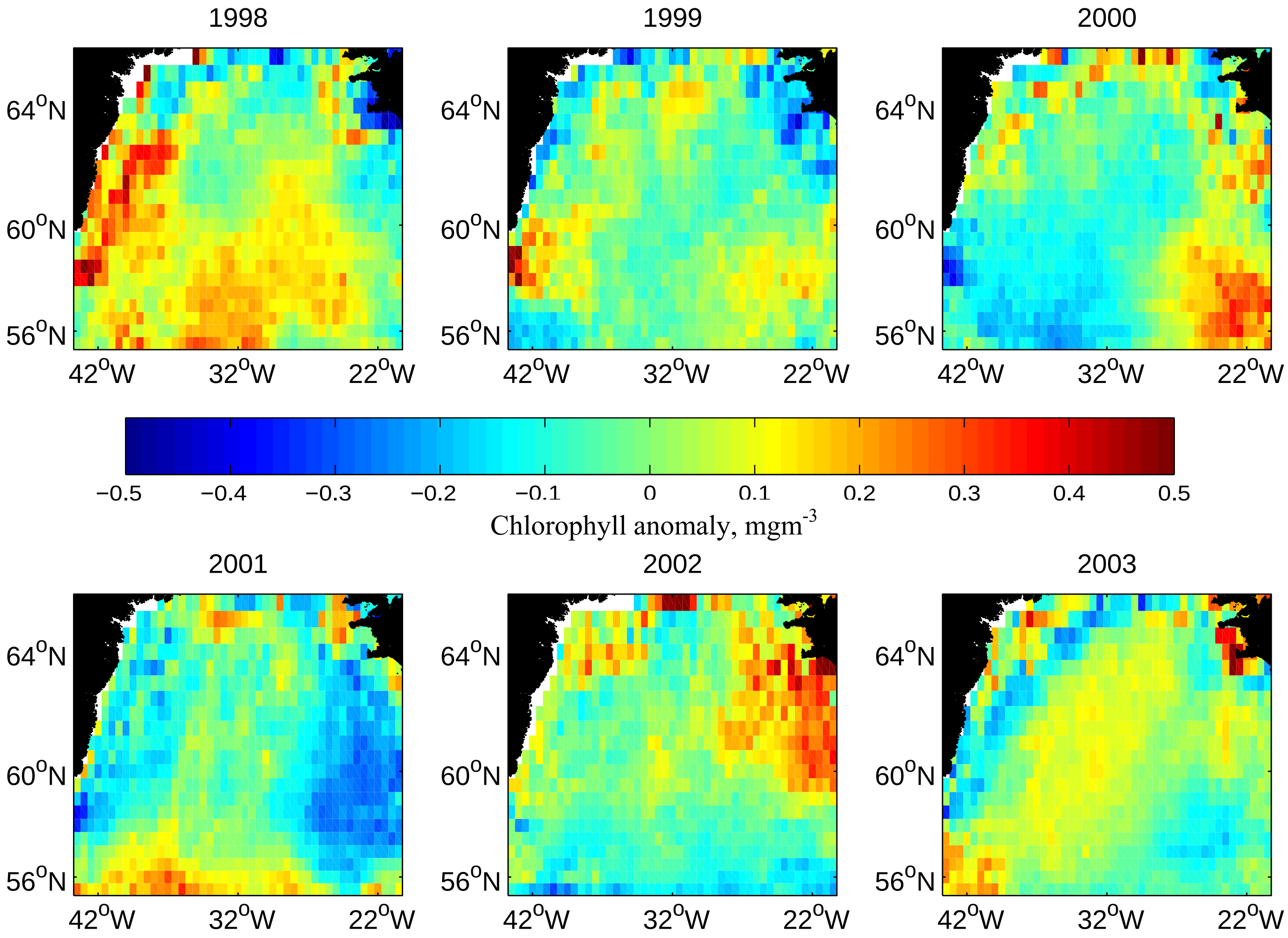

Figure 6.8: Anomalies from the seasonal mean for late spring (31st May to 19th July) for each year. Warm colours indicate a positive anomaly i.e. more chl-a than the mean, and cold colours indicate a negative anomaly. The seasonal mean (calculated from 1998 – 2003) for late spring is in Figure 5.5.

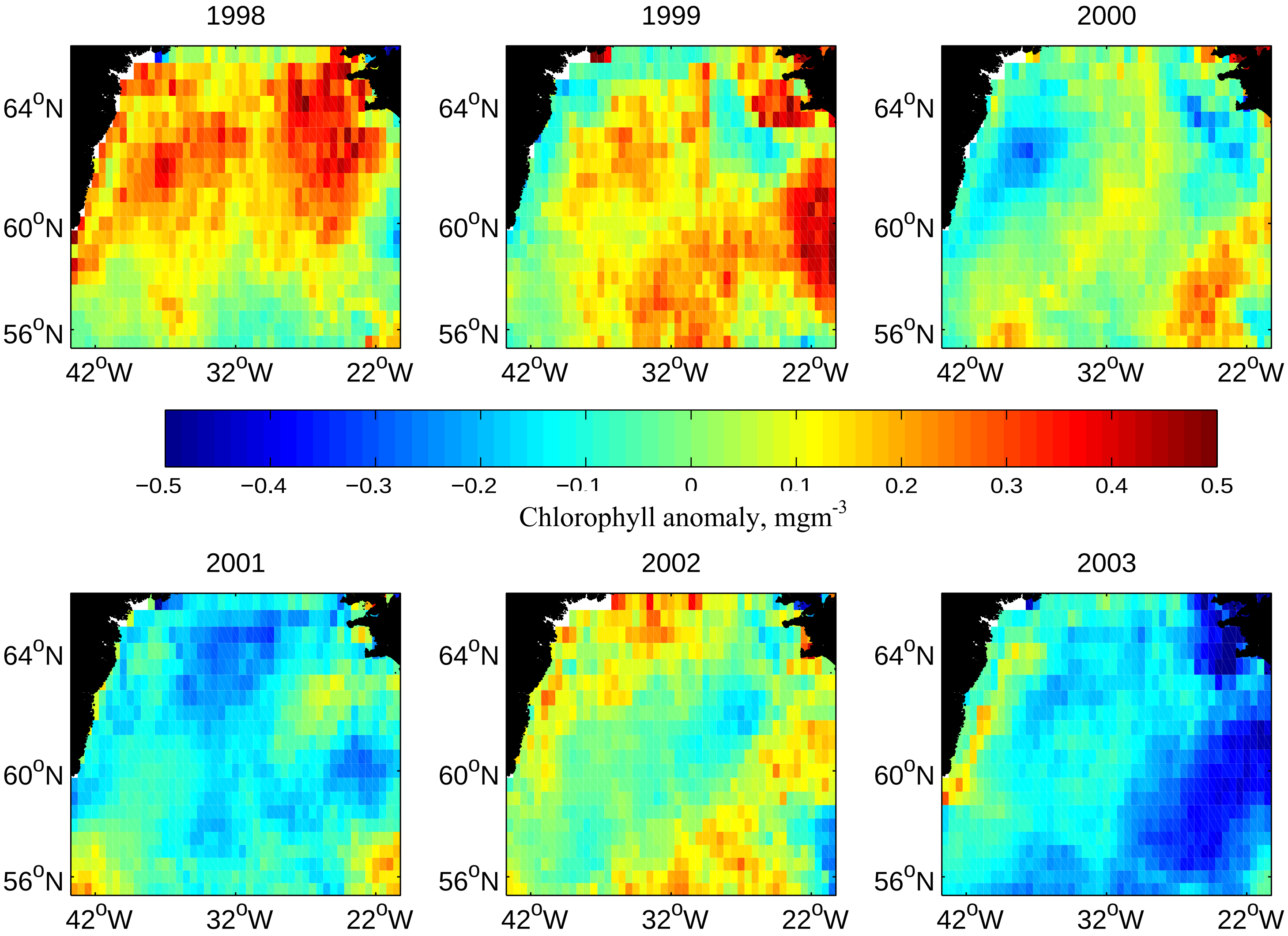

Figure 6.9: Anomalies from the seasonal mean for summer (20th July to 7th September) for each year. Warm colours indicate a positive anomaly i.e. more chl-a than the mean, and cold colours indicate a negative anomaly. The seasonal mean (calculated from 1998 – 2003) for summer is in Figure 5.5.

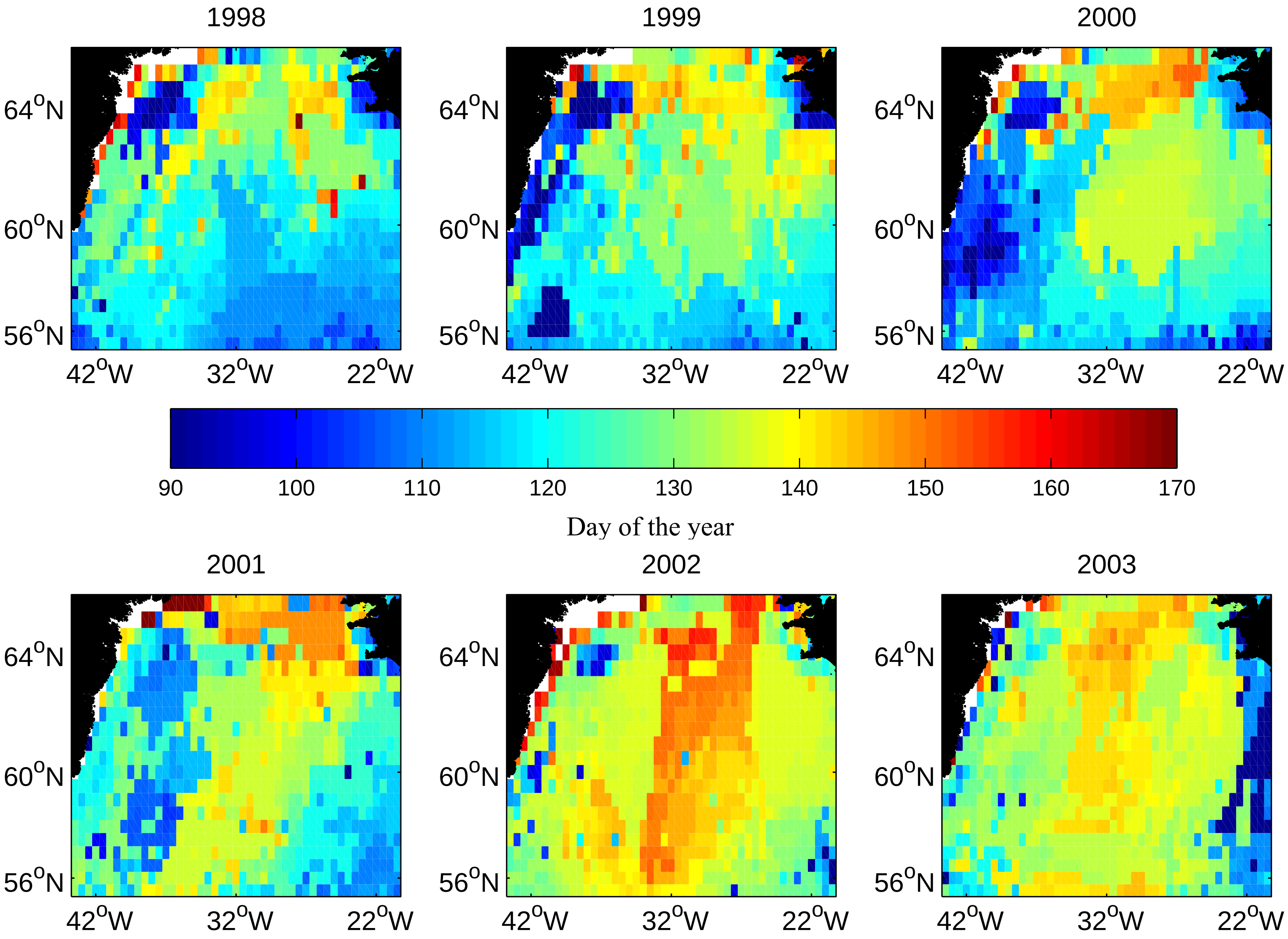

Figure 6.10: The day of the year on which the spring bloom starts in each year. The start of the bloom is defined as the day when chl-a first rises 5 % above the yearly median value and remains elevated for at least three days.

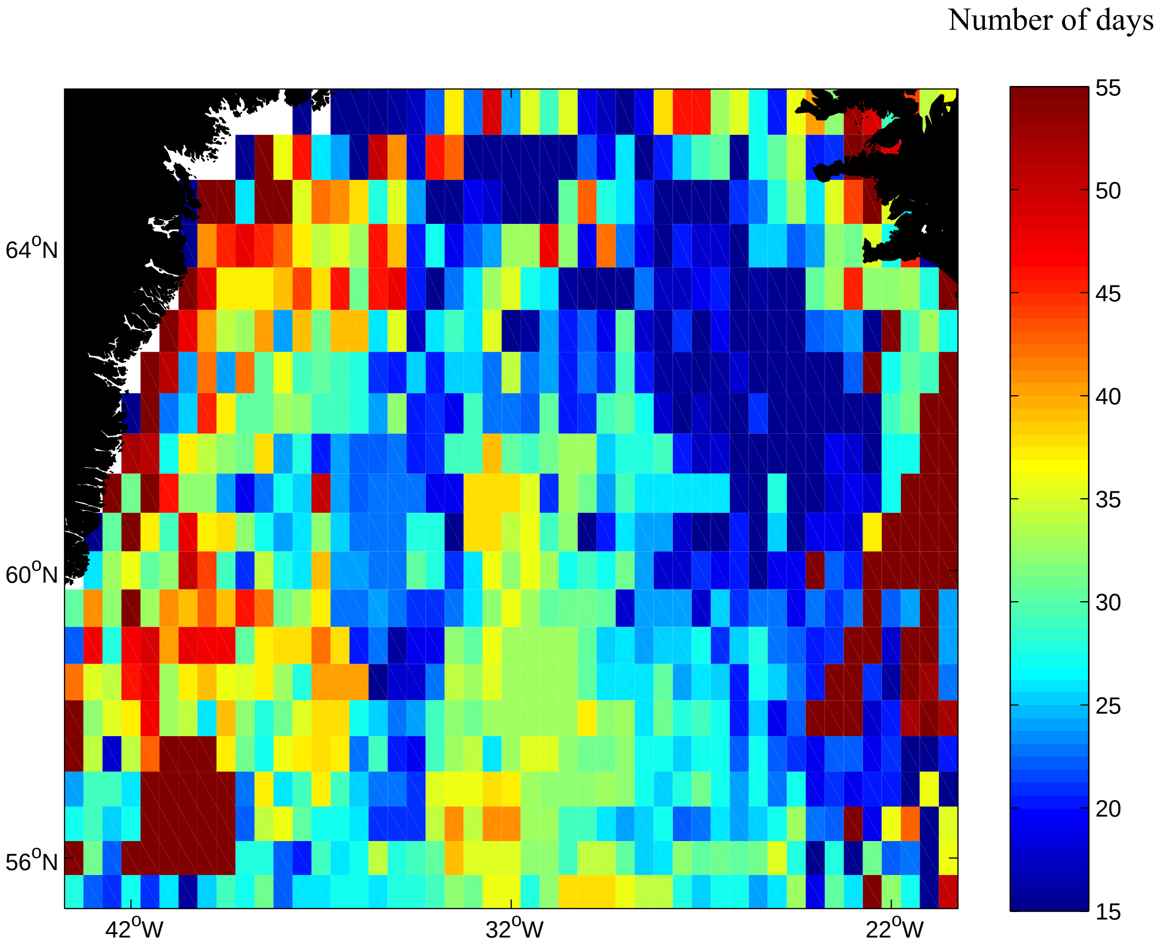

Figure 6.11: Range in start days at each pixel across all six years.

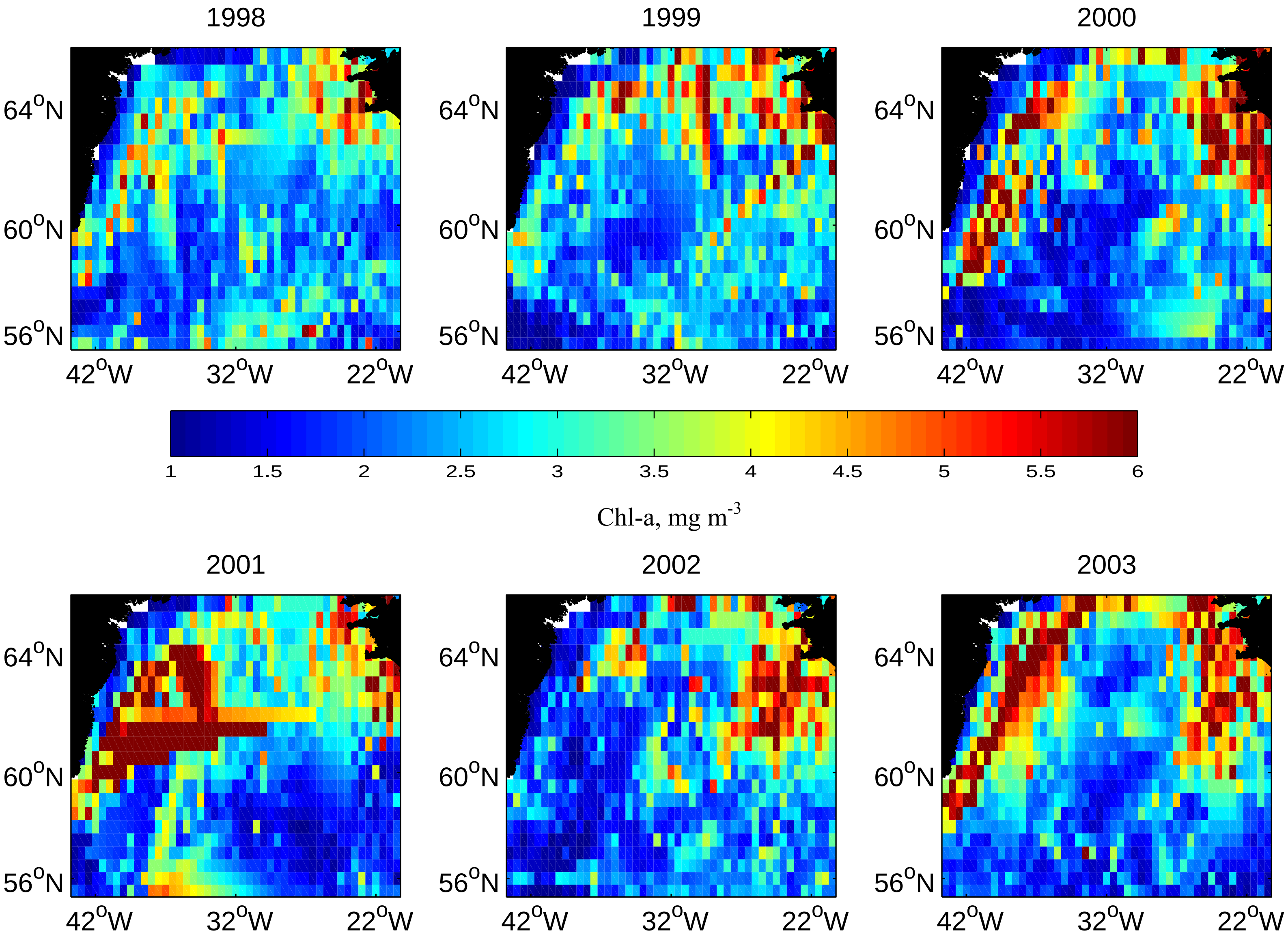

Figure 6.12: Maximum chl-a observed at each pixel for each year.

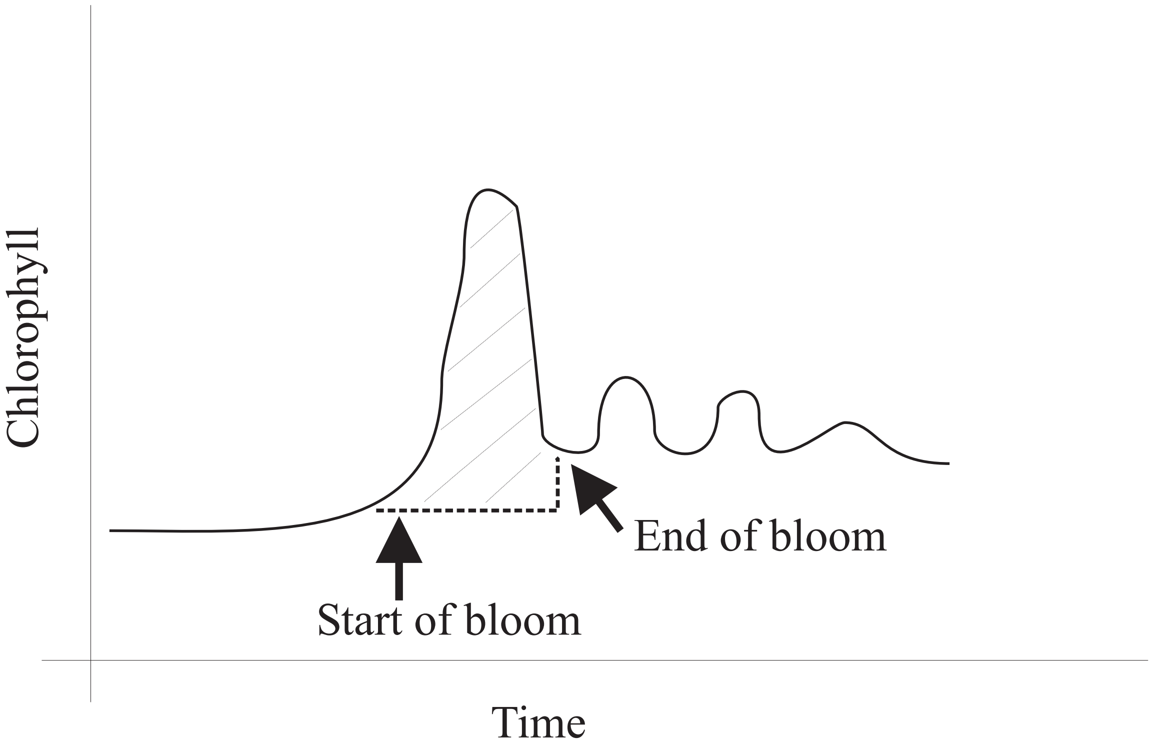

Figure 6.13: Schematic of the chl-a concentration during a typical year. The hashed area represents the summed chlorophyll (see Chapter 6.3).

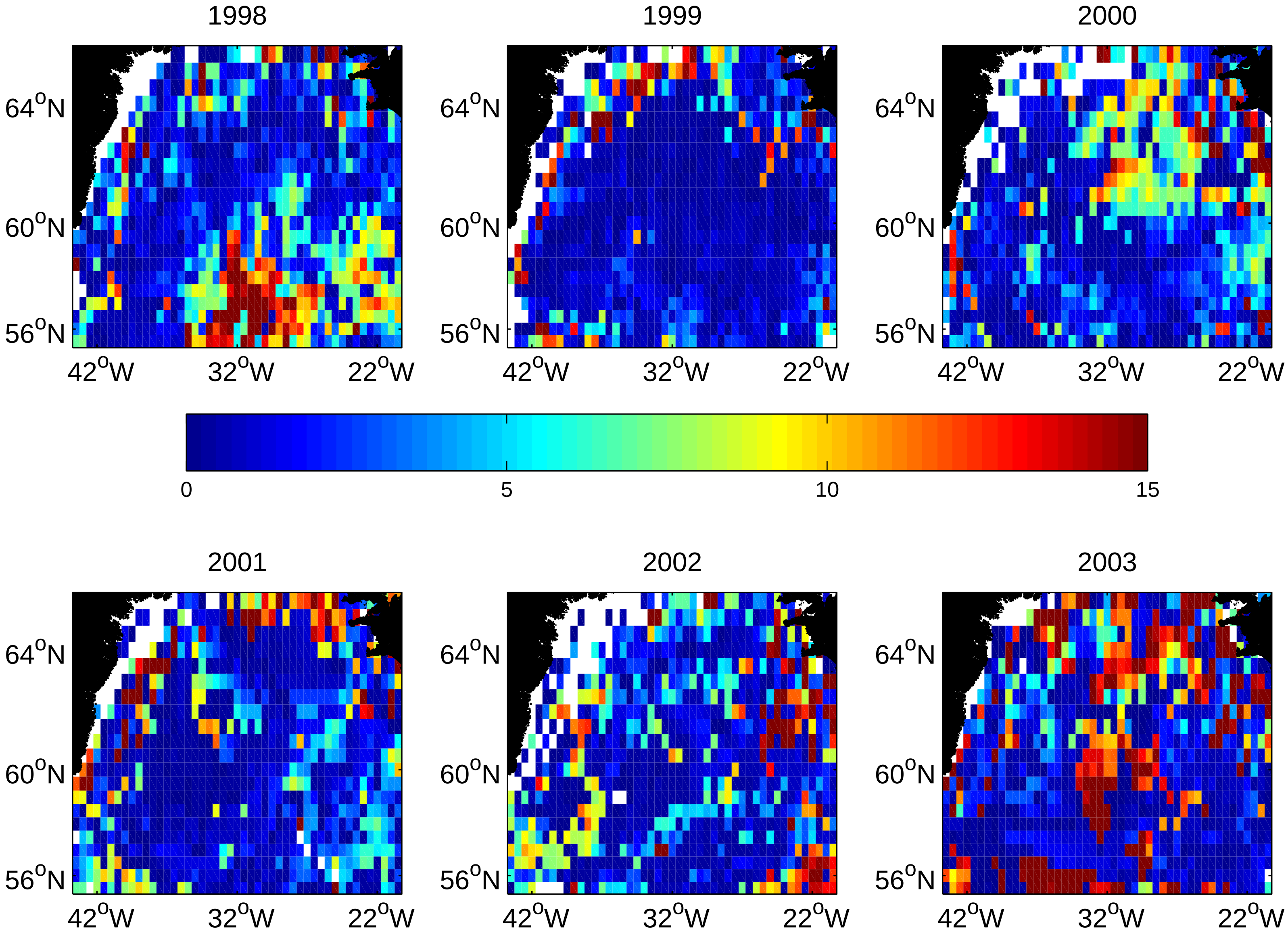

Figure 6.14: Summed chl-a over the bloom period (as defined in Section 6.3).

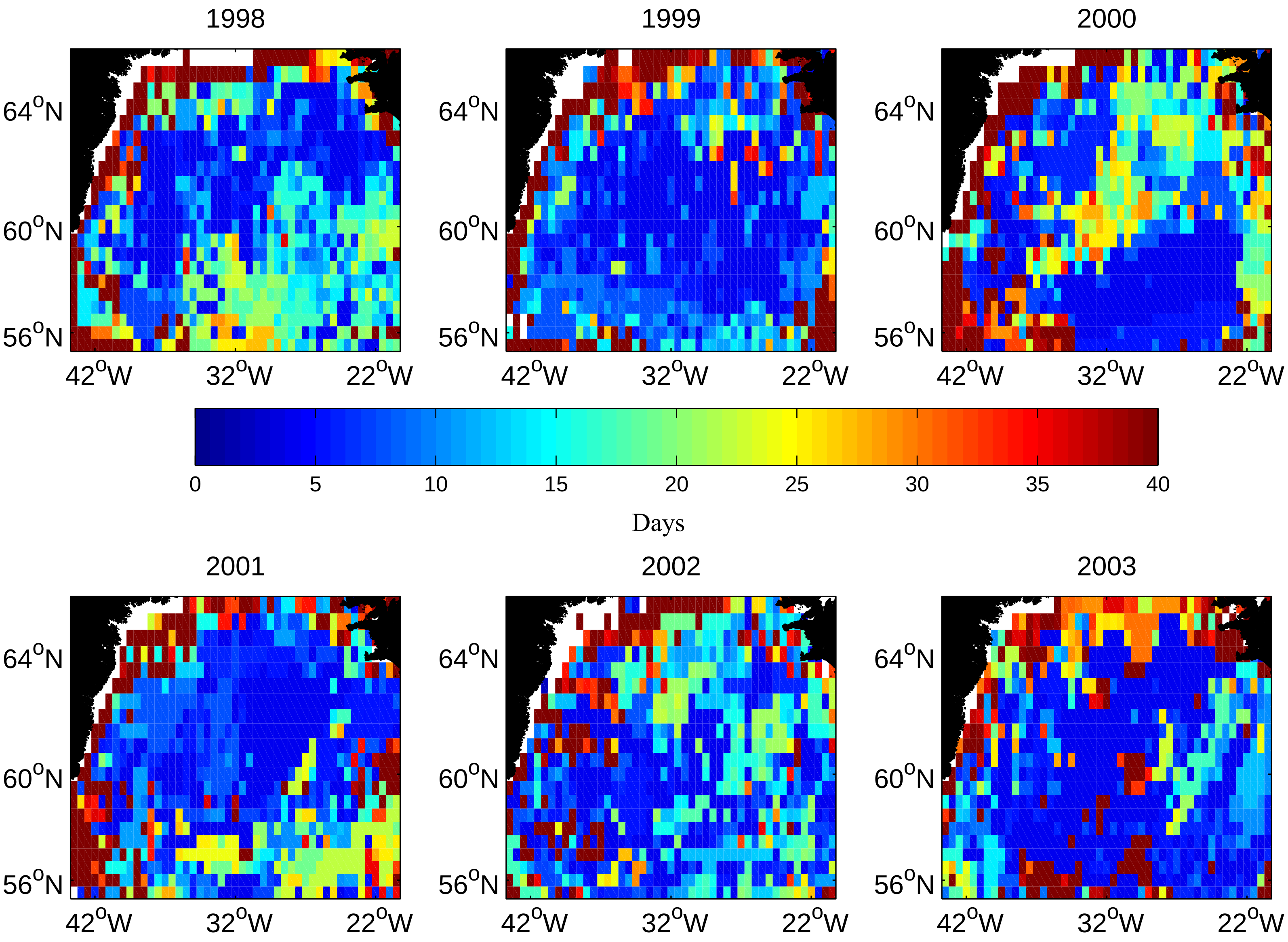

Figure 6.15: Duration of the bloom in days (as defined in Section 6.3).

7. PHYSICAL CONTROLS ON THE SPRING BLOOM:

Having concluded in the previous chapter that interannual variability in the spring bloom is occurring in the Irminger Basin, this chapter will examine the influence of meteorological forcing on chlorophyll concentrations, the conditions which need to be met for a bloom to start and the mechanisms affecting the decline of the bloom. Firstly the influence of meteorological forcing on chlorophyll concentrations is examined through Generalised Linear Modelling. Then the specifics of the conditions for the start of the bloom are examined. Sverdrup’s critical depth model is discussed and estimates of critical depth are made from satellite data. These are compared to mixed layer depth estimates from Argo floats and a 1-D physical model. Then the requirements are established for bloom initiation in terms of net heat flux and PAR. The factors controlling the magnitude of chl-a in summer - nutrient and light limitation and grazing - are examined. The chapter concludes by examining the particular bloom conditions and causes of interannual variability in the East Greenland coast region, which differs markedly from the rest of the Irminger Basin.

7.1. INFLUENCE OF METEOROLOGY ON CHLOROPHYLL CONCENTRATION:

The start of a spring bloom is reliant on many conditions being satisfied: in addition to a shallow mixed layer other environmental factors, such as wind speed, sea surface temperature (SST) or irradiance are influential. The shallowing of the mixed layer (ML) is influenced primarily by the net heat flux into the ocean. During winter a negative net heat flux (i.e. out of the ocean) results from low air temperatures, strong winds and lack of solar heating. During spring the increasing day length and elevation of the sun prompt surface warming. High wind speeds can counteract the effects of a positive net heat flux by mixing the water column and retarding the establishment of a stable mixed layer. Low SST can also suppress phytoplankton growth, as it limits the absolute rate of some biological reactions (Eppley, 1972; Davison, 1991) and adequate light throughout the ML is required for growth.

Later in the growth season, once the initial peak of the bloom is over, other factors will affect the phytoplankton population. Light is no longer limiting, due to a shallow ML, however nutrients are likely to be depleted in the surface waters. All of these parameters may have an impact on phytoplankton populations, but determining the balance of forcing that causes a particular response in chl-a concentration is complicated by their interactions. The following section examines the influence of meteorological forcing, as represented by the wind speed, net heat flux, SST and PAR, on chlorophyll concentrations. Initially an attempt was made at a Singular Value Decomposition (SVD) analysis – an extension of the EOF analysis of Chapter 5.3 which examines the coupled variability of two fields. However, for the reasons outlined below the analysis was rejected in favour of the simpler Generalised Linear Modelling, which will be returned to after a brief explanation of the inappropriateness of SVD for this study.

7.1.1. A NOTE ON SINGULAR VALUE DECOMPOSITION:

Often in climate studies there is an interest in the influence one parameter may have on another. The Singular Value Decomposition method allows the examination of the coupled variability of two fields by forming the cross covariance matrix. An SVD analysis will identify only those modes of behaviour in which the variations of the two fields are strongly coupled. The purpose of this aside is not to provide details of SVD analysis, but only to set out some provisos on its use and explain why it is inappropriate in this study. The mathematics of SVD analysis can be found in Preisendorfer (1988) or Björnsson and Venegas (1997).

An SVD analysis can only be rigorously successful if the transformation linking the two variables x and y is orthogonal, or if the covariance matrix of x or

y is the identity matrix (Newman and Sardeshmukh, 1995). In real terms this means that we have to assume that the relationship between the two data fields is linear. In the simplest case this indicates that y is causally related to x by a linear operator. Newman and Sardeshmukh (1995) demonstrate that even in this simple case the successful recovery of the relationship between x and y depends on the criteria stated above. In a more complex case where x and y are part of a larger system or y represents an external forcing for x (which is just what we would expect in climate studies) the interpretation of SVD products becomes even more problematic. Newman and Sardeshmukh (1995) suggest two simple tests to check whether a completed SVD analysis is valid. Firstly, if the SVD time series of x and y are not highly correlated, or secondly if the SVD time series are highly correlated but the SVD patterns of x and y are completely dissimilar to the corresponding EOF patterns of x and y, then the simultaneous occurrence of x and y is dubious. If either of these conclusions is reached Newman and Sardeshmukh (1995) suggest rejecting the SVD analysis.

For this study an SVD analysis was performed between the chl-a and several meteorological fields (net heat flux, SST, wind speed and PAR). The SVD analysis was carried out in Matlab using the standard function *svd*. The results failed the first criteria of Newman and Sardeshmukh (1995); that is, the SVD time series of x (chl-a) and y (meteorology) were poorly correlated. On this basis a continuation of the SVD analysis was rejected in favour of generalised linear modelling.

7.1.2. GENERALISED LINEAR MODELLING:

In order to examine the relationship between chl-a and the potential forcing parameters (i.e. the meteorology) generalised linear modelling (GLM) is introduced. GLM can be used to examine the interaction between a response parameter (in this case chl-a) and one or more predictors (here, meteorological forcing). GLM is an umbrella name for a variety of relationships between response parameters and predictors, which have a variety of distributions. The characteristics of a GLM are: the response has a distribution that may be normal, binomial, Poisson, gamma, or inverse Gaussian, with parameters including a mean μ; a coefficient vector **b** defines a linear combination **X*b** of the predictors **X**; and a link function f(·) defines the link between the two as f(μ) = **X*b** (Dobson, 1990).

For this study the simplest sort of GLM was employed: it assumes a normal distribution of response and predictors and a linear relationship between them. The response parameter is chl-a (C) and the predictors are net heat flux (Q), sea surface temperature (T), wind speed (U) and PAR (P). The form of the model is:

$$y = \mathbf{X}\beta + \varepsilon \qquad \text{[Eqn 7.1]}$$

where y is the observations (chl-a), **X** is the predictors (meteorology), β are regression coefficients and ε is the error. The term **X** not only contains Q, T, U and P, but also terms for the interaction of two or more variables. An example of the full equation is:

$$C = \varepsilon + \beta 1.Q + \beta_2.T + \beta_3.U + \beta_4.P + \beta_5.QT + \beta_6.QU + \beta_7.QP + \beta_8.TU + \beta_9.TP + \beta_{10}.UP + \beta_{11}.QTU + \beta_{12}.QTP + \beta_{13}.QUP + \beta_{14}.TUP + \beta_{15}.QTUP \qquad \text{[Eqn 7.2]}$$

The solution of the equation will be essentially a linear least squares fit to the observations (chl-a).

After the parameters are transformed to a normal distribution using the Box-Cox method (for details see Chapter 6.1.1) the Matlab function *regress* is used to solve the equation. The equation is solved initially for all terms, then the terms are sequentially removed and the equation solved again. The purpose of this is to determine which parameters, when removed, have a significant impact on the results of the model. The question is whether a more complex model adds to the explanatory power over a simpler model (i.e. one with fewer terms). A 'significant impact' is judged by the F-statistic:

$$F = \frac{(RSS_n - RSS_{(n+m)})/m}{RSS_{(n+m)}/(t-(m+n))} \qquad \text{[Eqn 7.3]}$$

where *RSS* is the residual sum of squares, *n* is the number of terms in the simpler model, *m* is the difference in number of terms between the simple and the more complex model and *t* is the total number of observations. If *F* is greater than a critical value then the model is deemed to have been improved by the increasing complexity. A table of critical *F* values can be found at the back of almost every statistics textbook. Finding the critical value requires knowledge of the number of degrees of freedom both between the terms (i.e. the total number of terms) and within the terms (i.e. the number of observations).

As varying the order of the predictors in the equation produces different results, a series of tests are required. An example of the result of this process is shown in Table 7.1. These results are for the East Greenland region in 2002. The first row compares a model with just P (letters in first column) to a model with an increasing number of terms: first a model with just P is compared to a model with P and U, then a model with just P is compared to a model with P and U and T etc. (letters in top row). The second row compares a model with P and U together to a model with P, U and T and so on. The highlighted numbers are those above the relevant critical *F* value. In this case a model with P on its own is always improved by adding more terms (row 2), and similarly for a model with P and U (row 3). Once T is added (row 4) the model's explanatory power is increased, and only a couple of the three-variable interaction terms improve the model; and so on. This indicates that a combination of P, U and T is a good predictor for chl-a.

A series of tests were carried out for each of the CIS, RR and EG zones, dividing the data into pre-bloom and post-bloom sections (pre-bloom is day of year 50 to 150: 19th February to 30th May; post-bloom is days 150 to 250: 30th May to 7th September). A selection of the results are presented in Tables 7.2 to 7.7 for the pre-bloom and post-bloom CIS, RR and EG regions respectively in the same format as the example above. In summary, in the pre-bloom CIS region chl-a is well explained by net heat flux and PAR. Post-bloom, temperature and wind speed totally dominate the model, with PAR playing a secondary role. No one meteorological factor dominates the model in the pre-bloom RR region, although the interaction term between Q and P is influential as the model becomes more complex. Post-bloom temperature and wind speed are influential and, unlike in the other regions, adding the higher order interaction terms to the model improves it. No one factor dominates the model in the pre-bloom EG region, whilst post-bloom wind speed has limited influence.

The model suggests that the balance of forces affecting the chl-a is different in each of the three biological zones. The full 16-term GLM equation was used to derive the coefficients (β_n of equation 7.2) which maximised the correlation between the predicted chl-a and the measured chl-a. The equation derived at one location (representative of, for example, the CIS zone) was then applied across the whole basin. For the CIS the coefficients were derived for the time series of data at 60 °N 36 °W; for the RR at 58.5 °N 32.5 °W, and for the EG at 62 °N 40 °W (as in previous analyses). At each pixel the relevant meteorological data and the derived coefficients were used to estimate chl-a. The correlation coefficient between the measured chl-a and the predicted chl-a, as derived separately for the CIS, RR and EG zones, is plotted in Figure 7.1. Although the coefficients are derived for one pixel only, the area over which the predicted chl-a correlates well with the measured chl-a extends throughout the biological zones. Within the region for which the coefficients were derived the correlation is ~0.7, but quickly decreases to <0.3 outside of the region. The boundaries between the regions are thus well delineated and correspond closely to the biological zones deduced from the EOF analysis (see Chapter 5.3 and Figure 5.9). This is further confirmation that the biological zones used throughout this study are robust, but more than that, it also indicates that the balance of physical processes influencing the chl-a signal is different in each region, and that this balance is different pre- and post-bloom. The conditions for initiation of the bloom are examined in the next section and the post-bloom period is returned to in Section 7.3.

7.2. INITIATION OF THE SPRING BLOOM:

The generalised linear modelling suggested that net heat flux and PAR are influencing chlorophyll concentration in the pre-bloom period, but it is not able to establish the specific conditions under which a bloom may occur. This section will examine these conditions: firstly from the perspective of Sverdrup's critical depth model (Sverdrup, 1953) and then with specific reference to net heat flux and PAR.

7.2.1. CRITICAL DEPTH VS MIXED LAYER DEPTH:

The increasing stability of the upper water column during spring is vital to the initiation of the bloom. As outlined in Chapter 2.1 the mixed layer (ML) depth must be sufficiently shallow for the phytoplankton to receive adequate light for growth. In Sverdrup's critical depth model (SCDM), described in Chapter 2.1, the ML must be shallower than the critical depth for a bloom to start. The critical depth is defined as the depth at which production integrated over the water column is equal to losses by metabolic processes and sinking. To test this hypothesis in this section the critical depth will be estimated from satellite PAR data and then compared to the ML depth estimated from Argo floats and a 1-D physical model.

Quantitatively SCDM assumes that under nutrient replete conditions primary production, $PP(z)$, is log linearly related to the light flux, $I(z)$, and that the effect of respiration, $R(z)$, is depth independent:

$$PP(z) = \alpha.I(z) = \alpha.I_0 e^{-Kz} = PP_0 e^{-Kz} \qquad \text{[Eqn 7.4]}$$

$$\text{and } R(z) = R_0$$

where α is the slope of the light-productivity relationship, I_0 is the flux of incident photosynthetically available radiation (PAR), K is the diffuse attenuation coefficient for PAR, PP_0 is the surface productivity and z is depth. Net production occurs above depths where $PP(z)$ is greater than R_0, known as the compensation depth Z_C,

$$Z_C = (1/K)\ln(PP_0/R_0) \qquad \text{[Eqn 7.5]}$$

or the compensation irradiance,

$$I_C = I_0 R_0 / PP_0 \qquad \text{[Eqn 7.6]}$$

Net community growth occurs above the critical depth, Z_{CR}, defined as:

$$\frac{1}{KZ_{CR}}\left(1 - e^{-KZ_{CR}}\right) = \frac{R_0}{PP_0} = \frac{I_C}{I_0} \qquad \text{[Eqn 7.7]}$$

Calculation of the critical depth, as defined by Sverdrup (1953), therefore requires knowledge of the compensation irradiance and attenuation coefficient.

Sverdrup's formulation assumes non-limiting nutrient concentrations and homogenous mixing of phytoplankton cells in the upper mixed layer. This condition is expected to be met during the first stages of the spring bloom (at least in the North Atlantic). There is continuing debate on the shortcomings of SCDM with regard to the definition of the respiration term (Smetacek and Passow, 1990; Nelson and Smith, 1991; Platt et al., 1991b). This arises because Sverdrup's original description of the compensation depth, where respiration is equal to production, includes not only phytoplankton respiration, but also grazing by zooplankton. This meaning has generally been lost in the intervening years and the respiration term (and compensation irradiance) has been used to refer to that of the plankton community only. Exclusion of the grazing term will result in estimates of the critical depth deeper than those based on the original formulation (Smetacek and Passow, 1990). To more clearly express the light level where photosynthetic and ecosystem community loss processes are equal the phrase ‘community compensation irradiance’ has been coined in more recent times. Sverdrup’s equations do not, however, require explicit knowledge of the processes contributing to respiration. In the method used below (partly based on Siegel et al., 2002) the community compensation irradiance is estimated from the ML depth at the start of the bloom – note that there is no requirement here for knowledge of the details of the total production or respiration occurring within the water column; if a bloom has started, biomass is increasing and phytoplankton community gains (growth) are therefore greater than community losses (respiration, excretion and losses to grazing and sinking). In the following calculations it is assumed that the community compensation irradiance, I_C, stays constant throughout the year. It is probable that I_C varies with time (Smetacek and Passow, 1990; Platt et al., 1991b), but the extent of the variability is unclear. Marra (2004) estimated I_C over a period of ~1 week using data from a mooring in the North Atlantic and found that it had a small range of values. With the exception of Marra’s (2004) study, the time variance of I_C is completely unknown, so a time-invariant I_C will be assumed. On the other hand, the spatial variability of I_C is accounted for, as the calculations are carried out at each data pixel.

Of the parameters in equation 7.7 the incident irradiance, I_0, and the attenuation coefficient, K, are relatively easy to estimate, either from *in situ* light profiles or from satellite PAR data. The compensation irradiance, I_C, however has proved difficult to define. Estimates from laboratory experiments based on the minimum irradiance required for a phytoplankton population to survive range from 0.1 to 3.5 mol photons m^{-2} day^{-1} (≡ Einsteins m^{-2} day^{-1}; Langdon, 1988; Riley, 1957). The lower values generally derive from phytoplankton-based studies, whereas the higher values account for zooplankton grazing and other loss processes and are community level estimates.

In a study by Obata et al. (1996) the authors relied on Sverdrup’s original (1953) compensation irradiance value (0.6 mol photons m^{-2} day^{-1}). They combined a global monthly mean ML depth from the Levitus (1982) climatology with an estimate of incident light derived from the solar zenith angle and a cloud climatology to estimate the monthly global critical depth. Whilst comparing the results to monthly mean CZCS chl-a data showed that SCDM is applicable at high latitudes, the authors admit a lack of suitably high spatial and temporal resolution data hampered their study.

The subject was taken up again by Siegel et al. (2002) who point out that, following Sverdrup's hypothesis, at the time of spring bloom initiation the depth of the mixed layer is equal to the critical depth, Z_{CR}. Along with knowledge of the attenuation coefficient and PAR at the initiation of the bloom, equation 7.7 can be used to calculate the community compensation irradiance, I_C, and therefore the compensation depth, Z_C, using equations 7.5 and 7.6. The authors estimate the start day of the bloom in the North Atlantic from daily, 1° SeaWiFS chl-a data and the mixed layer depth is extrapolated from a monthly climatology (World Ocean Atlas 1998 in Antonov et al., 1998). They go on to estimate the community compensation irradiance across the North Atlantic basin using incident PAR data from the SeaWiFS satellite. The attenuation coefficient is estimated empirically from the SeaWiFS surface chl-a concentration (Morel, 1988). Unfortunately the monthly climatology of ML depth has large gaps across the Irminger Basin and only patchy data on the compensation depth is available. In addition, as well as being spatially patchy, monthly climatologies of ML depth are not capable of capturing sufficient temporal variability to make satisfactory comparisons with higher resolution satellite chlorophyll data.

Profiles of temperature and salinity are available every ten days from drifting Argo floats, which are distributed throughout the world oceans. For this study, Argo data in the Irminger Basin were processed and the ML depth calculated as described in Section 3.8. To calculate the compensation depth and irradiance an estimate of the ML depth at the time of the initiation of the bloom was made. The ML at the initiation of the bloom $\pm$ 3 days (as calculated in Section 6.2) was extracted for all years (1998 – 2003) within three boxes representing the East Greenland (58 to 64 °N, 38 to 44 °W), Central Irminger Sea (59 to 64 °N, 30 to 36 °W) and the Reykjanes Ridge (55 to 59 °N, 28 to 34 °W) regions. The mean ML depth at the start of the bloom was found to be similar in all regions (EG: 142 m, CIS: 125 m, RR: 154 m). A plot of all ML depth data against coincident SeaWiFS chl-a for the entire Irminger Basin is shown in Figure

7.2. The plot demonstrates that the spring bloom only commences once the ML is shallower than ~100 m. The critical depth (i.e. the ML depth at the initiation of the bloom) for the whole basin is therefore set to a value of 100 m. This is in comparison to Siegel et al. (2002) who estimate the critical depth to be 185 m for the 60 to 65 °N band across the North Atlantic, and to Obata et al. (1996) who estimate the mixed layer depth (from Levitus, 1982) in the Irminger Basin during April/May (i.e. the start of the bloom) at ~100-200 m.

A critical depth of 100 m at the start of the bloom was used in Equation 7.7 to estimate the community compensation irradiance, I_C. For each pixel the values of the attenuation coefficient, K, and the incident PAR, $I_{0,}$ at the initiation of the bloom were extracted. The attenuation coefficient for PAR, K, was estimated from the SeaWiFS K490 product as:

$$K = 0.0085 + 1.6243 k_{490} \qquad \text{[Eqn 7.8]}$$

This equation is valid for $k_{490} \leq 1$ (Rochford et al., 2001). This criteria was met for all the K490 data in the Irminger Basin. For details of the algorithms and processing of K490 see Section 3.6. For I_0, the relevant daily SeaWiFS PAR data were used (see Section 3.5 for details of algorithm and processing). The community compensation irradiance, I_C, was calculated at each pixel for each year of data (1998 – 2003) using Equation 7.7 and similarly the compensation depth, Z_C, using Equation 7.5 (substituting I_0/I_C for PP_0/R_0). The mean compensation depth is ~20 m, similar to the 24 m estimated by Siegel et al. (2002) for the 60 to 65 °N band in the North Atlantic. The mean community compensation irradiance calculated is ~2.5 mol photons m^{-2} day^{-1}. This is within the range estimated in laboratory experiments, but greater than the mean value calculated by Siegel et al. (1.33 mol photons m^{-2} day^{-1}) for the 60 to 65 °N band. However, Siegel et al.'s published mean I_C values are calculated for the North Atlantic stretching from Canada to Norway and the few pixels in the Irminger Basin which contain data have values between 2 and 5 mol photons m^{-2} day^{-1}. The monthly climatological ML depths used in Siegel et al. (2002) smooth out the small temporal and spatial scale variability observable by Argo floats, which take profiles ten days apart and are effectively a single point measurement. In addition, because Siegel et al. (2002) have reported their results as means over large latitudinal ranges the high degree of variability in I_C estimates is masked.

Daily values of the critical depth, Z_{CR}, can now be calculated for each of the CIS, EG and RR zones. This is achieved by solving Equation 7.7 for each day using the relevant attenuation coefficient, K, and incident PAR, I_0, data averaged over the 1° regional boxes shown in Figure 6.1 (CIS centred on 60 °N, 36 °W; EG on 62 °N, 40 °W; and RR on 58.5 °N, 32.5 °W). Equation 7.7 must be solved iteratively and the Symbolic Math Toolbox (available only in Matlab version 14) was used. This toolbox has a function, *solve*, which allows the user to enter an equation in symbolic form which is solved iteratively using Newton's method with a randomly generated intital guess of the roots (an explanation of Newton's method can be found in, for example, Epperson, 2002). Equation 7.7 was first re-arranged so that:

$$\frac{1}{K.Z_{CR}} - \frac{e^{-K.Z_{CR}}}{K.Z_{CR}} - \frac{I_C}{I_0} = 0 \qquad \text{[Eqn 7.8]}$$

The critical depth for each region is plotted along with the ML depth from available Argo profiles and the SeaWiFS chl-a concentration for each of the CIS, RR and EG zones in Figures 7.3 to 7.5. Although the ML depth plots suffer from a lack of data at times, the impression is that chlorophyll concentration increases once the ML becomes shallower than Z_{CR}. In the CIS and RR regions the sharp increase in chl-a occurs several days after the ML has become shallower than the critical depth. In the EG region there appears to be a longer delay before the chl-a increases. According to Sverdrup's formulation, provided there is no nutrient limitation or grazing by zooplankton, a bloom may continue whilst the ML is shallower than the critical depth. In reality the peak of the bloom quickly dies back, but elevated chlorophyll concentrations (above winter values) are observed until the ML again becomes deeper than Z_{CR} in autumn (Figures 7.3 to 7.5).

In order to test the critical depth model thoroughly it is necessary to fill in the gaps in the Argo ML depth record. The 1-D vertical mixing model described in Section 3.9 is used. Mixed layer depth is calculated from the temperature profiles by applying the same criteria as for the Argo float data (see Section 3.8.1). The ML depths calculated from the model and from Argo data for the CIS, RR and EG regions are compared in Figures 7.6 to 7.8 respectively. The model successfully reproduces the Argo float estimates of ML depth throughout the year, and allows the gaps in the ML record to be filled. Note that whilst the model reproduces the *in situ* ML depth successfully for the CIS and RR regions, it does not work as well in the EG zone. This is most likely due to the effects of freshwater stratification in the coastal area (Waniek et al., 2005) - an effect which is not parameterised in the model. The model ML depth is plotted along with the critical depth and SeaWiFS chl-a for all zones in Figures 7.9 to 7.11. In the CIS region an increase in chl-a occurs very quickly after the ML becomes shallower than the critical depth. In the RR region in the years 2001-2003 there appears to be ~10 days delay before the chl-a increases rapidly, whilst in the EG region a delay of ~20 days is observed.

In summary, Sverdrup's critical depth model is valid in the Irminger Basin. In the regions investigated the bloom generally starts within a few days of the ML becoming shallower than the critical depth. On occasion there is a longer delay, emphasising the point made by Platt et al. (1991b) that Sverdrup's critical depth criterion is a necessary, *but not sufficient*, condition for the initiation of a phytoplankton bloom. Sverdrup's formulation tells us only whether growth is possible in the mixed layer, but provides no information on how quickly the biomass might accumulate.

The method detailed above allows the critical depth to be estimated at high spatial and temporal resolution from readily accessible satellite and Argo float data. Previous methods have relied on mooring or ship-board data, neither of which can provide the same synoptic coverage as remotely sensed data. This technique offers a way to assess whether a region's bloom may be predicted from the critical depth model. In comparison to regions where SCDM has been reported as lacking (principally the subtropical gyres and Southern Ocean – see

Section 2.1.3), a distinct seasonal pattern in ML depth and nutrient-replete conditions at the start of the bloom are observed in the northern North Atlantic. If this exercise were repeated for the entire North Atlantic, one would expect to find that SCDM becomes less applicable further south into the sub-tropical gyres (as seen in the modelling study of Dutkiewicz et al., 2001).

7.2.2. INFLUENCE OF NET HEAT FLUX AND PAR ON BLOOM TIMING:

If the start of the spring bloom in the Irminger Basin conforms to SCDM (as suggested in the previous section), the timing of the bloom must be dominated by the shallowing of the mixed layer, which in turn relies on the air-sea temperature difference. This is affected by the wind speed, solar insolation, cloudiness, latent heat of the ocean etc. Except for wind speed, these factors can be parameterised as the net heat flux.

The GLM confirmed that over large parts of the basin net heat flux (Q) is influential in determining the chl-a in the initial stages of the bloom. We might expect then that there is a correlation between Q and chlorophyll concentration. A positive net heat flux (i.e. into the ocean) will lead to stabilisation of the water column and the development of a surface mixed layer, and reflects a period of calm, warm weather. On the other hand a negative net heat flux (i.e. out of the ocean) will lead to erosion of the surface layer, and reflects cold or stormy weather. Figures 7.12 to 7.14 show time series of 3-day means of Q and SeaWiFS chl-a for the CIS, RR and EG regions (averaged over the 1° boxes centred on 60 °N, 36 °W; 58.5 °N, 32.5 °W and 62 °N, 40 °W respectively, as in the previous chapters). The net heat flux is positive only during the late spring and summer period but is occasionally interrupted by a spell of negative net heat flux, indicating a storm. The general impression is that during spring the chl-a increases when Q is positive. In the case of the CIS each occasion that Q becomes positive results in a pulse of increased chl-a, but it is not until Q remains positive for a period of ~5-10 days that the peak of the bloom occurs. In contrast, in the

EG region there appears to be a longer delay of up to ~20 days between Q remaining positive and the very rapid increase in chl-a characteristic of the spring bloom in this zone.

Performing a linear correlation of Q and chl-a returns $r = 0.44$ for the CIS and EG zones and $r = 0.64$ for the RR region ($p < 0.01$ in all cases). However, repeating the test for only day of year 1 to 150 (i.e. spring time; 1st January to 30th May) improves the correlation to $r = 0.58$ for the CIS zone, $r = 0.55$ for the EG zone and $r = 0.70$ for the RR zone ($p < 0.01$ in all cases). Compare this to the results if days 151 to 300 (i.e. summer into autumn; 31st May to 27th October) are considered: $r = 0.20$, 0.37 and 0.50 for the CIS, EG and RR zones respectively ($p < 0.01$ for the RR zone only). In other words the net heat flux correlates best with the chl-a during spring time. During spring the ML depth is highly dependent on the net heat flux: positive Q leads to a shallowing of the ML, whilst a period of negative Q results in the ML deepening again. Phytoplankton will respond positively to a shallowing of the ML, if sufficient light and nutrients are available, and an increase in remotely sensed chl-a may be detected provided the period of shallowing is sufficiently long for net growth to occur. If the ML then deepens again the phytoplankton population will be diluted and a decrease in chl-a may be observed. In summer the upper waters are strongly stratified and variations in Q, which generally remains positive, will not greatly affect the ML depth. Thus chl-a is not influenced by Q during the summer months.

Although a period of continuously positive net heat flux is necessary to induce the principal bloom in chl-a, the peak value is often preceded by a series of ‘false starts’, where the chl-a increases slightly but soon decreases again. Generally, prior to the peak of the bloom there is a gradual increase of chl-a above winter concentrations. How is this possible with a ML that is still hundreds of metres deep? Although the main thermocline, which is detected in the estimation of ML described in Chapter 3.8.1, remains deep, a diurnal mixed layer may be established. During the course of a day which is sunny and not windy a very shallow surface layer may be established, even in winter. The balance between the positive buoyancy flux, related to the insolation, and the turbulent energy provided by the wind, determines the depth to which warming penetrates (Price et al., 1986). At night convection, triggered by falling air temperatures, erodes the diurnal layer. The layer may only be 1-2 metres thick (Stramma et al., 1986), but is sufficient to trap a portion of the phytoplankton in the well-lit, nutrient-rich surface waters. These phytoplankton should be capable of net growth, but the likelihood is that this signal will not be detectable by satellite, due to its transient nature.

An alternative explanation stems from the convective mixed layer theory by Backhaus et al. (2003), which accounts for the presence of an over-wintering phytoplankton population. The theory states that overturning within convection cells repeatedly brings phytoplankton to the illuminated surface waters where, over the long term and on a community basis, growth can occur prior to the establishment of the seasonal thermocline. The corollary is that a shallowing mixed layer in spring results in an increasing length of time that a single phytoplankter spends in the euphotic zone, and so leads to an overall increase in production. A modelling study by Wehde (2003) concluded that a mixed layer of 400 m results in each phytoplankter spending on average 33 hours in the euphotic zone before being mixed into deep waters, whereas a mixed layer of 100 m allows each phytoplankter to remain in the euphotic zone for 133 hours, presumably with a corresponding increase in production (assuming sufficient nutrients are available). Whilst a shallowing mixed layer would result in a proportion of the population returning more frequently to the euphotic zone, it would also lead to loss of the phytoplankton which become trapped beneath the upper mixed layer and are unable to regain the sun-lit upper waters. However, the model ML depth decreases suddenly (over a couple of days) during spring, whilst the satellite chl-a increases slowly over a longer time scale. Of course, the model estimates of ML depth could be inaccurate and the Argo float data, at 10 day resolution, is not capable of addressing this theory.

Whatever the cause, a slow increase of chl-a is seen during the early part of spring, but the peak of the bloom does not occur until the daily average net heat flux has become continually positive. A delay between the two events is discernible in Figures 7.12 to 7.14. Lagged correlations between net heat flux and chl-a for each of the CIS, RR and EG regions are shown in Figure 7.15. In the

CIS region the correlation peaks at a lag of ~10 days (where net heat flux is leading chl-a), whilst in the EG region the lag is closer to ~25 days. In the RR region the maximum correlation occurs at zero lag.

So it seems that a positive net heat flux, which results in a ML shallower than the critical depth, is not the only requirement for a bloom to begin. The critical depth theory only defines when growth becomes possible, not whether, or how fast, growth will occur. What other factors could be causing this delay? Nutrient concentrations are well above limiting levels in spring (see Chapter 4) and, although zooplankton grazing may be able to keep the phytoplankton population in check, that is not expected to be the case at the very start of the spring bloom (see Chapter 2.2 for a discussion of *Calanus finmarchicus* overwintering in the Irminger Basin). The other possibility is that there is insufficient irradiance for growth to occur.

Figures 7.16 to 7.18 plot SeaWiFS chl-a against SeaWiFS PAR, with the start of the bloom, as calculated in Chapter 6.2, marked (details on the algorithm and processing of SeaWiFS PAR can be found in Chapter 3.5). At each pixel in the basin, the PAR on the day of the year on which the bloom started was found. The basin wide mean was ~81 W m^{-2}. This suggests that the minimum illumination required for a bloom to start is similar across the basin and that below this level phytoplankton growth may be restricted. Only above this level can the peak of the bloom occur. A theoretical depth-averaged total irradiance over the whole upper mixed layer required for a bloom to commence is often quoted as 20.9 W m^{-2} (Riley, 1957). To compare the estimate made here of the irradiance required for a bloom to start with that of Riley (1957), the surface incident PAR has to be converted into the depth-averaged irradiance, $\bar{I}$, by:

$$\bar{I} = \frac{I_0(1-e^{-Kz})}{Kz} \qquad \text{[Eqn 7.9]}$$

where I_0 is the incident surface PAR (W m^{-2}), K is the attenuation coefficient of PAR (m^{-1}) and z is the depth of the mixed layer (m). On the start day of the bloom the attenuation coefficient for PAR (as calculated in Equation 7.8) and the incident SeaWiFS PAR were determined. The mixed layer depth at the start of the bloom is assumed to be 100 m (as estimated in Section 7.2.1). The 6-year mean $\bar{I}$ is plotted in Figure 7.19. In the central basin $\bar{I}$ is ~18 W m^{-2} – close to Riley's (1957) estimate. It is remarkable that Riley's (1957) estimate is valid almost fifty years after it was published, despite improvements to measuring techniques and technology. Riley's original estimate was also made in the sub-tropical Sargasso Sea and it might be expected that different critical light levels may apply in different regions. However, numerous field studies have concluded that Riley's estimate is applicable – in estuaries and in sub-tropical or sub-polar open ocean (e.g. Hitchcock and Smayda, 1977; Sinclair et al., 1981; Horn and Paul, 1984; Morin et al., 1991; Townsend et al., 1994; Labry et al., 2001). It seems that it is also valid for the central Irminger Basin spring bloom. In the coastal regions $\bar{I}$ is lower at ~8 W m^{-2}, suggesting that a bloom can begin under lower light conditions in these areas. This is discussed further in Section 7.4.1.

It was determined previously that an extended period of positive net heat flux is required before a bloom can commence. A second criterion is now added: that PAR needs to be greater than ~81 W m^{-2}. These criteria were deduced by studying plots of the data at single points in the basin (albeit points which are expected to represent large areas of the basin). Is it possible to extend the conclusions drawn for particular point measurements to the whole basin, and estimate the initiation of the bloom from the net heat flux and PAR alone?

At each pixel the day of the year (DY) was determined on which the condition that net heat flux (Q) is positive for at least five consecutive days and coincides with PAR exceeding 81 Wm^{-2} for at least two consecutive days is met. The mean DY at each pixel from six years of data (1998-2003) was calculated. This was compared to the mean DY at the start of the bloom, as estimated in Chapter 6.2 from the SeaWiFS chl-a. In Figure 7.20, the difference between the start date calculated from the chl-a and the date when the criteria for Q and PAR have been met, is plotted. A negative value indicates that the bloom starts prior to the conditions for Q and PAR being met, whilst a positive value indicates that the bloom starts after the Q and PAR criteria has been satisfied. The majority of the pixels in the central basin and over the Reykjanes Ridge have a value of $\pm$ 2 days, suggesting that the net heat flux and PAR criteria are approximately correct for these regions.

On the East Greenland coast however, the difference is ~ -20 days, indicating that the bloom starts long before the Q and PAR conditions are met. But, as was noted earlier (Figure 7.14), the East Greenland bloom seems to start ~ 20 days *after* the net heat flux has become positive. Examination of the Q and PAR data in the region revealed that the discrepancy results from the requirement that PAR exceeds 81 Wm^{-2} is too stringent for the EG region. Figure 7.21 shows the mean PAR at the start of the bloom. Throughout the majority of the basin PAR at the beginning of the bloom is ~80 Wm^{-2}, although it varies between ~70 and 90 Wm^{-2}. Along the East Greenland coast however PAR can be as low as ~30 Wm^{-2} and rarely exceeds ~60 Wm^{-2} at the start of the bloom. This will be examined in more detail in Section 7.4.1.

Outside of the East Greenland coast region the conditions which must be met for the initiation of a spring bloom in the Irminger Basin have been determined. If the net heat flux remains positive for at least five consecutive days and PAR exceeds 81 Wm^{-2} for at least two consecutive days a bloom can occur. But once the bloom has begun, what then controls the duration and the magnitude of the period of elevated chlorophyll concentrations?

7.3. THE POST-BLOOM PERIOD:

The GLM suggested that in the post-bloom period wind speed and SST are influential in determining the chl-a, whilst net heat flux and PAR do not significantly affect it. (Note that here ‘post-bloom’ refers to the period after the peak of the bloom, when chl-a is elevated above winter concentrations, and before levels drop back towards winter values.) With the shallow summer ML in place variations in Q will not greatly affect the ML depth (until the onset of autumn mixing). So why does the bloom not continue at its peak level until autumn? The phytoplankton population can be limited by nutrient depletion, poor light levels or zooplankton grazing.

Is it possible that poor light levels are limiting growth later in the season? In Section 7.2.2 the minimum PAR required for a bloom to start was estimated as ~80 Wm^{-2} for the majority of the basin. Figures 7.16 and 7.17 show plots of PAR and chl-a against time for the CIS and RR regions respectively. PAR drops below 80 Wm^{-2} around mid-July, however chl-a concentrations remain elevated above winter levels throughout August and occasionally into early September. Whilst diatoms are expected to dominate the early stages of the spring bloom, flagellates and small plankton are expected to dominate the summer community composition (e.g. Barlow et al., 1993). These species may have a lower light requirement for growth than diatoms (Cota et al., 2003), allowing them to continue flourishing until late in the season. Therefore light does not appear to be limiting growth during the summer.

Zooplankton grazing, particularly by microzooplankton, is capable of reducing a phytoplankton population very quickly. A delay between the increase in phytoplankton and an increase in grazers may be expected, as zooplankton require longer to reproduce (a few days compared to ~ 1 day). However, after this initial period, grazing results in large phytoplankton stock turnover and may keep pace with phytoplankton growth, restricting the spring bloom (Miller, 2004). Surface chlorophyll concentrations can appear low whilst primary production remains moderately high, because zooplankton are removing the phytoplankton biomass almost as fast as it is produced (e.g. Platt and Irwin, 1968). Unfortunately there is no way of estimating zooplankton populations from remotely sensed data, so the question of grazing cannot be addressed directly in this study. Nutrient limitation can however be assessed, and although grazing is likely to play a role in the decline of the spring bloom, nutrient availability will also be a significant factor.

Nutrient concentrations can be estimated from satellite SST and chl-a (see Chapter 4 for the method and equations). Using remotely sensed data 3-day, 0.5° resolution maps of nitrate, phosphate and silicate concentrations were calculated for each year of the dataset (1998 – 2003). As examples of the data Figures 7.22 to 7.24 show chl-a against nitrate, phosphate and silicate for each year in the CIS, RR and EG regions respectively. The general pattern is of high nutrient concentrations during winter, which fall rapidly as the bloom begins. Concentrations continue to drop throughout the post-bloom summer, but start to increase again around September. There is also considerable interannual variability in the summertime nutrient concentrations.

Following the peak of the bloom, phytoplankton consumption will have depleted some of the essential macro-nutrients to the point where they limit growth, and the presence of the seasonal thermocline restricts supply of new nutrients into the surface waters. Post-bloom, other sources of nitrate, such as regenerated ammonia or urea, or fixation of atmospheric nitrogen may become important. All macro- and micro-nutrients may also be supplied through mixing events which erode the base of the thermocline and entrain new nutrients into the surface waters. In a high-latitude region, such as the Irminger Basin, high wind speeds are encountered even in summer, the ML stratification can be relatively weak and nutrient concentrations below the thermocline are high. Under these circumstances it is feasible that mixing events are able to resupply the upper waters with new nutrients, and that the phytoplankton will respond, given sufficient light, with a burst of growth, until the nutrients have been depleted again. Wind speed (from QuikSCAT sensor; see Section 3.4 for description of data) was not however significantly correlated with nitrate, phosphate or silicate during the post-bloom period. This suggests that either the wind mixing in summer is not sufficient to erode the base of the mixed layer and entrain new nutrients, or that the nutrients are consumed so rapidly within the water column that a surface signal is not observed. *In situ* species biomass data suggest that diatoms are concentrated at the base of the thermocline in summer (Claire Holeton, NOCS, pers. comm.), presumably due to a lack of silica in the surface waters. It is likely then that any nutrients resupplied by wind mixing in summer will be consumed very rapidly at the base of the mixed layer and a surface nutrient signature may not be observable.

Figures 7.22 to 7.24 suggest that phytoplankton growth in the post-bloom period may be suffering from a lack of nutrients, but how exactly can nutrient limitation be defined? The mean (over 1998 – 2003) minimum nitrate, silicate and phosphate concentrations across the basin are shown in Figure 7.25. In the east of the basin and over the Reykjanes Ridge nitrate, phosphate and silicate all reach a minimum concentration close to zero. In the west of the basin nitrate and phosphate remain well above zero, whilst silicate concentrations are close to zero across the whole basin, with the exception of the East Greenland coast and a section of the south-western central basin. In Figure 7.25 silicate is the only nutrient which drops to zero. Nutrients do not, however, have to be at zero concentration to be limiting to phytoplankton growth. The concept of nutrient limitation was originally formulated for agricultural systems as Liebig's Law of the Minimum (Liebig, 1840; see De Baar (1994) for a review of its applications in the marine environment). Essentially the amount of nutrient regulates phytoplankton growth and biomass through a yield-dose response. For *net* growth to occur nutrient supply must be greater than required for the biosynthetic capacity of a cell. Typically nutrient limitation in the sense of Liebig's Law is evaluated with a stoichiometric approach that compares environmental nutrient ratios with the composition ratio of biomass (assuming balanced growth) to determine which nutrient will be exhausted first (e.g. Hecky and Kilham, 1988). A lack of any nutrient that causes photosynthesis to be retarded can be regarded as limiting (Falkowski and Raven, 1997). In addition, as different phytoplankton species are dependent on different nutrients, concentrations that are limiting to one species may not be limiting to another. For example, diatoms require silica to form their cell wall and at concentrations of silicate < 2 μmol l^{-1} they may be out-competed by other species that are not so dependent on silica, such as flagellates (Egge and Aksnes, 1992; Brown et al., 2003). Co-limitation of nutrients further confuses the issue, making it difficult to define exactly the limiting concentration of a certain nutrient. Nutrient uptake rate experiments can be used to determine concentrations which are limiting to growth, but these are not routinely performed *in situ*. Alternatively the half-saturation constant for growth for a nutrient gives an indication of the nutrient concentration at which phytoplankton growth is not meeting its full potential. For nitrate this is < 0.5 μmol l^{-1} (Eppley et al., 1969) whilst for phosphate it is < 0.03 μmol l^{-1} (Davies and Sleep, 1981).

In the absence of any uptake rate experiments carried out *in situ* in the Irminger Basin, nutrient depletion concentrations will be set at 2 μmol l^{-1} for silica, 0.5 μmol l^{-1} for nitrate and 0.03 μmol l^{-1} for phosphate. Figures 7.26 to 7.28 show the day when silicate, nitrate and phosphate concentrations, respectively, first become depleted for each year 1998-2003. Silica becomes depleted across most of the basin (Figure 7.26), starting earliest east of the Reykjanes Ridge in mid to late April. The Reykjanes Ridge region itself becomes depleted in late May/early June, with the central basin following in July to August. Note that nutrients do not appear to become depleted along the East Greenland coast – this conclusion is thought to be unreliable for reasons which will be outlined in Section 7.4.1. Whilst the geographical pattern of silica depletion remains the same throughout the six years, there is considerable interannual variability in the timing of depletion. For example in 1998 and 2003 depletion occurs in the central basin in mid-June, whilst in 1999 and 2000 the Reykjanes Ridge does not experience depletion until early July. Concentrations are similar in the winter of each year and, as Olafsson (2003) notes, the depth of winter mixing is not correlated to the spring time nutrient concentrations in the Irminger Basin. This suggests that the interannual variability in the timing of depletion is dependent on the bloom characteristics (timing and magnitude), rather than winter conditions. In contrast to silicate, nitrate (Figure 7.27) does not become depleted in the western regions of the basin at all. To the east of the Reykjanes Ridge nitrate becomes depleted long after silica, in August. Similarly phosphate (Figure 7.28) does not become depleted in the western part of the basin, but is depleted in August to the east of the Reykjanes Ridge.

If at silica concentrations less than 2 μmol l^{-1} diatoms are out-competed, then the timing of silica depletion also represents the timing of the transition from diatom dominance of the community composition to smaller, non-siliceous plankton. Although satellite-derived silica depletion gives only a first-order approximation of community composition it nevertheless provides a time and space-resolved estimate. This will be discussed further in Chapter 8.1.

As silica depletion is so widespread in the basin, it is possible to speculate that silica is the nutrient limiting the Irminger Basin spring bloom. But does a drop below 2 μmol l^{-1} concentration of silica bring about the end of the peak of the bloom? The end of the bloom peak was defined in Section 6.3 as the day of the year when chl-a drops below one-third of the maximum concentration and is shown in the sketch of bloom progression in Figure 6.14. Figure 7.29 shows maps of the timing of the end of the bloom peak for each year 1998-2003 (plotted on the same scale as the nutrient depletion maps). Although noisy the figure gives the impression of a westwards progression of the end of the bloom peak that coincides reasonably well with the progression of silica depletion across the basin (Figure 7.26), however the similarity is not sufficient to be able to categorically state that silica depletion is limiting the bloom. It is likely that grazing by zooplankton also reduces the phytoplankton biomass and may keep pace with phytoplankton growth. Unfortunately there is no way of addressing this point with the data set available to this study.

During summer, it might be expected that increased wind speeds may lead to erosion of the seasonal thermocline and entrainment of new nutrients into the surface waters, thus alleviating nutrient depletion and resulting in an increase in surface chl-a. The correlations between the late summer/early autumn (mid-July to October) wind speed and nutrient concentration or wind speed and chl-a were calculated. Whilst there was a trend for increased wind speeds to result in increased surface silica and nitrate concentrations ($r = 0.4$), there was no correlation between wind speed and chl-a. This suggests that whilst increased wind speeds may be able to introduce new nutrients the phytoplankton are not able to use them. This may be due to poor light conditions (although, as discussed earlier in this section this is believed to be unlikely), extensive grazing of the phytoplankton, changes in the community composition or limitation by another nutrient, such as iron. Diatoms are the only functional group found in the Irminger Basin which consumes significant quantities of silica. If they are not abundant in late summer, silica will remain unused. Nitrate never becomes limiting over large parts of the basin, so introduction of new nitrate is unlikely to promote an increase in chl-a, and hence the lack of correlation between wind speed and chl-a. The reasons why nitrate does not become limiting are discussed in Chapter 8.2. The implications of nutrient depletion for community succession and export production will also be discussed in Chapter 8.

7.4. THE EAST GREENLAND COAST:

The remainder of this chapter will focus on the East Greenland coast region which throughout this study of spring bloom dynamics in the Irminger Basin has consistently displayed characteristics different from those in the rest of the basin. In this section the particular conditions controlling the spring bloom and interannual variability in this region are examined.

7.4.1. BLOOM CONDITIONS:

On the East Greenland coast the spring bloom starts earlier and lasts longer and the maximum chl-a concentrations are approximately double those observed in the rest of the basin (Figures 6.10. 6.15 and 6.12 respectively). Why is this? It was noted in Section 7.2.2 that PAR at the start of the bloom on the EG coast can be as low as ~30 Wm^{-2}, compared to ~80 Wm^{-2} in the rest of the basin. A positive net heat flux (Q) extending over five consecutive days has been established as a requirement for initiation of the bloom in the rest of the basin (Chapter 7.2.2). However, on the EG coast, there is a long delay between net heat flux becoming positive and the start of the bloom (Figure 7.14). There is also a long delay between the mixed layer depth becoming shallower than the critical depth and the start of the bloom (Chapter 7.2.1). In addition Q has poor explanatory power in the EG pre-bloom GLM, in contrast to the RR and CIS zones (Chapter 7.1.2). This suggests that the initiation of the EG bloom is somewhat decoupled from the net heat flux. Processes other than the simple shallowing of the mixed layer due to heating may be occurring in this region. Only by considering satellite derived information in combination with *in situ* data can a complete picture of the bloom conditions be established.

In situ data are available from the spring Marine Productivity cruise (D262; Richards et al., 2002), which sampled several CTD stations on the East Greenland coast in mid-May 2002 (days 129 to 137; see Section 3.1.2 for details of CTD casts). An area of cold, fresher water (33.5 to 34.5 psu and 2-3 °C compared to ~35 psu and 6-7 °C in the central basin) was observed, likely resulting from the spring melting of seasonal ice cover. The salinity difference had led to the establishment of density-driven stratification (rather than thermal stratification, resulting from surface heating). Light conditions were still poor at the time of the cruise, and in the rest of the basin only a weakly stratified surface layer and low concentrations of flagellates and picoplankton were evident (Holeton et al., 2004). On the coast however a dense bloom of the flagellate *Phaeocystis* sp. had been able to take advantage of the early appearance of a mixed layer (Waniek et al., 2005). *Phaeocystis* sp. colonies are common in high latitude regions and are known to be typically more successful than competing diatoms under conditions of low light and temperature (Cota et al., 1994; Moisan and Mitchell, 1999). The conclusions drawn from an analysis of the satellite data are thus confirmed and clarified by the *in situ* data: the bloom relies on an input of ice-melt freshwater to induce stratification. Because this stratification occurs early in the year, light levels are poor. However, the low-light adapted flagellates, *Phaeocystis* sp., are able to take advantage of the conditions and results in a massive, early bloom.

A dense bloom would be expected to strip the surface waters of nutrients. However in the estimates of silica depletion made in Section 7.3 silica does not appear to become depleted along the East Greenland coast (Figure 7.26). Inspection of the *in situ* CTD nutrient profiles show silica to be below depleted concentrations (2 μmol l^{-1}) during the summer cruise (August 2002). Silica calculated from satellite SST and chl-a is therefore over-estimated in this region. The silica depletion temperature i.e. the temperature at which silica < 2 μmol l^{-1} is ~9 °C (from Figure 4.9). However, SST never becomes this warm on the northern East Greenland shelf, principally due to the influence of seasonal ice melt and freshwater run-off. This region therefore requires a unique temperature-silica relationship. This could not however be established due to the lack of *in situ* measurements in this region. This emphasises the point that while satellite data are the only way to provide large-scale context, the *in situ* data should be borne in mind to ensure spurious conclusions are not drawn.

Are the conditions observed *in situ* during 2002 the typical sequence of events for a bloom on the East Greenland coast? Or was the 2002 bloom unusual? Whilst the *in situ* data elucidate the reasons behind the early bloom, only the temporal context provided by the satellite data can determine whether this event is the norm or anomalous.

7.4.2. INTERANNUAL VARIABILITY:

As well as defining the biogeographical zones used in this study, the Empirical Orthogonal Function analysis of Chapter 5.3.3 also provides information on interannual variability. Mode 2 of the EOF analysis defines the spatial extent of the EG region (Figure 5.9), whilst the time series defines the variability of the signal in the mode (Figure 5.10). The negative parts of the time series correspond to a chl-a signal over the EG region in April/May. This signal becomes stronger from 1998 to 2001, is completely absent in 2002 and returns in 2003. What is causing this variability in the time series? Comparing the spatial maps in Figures 5.9 and the time series in Figure 5.10 to the chl-a anomalies during April/May (Figure 6.7) it is clear that the EOF analysis is reflected in the anomaly maps: both highlight the unusually low chl-a concentrations observed on the Greenland coast during early spring 2002.

The *in situ* data, however, demonstrated that a large *Phaeocystis* sp. bloom was occurring on the shelf during May 2002. Perhaps the satellite data is not detecting this bloom leading to spurious results? The percentage of days on which cloud obscured the EG zone in early spring 2002 is not significantly different than in other years (2002 was ~60 % cloud free compared to an average of ~62 %). The peak of the bloom does not occur later in 2002 than in other years, thereby skewing the seasonal anomalies (see Figure 6.6). It is possible that, although the

Phaeocystis sp. bloom observed in 2002 dominated the spring cruise phytoplankton, this was still an uncharacteristically small bloom and it was even more dense in other years. Another alternative is that the bloom in other years had a different community composition, resulting in a different SeaWiFS chl-a signal. As discussed in Chapter 3.2.2 different phytoplankton species contain different proportions of chl-a. Diatoms are chl-a rich, whilst flagellates (such as *Phaeocystis*) are relatively chl-a poor. If a chl-a rich species dominated the bloom in other years, the SeaWiFS chl-a would appear greater than for a bloom of a chl-a poor species. Finally at some of the CTD stations in the EG region the peak biomass was observed below 10 m depth (Waniek et al., 2005). A sub-surface chlorophyll maximum may not be detected by the SeaWiFS instrument. In other years the peak biomass may have been consistently at the surface, rather than occasionally sub-surface, as in 2002, resulting in apparently higher chl-a, as detected by SeaWiFS. Unfortunately this question cannot be fully resolved with the data available, but regardless, interannual variability is clearly occurring in the satellite data.

What physical processes could be contributing to the anomalously low chl-a in 2002? The pre-conditioning of the water column in the winter will be vital to the success of the following spring's bloom. Meteorological conditions during winter will affect the depth of winter mixing and the subsequent development of the seasonal thermocline. Modelling studies by Waniek (2003) suggest that in years with few storms the bloom is relatively short-lived with high biomass but low total annual primary production. In contrast in years which experience many storms, the bloom has lower amplitude and biomass, but the total annual primary and export production are higher. In the Irminger Basin Moore (2003) defined a storm as an occasion when the wind speed exceeds 17 ms^{-1}. Daily wind speed and direction data are available at 0.25° resolution from the QuikSCAT instrument from 19th July 1999 to the present (see Chapter 3.4 for a description of the data). Prior to the launch of QuikSCAT, ERS-2 data are available, but only at weekly resolution. As a high wind speed event is expected to last only a few days the ERS-2 data are not suitable and the analysis will focus only on the period covered by QuikSCAT data. The percentage of days during January, February and March 2000-2003 on which wind speed > 17 ms^{-1} is shown in Figure 7.30. The majority of the basin away from the East Greenland coast experiences ~ 15-20% stormy days. Along the EG coast stormy days are ~30-50% of days. The number of storm days on the East Greenland coast in 2002 is greater than in other years. Additionally the area affected by storms extends further into the central basin in 2002 than in other years. Notably in 2001 relatively few storms occur in the basin with only 10-15% stormy days. 2002 appears to have been an especially stormy year, particularly in comparison to 2001. The tendency towards high wind speeds during winter of 2002 is also reflected in the anomalies from the mean wind speed during winter (Figure 7.31; days 1 to 90; 1st January to 31st March). The western side of the basin experiences higher wind speeds in winter 2002 than the average, whilst winter 2001 is characterised by wind speeds lower than the average.

Winter storms in the Irminger Basin often result from high speed topographically forced wind events, known as the tip-jet (Doyle and Shapiro, 1999). It forms when high-level northwesterly winds are accelerated over the steep topography of the eastern (leeward) side of Greenland, drawing cold air over the Irminger Basin (see Chapter 2.2.1). These events have the ability to influence the depth of winter mixing and may lead to deep convection in the Irminger Basin (Pickart et al., 2003b). Could this large-scale physical process be affecting the spring bloom characteristics? A tip jet event is expected to have a large zonal component, with strong winds towards the east. Following Pickart et al. (2003b) the daily wind direction is averaged over the region 59-60° N, 37-42° W where the tip-jet winds are strongest (note that Pickart et al. used the COAMPS model which is at a coarser resolution of ~2° than the QuikSCAT data). The daily wind direction during winter over all four years is displayed as a histogram in Figure 7.32 (0° is wind towards the north; data in 20° degree bins). The histogram has a well-defined peak at ~90° with a smaller, more diffuse peak at ~210° i.e. in winter the wind blows principally towards the east, with frequent winds towards the south-south-west. The eastward winds are likely to be associated with the tip-jet phenomenon, suggesting that it is a common occurrence during winter. The SSW winds could be associated with 'reverse tip-jet events', defined by Moore (2003). After an analysis of 52 years of NCEP reanalysis winds Moore (2003) concluded that in addition to the strong eastward winds associated with tip-jets, strong westwards winds occurred almost as often. He suggests that whilst the axis of the tip-jet appears to be oriented in the zonal direction, the reverse tip-jet has a meridional component. The conclusions drawn from Figure 7.32 are in agreement with Moore's (2003) hypothesis and suggest that the winter wind field in the Irminger Basin is bimodal.

Could interannual variability in the winter occurrence of tip-jets, or reverse tip-jets, be causing the differences in spring time chl-a? In Figure 7.33 the wind direction for winter of each year (2000 – 2003) is displayed as a rose plot. In 2000, 2002 and 2003 the principal wind direction is towards the east. In 2001 however the wind direction is mostly in a south-eastward direction, with occasional eastward winds. Perhaps the lack of tip-jet events in 2001 is responsible for the above average chl-a in the EG region in spring (Figure 6.7)? However, the wind direction during winter of 2000, 2002 and 2003 is similar, yet 2002 experiences a much reduced spring bloom. Figure 7.34 shows a rose plot of wind direction in each year for spring/summer (days 100 to 200; 10th April to 19th July). In all years except 2002 the wind direction becomes variable with little directional constancy (although in 2003 there is a southward wind). In 2002, when chl-a is much lower than the mean, the prevailing wind direction continues to be towards the east, typical of the tip-jet. In summary, 2000 and 2003 have similar spring time chlorophyll concentrations and in both years there is a prevailing eastward wind during winter, whilst in spring there is either little directional constancy (2000) or a southward wind (2003). In 2001 the EG coast has more chl-a than the mean and in winter and spring there is no prevailing wind direction. Chl-a is lower than the mean in 2002, which experiences strong eastward winds (i.e. tip-jet winds) in both winter and spring.

Not only the strength of the wind in winter, but also the prevailing direction, seem to have an impact on the following spring's chl-a. Storms in the sub-polar North Atlantic tend to follow a track which passes between the east coast of Greenland and Iceland. These low pressure systems draw cold, dry air over the Irminger Basin and result in a predominately eastward wind (Pickart et al., 2003b). Moore (2003) demonstrated that when the storm track shifts southwards, the result is a warmer, wetter winter and southward winds prevail. So changes in the wind field may also be reflected in the net heat flux (Q) during winter. In Figure 7.35 the anomalies from the mean winter Q are shown. In 2000 and 2002 on the EG coast the Q is more negative i.e. more heat is leaving the ocean surface than the mean, and in 2001 and 2003 the Q is less negative i.e. more heat is entering the ocean surface than the mean.

There seem to be two modes of meteorological forcing and chl-a response in the Irminger Basin. These modes may be responding to the index of the North Atlantic Oscillation (NAO). The NAO index is based on the surface air pressure difference between a weather station in the Azores and one in Iceland. When the NAO is positive a northerly storm track is likely to bring cold, dry winters to the Irminger Basin, and a negative NAO will result in a southern storm track and a warm, wet winter. The NAO is positive throughout the study period, except for the winter of 2000/2001 when it is negative. The winter of 2000/2001 is unusually warm and experiences no dominant wind direction, which results in anomalously high concentrations of chl-a in the following spring.

In 2002 however, it seems that persistent eastward winds, combined with an anomalously cold winter led to lower than average spring chl-a concentrations. This may be because the meteorological conditions result in a deeper winter mixed layer, which takes longer to restratify in the spring. The ML depth estimated from Argo floats and the 1-D model for 1998 – 2003 in the East Greenland region was presented in Figure 7.8. There is a suggestion in the Argo data that the maximum ML in 2002 was ~ 500 m, compared to ~ 400 m in other years. The model also shows a deeper maximum ML in 2002 with ~ 450 m compared to ~ 400 m in other years. However, this difference in mixing depth does not seem to affect the development of the seasonal thermocline, which becomes established at a similar time in 2002 as for the other years. Similarly, although the winter of 2001 is anomalously warm, there seems to be little impact on the ML depth.

Although it is possible to surmise that interannual variability in meteorological conditions is causing the interannual differences in chlorophyll concentration, the mechanism unfortunately remains elusive. *In situ*, depth-resolved data on an interannual time scale or, alternatively, a 3-D coupled physical-biological model would be necessary to further address the questions raised by the satellite data, however this is outside the scope of this study.

7.5. CHAPTER SUMMARY:

This chapter has addressed the meteorological forcing that controls the initiation and decline of the spring bloom, and the special conditions on the East Greenland coast.

- Generalised Linear Modelling shows that net heat flux and PAR strongly influence the initiation of the bloom, whilst SST and wind speed are more important in the summer.
- Sverdrup's critical depth can be estimated from satellite PAR and knowledge of the timing of the start of the spring bloom.
- Sverdrup's critical depth model is valid for the Irminger Basin, although a mixed layer depth shallower than the critical depth is not the only condition necessary for a bloom to start.
- Outside of the East Greenland region, a positive net heat flux (i.e. into the ocean) for at least five consecutive days and a PAR > 81 Wm^{-2} for at least two consecutive days is necessary for the bloom to start.
- The timing of nutrient depletion can be estimated from the satellite-derived nutrient concentrations. Silica becomes depleted over most of the basin, whilst nitrate and phosphate become depleted only late in the season and to the east of the Reykjanes Ridge.
- On the East Greenland coast the spring bloom starts at lower light levels than in the rest of the basin. This is because *Phaoecystis* sp. are able to exploit early freshwater stratification from ice melt run-off.
- In 2002 the East Greenland region experienced anomalously low chl-a concentrations. Strong easterly winds, associated with the tip-jet phenomena, occured throughout winter and spring and net heat flux was anomalously low in 2002. This implies that the spring bloom in the

Irminger Basin can be affected by large scale climatic events, such as shifts in the North Atlantic Oscillation.

	U	T	Q	PU	PT	PQ	UT	UQ	TQ	UTQ	PUQ	PTQ	PUT	PUTQ
P	6.75	165	109	81.2	68.73	57.13	48.63	42.8	41.7	37	33.9	37.8	35.71	32.9
U		314	155	103	81.72	65.21	53.97	46.5	44.6	39.1	35.6	39.3	36.91	33.8
T			0.04	0.29	1.601	1.366	1.173	1.17	1.96	1.69	1.67	3.01	2.995	2.75
Q				0.54	2.382	1.808	1.456	1.4	2.28	1.93	1.87	3.34	3.29	2.99
PU					4.201	2.432	1.756	1.61	2.61	2.15	2.06	3.67	3.576	3.22
PT						0.683	0.56	0.76	2.15	1.7	1.66	3.45	3.354	2.99
PQ							0.443	0.8	2.62	1.94	1.85	3.88	3.708	3.26
UT								1.15	3.69	2.43	2.19	4.54	4.231	3.64
UQ									6.14	3.04	2.51	5.31	4.782	4.01
TQ										0.04	0.72	4.69	4.146	3.36
UTQ											1.41	7.01	5.514	4.19
PUQ												12.4	7.422	5.02
PTQ													2.235	1.3
PUT														0.38

Table 7.1: An example of the result of a GLM run for the East Greenland region in 2002. The letters in the first column are the terms in the first model (P = PAR, U = wind speed, T = SST and Q = net heat flux). The letters in the first row are the terms in the second model. The numbers are the F-statistic from comparing model 1 with model 2. The highlighted numbers are greater than the critical F value.

	U	P	T	QU	QP	QT	UP	UT	PT	UPT	QUT	QPT	QUP	QUPT
Q	3.03	34.70	133.5	99.99	82.55	68.52	58.65	51.91	46.14	41.71	37.96	35.78	32.88	31.21
U		65.99	198.7	132.4	102.2	81.44	67.78	58.77	51.42	45.91	41.36	38.68	35.29	33.30
P			322.2	160.9	111.0	82.95	66.29	55.95	47.98	42.19	37.56	34.86	31.54	29.62
T				0.42	2.81	1.89	1.53	1.69	1.52	1.48	1.40	1.79	1.60	1.82
QU					5.20	2.63	1.90	2.01	1.74	1.66	1.54	1.95	1.73	1.96
QP						0.08	0.27	0.95	0.87	0.95	0.93	1.48	1.29	1.59
QT							0.45	1.38	1.14	1.17	1.10	1.71	1.46	1.77
UP								2.30	1.48	1.41	1.26	1.96	1.63	1.96
UT									0.66	0.96	0.91	1.87	1.49	1.90
PT										1.26	1.04	2.27	1.70	2.14
UPT											0.81	2.76	1.84	2.35
QUT												4.69	2.35	2.86
QPT													0.03	1.92
QUP														3.81

	P	Q	T	UP	UQ	UT	PQ	PT	QT	PQT	UPT	UQT	UPQ	UPQT
U	226.8	148.9	219.5	163.9	131.0	110.4	97.17	84.98	75.21	70.20	63.53	57.97	53.27	50.39
P		48.63	188.5	125.1	93.85	76.15	65.52	56.17	48.94	45.44	40.71	36.84	33.62	31.73
Q			322.2	160.4	106.9	81.45	67.42	56.21	47.98	43.97	38.91	34.86	31.54	29.62
T				0.01	0.31	1.08	2.11	1.82	1.52	2.31	2.02	1.79	1.60	1.82
UP					0.60	1.61	2.81	2.27	1.82	2.70	2.30	2.01	1.78	2.00
UQ						2.62	3.90	2.82	2.12	3.11	2.58	2.20	1.92	2.16
UT							5.14	2.90	1.94	3.21	2.55	2.12	1.81	2.08
PQ								0.68	0.36	2.53	1.89	1.51	1.25	1.63
PT									0.04	3.44	2.29	1.71	1.37	1.79
QT										6.84	3.41	2.27	1.70	2.14
PQT											0.01	0.01	0.02	0.97
UPT												0.02	0.02	1.28
UQT													0.03	1.92
UPQ														3.81

	U	Q	T	PU	PQ	PT	UQ	UT	QT	UQT	PUT	PQT	PUQ	PUQT
P	1.06	24.90	126.1	94.20	78.32	65.10	55.54	49.32	43.65	39.68	35.91	33.88	31.13	29.56
U		48.63	188.5	125.1	97.57	77.85	64.58	56.17	48.94	43.94	39.37	36.84	33.62	31.73
Q			322.2	160.4	111.4	83.38	66.40	56.21	47.98	42.44	37.56	34.86	31.54	29.62
T				0.01	3.06	2.13	1.59	1.82	1.52	1.60	1.40	1.79	1.60	1.82
PU					6.11	3.18	2.11	2.27	1.82	1.86	1.60	2.01	1.78	2.00
PQ						0.27	0.14	0.99	0.75	1.01	0.85	1.41	1.23	1.53
PT							0.00	1.35	0.91	1.20	0.96	1.60	1.37	1.69
UQ								2.70	1.37	1.60	1.20	1.92	1.59	1.93
UT									0.04	1.04	0.71	1.71	1.37	1.79
QT										2.04	1.04	2.27	1.70	2.14
UQT											0.04	2.37	1.58	2.15
PUT												4.69	2.35	2.86
PQT													0.03	1.92
PUQ														3.81

	Q	U	T	PQ	PU	PT	QU	QT	UT	QUT	PQT	PUT	PQU	PQUT
P	46.81	24.90	126.1	97.86	78.32	65.10	55.54	48.49	43.65	39.68	37.13	33.88	31.13	29.56
Q		3.08	162.8	112.5	84.47	67.41	55.92	47.83	42.42	38.12	35.37	32.01	29.21	27.62
U			322.2	167.0	111.4	83.38	66.40	55.22	47.98	42.44	38.90	34.86	31.54	29.62
T				5.42	3.06	2.13	1.59	1.33	1.52	1.60	2.01	1.79	1.60	1.82
PQ					0.71	0.49	0.33	0.33	0.74	0.96	1.51	1.32	1.17	1.45
PU						0.27	0.14	0.20	0.75	1.01	1.65	1.41	1.23	1.53
PT							0.00	0.17	0.91	1.20	1.92	1.60	1.37	1.69
QU								0.33	1.37	1.60	2.40	1.92	1.59	1.93
QT									2.40	2.23	3.09	2.31	1.85	2.19
UT										2.04	3.40	2.27	1.70	2.14
QUT											4.73	2.37	1.58	2.15
PQT												0.02	0.03	1.29
PUT													0.03	1.92
PQU														3.81

Table 7.2: Selected results of GLM tests for the pre-bloom CIS region. The highlighted numbers are greater than the critical F value.

	Q	P	T	UQ	UP	UT	QP	QT	PT	QPT	UQT	UPT	UQP	UQPT
U	2.62	2.40	99.33	74.47	59.40	49.34	42.39	37.00	33.00	29.97	27.14	24.78	23.14	21.39
Q		2.18	147.5	98.34	73.53	58.64	48.98	41.88	36.78	32.99	29.58	26.77	24.83	22.82
P			292.7	146.3	97.25	72.70	58.30	48.47	41.69	36.81	32.60	29.21	26.87	24.53
T				0.50	0.33	0.26	0.41	0.37	0.48	0.66	0.59	0.52	0.68	0.61
UQ					0.16	0.14	0.38	0.34	0.48	0.69	0.60	0.52	0.70	0.63
UP						0.13	0.50	0.41	0.56	0.80	0.67	0.57	0.77	0.68
UT							0.86	0.55	0.70	0.97	0.78	0.65	0.86	0.75
QP								0.23	0.63	1.00	0.76	0.61	0.86	0.73
QT									1.02	1.38	0.94	0.70	0.98	0.82
PT										1.75	0.90	0.60	0.97	0.78
QPT											0.06	0.03	0.72	0.54
UQT												0.00	1.05	0.70
UPT													2.10	1.04
UQP														0.00

	Q	P	U	TQ	TP	TU	QP	QU	PU	QPU	TQU	TPU	TQP	TQPU
T	1.58	1.16	4.03	3.12	2.73	2.26	1.96	1.82	1.65	1.69	1.54	1.41	1.44	1.33
Q		0.75	5.25	3.63	3.01	2.40	2.02	1.85	1.66	1.71	1.54	1.40	1.43	1.31
P			9.73	5.06	3.76	2.81	2.27	2.04	1.79	1.83	1.63	1.47	1.49	1.36
U				0.41	0.78	0.52	0.43	0.52	0.48	0.71	0.63	0.56	0.68	0.61
TQ					1.16	0.58	0.44	0.54	0.50	0.76	0.66	0.58	0.71	0.64
TP						0.00	0.08	0.34	0.34	0.68	0.58	0.50	0.65	0.58
TU							0.15	0.51	0.45	0.85	0.69	0.59	0.75	0.65
QP								0.88	0.59	1.08	0.83	0.68	0.85	0.72
QU									0.32	1.19	0.81	0.63	0.84	0.70
PU										2.06	1.06	0.73	0.97	0.78
QPU											0.07	0.08	0.62	0.46
TQU												0.08	0.89	0.59
TPU													1.70	0.85
TQP														0.00

	U	P	Q	TU	TP	TQ	UP	UQ	PQ	UPQ	TUQ	TPQ	TUP	TUPQ
T	10.65	5.68	4.03	3.01	2.72	2.26	2.01	1.80	1.65	1.69	1.54	1.54	1.44	1.33
U		0.81	0.77	0.52	0.77	0.62	0.61	0.57	0.55	0.72	0.65	0.73	0.69	0.64
P			0.74	0.38	0.76	0.58	0.57	0.53	0.52	0.71	0.64	0.72	0.68	0.62
Q				0.01	0.78	0.52	0.53	0.49	0.48	0.71	0.63	0.72	0.68	0.61
TU					1.54	0.78	0.70	0.61	0.58	0.82	0.71	0.81	0.75	0.68
TP						0.02	0.28	0.30	0.34	0.68	0.58	0.71	0.66	0.58
TQ							0.54	0.44	0.45	0.85	0.69	0.82	0.75	0.65
UP								0.34	0.40	0.95	0.73	0.88	0.78	0.67
UQ									0.46	1.26	0.86	1.01	0.87	0.72
PQ										2.06	1.06	1.20	0.97	0.78
UPQ											0.07	0.77	0.62	0.46
TUQ												1.46	0.89	0.59
TPQ													0.32	0.16
TUP														0.00

	P	U	T	QP	QU	QT	PU	PT	UT	PUT	QPT	QUT	QPU	QPUT
Q	2.84	5.86	101.8	76.31	61.13	50.81	43.52	38.21	33.84	30.36	27.81	25.40	23.72	21.93
P		8.86	151.2	100.7	75.63	60.36	50.26	43.23	37.68	33.39	30.29	27.43	25.43	23.38
U			292.7	146.2	97.61	73.03	58.38	48.83	41.69	36.37	32.58	29.21	26.87	24.53
T				0.41	0.57	0.46	0.46	0.57	0.48	0.43	0.58	0.52	0.68	0.61
QP					0.74	0.48	0.47	0.61	0.50	0.44	0.60	0.53	0.71	0.64
QU						0.23	0.34	0.57	0.44	0.38	0.58	0.51	0.71	0.63
QT							0.46	0.74	0.51	0.42	0.65	0.55	0.78	0.68
PU								1.03	0.54	0.41	0.70	0.57	0.83	0.71
PT									0.05	0.10	0.60	0.46	0.79	0.66
UT										0.15	0.87	0.60	0.97	0.78
PUT											1.60	0.82	1.25	0.93
QPT												0.06	1.08	0.72
QUT													2.10	1.04
QPU														0.00

Table 7.3: Selected results of GLM tests for the post-bloom CIS region. The highlighted numbers are greater than the critical F value.

	U	T	Q	PU	PT	PQ	UT	UQ	TQ	UTQ	PUQ	PTQ	PUT	PUTQ
P	34.07	162.1	152.4	125.1	102.6	90.83	77.51	67.96	60.58	54.28	49.42	46.62	43.17	39.95
U		289.9	207.4	151.8	116.8	99.42	82.48	70.86	62.20	55.04	49.62	46.46	42.73	39.32
T			54.85	36.54	26.28	23.08	18.39	15.50	13.46	11.73	10.53	10.18	9.37	8.58
Q				14.82	9.82	10.22	7.63	6.31	5.46	4.66	4.20	4.38	4.07	3.70
PU					4.57	7.48	4.97	3.99	3.42	2.84	2.57	2.95	2.75	2.49
PT						10.19	5.08	3.73	3.09	2.47	2.21	2.68	2.49	2.23
PQ							0.02	0.53	0.74	0.56	0.64	1.41	1.38	1.23
UT								1.04	1.10	0.74	0.79	1.68	1.60	1.40
UQ									1.16	0.59	0.71	1.84	1.71	1.46
TQ										0.02	0.49	2.06	1.85	1.52
UTQ											0.96	3.09	2.46	1.89
PUQ												5.20	3.20	2.20
PTQ													1.19	0.71
PUT														0.23

	Q	U	T	PQ	PU	PT	QU	QT	UT	QUT	PQT	PUT	PQU	PQUT
P	80.19	76.17	152.4	118.3	109.1	90.83	78.02	68.47	60.58	54.28	50.74	46.51	43.17	39.95
Q		63.09	182.8	126.5	110.5	88.37	73.84	63.51	55.31	48.95	45.39	41.28	38.07	35.03
U			300.8	156.6	123.0	92.24	74.02	61.93	52.84	46.03	42.25	38.05	34.83	31.83
T				5.89	15.09	10.22	7.93	6.58	5.46	4.66	4.79	4.33	4.07	3.70
PQ					23.68	12.09	8.41	6.61	5.26	4.37	4.54	4.06	3.79	3.42
PU						0.54	0.80	0.92	0.69	0.55	1.32	1.23	1.27	1.15
PT							1.05	1.11	0.74	0.56	1.47	1.34	1.38	1.23
QU								1.18	0.59	0.39	1.57	1.40	1.43	1.25
QT									0.00	0.01	1.70	1.45	1.48	1.27
UT										0.02	2.55	1.94	1.85	1.52
QUT											5.08	2.89	2.46	1.89
PQT												0.72	1.14	0.84
PUT													1.57	0.89
PQU														0.23

	U	P	T	QU	QP	QT	UP	UT	PT	UPT	QUT	QPT	QUP	QUPT
Q	128.7	141.3	197.0	149.4	121.5	102.9	100.0	87.18	77.25	69.30	62.72	59.17	54.89	50.80
U		124.3	214.3	144.6	110.5	90.09	86.13	73.51	64.13	56.83	50.92	47.77	44.04	40.52
P			300.8	152.6	104.0	79.75	74.50	61.82	52.84	46.10	40.80	38.05	34.83	31.83
T				2.49	2.96	3.14	8.18	6.53	5.46	4.70	4.10	4.33	4.07	3.70
QU					3.41	3.44	9.97	7.46	6.00	5.02	4.29	4.52	4.20	3.79
QP						3.44	13.07	8.69	6.56	5.28	4.38	4.63	4.25	3.79
QT							22.37	11.16	7.50	5.66	4.52	4.77	4.32	3.79
UP								0.06	0.15	0.18	0.15	1.22	1.28	1.13
UT									0.24	0.24	0.17	1.51	1.53	1.31
PT										0.24	0.14	1.94	1.85	1.52
UPT											0.05	2.78	2.38	1.84
QUT												5.52	3.55	2.43
QPT													1.57	0.89
QUP														0.23

	P	Q	U	TP	TQ	TU	PQ	PU	QU	PQU	TPU	TQU	TPQ	TPQU
T	90.14	75.78	56.72	46.11	37.86	31.57	27.36	27.96	24.82	22.43	20.40	18.61	18.02	16.69
P		44.08	28.81	22.70	17.96	14.45	12.34	13.89	12.17	10.92	9.86	8.92	8.85	8.16
Q			11.47	10.19	7.89	6.04	5.17	7.56	6.52	5.82	5.23	4.68	4.88	4.48
U				8.52	5.85	4.08	3.46	6.49	5.46	4.82	4.27	3.78	4.07	3.70
TP					3.09	1.82	1.75	5.80	4.70	4.08	3.57	3.11	3.48	3.14
TQ						0.55	1.07	6.63	5.05	4.23	3.61	3.08	3.49	3.11
TU							1.59	9.64	6.54	5.14	4.22	3.50	3.90	3.43
PQ								17.58	8.95	6.29	4.84	3.86	4.26	3.67
PU									0.38	0.67	0.63	0.47	1.55	1.33
QU										0.96	0.76	0.50	1.85	1.52
PQU											0.55	0.28	2.14	1.65
TPU												0.00	2.92	2.02
TQU													5.85	3.03
TPQ														0.23

Table 7.4: Selected results of GLM tests for the pre-bloom RR region. The highlighted numbers are greater than the critical F value.

	U	Q	T	PU	PQ	PT	UQ	UT	QT	UQT	PUT	PQT	PUQ	PUQT
P	2.00	1.16	89.11	68.15	54.52	45.29	39.43	36.10	32.06	30.84	28.00	25.65	24.48	23.96
U		0.33	132.6	90.18	67.64	53.94	45.65	40.95	35.81	34.02	30.58	27.79	26.33	25.63
Q			264.9	135.1	90.07	67.34	54.71	47.72	40.87	38.23	33.94	30.53	28.69	27.73
T				3.13	1.82	1.24	1.58	2.64	2.27	3.43	3.04	2.75	3.04	3.59
PU					0.51	0.30	1.06	2.50	2.08	3.45	3.00	2.68	3.01	3.61
PQ						0.09	1.34	3.17	2.48	4.03	3.42	2.99	3.32	3.95
PT							2.59	4.70	3.27	5.02	4.08	3.47	3.78	4.43
UQ								6.76	3.59	5.78	4.42	3.62	3.94	4.66
UT									0.43	5.19	3.57	2.79	3.32	4.22
QT										9.94	5.14	3.57	4.04	4.98
UQT											0.37	0.41	2.04	3.64
PUT												0.46	2.87	4.72
PQT													5.27	6.84
PUQ														8.27

	P	Q	U	TP	TQ	TU	PQ	PU	QU	PQU	TPU	TQU	TPQ	TPQU
T	3.02	1.93	2.36	2.05	1.75	2.22	1.97	2.06	2.32	2.11	2.11	3.16	2.92	3.38
P		0.86	2.03	1.72	1.43	2.05	1.79	1.92	2.22	2.00	2.01	3.16	2.90	3.39
Q			3.20	2.16	1.62	2.35	1.97	2.09	2.42	2.14	2.14	3.38	3.08	3.59
U				1.11	0.83	2.05	1.65	1.86	2.27	1.98	1.99	3.37	3.04	3.59
TP					0.56	2.51	1.83	2.04	2.49	2.12	2.12	3.64	3.25	3.83
TQ						4.46	2.46	2.54	2.97	2.43	2.37	4.07	3.58	4.19
TU							0.48	1.56	2.45	1.91	1.94	3.96	3.41	4.10
PQ								2.65	3.44	2.38	2.30	4.65	3.89	4.61
PU									4.19	2.24	2.17	5.11	4.11	4.90
QU										0.29	1.16	5.34	4.04	4.98
PQU											2.02	7.86	5.28	6.14
TPU												13.60	6.87	7.47
TQU													0.18	4.23
TPQ														8.27

	U	P	Q	TU	TP	TQ	UP	UQ	PQ	UPQ	TUQ	TPQ	TUP	TUPQ
T	5.99	3.16	2.36	2.42	2.57	2.22	2.36	2.59	2.32	2.11	3.46	3.18	2.92	3.38
U		0.38	0.57	1.25	1.71	1.46	1.75	2.09	1.85	1.67	3.17	2.89	2.64	3.14
P			0.77	1.68	2.16	1.73	2.02	2.37	2.06	1.83	3.48	3.14	2.84	3.37
Q				2.59	2.84	2.05	2.33	2.69	2.27	1.98	3.81	3.39	3.04	3.59
TU					3.08	1.78	2.23	2.70	2.19	1.87	3.95	3.47	3.07	3.67
TP						0.47	1.80	2.55	1.96	1.62	4.06	3.49	3.05	3.70
TQ							3.12	3.58	2.45	1.91	4.77	3.99	3.41	4.10
UP								4.00	2.11	1.50	5.13	4.13	3.43	4.20
UQ									0.22	0.26	5.44	4.11	3.28	4.19
PQ										0.29	8.05	5.41	4.04	4.98
UPQ											15.79	7.96	5.28	6.14
TUQ												0.18	0.09	2.82
TPQ													0.00	4.14
TUP														8.27

	T	Q	P	UT	UQ	UP	TP	TQ	QP	TQP	UTP	UQP	UTQ	UTQP
U	272.8	136.5	90.36	68.82	54.94	48.25	41.89	36.63	32.49	29.39	26.88	24.62	24.79	24.26
T		0.69	0.57	1.25	0.99	2.36	2.37	2.09	1.85	1.78	1.74	1.62	2.64	3.14
Q			0.46	1.53	1.09	2.78	2.70	2.32	2.01	1.92	1.86	1.71	2.81	3.34
P				2.59	1.40	3.55	3.25	2.69	2.27	2.12	2.03	1.84	3.04	3.59
UT					0.23	4.00	3.45	2.70	2.19	2.03	1.94	1.74	3.07	3.67
UQ						7.77	5.06	3.52	2.68	2.39	2.22	1.96	3.42	4.05
UP							2.32	1.38	0.99	1.05	1.11	0.99	2.75	3.51
TP								0.45	0.33	0.63	0.81	0.73	2.81	3.66
TQ									0.22	0.72	0.93	0.80	3.28	4.19
QP										1.23	1.29	0.99	4.04	4.98
TQP											1.35	0.88	4.96	5.89
UTP												0.41	6.74	7.38
UQP													13.04	10.84
UTQ														8.27

Table 7.5: Selected results of GLM tests for the post-bloom RR region. The highlighted numbers are greater than the critical F value.

	P	U	Q	TP	TU	TQ	PU	PQ	UQ	PUQ	TPQ	TUQ	TPU	TPUQ
T	180.97	140.39	102.48	76.39	64.50	53.45	47.77	60.42	53.65	48.04	43.42	39.71	36.59	34.30
P		77.79	46.32	30.69	25.42	20.23	18.17	27.12	23.75	21.02	18.81	17.09	15.67	14.68
U			10.32	5.14	5.69	4.26	4.53	12.89	11.12	9.69	8.58	7.74	7.07	6.67
Q				0.02	3.23	2.16	2.95	12.65	10.63	9.08	7.91	7.06	6.39	6.01
TP					6.43	3.24	3.93	15.81	12.75	10.59	9.04	7.94	7.10	6.61
TU						0.08	2.62	18.23	13.80	11.01	9.14	7.88	6.94	6.41
TQ							5.15	27.29	18.36	13.74	10.94	9.17	7.92	7.20
PU								47.87	24.20	16.10	12.02	9.69	8.14	7.28
PQ									0.64	0.40	0.30	0.34	0.39	0.63
UQ										0.16	0.13	0.25	0.33	0.63
PUQ											0.09	0.29	0.38	0.75
TPQ												0.49	0.53	0.96
TUQ													0.56	1.20
TPU														1.83

	U	Q	T	PU	PQ	PT	UQ	UT	QT	UQT	PUT	PQT	PUQ	PUQT
P	80.13	62.64	114.1	90.04	103.2	85.80	73.85	66.76	58.96	52.86	47.93	43.73	40.20	37.67
U		35.87	118.5	83.74	93.68	74.75	62.61	55.63	48.36	42.84	38.46	34.81	31.78	29.64
Q			194.7	103.7	105.9	79.30	63.80	55.23	47.03	41.02	36.38	32.60	29.52	27.37
T				6.29	28.23	18.90	14.51	12.83	10.63	9.12	8.01	7.11	6.39	6.01
PU					48.29	24.27	16.63	13.95	11.09	9.26	7.97	6.97	6.20	5.79
PQ						0.43	0.85	2.15	1.60	1.34	1.19	1.05	0.95	1.05
PT							1.27	3.01	1.99	1.57	1.35	1.15	1.03	1.13
UQ								4.72	2.35	1.67	1.36	1.13	0.99	1.11
UT									0.01	0.17	0.27	0.26	0.26	0.53
QT										0.33	0.40	0.34	0.33	0.63
UQT											0.46	0.35	0.33	0.70
PUT												0.23	0.26	0.79
PQT													0.29	1.06
PUQ														1.83

	P	Q	T	UP	UQ	UT	PQ	PT	QT	PQT	UPT	UQT	UPQ	UPQT
U	137.3	94.55	139.2	109.4	90.53	77.31	90.54	79.66	70.36	62.94	56.84	52.17	47.95	44.91
P		35.87	118.5	83.74	65.41	53.93	64.44	55.63	48.36	42.73	38.21	34.81	31.78	29.64
Q			194.7	103.7	72.31	56.05	65.76	55.23	47.03	40.91	36.13	32.60	29.52	27.37
T				6.29	5.54	4.96	15.62	12.83	10.63	9.06	7.88	7.11	6.39	6.01
UP					4.64	4.17	18.04	13.95	11.09	9.20	7.83	6.97	6.20	5.79
UQ						3.62	24.07	16.59	12.37	9.85	8.15	7.12	6.24	5.78
UT							43.52	22.58	14.96	11.16	8.87	7.55	6.48	5.93
PQ								1.49	0.75	0.52	0.38	0.50	0.46	0.66
PT									0.01	0.04	0.02	0.26	0.26	0.53
QT										0.06	0.03	0.34	0.33	0.63
PQT											0.00	0.48	0.42	0.77
UPT												0.96	0.62	1.03
UQT													0.29	1.06
UPQ														1.83

	P	U	T	QP	QU	QT	PU	PT	UT	PUT	PQT	QUT	QPU	QPUT
Q	45.40	62.58	114.1	129.1	104.1	86.28	73.56	64.29	58.94	52.70	47.62	43.71	40.18	37.65
P		79.46	144.2	148.0	111.9	89.05	73.82	63.21	57.12	50.44	45.12	41.10	37.52	34.97
U			194.7	158.9	107.1	79.84	63.54	52.93	47.03	40.89	36.13	32.60	29.52	27.37
T				55.94	28.99	19.22	14.37	11.59	10.63	9.05	7.88	7.11	6.39	6.01
QP					1.77	0.90	0.64	0.63	1.42	1.17	1.01	1.00	0.92	1.01
QU						0.03	0.08	0.26	1.32	1.05	0.88	0.89	0.81	0.93
QT							0.13	0.38	1.75	1.31	1.05	1.04	0.93	1.04
PU								0.62	2.56	1.70	1.28	1.22	1.06	1.17
PT									4.49	2.23	1.50	1.36	1.14	1.26
UT										0.00	0.03	0.34	0.33	0.63
PUT											0.06	0.51	0.43	0.79
PQT												0.96	0.62	1.03
QUT													0.29	1.06
QPU														1.83

Table 7.6: Selected results of GLM tests for the pre-bloom EG region. The highlighted numbers are greater than the critical F value.

	U	P	T	QU	QP	QT	UP	UT	PT	UPT	QUT	QPT	QUP	QUPT
Q	67.70	40.38	94.96	71.64	57.18	53.24	45.65	40.00	35.91	33.80	30.59	30.47	28.00	25.87
U		11.56	105.5	70.91	53.08	48.21	40.22	34.54	30.59	28.60	25.63	25.57	23.33	21.43
P			19888	100.2	66.68	56.99	45.64	38.12	33.08	30.49	26.99	26.72	24.17	22.05
T				1.28	0.79	5.45	4.25	3.55	3.28	3.79	3.31	4.38	3.92	3.55
QU					0.30	7.50	5.21	4.10	3.66	4.18	3.58	4.74	4.20	3.76
QP						14.68	7.65	5.35	4.50	4.96	4.12	5.37	4.68	4.14
QT							0.65	0.71	1.10	2.42	1.95	3.63	3.10	2.70
UP								0.77	1.32	3.01	2.27	4.21	3.50	2.99
UT									1.87	4.11	2.76	5.06	4.03	3.35
PT										6.31	3.18	6.08	4.54	3.62
UPT											0.08	5.81	3.86	2.89
QUT												11.54	5.75	3.83
QPT													0.02	0.03
QUP														0.03

	U	Q	T	PU	PQ	PT	UQ	UT	QT	UQT	PUT	PQT	PUQ	PUQT
P	63.00	33.32	89.95	67.14	53.61	45.97	39.53	34.64	34.13	30.58	29.11	29.04	26.68	24.65
U		3.27	101.1	67.13	50.27	41.58	34.81	29.90	29.41	26.03	24.67	24.65	22.49	20.66
Q			198.8	98.97	65.88	51.10	41.07	34.30	33.08	28.82	26.99	26.72	24.17	22.05
T				0.01	0.17	1.43	1.32	1.20	3.28	2.81	3.31	4.38	3.92	3.55
PU					0.33	2.14	1.75	1.50	3.93	3.27	3.78	4.92	4.36	3.91
PQ						3.95	2.46	1.88	4.83	3.86	4.35	5.57	4.85	4.30
PT							0.97	0.85	5.04	3.78	4.36	5.75	4.91	4.28
UQ								0.74	7.05	4.70	5.19	6.68	5.54	4.73
UT									13.32	6.66	6.66	8.14	6.48	5.38
QT										0.06	3.18	6.08	4.54	3.62
UQT											6.30	9.08	6.03	4.51
PUT												11.54	5.75	3.83
PQT													0.02	0.03
PUQ														0.03

	Q	P	T	UQ	UP	UT	QP	QT	PT	QPT	UQT	UPT	UQP	UQPT
U	0.00	5.78	70.40	53.19	42.46	35.61	30.45	30.22	27.19	27.36	24.76	23.44	21.53	19.90
Q		11.56	105.5	70.91	53.07	42.74	35.52	34.54	30.59	30.40	27.23	25.57	23.33	21.43
P			198.8	100.2	66.67	50.35	40.18	38.12	33.08	32.46	28.72	26.72	24.17	22.05
T				1.28	0.78	0.92	0.74	3.55	3.28	4.94	4.30	4.38	3.92	3.55
UQ					0.29	0.74	0.57	4.10	3.66	5.52	4.71	4.74	4.20	3.76
UP						1.19	0.71	5.36	4.50	6.56	5.45	5.37	4.68	4.14
UT							0.24	7.41	5.58	7.86	6.27	6.04	5.16	4.49
QP								14.56	8.24	10.39	7.77	7.19	5.97	5.10
QT									1.87	7.82	5.20	5.06	4.03	3.35
PT										13.66	6.81	6.08	4.54	3.62
QPT											0.03	2.20	1.47	1.10
UQT												4.38	2.19	1.46
UPT													0.02	0.03
UQP														0.03

	Q	T	U	PQ	PT	PU	QT	QU	TU	QTU	PQU	PTU	PQT	PQTU
P	3.03	97.60	89.95	67.33	55.40	45.97	43.73	38.41	34.13	30.58	28.04	26.57	26.68	24.65
Q		192.1	133.1	88.59	68.35	54.45	50.38	43.36	37.93	33.56	30.46	28.64	28.56	26.24
T			45.27	22.73	16.67	12.46	13.28	11.25	9.70	8.46	7.72	7.55	8.26	7.53
U				0.33	2.12	1.43	4.52	3.83	3.28	2.81	2.67	2.94	3.92	3.55
PQ					3.91	1.98	5.91	4.70	3.87	3.22	3.00	3.26	4.32	3.87
PT						0.07	6.79	4.90	3.80	3.04	2.81	3.13	4.30	3.81
PU							13.51	7.31	5.04	3.78	3.36	3.64	4.91	4.28
QT								1.09	0.82	0.57	0.83	1.63	3.32	2.84
QU									0.55	0.31	0.75	1.76	3.75	3.12
TU										0.06	0.84	2.15	4.54	3.62
QTU											1.63	3.20	6.03	4.51
PQU												4.74	8.18	5.44
PTU													11.37	5.68
PQT														0.03

Table 7.7: Selected results of GLM tests for the post-bloom EG region. The highlighted numbers are greater than the critical F value.

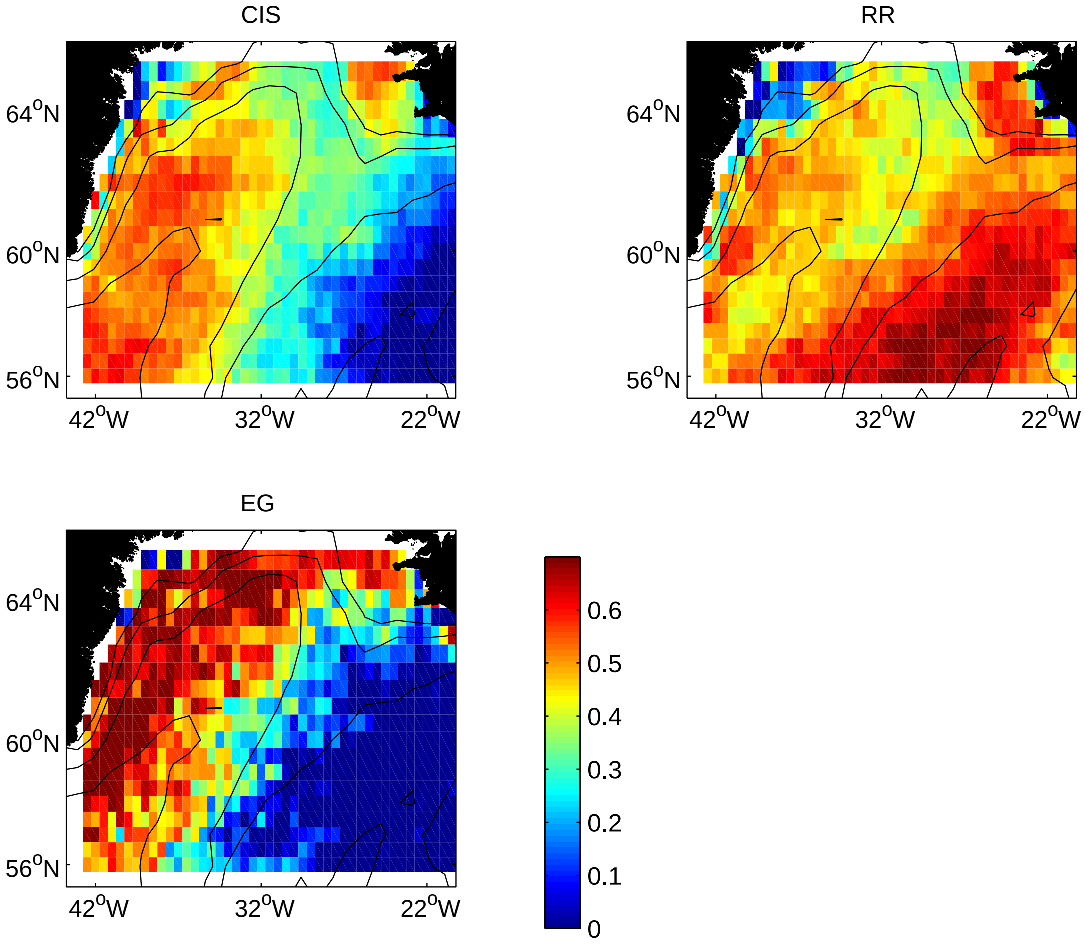

Figure 7.1: The correlation coefficient between chlorophyll predicted by the GLM and measured chlorophyll for all six years, 1998 - 2003. The GLM was parameterised for the three regions separately. The best-fit GLM for a particular region was then applied to the entire basin. (a) Parameterisation of the GLM based on the CIS region, (b) based on the RR region and (c) based on the EG region.

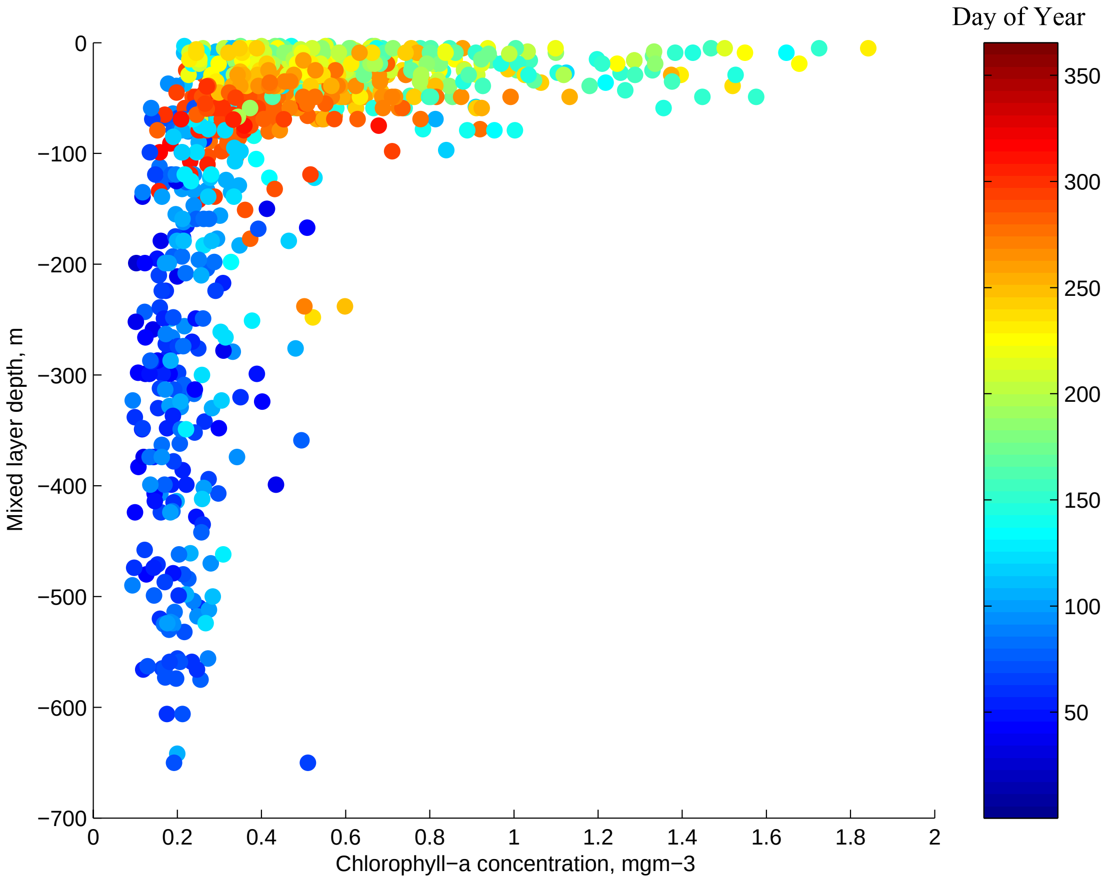

Figure 7.2: Mixed layer depth estimated from Argo float temperature profiles against coincident SeaWiFS chlorophyll for the entire Irminger Basin. The colour of the dots represents the day of the year on which the measurements were taken.

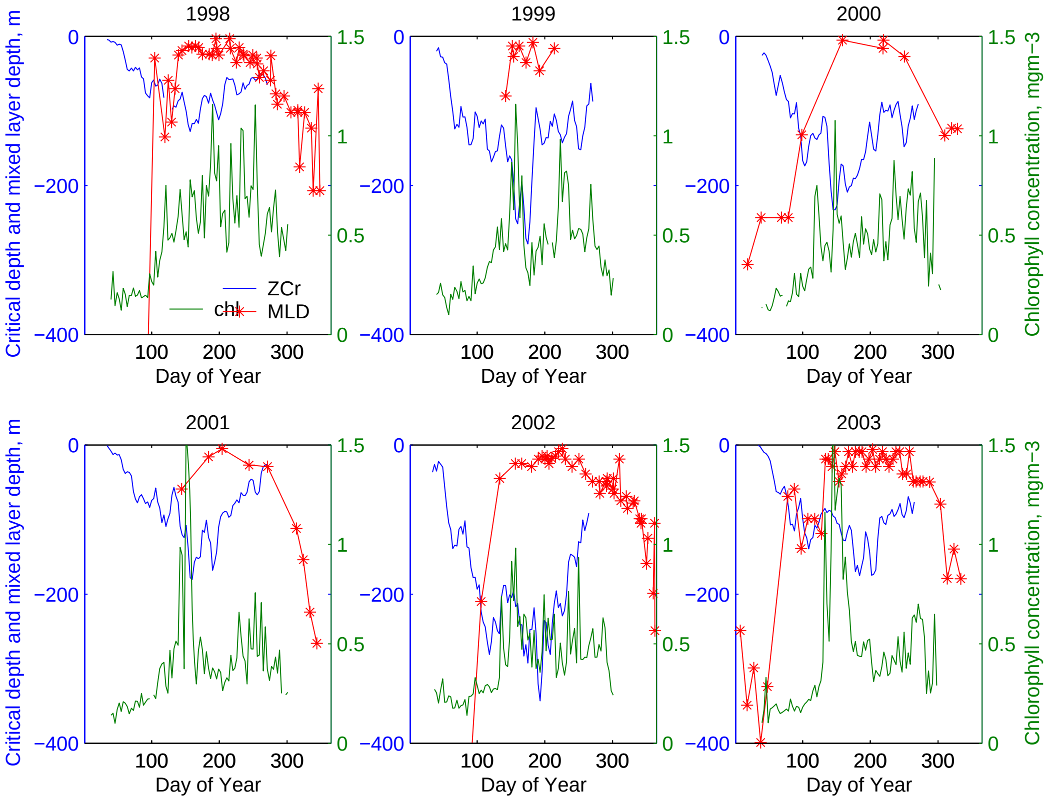

Figure 7.3: Critical depth (blue line), mixed layer depth from Argo floats (red line) and chlorophyll (green line) for the CIS region. Critical depth and chlorophyll are 3-day averages.

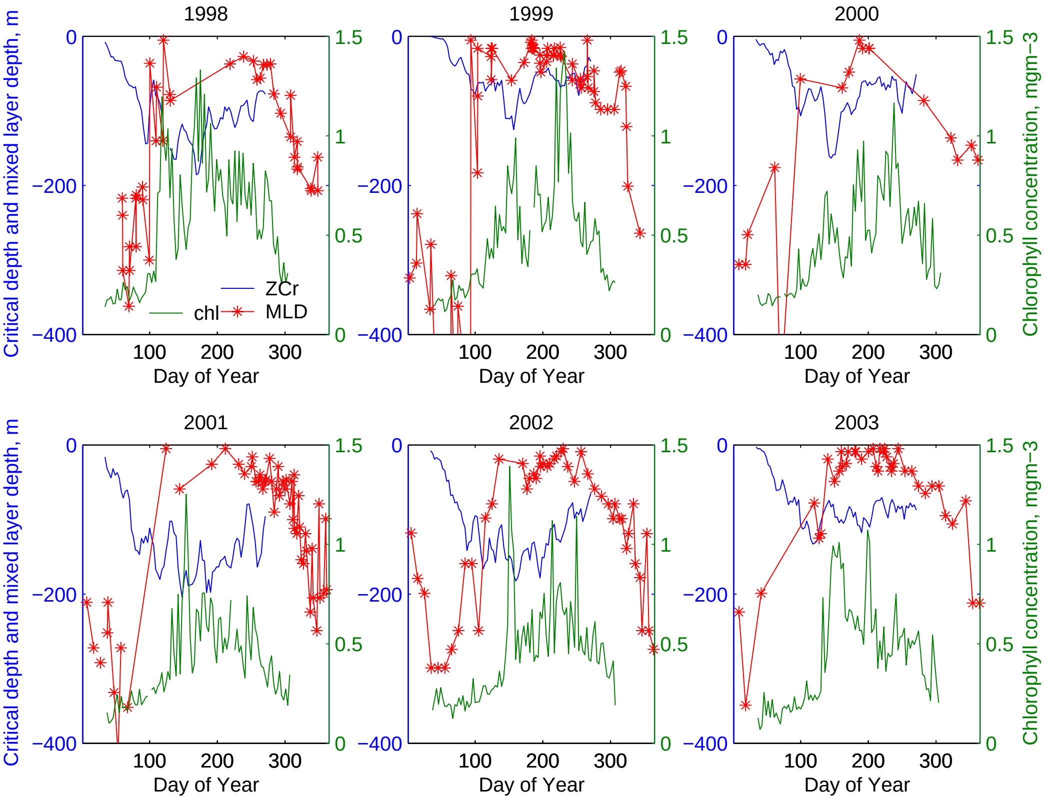

Figure 7.4: Critical depth (blue line), mixed layer depth from Argo floats (red line) and chlorophyll (green line) for the RR region. Critical depth and chlorophyll are 3-day averages.

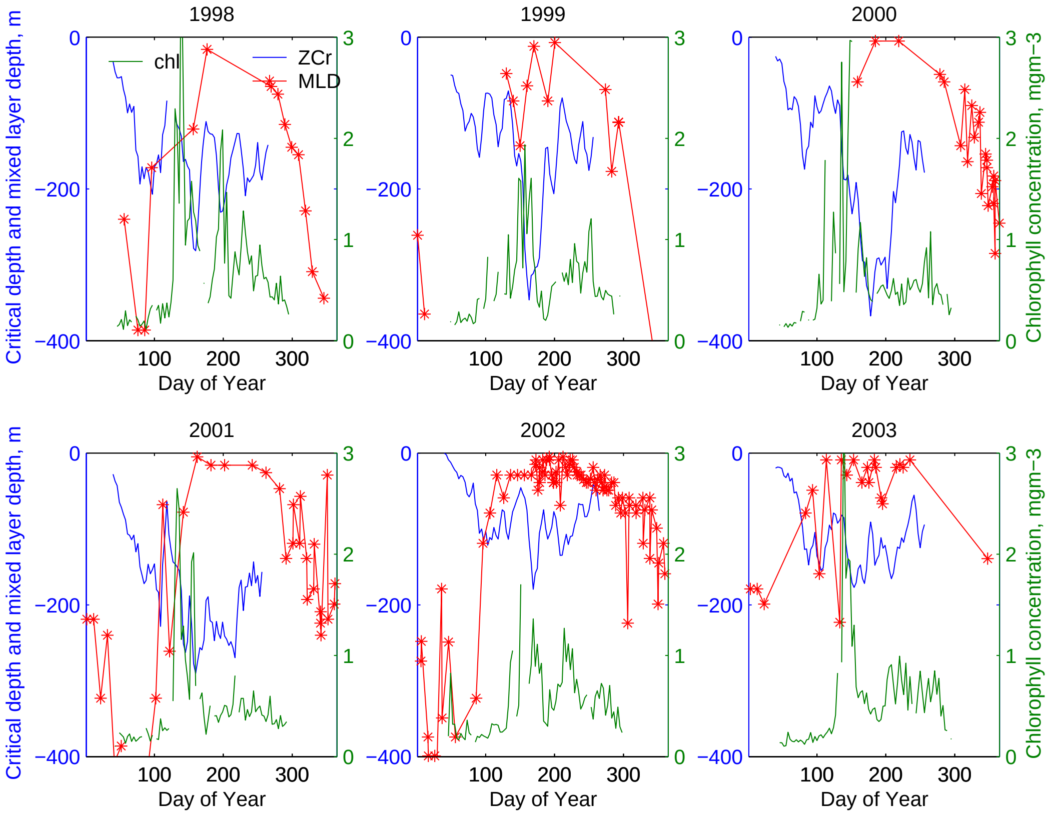

Figure 7.5: Critical depth (blue line), mixed layer depth from Argo floats (red line) and chlorophyll (green line) for the EG region. Critical depth and chlorophyll are 3-day averages.

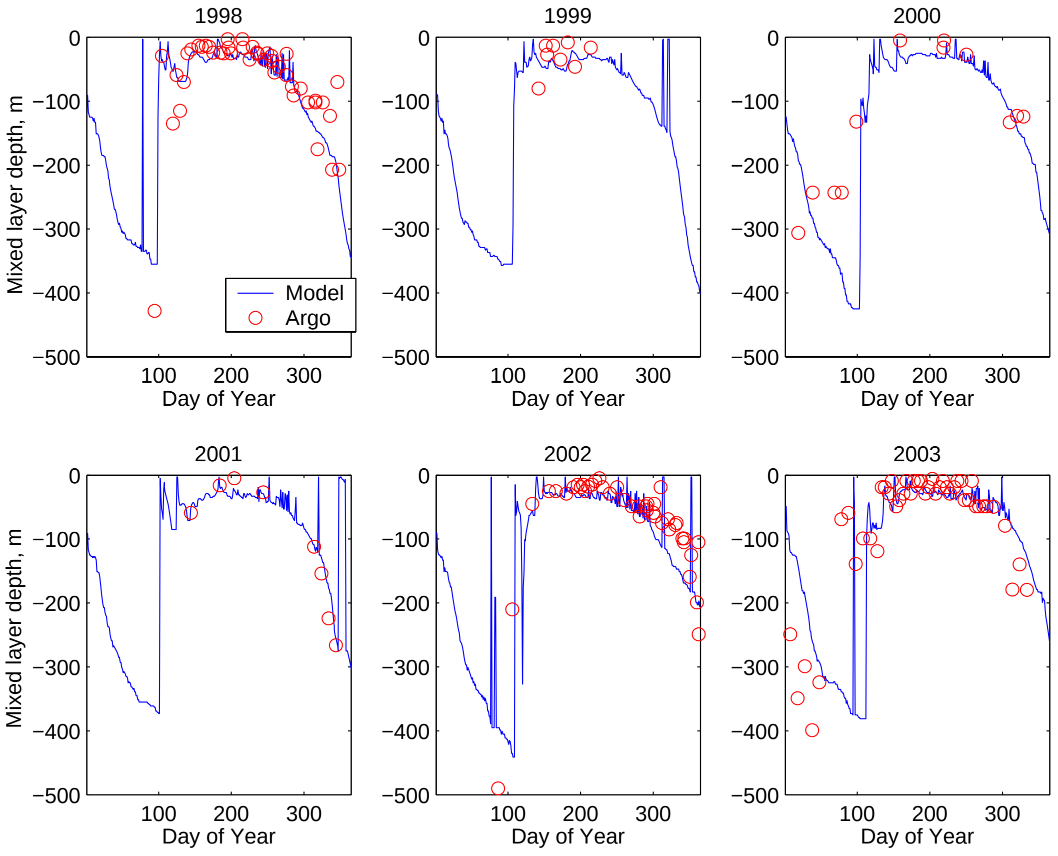

Figure 7.6: Mixed layer depth estimated from Argo float temperature (red dots) and 1-D modelled mixed layer (blue line) for the CIS region.

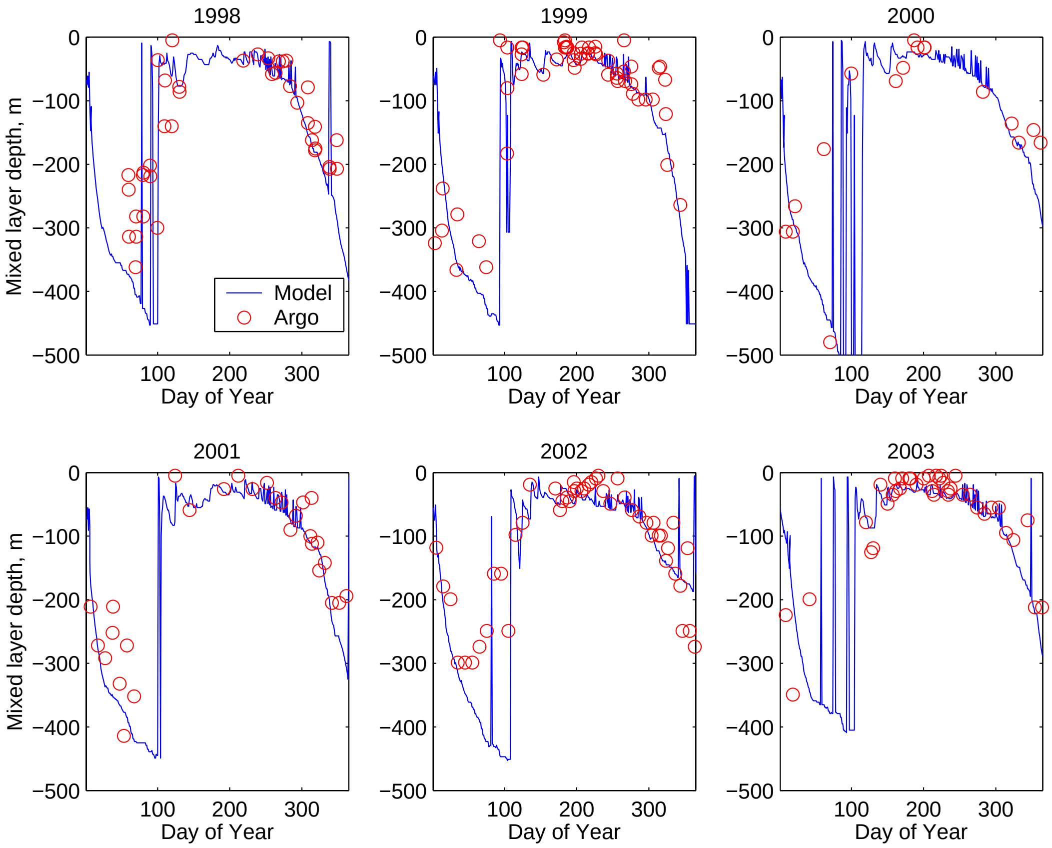

Figure 7.7: Mixed layer depth estimated from Argo float temperature (red dots) and 1-D modelled mixed layer (blue line) for the RR region.

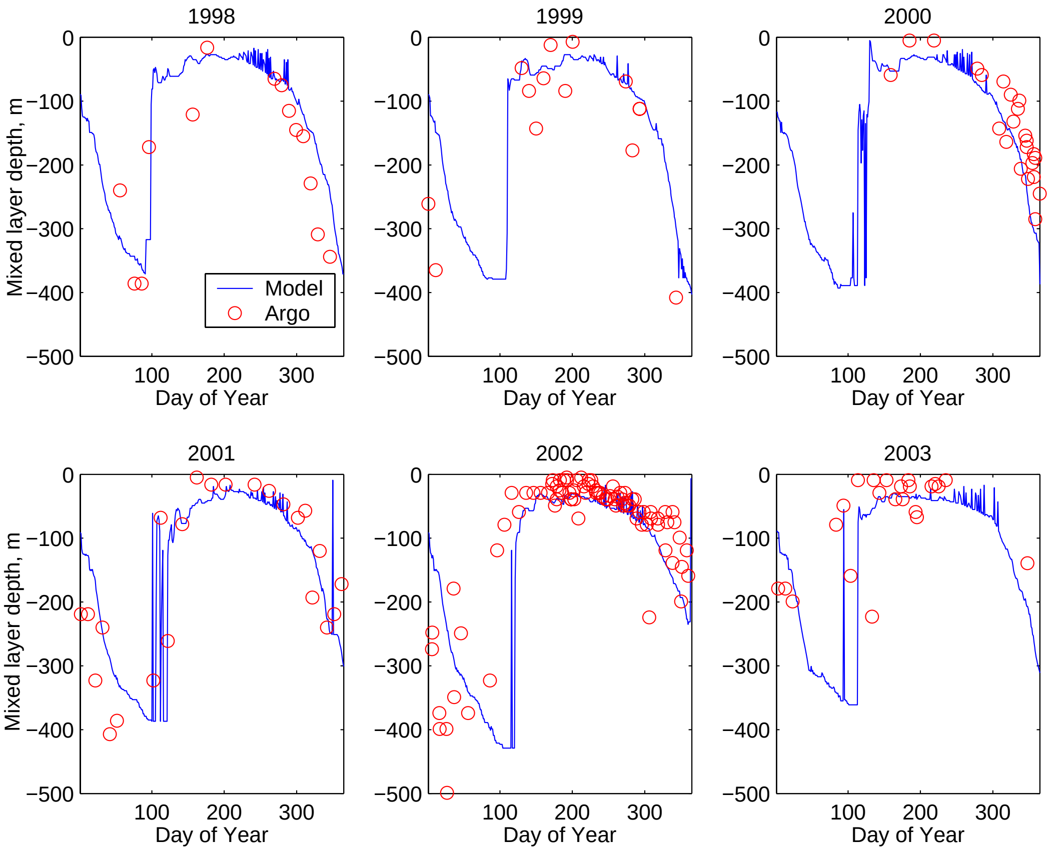

Figure 7.8: Mixed layer depth estimated from Argo float temperature (red dots) and 1-D modelled mixed layer (blue line) for the EG region.

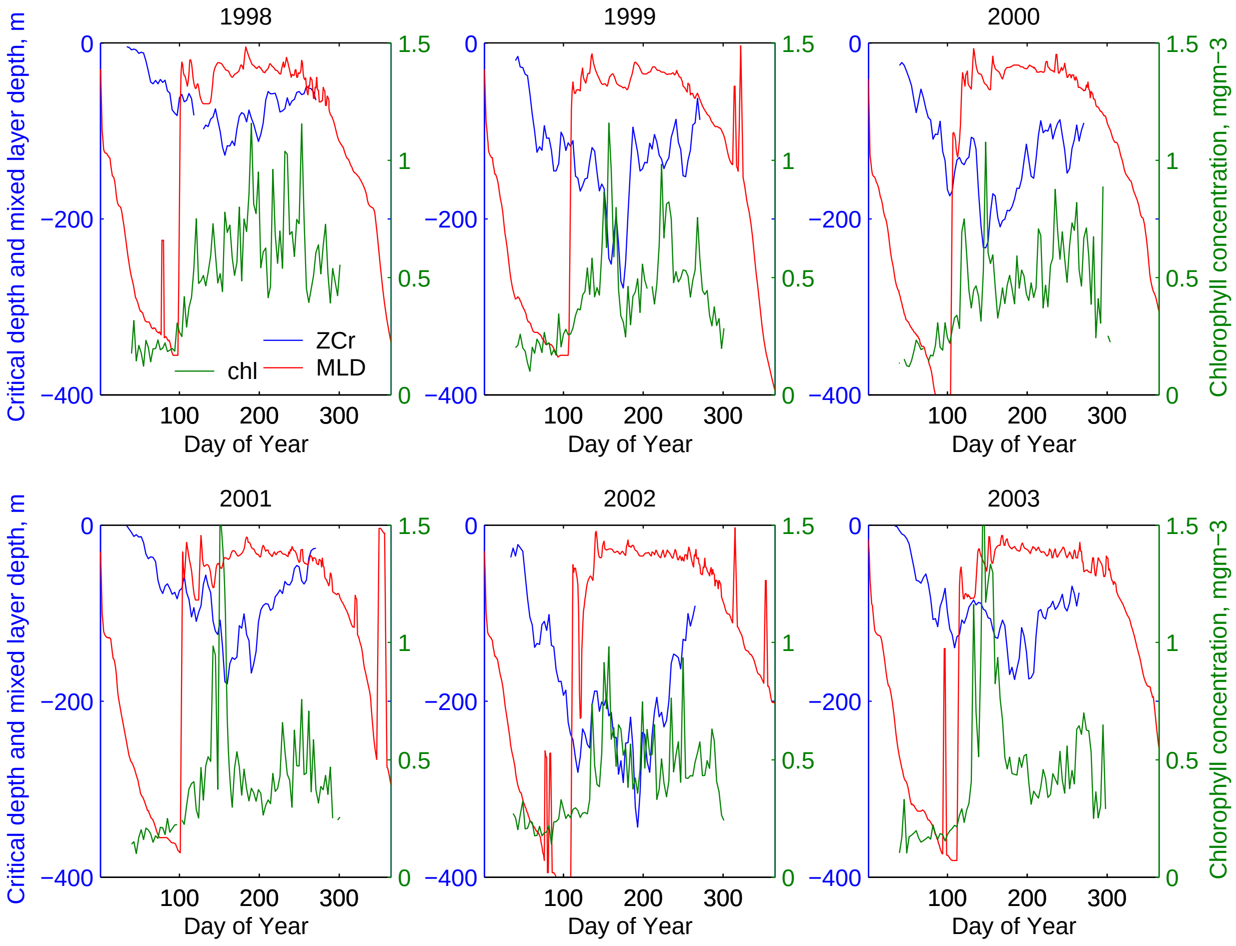

Figure 7.9: Critical depth (blue line), mixed layer depth from 1-D model (red line) and chlorophyll (green line) for the CIS region. Critical depth and chlorophyll are 3-day averages.

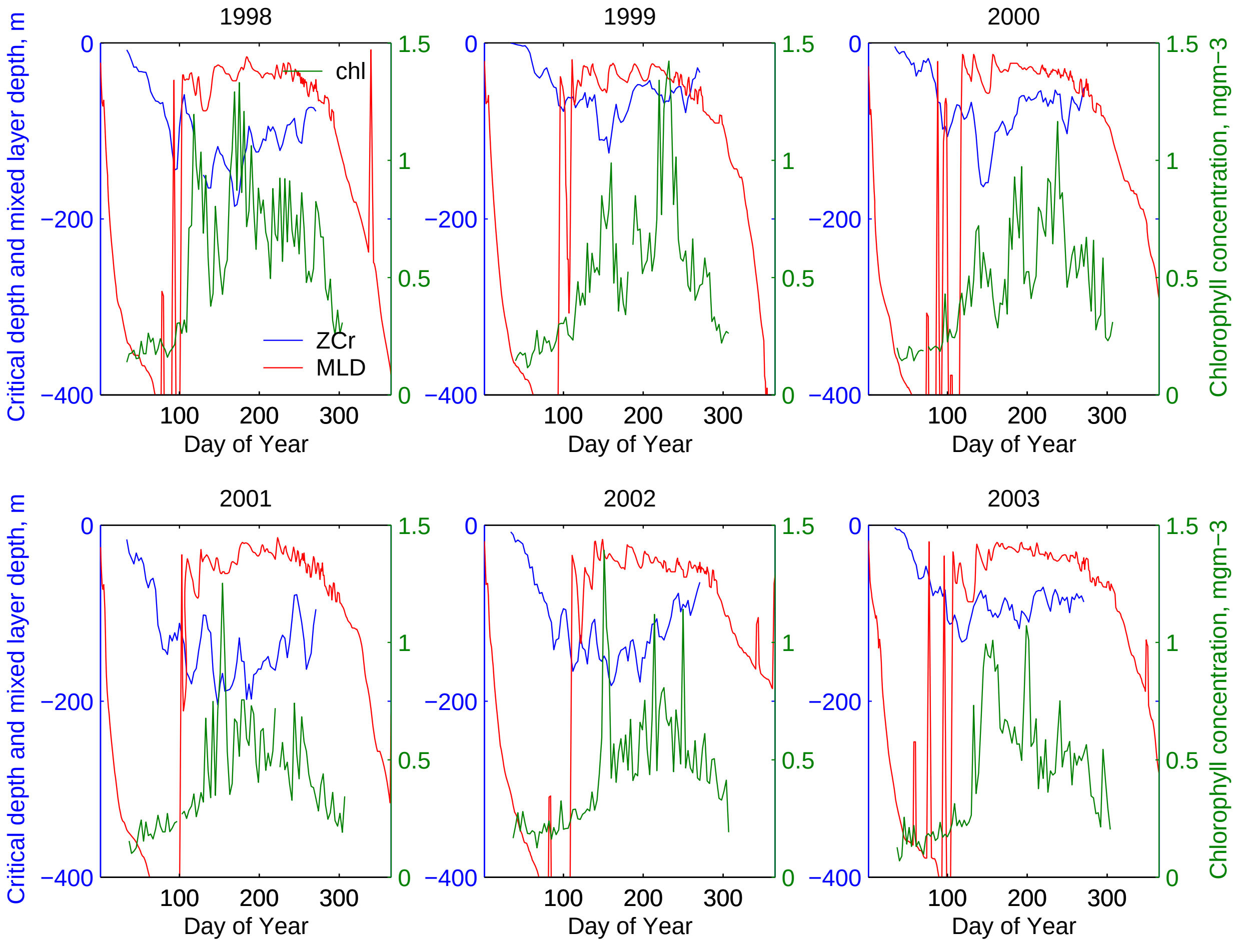

Figure 7.10: Critical depth (blue line), mixed layer depth from 1-D model (red line) and chlorophyll (green line) for the RR region. Critical depth and chlorophyll are 3-day averages.

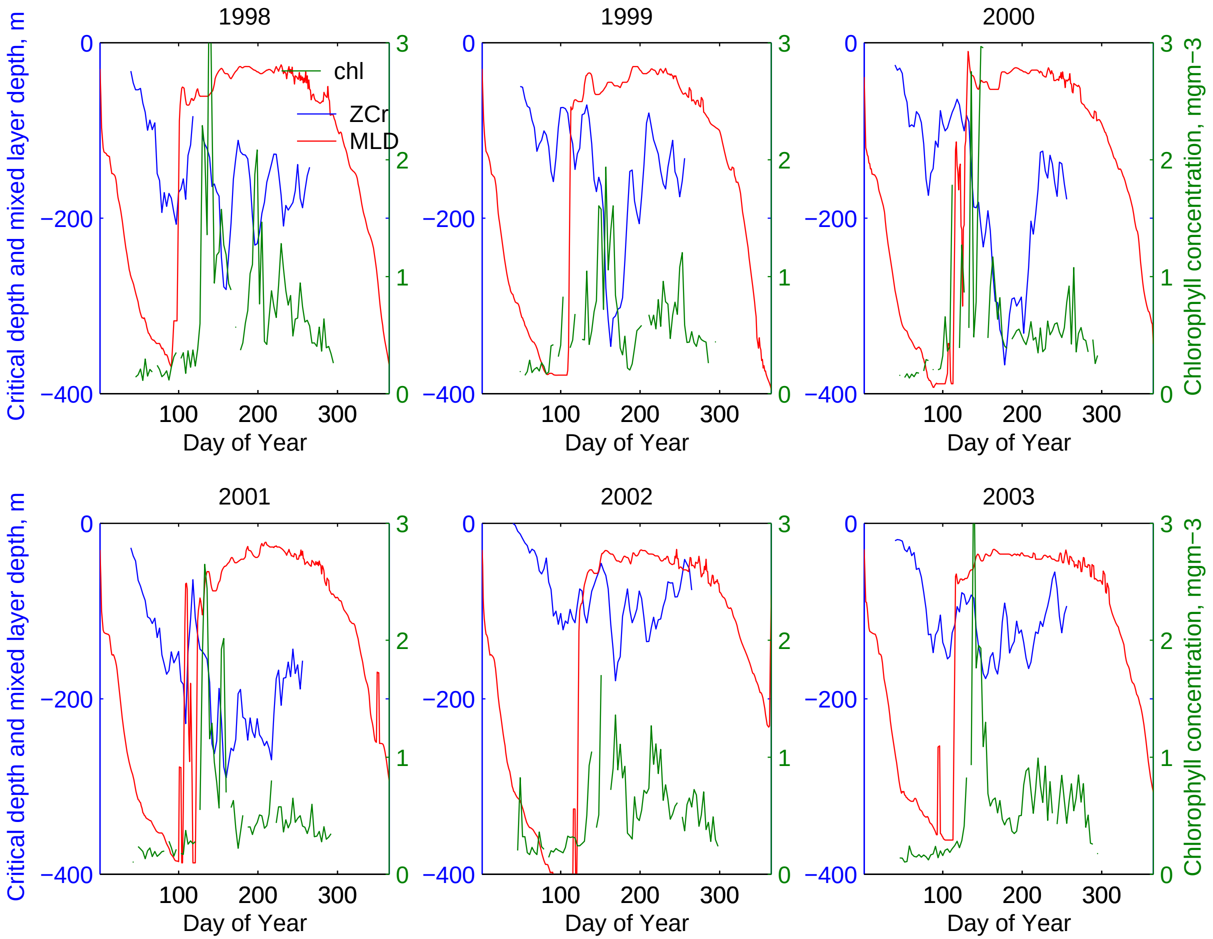

Figure 7.11: Critical depth (blue line), mixed layer depth from 1-D model (red line) and chlorophyll (green line) for the EG region. Critical depth and chlorophyll are 3-day averages.

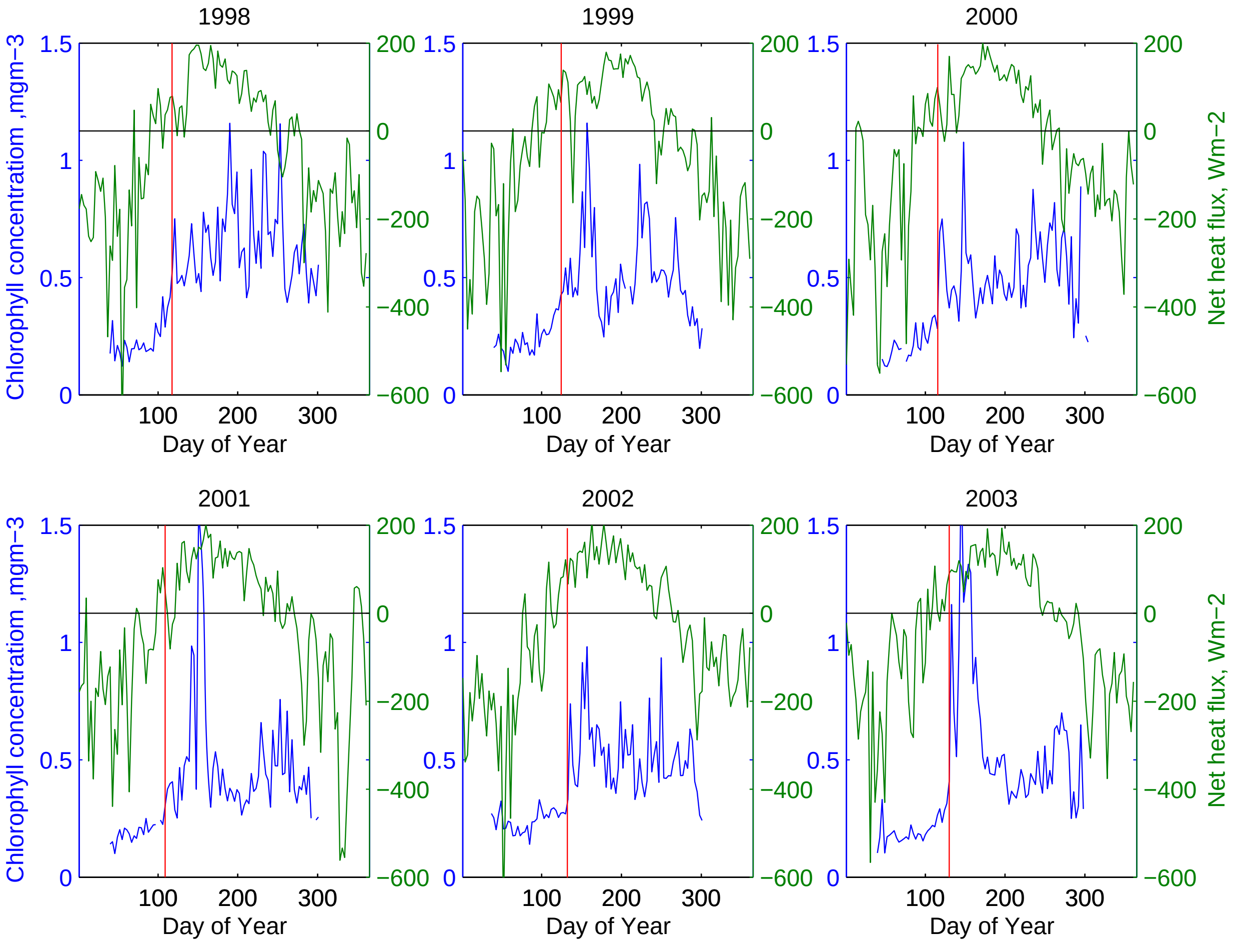

Figure 7.12: 3-day averages of net heat flux (green line) and SeaWiFS chlorophyll (blue line) for the CIS region. The red line marks the start of the spring bloom as estimated in Chapter 6.3.

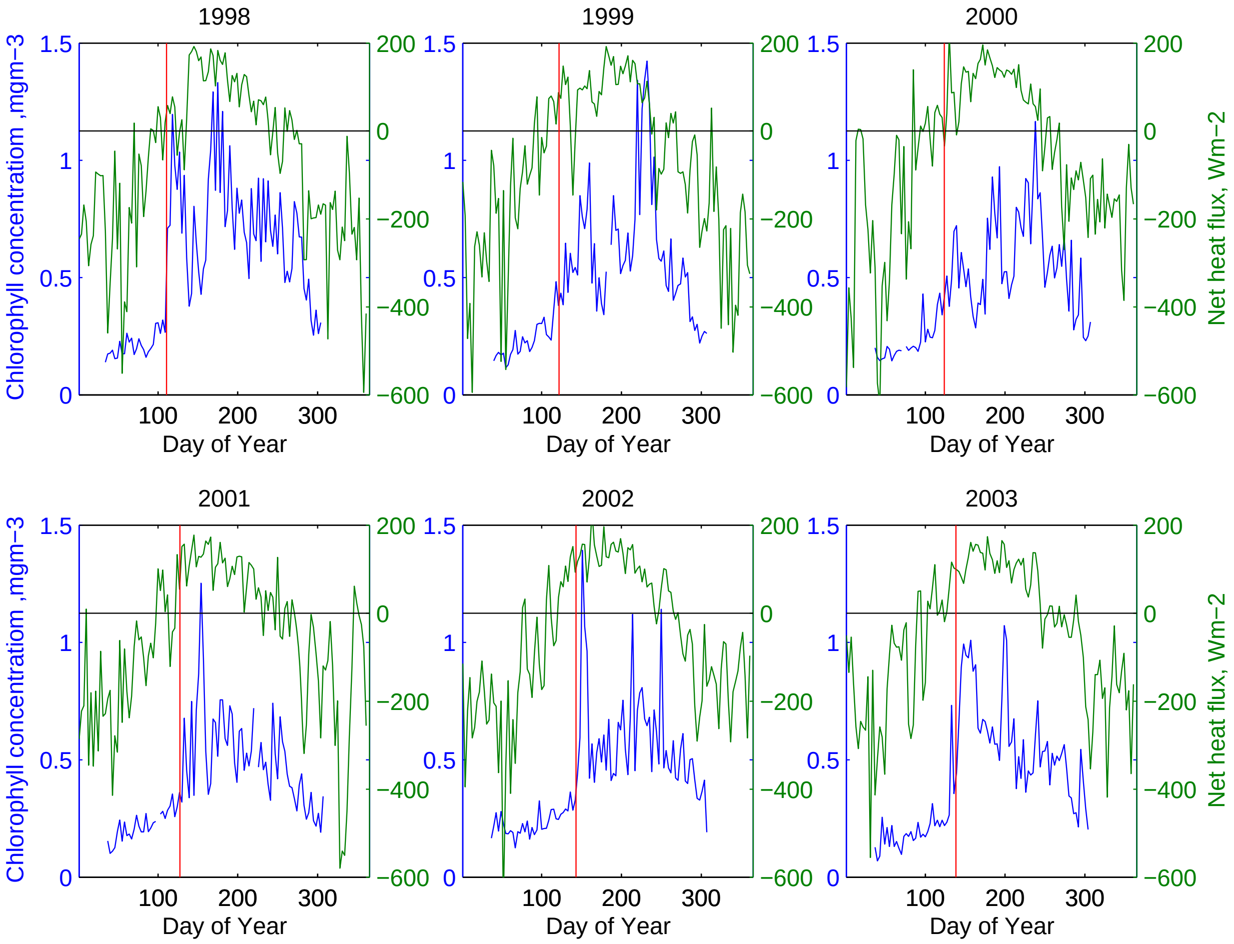

Figure 7.13: 3-day averages of net heat flux (green line) and SeaWiFS chlorophyll (blue line) for the RR region. The red line marks the start of the spring bloom as estimated in Chapter 6.3.

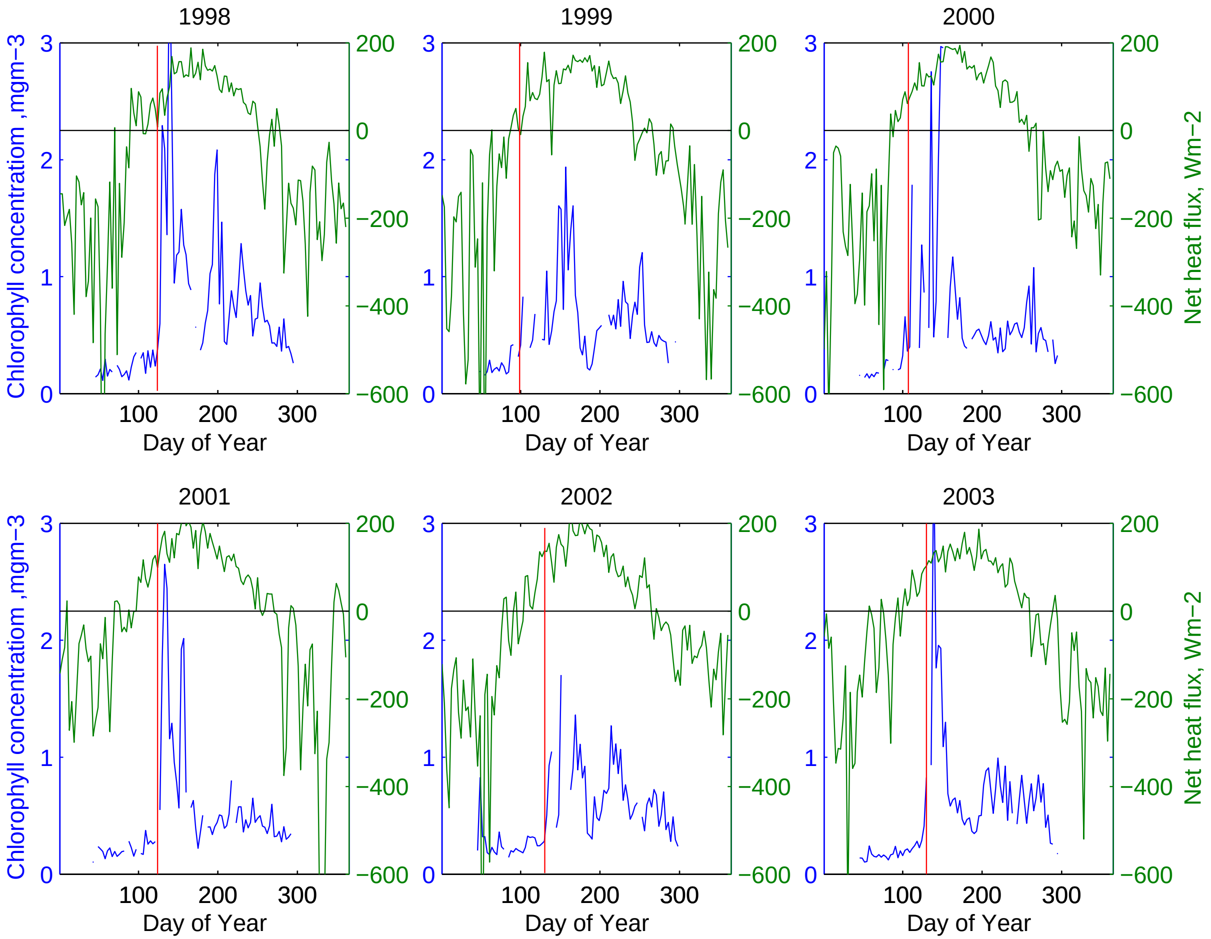

Figure 7.14: 3-day averages of net heat flux (green line) and SeaWiFS chlorophyll (blue line) for the EG region. The red line marks the start of the spring bloom as estimated in Chapter 6.3.

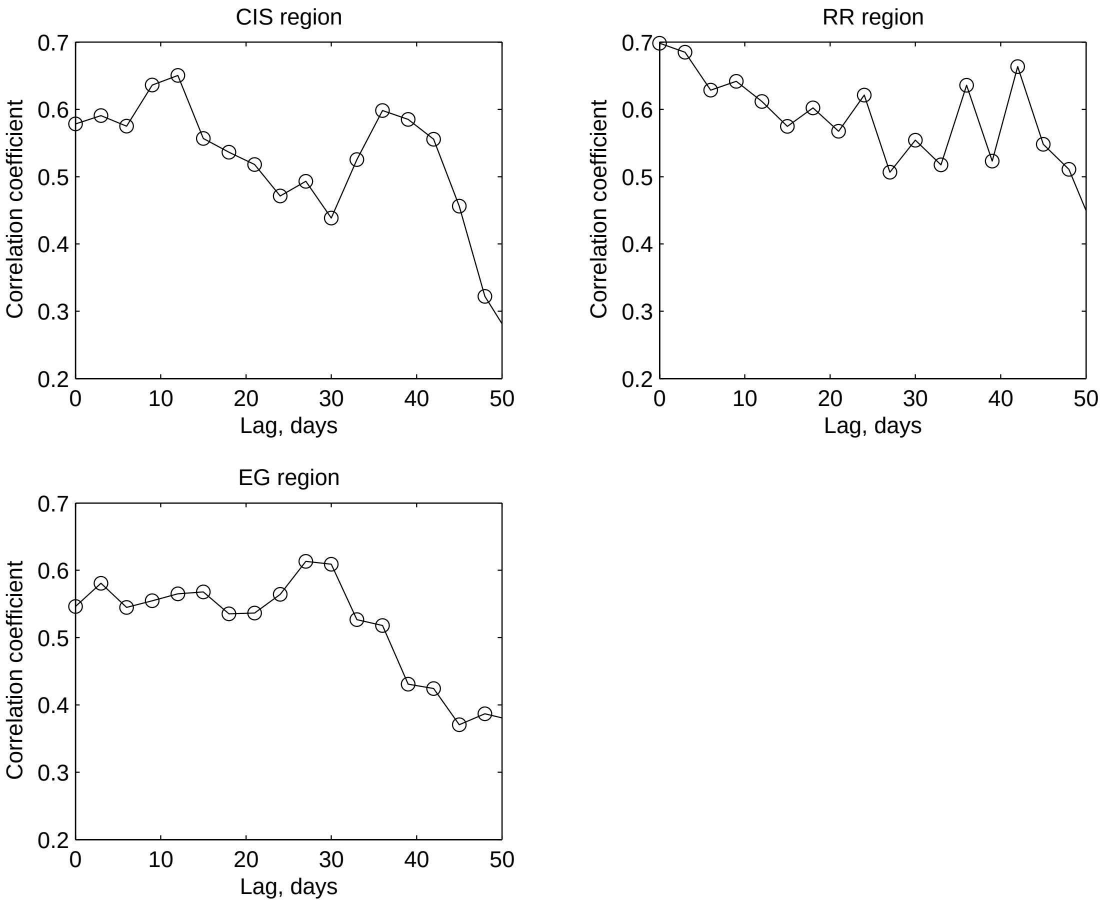

Figure 7.15: Lagged correlations between net heat flux and chlorophyll concentration for the CIS, RR and EG regions.

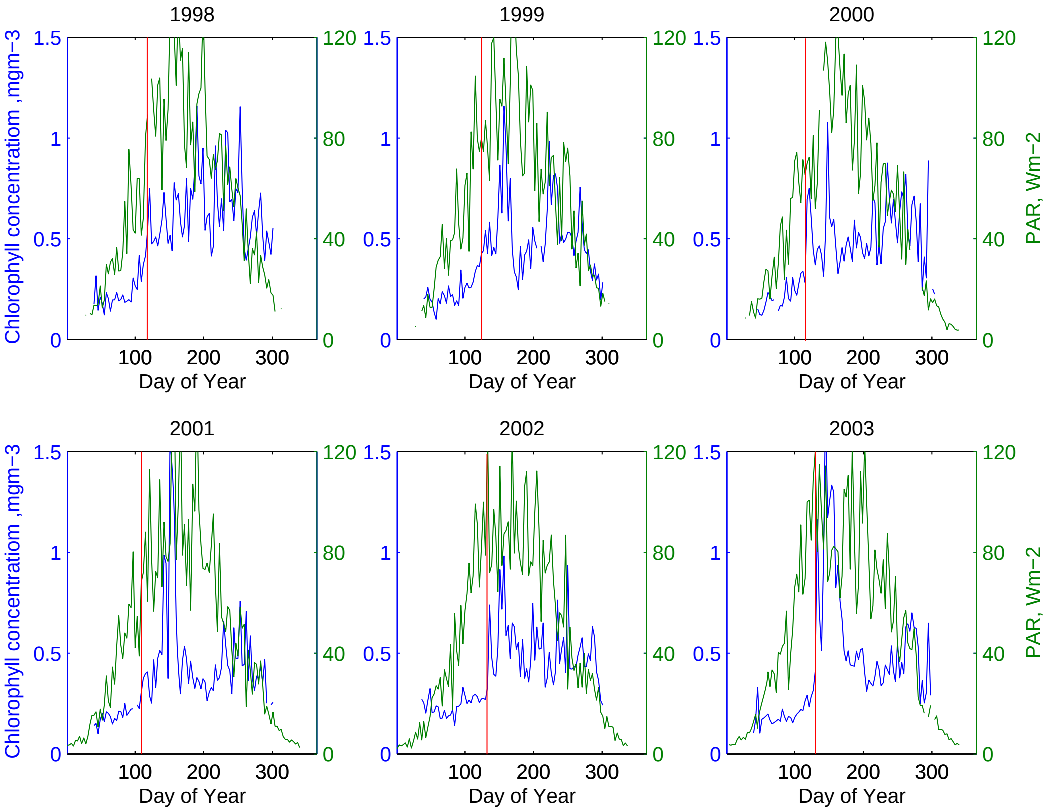

Figure 7.16: PAR (green line) against SeaWiFS chlorophyll concentration (blue line) for the CIS region. The start of the bloom is marked with a red line.

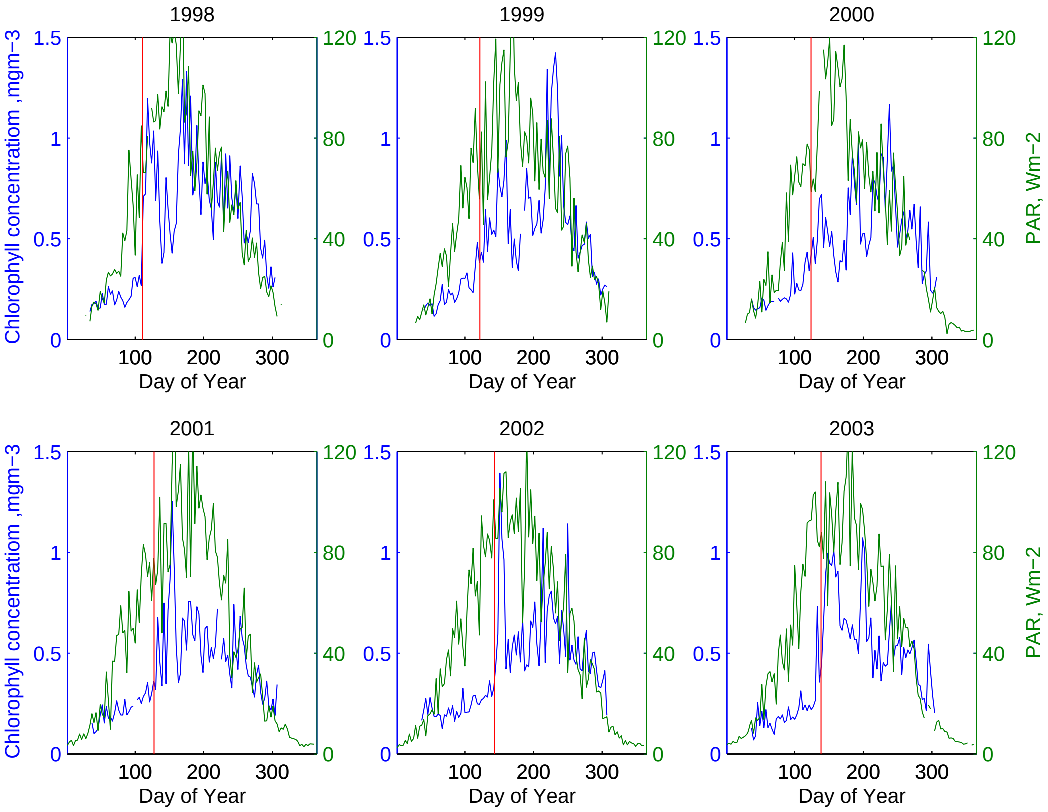

Figure 7.17: PAR (green line) against SeaWiFS chlorophyll concentration (blue line) for the RR region. The start of the bloom is marked with a red line.

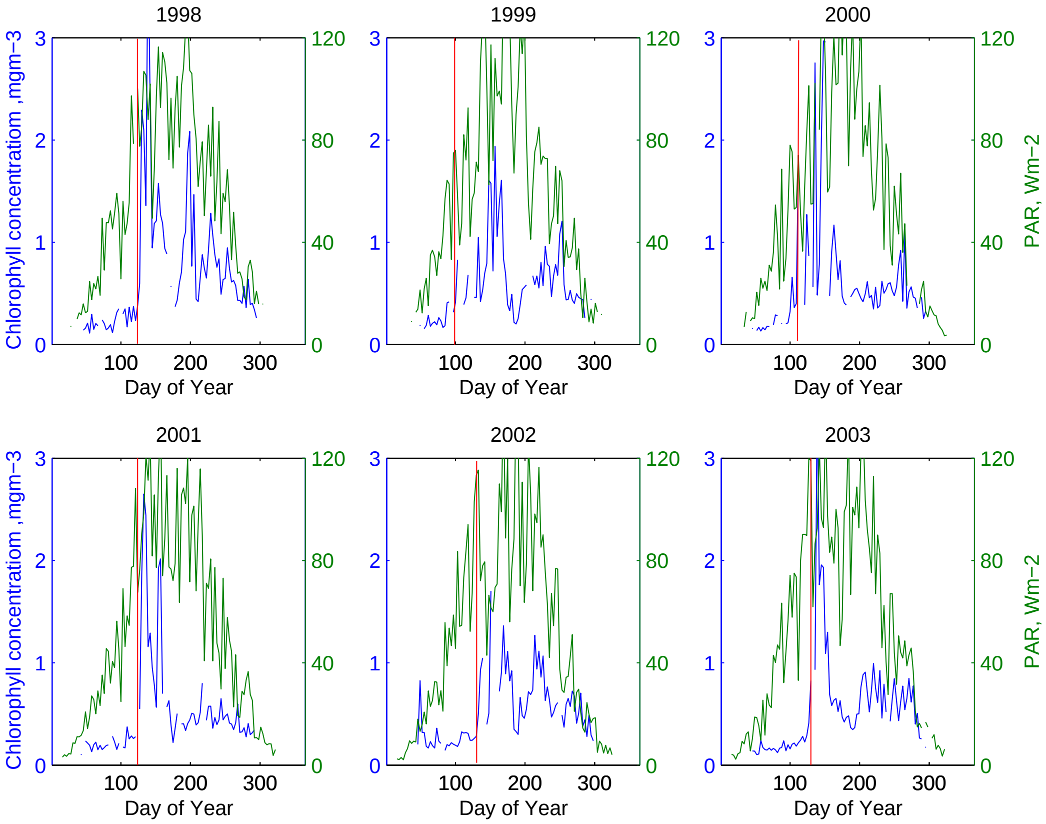

Figure 7.18: PAR (green line) against SeaWiFS chlorophyll concentration (blue line) for the EG region. The start of the bloom is marked with a red line.

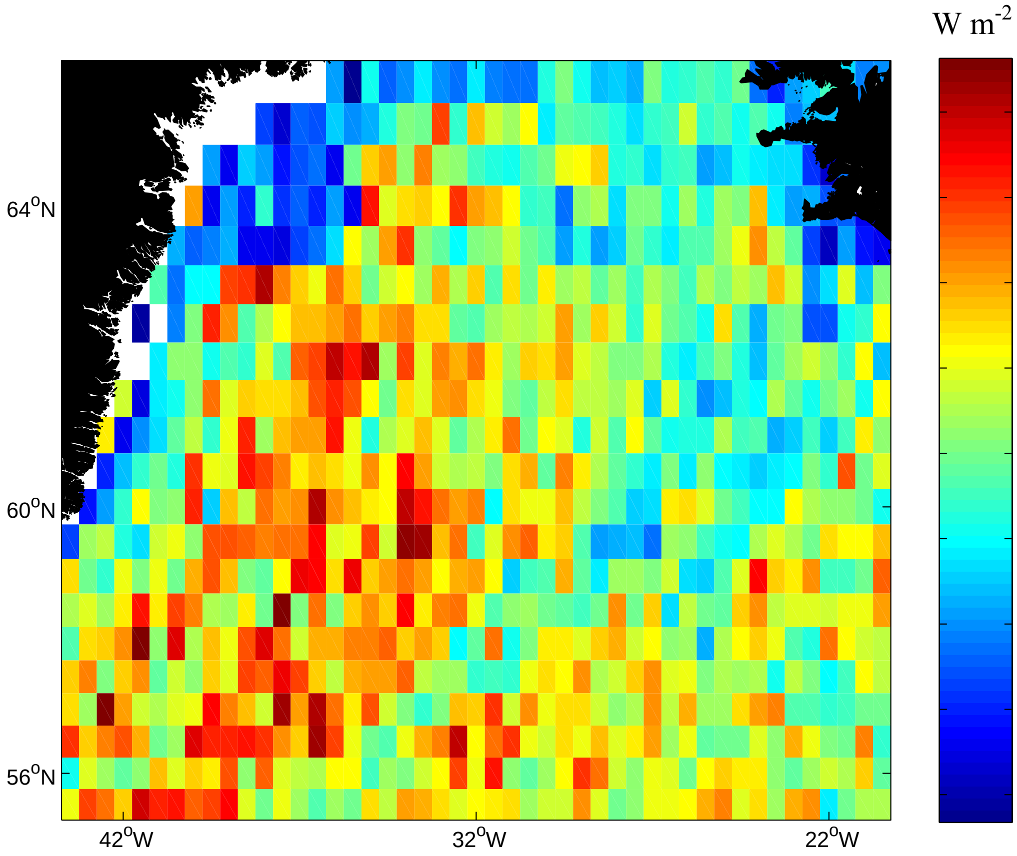

Figure 7.19: Mean (1998 – 2003) depth-averaged irradiance, $\bar{I}$ in W m^{-2}, as defined by Riley (1957).

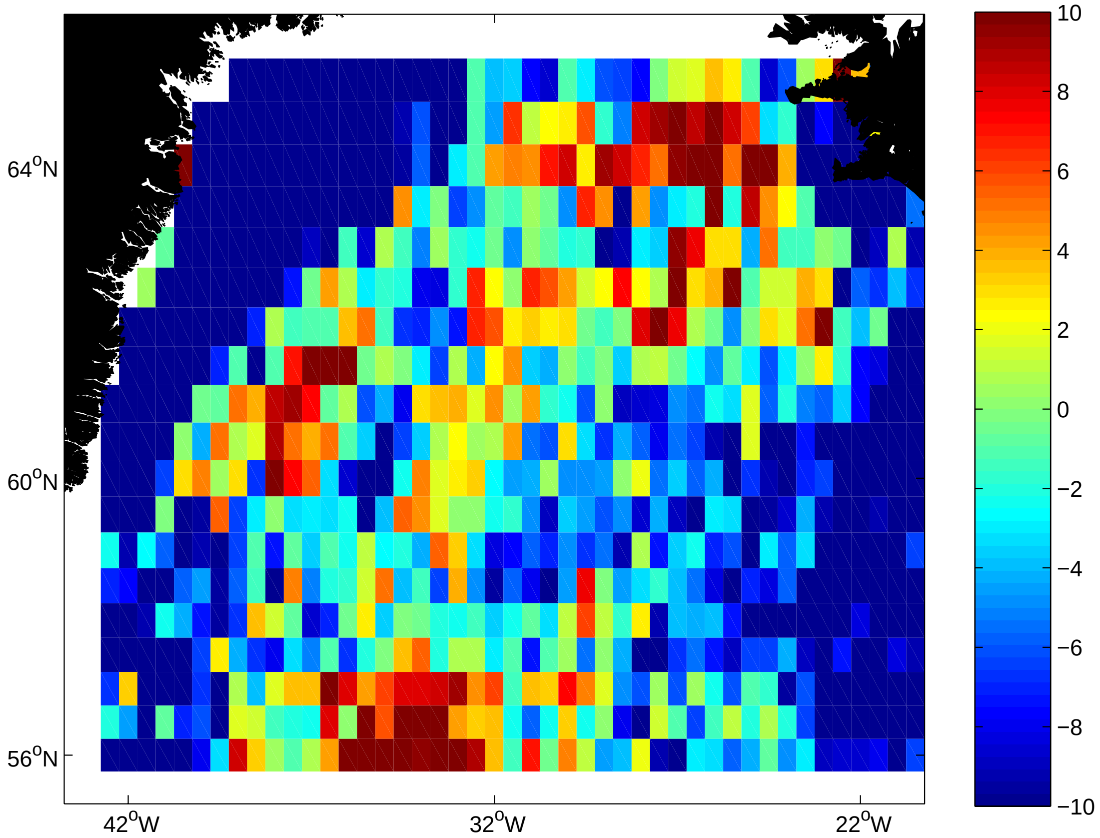

Figure 7.20: Difference between the mean bloom start date and the date when Q > 0 for at least 5 consecutive days and PAR > 81 Wm^{-2} for at least 2 consecutive days. A positive value indicates that the bloom starts after the conditions for Q and PAR have been met.

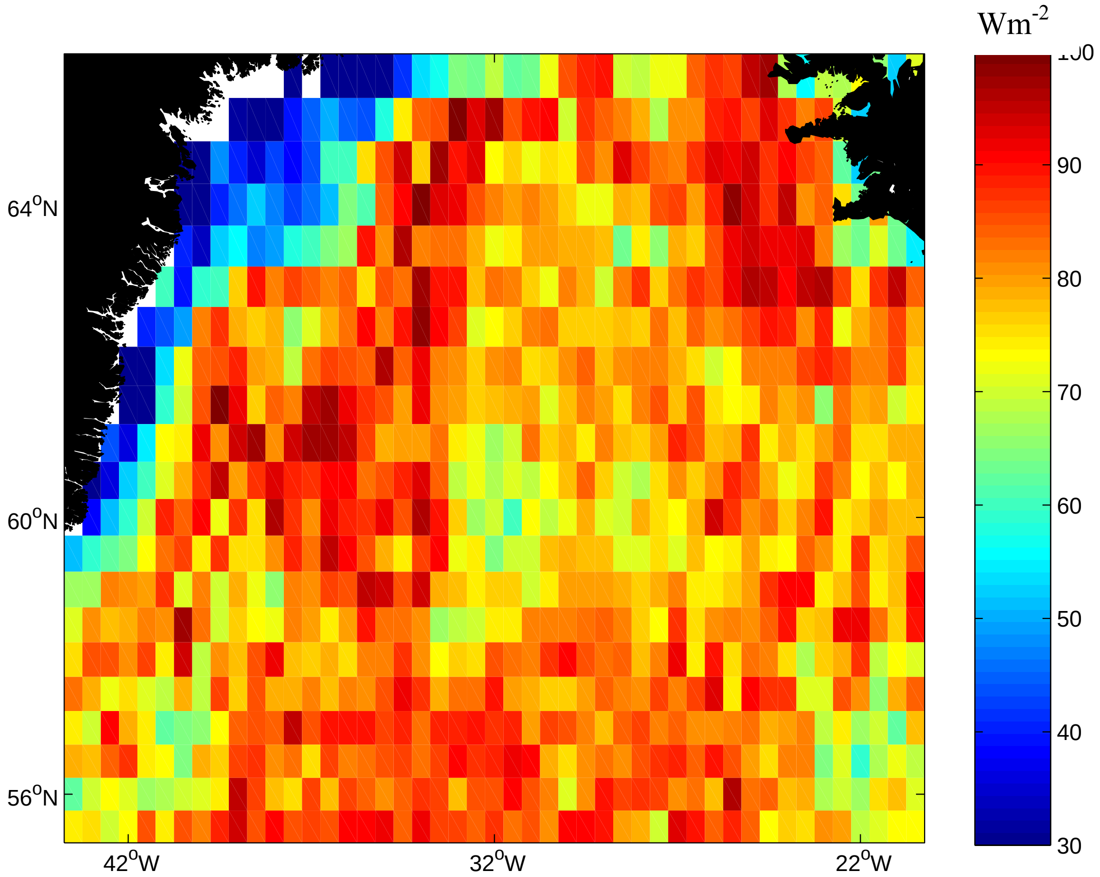

Figure 7.21: Mean PAR (Wm^{-2}) at the start of the bloom.

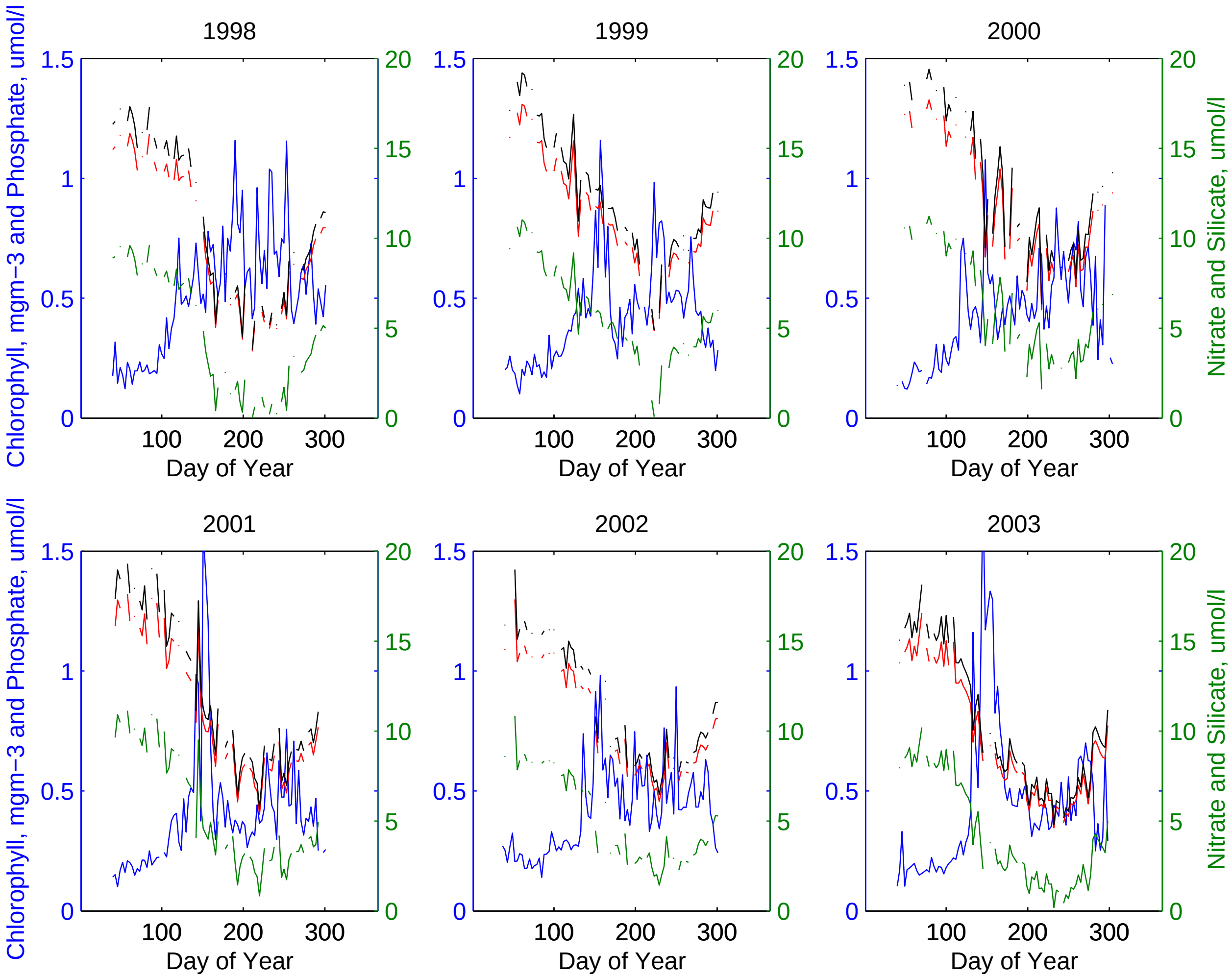

Figure 7.22: Chlorophyll (blue line), phosphate (red line), nitrate (black line) and silicate (green line) concentrations for the CIS region.

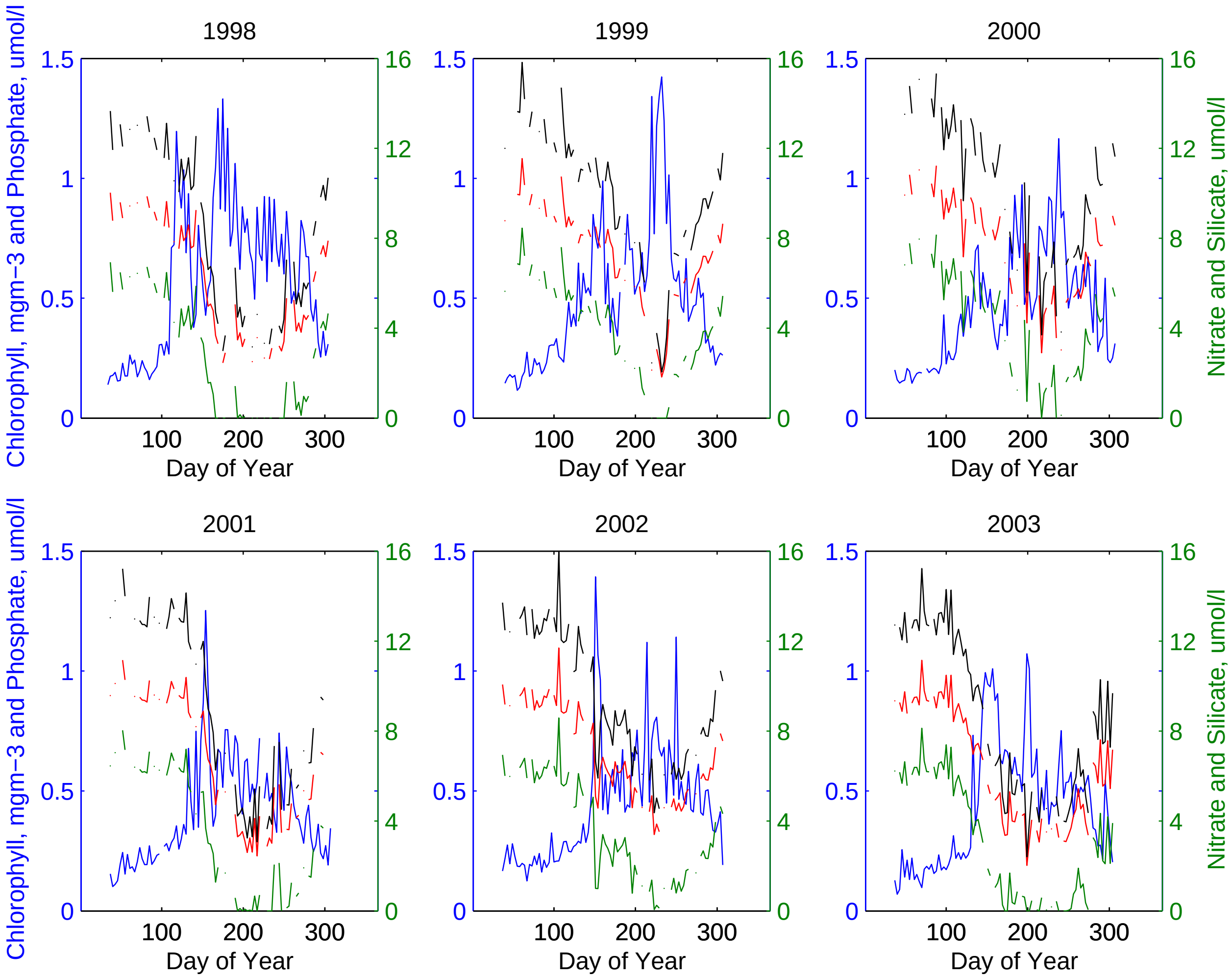

Figure 7.23: Chlorophyll (blue line), phosphate (red line), nitrate (black line) and silicate (green line) concentrations for the RR region.

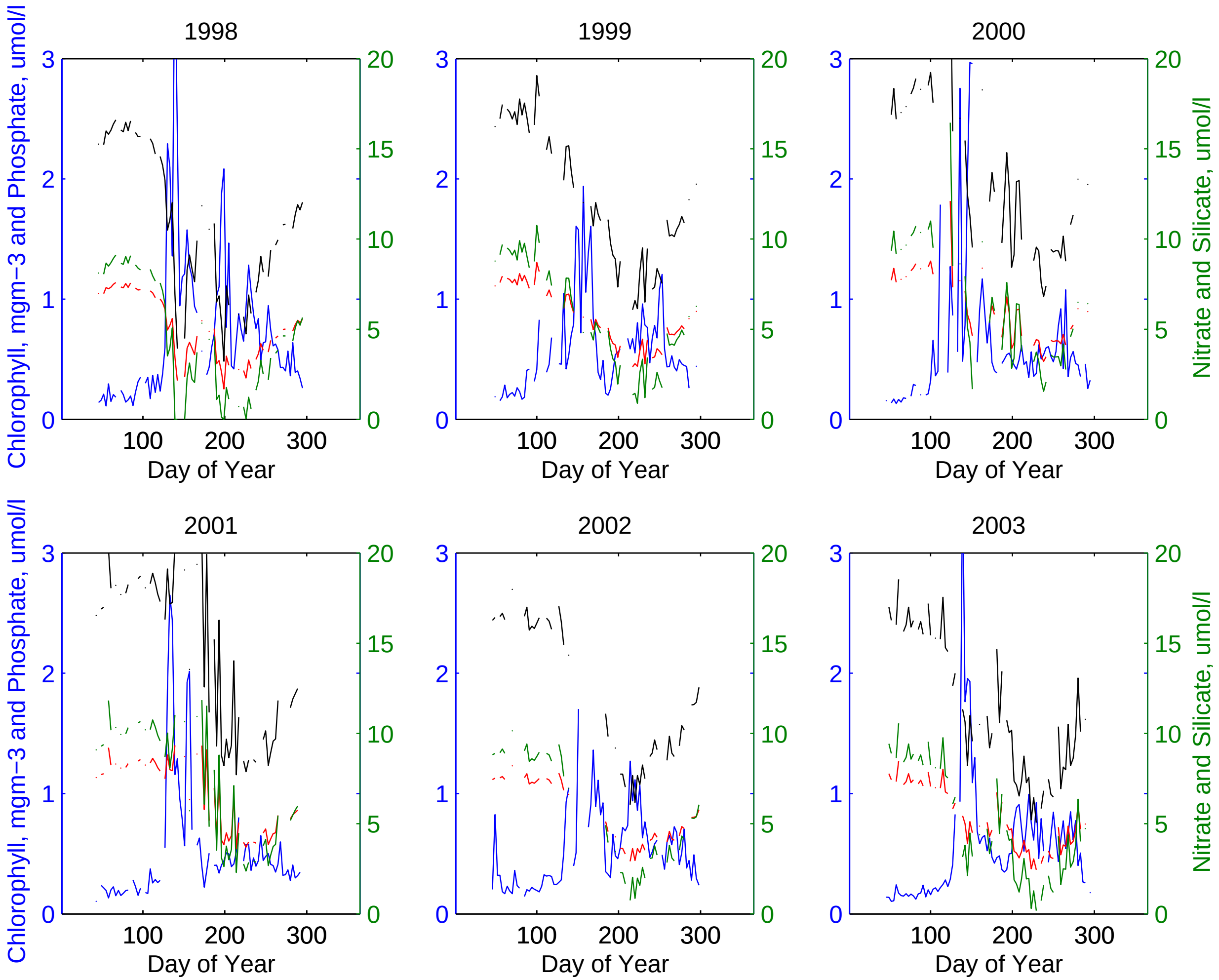

Figure 7.24: Chlorophyll (blue line), phosphate (red line), nitrate (black line) and silicate (green line) concentrations for the EG region.

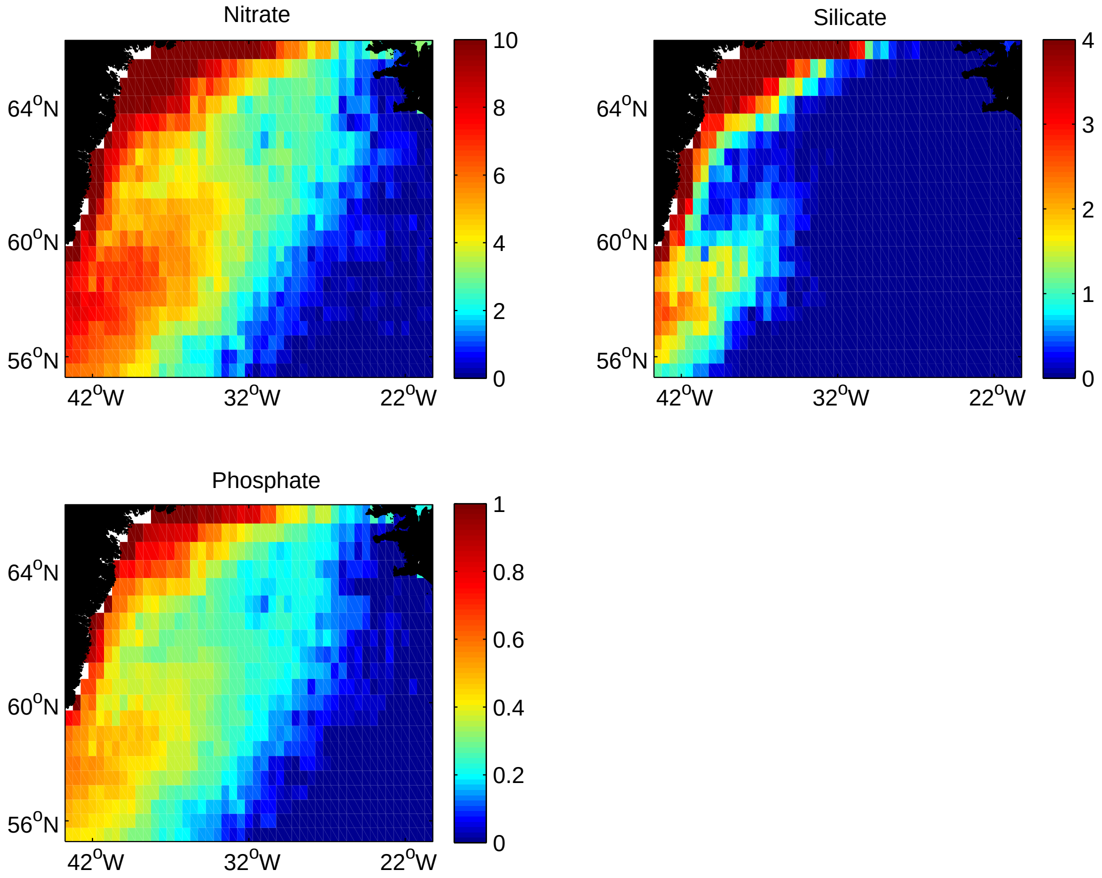

Figure 7.25: Mean (1998 – 2003) minimum nitrate, silica and phosphate concentration in μmol l^{-1}.

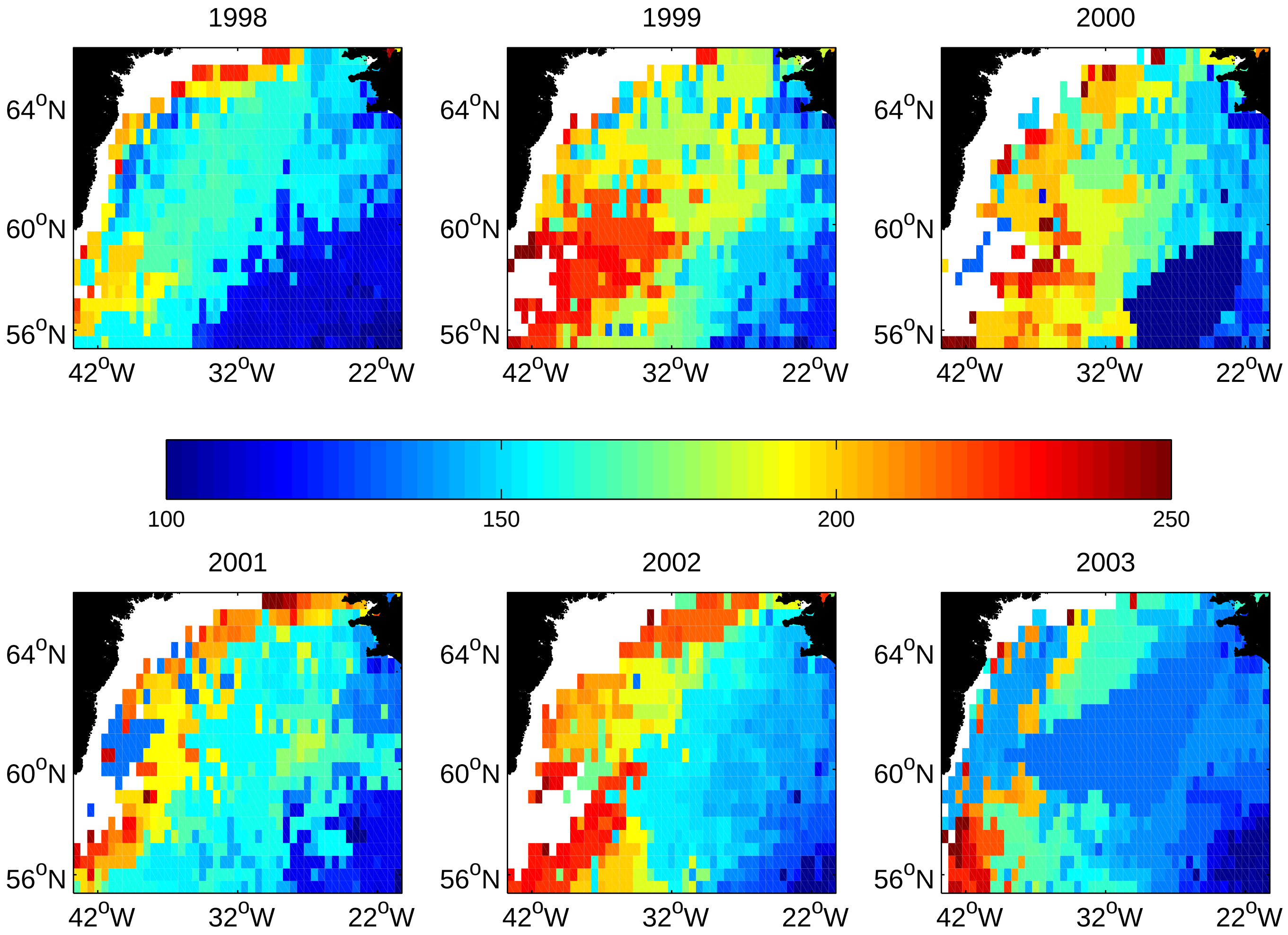

Figure 7.26: Day of the year on which silica becomes depleted (< 2 μmol l^{-1}). Silica does not become depleted in white areas.

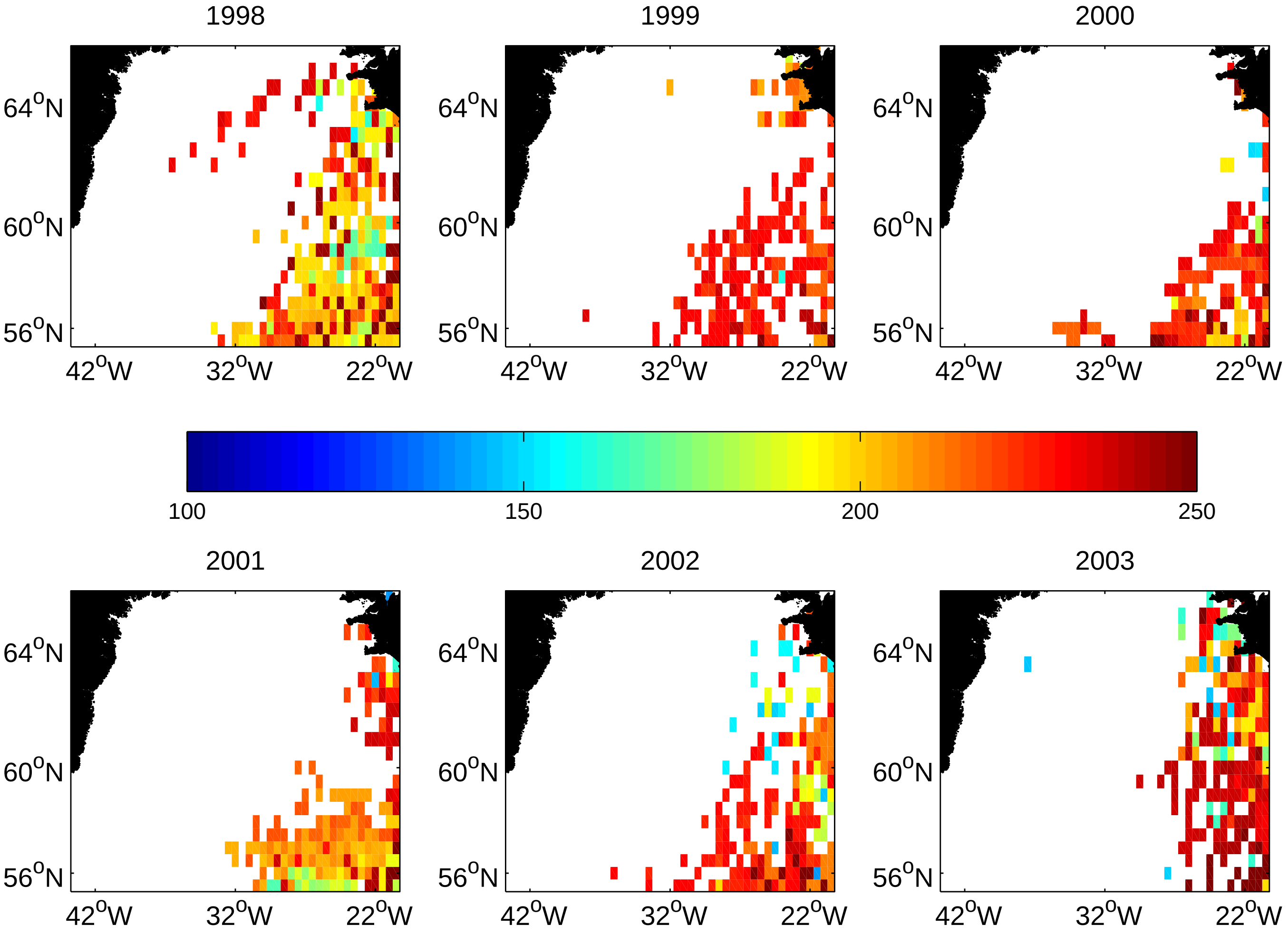

Figure 7.27: Day of the year on which nitrate becomes depleted (< 0.5 μmol l^{-1}). Nitrate does not become depleted in white areas.

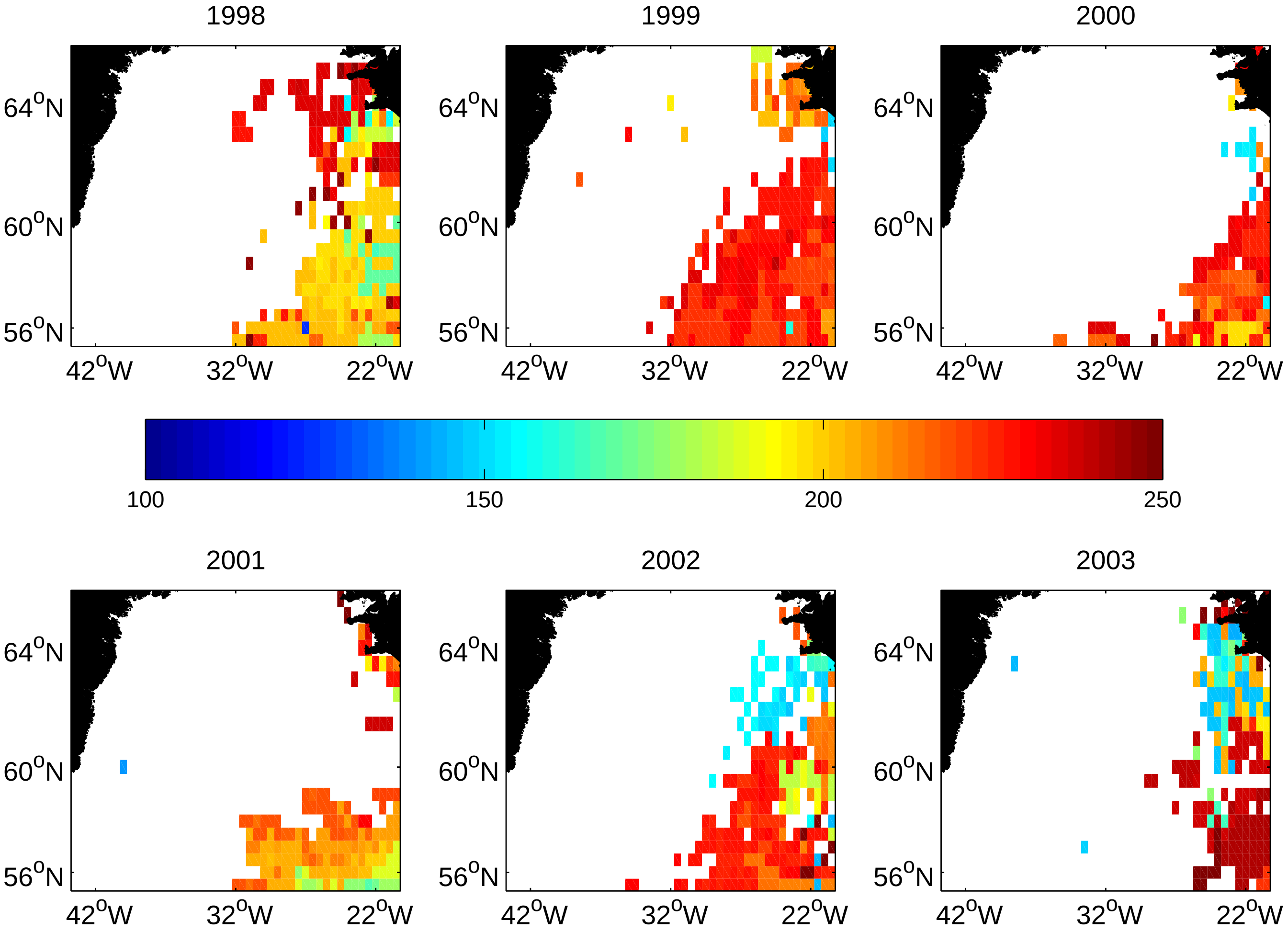

Figure 7.28: Day of the year on which phosphate becomes depleted (< 0.03 μmol l^{-1}). Phosphate does not become depleted in white areas.

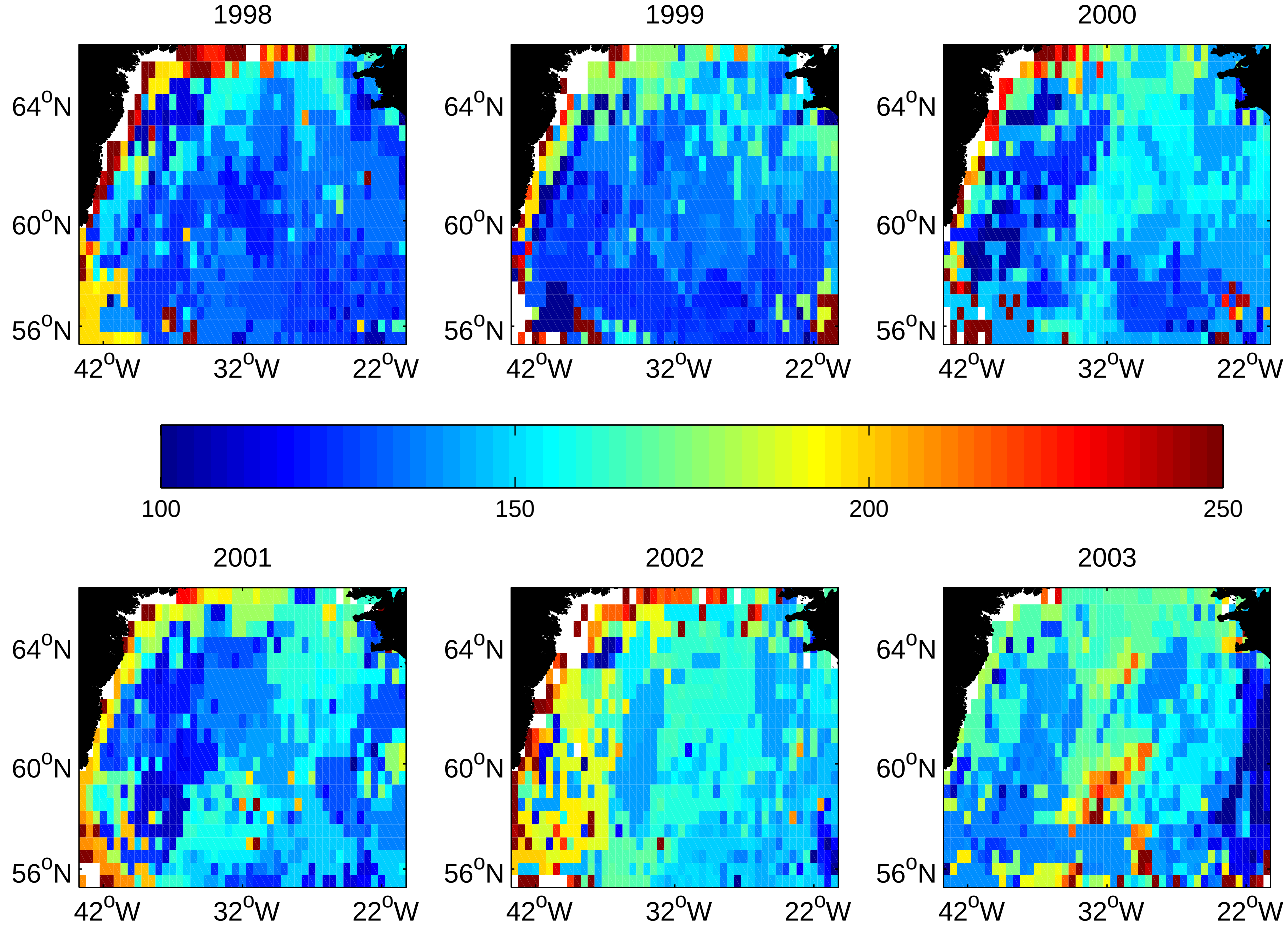

Figure 7.29: Timing of the end of the bloom peak (day of the year).

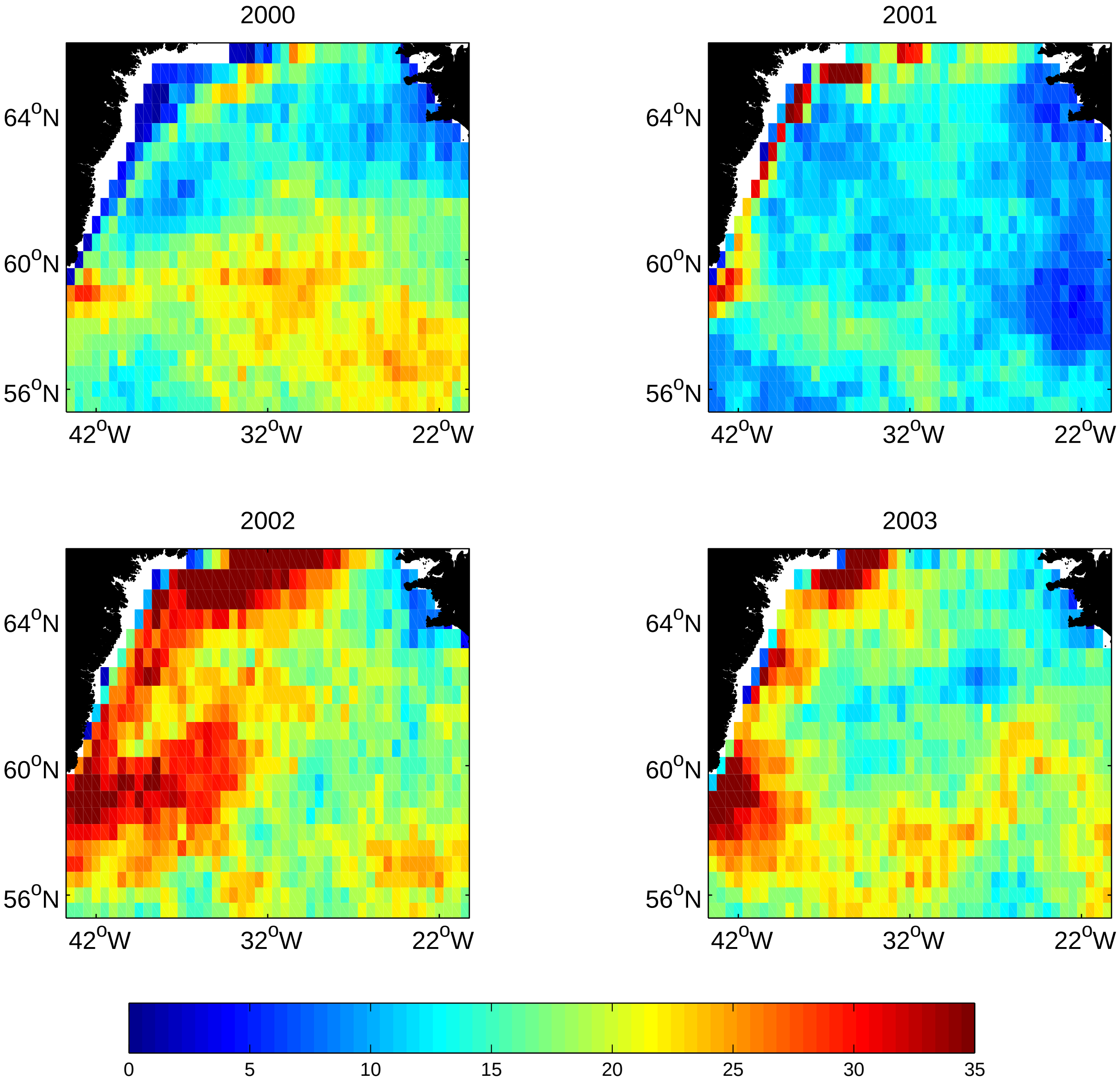

Figure 7.30: The percentage of days during January, February and March on which wind speed > 17 ms^{-1} (i.e. a storm event).

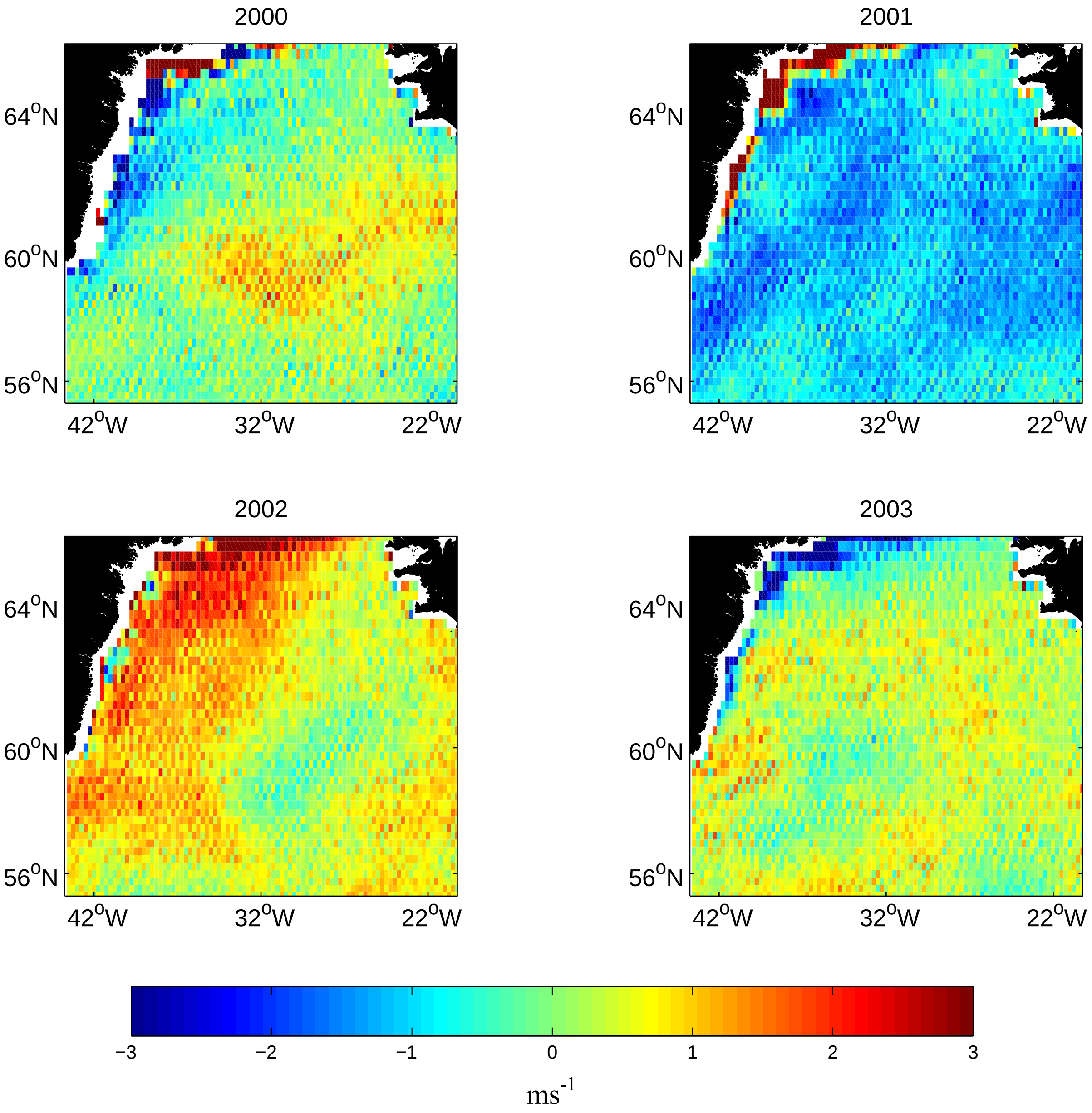

Figure 7.31: Anomalies from the mean winter wind speed for 2000 – 2003 (ms^{-1}).

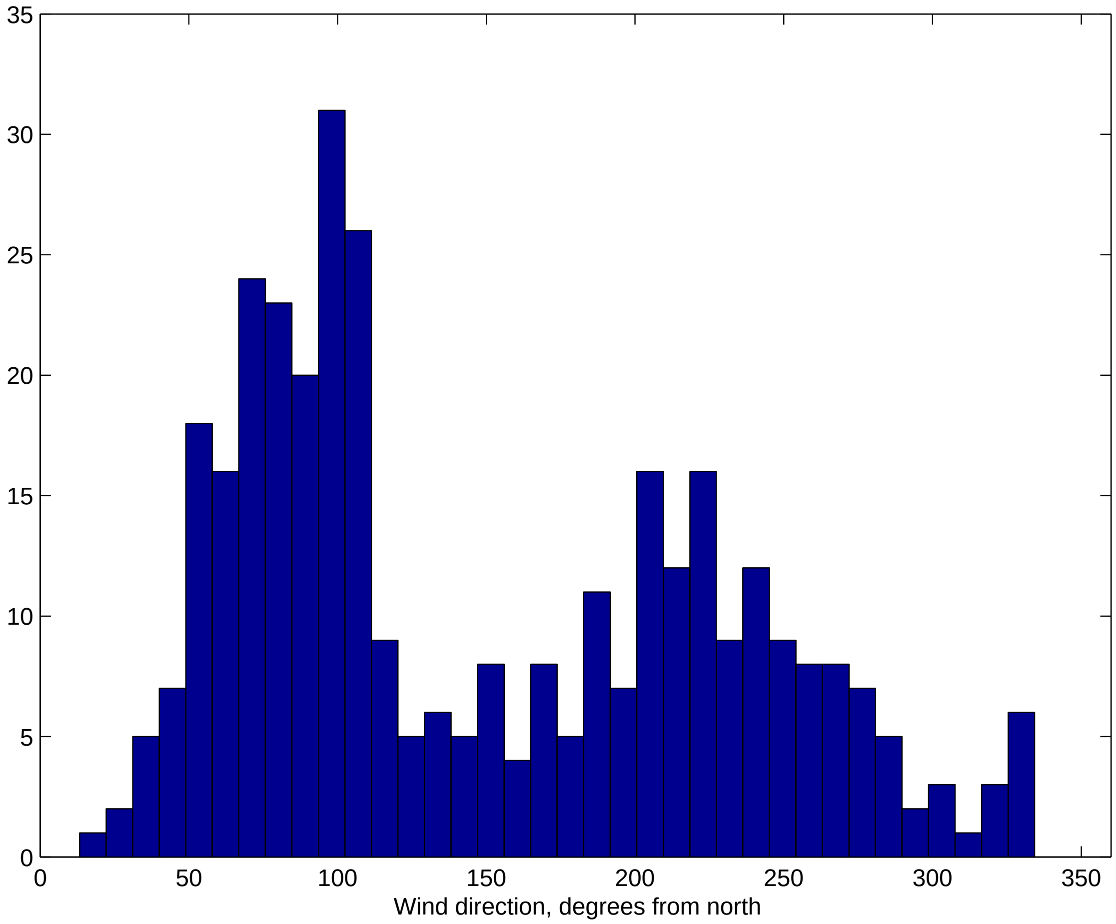

Figure 7.32: Histogram of daily wind direction data during winter for 2000 – 2003 averaged over Pickart et al.'s (2003b) tip-jet zone (59-60 °N, 37-42 °W). 0° indicates a wind blowing toward the north; data in 10° bins.

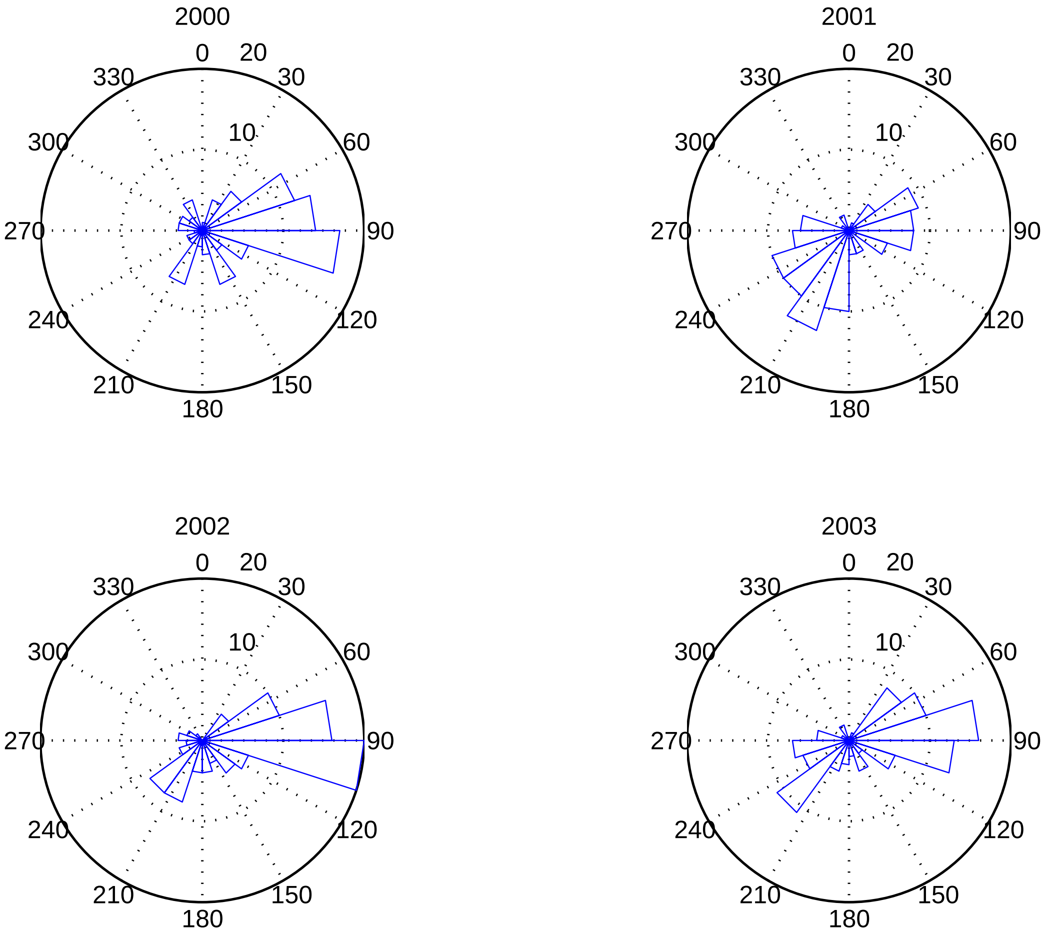

2000

2001

2002

2003

Figure 7.33: Compass plot of winter wind direction for each year in the tip-jet zone. Data is in 20° bins. Size of cones indicates number of days that the wind direction is in that bin (outer circumference = 20 days, inner circumference = 10 days).

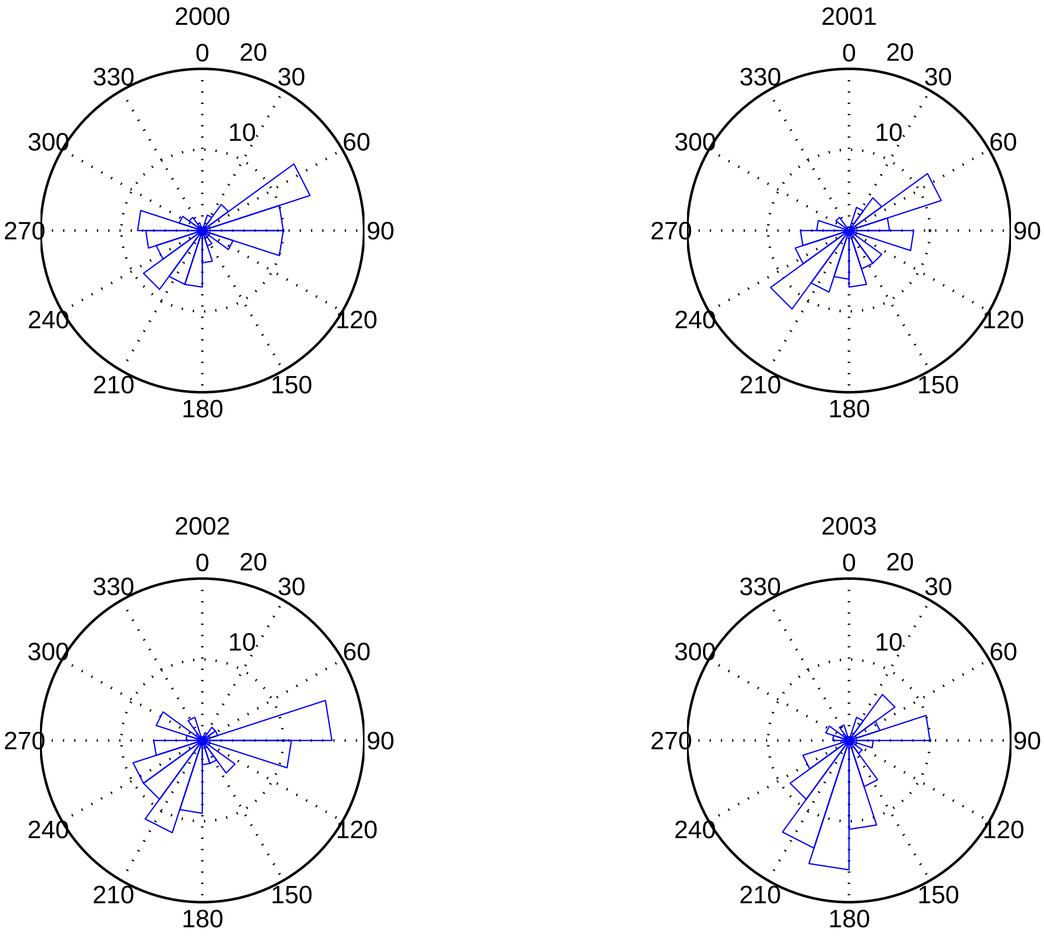

Figure 7.34: Compass plot of wind direction in spring/summer in the tip-jet zone. Data is in 20° bins. Size of cones indicates number of days that the wind direction is in that bin (outer circumference = 20 days, inner circumference = 10 days).

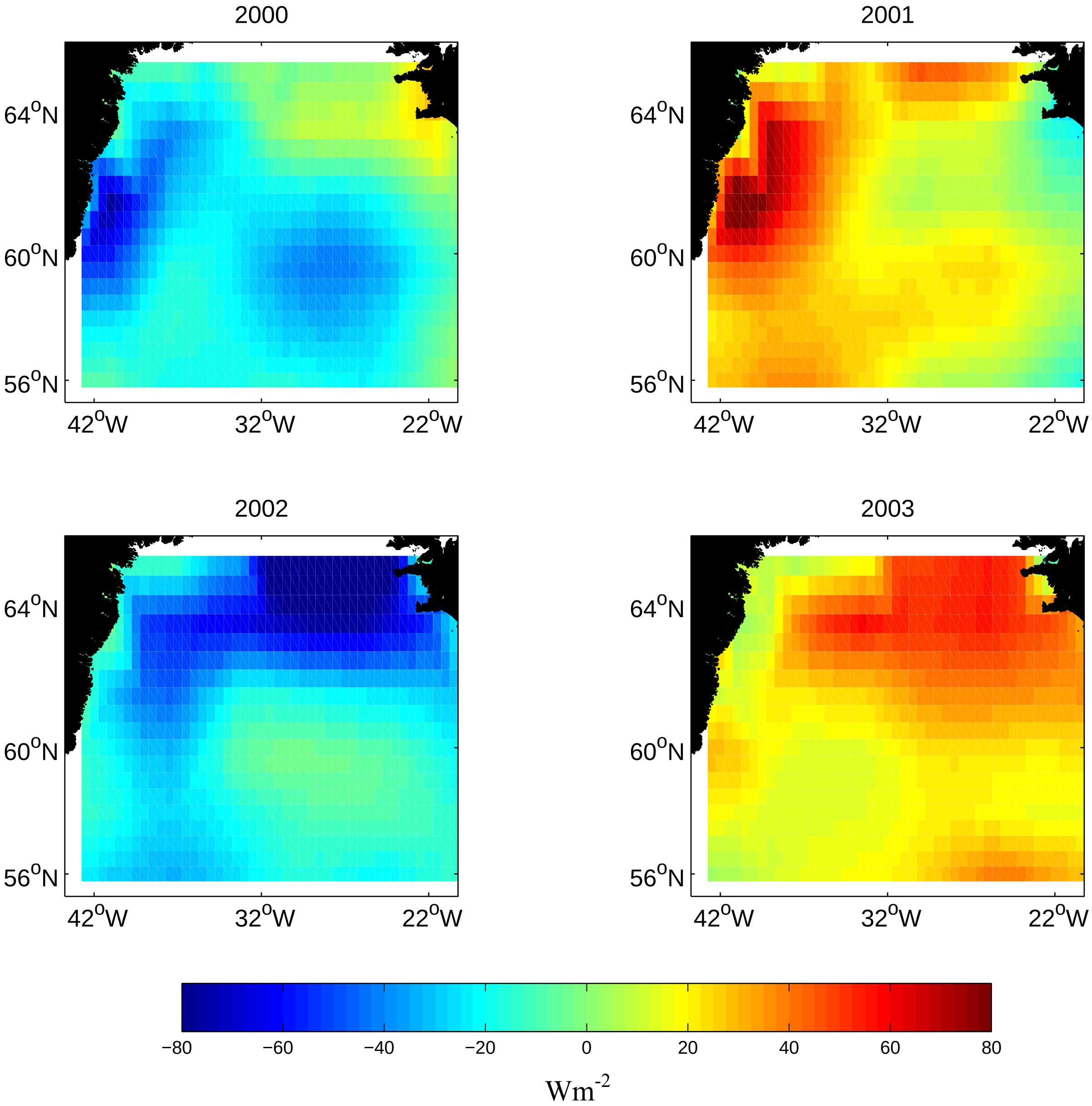

Figure 7.35: Anomalies from the mean winter net heat flux for 2000 – 2003 (Wm^{-2}).

8. NUTRIENT DEPLETION, COMMUNITY SUCCESSION AND THE TIMING OF EXPORT PRODUCTION:

This chapter discusses the possible role of nutrient depletion in community succession and its impact on export production. *In situ* data from the Marine Productivity cruises are used to augment the conclusions drawn from the satellite data.

8.1. COMMUNITY SUCCESSION DURING THE GROWTH SEASON:

The presence or absence of various nutrients plays a vital role in determining the dominant phytoplankton groups in a parcel of water. In the Irminger Basin silica is plentiful in the early spring, with concentrations reaching 10-12 μmol l^{-1}. By around mid-July silica concentrations have dropped to their annual minimum. This rapid and thorough consumption of silica is indicative of a diatom bloom, as diatoms are entirely dependent on silica for construction of their cell walls. Some diatoms are capable of growth rates which greatly outstrip non-diatom species (Furnas, 1990) allowing them to reach bloom concentrations very quickly and establish dominance in community composition.

On the Marine Productivity spring and summer cruises in 2002 samples for taxonomic identification of phytoplankton were typically taken at the surface, at the chlorophyll maximum and at 100 m depth. Figure 8.1 shows the distribution, for the spring and the summer cruises, of the depth-integrated carbon within the four principal plankton groups found in the IB: diatoms, flagellates, picoplankton and ciliates (microscope work performed by Russell Davidson and Claire Holeton, NOCS; see Section 3.1.2 for details of analysis). The cruise tracks of the spring and summer cruises, with arrows showing the route taken by the ship and numbers indicating the day of the year on which the ship passed that point, are also shown in Figure 8.1. Note that these data are by no means synoptic – each cruise lasted ~6 weeks, with 27 and 24 days between the first and last stations for the spring and summer cruises respectively. During the spring cruise (late April-early May) flagellates and picoplankton dominated and in particular a dense bloom of the flagellate *Phaeocystis* sp. was observed on the East Greenland shelf (see Sections 2.2.2 and 7.4.1 for a discussion). Diatoms are present mainly on the north-eastern Greenland shelf and over the Reykjanes Ridge. During the summer cruise (August) all taxonomic groups are present at similar concentrations.

It has been observed repeatedly that a seasonal community succession takes place during the North Atlantic spring bloom, from diatoms in early spring to flagellates in late spring once the diatoms have depleted the silicate (e.g. Mitchell, 1992; Barlow et al., 1993; Gregg et al., 2003; Moore et al., 2005). A diatom bloom was not observed in either the spring or the summer Marine Productivity cruise data. Comparison of the date on which the taxonomic samples were collected during the spring cruise with the start of the spring bloom in 2002, as calculated in Section 6.2 and displayed in Figure 6.10, suggests that the spring cruise took place before the bloom had started. With the exception of the north-eastern Greenland coast where a freshwater induced bloom was occurring (Waniek et al., 2005) there is not the magnitude of biological activity typically associated with a spring bloom. There is a hint that as RRS *Discovery* leaves the basin at the end of the cruise a diatom bloom was beginning over the Reykjanes Ridge, consistent with the estimates of the start of the spring bloom in Figure 6.10. On the summer cruise there was again no sign of a diatom bloom, however silica concentrations had been reduced from >10 μmol l^{-1} to <2 μmol l^{-1} between the spring and summer cruises (seen both in the *in situ* data (Figure 4.9) and the satellite-derived nutrient concentrations (Figure 7.24)). When considered in conjunction with the satellite chl-a data this suggests that the main diatom bloom occurred between the two cruises.

The maps of timing of silica depletion presented in Figure 7.26 effectively represent the timing of the switch from diatom dominance of the community composition to other functional groups, such as flagellates and picoplankton. Diatoms are able to bloom early in the growth season, consuming new nutrients (those introduced into the water column during winter overturning) – leading to new production. Later in the season the species which rely on recycled nutrients, such as flagellates and picoplankton, are able to bloom; however, (assuming a steady state system) recycled production does not contribute to export flux. Thus export production in high latitudes is believed to be dominated by diatoms (Dugdale et al., 1995). Nitrate does not become depleted west of the Reykjanes Ridge during the spring bloom (see Figure 7.27), suggesting that silica may be the nutrient controlling new production in this region. So the maps of the timing of silica depletion (Figure 7.26) may also give an indication of the timing of new (export) and recycled production. The timing of export production is investigated further in Section 8.3.

8.2. WHY IS NITRATE NOT DEPLETED DURING THE GROWTH SEASON?

Nitrate concentrations remain far above depletion throughout the majority of the Irminger Basin in every year of the study. Nitrate is traditionally thought to be the nutrient which limits open ocean spring blooms, with a typical bloom progression of diatoms dominating until silica is depleted, followed by production by non-siliceous phytoplankton that can utilise nutrients at relatively low concentrations until surface nitrate is exhausted. However, in the Irminger Basin nitrate remains unused at the end of the growth season. Throughout summer chl-a concentrations remain elevated above winter levels, without further consumption of nitrate. Several possible explanations for this are discussed in this section.

The possibility that light is limiting growth in the post-bloom period was deemed unlikely in Section 7.3 on the basis that chl-a would not remain elevated throughout the summer if light conditions were restrictive to growth. Another possibility is that recycled nitrogen is taken up preferentially to new nitrogen. As the productive season progresses recycled forms of nitrogen from the breakdown of organic material and excretion become available. Ammonium concentrations >1 μmol l^{-1} can inhibit nitrate uptake by phytoplankton (Wheeler and Kokkinakis, 1990), so that nitrate may remain unused at the end of the growth season.

Grazing of the phytoplankton population by zooplankton is likely to control growth to some extent. However, by the time of the Marine Productivity cruise in August *Calanus finmarchicus*, the primary phytoplankton consumers in this region, were found to be descending back to overwintering depths in the central basin (Heath et al., 2005). Unfortunately, the impact of either grazing or ammonia uptake cannot be assessed in this study.

Finally is it possible that lack of iron is limiting nitrate uptake? Although the supply of iron to the North Atlantic has traditionally been considered adequate for phytoplankton growth, several studies, both *in situ* (Martin et al., 1993; Boye et al., 2003) and modelled (Kamykowski et al., 2002; Moore et al., 2004) have suggested that iron may be limiting in the sub-polar North Atlantic. To assess this possibility data from the Fast Repetition Rate Fluorometer (FRRF), which has the potential to detect changes in the health of the photosynthetic machinery in phytoplankton, are considered. Two parameters are measured by the FRRF, F_v/F_m and σ_{PSII}, both of which are functions of photosystem II (PSII), which is one of two reaction centres (PSI and PSII) in phytoplankton chloroplasts. Reaction centres absorb light energy which is then used in hydrolysis, one of the first steps in photosynthesis, to excite an electron to a higher energy state. The wavelengths used by the two types of reaction centre differ; type I absorbs maximally at 700nm, type II at 680nm (Kirk, 1994). At the usual range of temperatures experienced by phytoplankton in the marine environment, the majority of fluorescence is emitted by PSII (Kolber and Falkowski, 1993). F_v/F_m is the maximum photochemical quantum efficiency; in effect it represents the probability that de-excitation of the photosystem occurs via photochemistry relative to other deactivation pathways (such as fluorescence or dissipation of energy through heat loss). σ_{PSII} is the functional absorption cross-section of PSII; a measure of the photochemical target size of PSII. It represents the product of absorption by the suite of PSII antenna pigments and the probability that an excitation within the antenna will cause a photochemical reaction (Kolber et al., 1998).

Limiting concentrations of nitrate or iron prevent the assembly of functional photosynthetic reaction centres and result in reduced values of F_v/F_m and increased values of σ_{PSII} (Falkowski et al., 1992). Silica or phosphate depletion is not thought to affect photosynthetic efficiency and is not reflected in the parameters measured by the FRRF (Moore et al., 2005). Factors other than nutrient stress, such as photoinhibition, diel variability, photoprotection and community composition can also cause changes in FRRF parameters (Geider et al., 1993). A particular difficulty in the interpretation of FRRF data is that taxon specific variability in photophysiology, as well as nutrient stress, can result in similar values of F_v/F_m and σ_{PSII} (Moore et al., 2005).

On the Marine Productivity cruises a FRRF was permanently attached to Discovery's non-toxic supply (see Section 3.1.1 for details of processing). Only data collected during night time were used in the analysis in order to minimise physiological effects associated with photoinhibition and daytime photochemical quenching. The surface F_v/F_m and σ_{PSII} for each of the four Marine Productivity cruises are plotted in Figure 8.2 (data courtesy of Claire Holeton, NOCS). Under optimal conditions F_v/F_m reaches an empirically derived maximum value of 0.65, but under the influence of nutrient limitation F_v/F_m decreases and is typically <0.4 in iron-limited communities (Behrenfeld and Kolber, 1999; Boyd and Abraham, 2001). During both winter cruises F_v/F_m is ~0.45 to 0.5, during spring it drops to ~0.4 and in summer it is ~0.25. σ_{PSII} varies from ~600 Å^2 photon^{-1} in winter to ~400 Å^2 photon^{-1} in spring, and back to ~800 Å^2 photon^{-1} in summer. The values of F_v/F_m and σ_{PSII} vary from cruise to cruise, i.e. seasonally, but are consistent within each cruise. During winter and spring high values of F_v/F_m and low values of σ_{PSII} indicate phytoplankton whose photosynthetic assemblages are in good health. The combination of low F_v/F_m and high σ_{PSII} values in summer suggest that the changes in F_v/F_m are consistent with nutrient limitation. Thus there is the possibility that the phytoplankton are not meeting their photosynthetic potential due to nutrient stress. As nitrate is not limiting on the western side of the Irminger Basin, this suggests the possibility of iron limitation of phytoplankton growth. Without *in situ* measurements of iron concentration this hypothesis unfortunately cannot be tested.

8.3. ESTIMATE OF EXPORT PRODUCTION:

Global estimates of export production have been derived in the literature from satellite chl-a by estimating the total production and then applying a second empirical algorithm to estimate the export production. These global estimates suggest that the Irminger Basin has an annual mean export production of ~100 to 150 gCm^{-2} (Falkowski et al., 1998; Laws et al., 2000). This is in contrast to new production estimates based on *in situ* measurements of nitrate drawdown which range from ~35 to 60 gCm^{-2} (see Chapter 2.2.2 for further details and Henson et al., 2003; Waniek et al., 2005; Sanders et al., 2005). The timing of silica depletion determined in the previous section suggests another method for estimating export production. In the Irminger Basin diatoms are expected to dominate the early stages of the spring bloom, consuming the silicate to depletion. Diatoms are also expected to dominate export production in the North Atlantic (Savidge et al., 1995; Dugdale and Wilkerson, 1998). Assuming that export production is the portion of total production which occurs between the start of the bloom and the time when silica has been depleted, a lower bound estimate of export production can be made.

Total primary production was calculated using the Vertically Generalised Production Model (VGPM) of Behrenfeld and Falkowski (1997). The VGPM was selected over other models (e.g. Antoine and Morel, 1996; Sathyendranath et al., 1995) because of its simplicity and wide usage. It is also the model used in the export estimates made by Falkowski et al. (1998) and Laws et al. (2000), to which the estimate made here will be compared. The model requires as inputs satellite measurements of surface chlorophyll concentration, sea surface temperature, daily PAR and daily photoperiod. The model consists of a temperature-dependent algorithm to estimate P^{B}_{opt}, the maximum carbon fixation rate within a water column and empirical relationships between satellite chl-a and euphotic depth. The core equation describing the relationship between surface chlorophyll and daily carbon fixation integrated from the surface to the euphotic depth in $mgCm^{-2}$, PP_{eu}, is:

$$PP_{eu} = 0.66125.P^{B}_{opt}.\frac{E_0}{E_0 + 4.1}.C_{SAT}.Z_{eu}.D_{irr} \qquad \text{[Eqn 8.1]}$$

where C_{SAT} is satellite surface chlorophyll concentration (mgm^{-3}), D_{irr} is the daily photoperiod in decimal hours (in this study estimated as a function of latitude using the equations of Forsythe et al., 1995), E_0 is the sea surface daily PAR (Einsteins m^{-2}day^{-1}), P^{B}_{opt} is the optimal rate of daily carbon fixation within a water column (mgC (mgChl)$^{-1}$ hour^{-1}) and Z_{eu} is depth (m) of the euphotic zone defined as the penetration depth of 1% surface irradiance based on the Beer-Lambert law. Z_{eu} is calculated from C_{SAT} following Morel and Berthon (1989) as:

$$Z_{eu} = \begin{cases} 568.2C_{TOT}^{-0.746} & \text{if } Z_{eu} < 102 \\ 200C_{TOT}^{-0.293} & \text{if } Z_{eu} > 102 \end{cases}$$

where C_{TOT} , total water column chlorophyll concentration, is:

$$C_{TOT} = \begin{cases} 38.0C_{SAT}^{0.425} & \text{if } C_{SAT} < 1.0 \\ 40.2C_{SAT}^{0.507} & \text{if } C_{SAT} > 1.0 \end{cases}$$

P^{B}_{opt} is defined as:

$$P^{B}_{opt} = \begin{cases} 1.13 & \text{if } T < -1 \\ 4.0 & \text{if } T > 28.5 \\ P^{B'}_{opt} & \text{otherwise} \end{cases}$$

where T is the sea surface temperature (°C). Finally $P^{B'}_{opt}$ is:

$$P^{B'}_{opt} = \begin{array}{l} 1.2956 + 2.749\times10^{-1}T + 6.17\times10^{-2}T^2 - 2.05\times10^{-2}T^3 + 2.462\times10^{-3}T^4 \\ -1.348\times10^{-4}T^5 + 3.4132\times10^{-6}T^6 - 3.27\times10^{-8}T^7 \end{array}$$

The VGPM was coded in Matlab and run for each day from 1998-2003. The total annual primary production was calculated by summing the daily primary production at each pixel and is plotted in Figure 8.3. In the central basin total production is ~120 gCm^{-2}yr^{-1}, increasing eastwards over the Reykjanes Ridge to ~220 gCm^{-2}yr^{-1}. The mean basin wide total production in 1998 is ~215 gCm^{-2}yr^{-1} and ~180 gCm^{-2}yr^{-1} in all other years. The Reykjanes Ridge experiences the highest total production in 1998 (~250 gCm^{-2}yr^{-1}), whilst in 2001 and 2003 total production in the RR is reduced to ~180 gCm^{-2}yr^{-1}. The CIS experiences low total production (~150 gCm^{-2}yr^{-1}) and in 2000, 2001 and 2002 a region of low productivity extends from the CIS into the northern central basin.

Sixteen total primary production measurements were taken on the summer 2002 Marine Productivity cruise using the ^{14}C method (Brierley et al., 2003). In Astoreca (2003) the data are reported as total daily primary production integrated to the 1 % light depth. Although there are insufficient data to fully evaluate the accuracy of the Behrenfeld and Falkowski (1997) algorithm in the Irminger Basin a rough comparison can be made between the two methods. Due to the cloud cover in both satellite SST and chl-a there were very few exact match-ups of *in situ* and satellite estimates of primary production. Astoreca (2003) divides the *in situ* estimates into four regions, the 'Greenland Shelf, Irminger Basin, Reykjanes Ridge and Iceland Basin'. The mean satellite derived daily primary production was calculated for a geographical area covering the positions of the ^{14}C measurements on the days when the corresponding *in situ* measurements were taken. In Table 8.1 the mean *in situ* and satellite-derived total daily primary production data are compared for each of Astoreca's (2003) regions. With the exception of the Reykjanes Ridge region the satellite derived estimate is ~ 25 % greater than the *in situ* primary production. In the Reykjanes Ridge zone however, the satellite estimate is double the *in situ* measurement. Considering the uncertainties in both methods, the satellite and *in situ* estimates are in fairly good agreement outside of the Reykjanes Ridge region.

Although the estimates of total primary production from the Behrenfeld and Falkowski (1997) algorithm are too high the general pattern of production seen in Figure 8.3 is believed to be correct. Comparing to Figure 8.4, which shows the mean annual chl-a for each year, the distribution of chl-a is similar to that of primary production. The Behrenfeld and Falkowski (1997) algorithm is thus very sensitive to the chlorophyll concentration. If sufficient *in situ* data were available the coefficients of the empirical relationship between satellite chl-a and primary production could be optimised for the Irminger Basin. In the absence of such data the Behrenfeld and Falkowski (1997) algorithm will be used as it stands to estimate export production.

A lower bound of export production can be estimated as that portion of the daily primary production which occurs between the start of the bloom and the day when silica first becomes depleted. The start of the bloom was calculated as described in Chapter 6.2 and the silica depletion day is as shown in Figure 7.26. The primary production during this period i.e. the export production is shown for each year in Figure 8.5. Blank areas along the east Greenland coast indicate where an accurate estimation of silica concentration was not possible (Chapter 7.4.1). Blank areas elsewhere in the basin indicate pixels where the estimated start date of the bloom occurs after silica has been depleted. This is due to inaccurate determination of the bloom start date, which may occur if the annual median chl-a is unusually high or if the bloom starts gradually, rather than with a sudden increase in chl-a. In the central basin export production is estimated at ~40-60 $gCm^{-2}yr^{-1}$, rising as high as ~80 $gCm^{-2}yr^{-1}$ in 1999. Towards the east of the Reykjanes Ridge export production is lower at ~20 $gCm^{-2}yr^{-1}$ in all years. The six-year mean export production is ~40 $gCm^{-2}yr^{-1}$, comparable to estimates from *in situ* methods (Henson et al., 2003; Waniek et al., 2005; Sanders et al., 2005) and lower than those estimates made from directly applying an export production algorithm to satellite chl-a (Falkowski et al., 1998; Laws et al., 2000).

This method offers another technique for estimating export production in regions where silica limits production and diatoms dominate export. It provides only a lower-bound estimate of export production however, as some assumptions are made. Firstly the method assumes that little new production occurs prior to the spring bloom. Diatoms are likely to be the first functional group to exploit the vernal shallowing of the mixed layer. During the winter months phytoplankton concentrations are at an annual minimum due to deep convective mixing, but a small population must survive the winter to seed the following spring's bloom (Huisman et al., 1999; Backhaus et al., 2003). The amount of new production, if any, that occurs in winter can be estimated by considering the drawdown of nutrients between the winter and spring Marine Productivity cruises. However, the *in situ* measurements of surface nitrate concentrations were found to be lower during the winter cruise (8-11 µmol l^{-1}) than in spring (12-14 µmol l^{-1}), indicating that the 'winter' cruises actually took place in late autumn, prior to the onset of convective mixing. An alternative method was used by Sanders et al. (2005) to estimate the winter nitrate concentration. The O_2 nitrate slope method of Koeve (2001) was employed to estimate the nitrate drawdown, and thus new production, prior to the spring Marine Productivity cruise. The estimated winter nitrate concentration was found to be similar to the observed spring concentrations (12-14 µmol l^{-1}). On this basis Sanders et al. (2005) concluded that no new production occurred in the Irminger Basin prior to the spring cruise in April/May. We have already concluded however that the spring bloom, on the basis of satellite chl-a data, began after the spring cruise. In order to determine if any new production may have occurred prior to the bloom the nitrate concentration on the start day of the bloom was estimated from coincident satellite SST and chl-a. The mean nitrate concentration, at ~12 µmol l^{-1}, is similar to the winter value estimated by Sanders et al. (2005), thus little new production is expected to have occurred prior to the start of the spring bloom.

The method requires that diatoms contribute significantly to export production, so that once silica depletion occurs and diatom dominance ends, the majority of export production also ceases. The importance of diatoms to export production was inferred by Brzezinski (1995) who suggested that if the ratio of nitrate to silica drawdown is similar to the nitrate to silica molar ratio in nutrient replete diatoms (N:Si ~1) then diatoms are taking up an amount of nitrate equal to the total new production of the system. The average nitrate to silica drawdown ratio in the Irminger Basin is ~1.17 (Sanders et al., 2005). This is close to the ratio of Brzezinski (1995), and so suggests that in the Irminger Basin diatoms are likely to be responsible for the majority of export production, until they become limited by silica depletion.

Once silica becomes limiting to diatom growth it might be expected that new production by non-siliceous phytoplankton would continue until all remaining nitrate has been consumed. However, this is not the case and during the summer cruise nitrate concentrations of several μmol l^{-1} were observed (Henson et al., 2003; Sanders et al., 2005). Henson et al. (2003) demonstrated, on the basis of temperature-nitrate relationships, that the majority of nitrate consumption occurs in spring before SST exceeds ~6° C. Once nitrate consumption ceases, any subsequent production must be relying on recycled forms of nitrogen. Satellite images of AVHRR SST show that a temperature of 6° C is reached in mid-May over the Reykjanes Ridge and by July in the central basin, suggesting that a transition from export to recycled production occurs around this time. The mean monthly maps of chl-a in Figure 5.1 show that chlorophyll remains elevated above winter levels throughout summer, indicating that production continues without consumption of new nitrate, and is therefore likely to be relying on recycled nutrients. Certainly by the time of the summer Marine Productivity cruise in August carbon biomass and primary production were dominated by the < 10 μm size fraction, indicative of small, recycling producers (Astoreca, 2003). Because nitrate does not become depleted during the Irminger Basin spring bloom, it suggests that silica may be limiting the bloom, and hence export production.

Although the method accounts for export production by diatoms and non-siliceous plankton prior to silica depletion, it assumes that there is little new production by non-siliceous plankton after silica has been depleted. Diatoms are out-competed later in the growth season by smaller phytoplankton, such as flagellates and picoplankton. As the productive season progresses recycled forms of nitrogen, such as ammonia or urea, become available from the breakdown of organic material and excretion. Recycled nitrogen is taken up by preferentially by plankton, as assimilating it has lower energetic costs than nitrate (Syrett, 1981) and ammonium concentrations >1 μmol l^{-1} can inhibit nitrate uptake by phytoplankton (Wheeler and Kokkinakis, 1990). Some taxonomic groups are able to increase ammonium uptake with increasing concentrations to a much greater extent than diatoms (Tungaraza et al., 2003). Although the non-siliceous species which dominate later in the growth season are expected to preferentially take up recycled forms of nitrogen, it is possible that they also consume new nitrogen – thus contributing to export production (see Figure 8.6 which shows a sketch of the expected progression of community composition in the Irminger Basin).

The amount of nitrate being consumed after silica has been depleted, and before nitrate reaches its annual minimum, can be estimated from the satellite derived nitrate concentrations. Once nitrate reaches its minimum annual value, all further production must be relying on recycled forms of nitrogen (Figure 8.6). To convert nitrate to an estimate of new production, the surface nitrate must be integrated over the mixed layer depth and converted to carbon using a Redfield ratio of 6.6 (Redfield et al., 1963). Using a mean summer mixed layer depth of 30 m, estimated from Argo float data (see Section 3.8.1), the estimated new production occurring after silica depletion is shown in Figure 8.7. To the west of the Reykjanes Ridge very little production (~5 $gCm^{-2}yr^{-1}$) occurs after silica depletion, whilst to the east of the ridge there is an extra ~15 $gCm^{-2}yr^{-1}$ in all years. This represents an additional contribution to export production after silica depletion (and hence by non-siliceous phytoplankton) of ~10 % of the original export production estimate to the west of the ridge and ~50 % to the east. With these adjustments to the original export production estimate applied the basin mean is ~60 $gCm^{-2}yr^{-1}$. This is on the upper limit of export production estimated from *in situ* nitrate drawdown (Henson et al., 2003; Waniek et al., 2005; Sanders et al., 2005), but still lower than the estimates from export algorithms applied directly to satellite-derived total production (Falkowski et al., 1998; Laws et al., 2000).

The estimate of new production occurring after silica has been depleted suggests that non-siliceous plankton contribute an additional few grams of export production once diatoms no longer dominate the community composition. But what is their contribution to export production whilst silica is abundant and diatoms dominate? As diatoms are expected to consume silica and nitrate in a 1:1

ratio (Brzezinski et al., 1998), nutrient drawdown ratios can be examined to estimate the contribution from diatoms. The total silica and nitrate drawn down for the period between the start of the bloom and the time when silica becomes depleted was calculated. In the west of the region the Si:N ratio for this period was ~0.8, indicating that more nitrate than silica is consumed. This suggests that non-siliceous plankton are consuming nitrate and thus contributing to export production. From the satellite estimates of nitrate and silica concentration it was estimated that approximately 30 % more nitrate than silica is consumed during the growth season. This suggests that diatoms are responsible for ~70 % of export production whilst they dominate the community composition. Thus, to an annual total export production of ~65 $gCm^{-2}yr^{-1}$ diatoms contribute ~40 $gCm^{-2}yr^{-1}$, prior to silica depletion. Non-siliceous plankton contribute the remaining ~25 $gCm^{-2}yr^{-1}$. Of this, 20 $gCm^{-2}yr^{-1}$ occurs prior to silica depletion and 5 $gCm^{-2}yr^{-1}$ occurs after silica depletion. To the east of the Reykjanes Ridge the Si:N ratio was ~1, and therefore diatoms are expected to be responsible for the vast majority of export production prior to silica depletion. To an annual total export production of ~45 $gCm^{-2}yr^{-1}$ diatoms are contributing ~30 $gCm^{-2}yr^{-1}$, prior to silica depletion, whilst non-siliceous plankton contribute ~15 $gCm^{-2}yr^{-1}$ after silica depletion. East of the Reykjanes Ridge diatoms are responsible for almost all the export production prior to silica depletion, whilst non-diatoms are responsible for almost all export production after silica depletion. Diatoms therefore contribute between 60 and 75 % of the total export production in the Irminger Basin.

The estimates of export production made in this study are comparable to *in situ*-based estimates (at ~60 $gCm^{-2}yr^{-1}$), but less than the 100-150 $gCm^{-2}yr^{-1}$ estimated by Falkowski et al. (1998) and Laws et al. (2000) – hereinafter F98 and L00. What causes this discrepancy in the estimates of export production? The estimates in this study and in F98 and L00 are all based on the primary production algorithm of Behrenfeld and Falkowski (1997), and yet they differ by a factor of two. The discrepancy may arise from interannual differences in the amount of export production between 1998-2003, the period of this study, and the years for which F98 and L00 made their estimates. F98 used monthly mean Coastal Zone Color Scanner (CZCS) data from 1978 – 1986, whilst L00 used monthly mean SeaWiFS data from October 1997 – September 1998. The estimates of F98 and

L00 do not overlap in time with the estimates made here and, although interannual variability in export production is occurring, it is unlikely to be on the order of a factor of two.

Another potential explanation is that the method outlined here underestimates the export production that occurs prior to the spring bloom and after nitrate reaches a minimum. The reasoning behind assuming export production is zero outside of this period has been detailed already. The estimates by F98 and L00 are made by applying an algorithm to the annual total primary production. This assumes implicitly that a portion of total production is export production throughout the year. In the Irminger Basin chl-a remains elevated above winter concentrations through the summer and therefore primary production is still occurring. However, as we have shown, much of this production is likely to be based on recycled nutrients and does not contribute to export production. This may be a source of possible over-estimation in the satellite-based export production algorithms.

Finally, it is possible that the algorithm to estimate total production from chl-a (Equation 8.1) is not correctly parameterised for the Irminger Basin. Behrenfeld and Falkowski's (1997) model consists of a series of empirical relationships between vertical distribution of biomass and chl-a, SST etc. which were defined by *in situ* measurements. They developed their productivity model from a database of ^{14}C measurements made on the seaboard of the northeastern USA. The model was then tested against a larger database, the majority of which also focussed on the northeastern USA. It may be that the productivity algorithm is inaccurate in regions for which it was not explicitly parameterised.

In conclusion, to the west of the Reykjanes Ridge export production effectively ends when silica becomes depleted. Export is dominated by diatoms and silica limits export production. Therefore the map of timing of silica depletion in Figure 7.26 represents the timing of the switch from new to recycled production in the western side of the basin. To the east of the Ridge export production by non-siliceous plankton continues after silica is depleted, indicating that export is not entirely dominated by diatoms. Non-siliceous plankton play a significant role in export and nitrate limits export production. We may conclude that this method of estimating export production is suitable for regions where silica is expected to limit export, but provides an underestimate in regions where nitrate limits export.

8.4. CHAPTER SUMMARY:

This chapter has demonstrated some novel uses of satellite data and its potential to extend *in situ* datasets spatially and temporally.

- Consideration of silica abundance/depletion allows an estimate of the timing of the transition from diatom dominance of the phytoplankton community to non-siliceous species.
- In summer production relied on recycled forms of nitrogen, despite plentiful nitrate. Fast Repetition Rate Fluorometer data suggest that the Irminger Basin spring bloom may be iron limited.
- Export production can be estimated from consideration of timing of the initiation of the bloom and silica depletion. Basin mean export production is estimated to be ~60 $gCm^{-2}yr^{-1}$.
- The relative contribution to export production by diatoms and non-diatoms is estimated from silica to nitrate drawdown ratios. Diatoms contribute on average ~65 % of the export production.

REGION	**DAY OF YEAR 2002**	**LATITUDE °N**	**LONGITUDE °W**	***IN SITU* ^{14}C TOTAL PP mgCm^{-2}**	**SATELLITE TOTAL PP mgCm^{-2}**
GREENLAND SHELF	222-227	60-65	36-42	545	603
IRMINGER BASIN	217-225	61-64	32-38	355	459
REYKJANES RIDGE	212-216	60-63	27-31	402	809
ICELAND BASIN	211	61	25	882	1169

Table 8.1: Regional mean total daily primary production as measured *in situ* by the ^{14}C method from sixteen stations during the summer Marine Productivity cruise, and the corresponding satellite-derived total daily primary production.

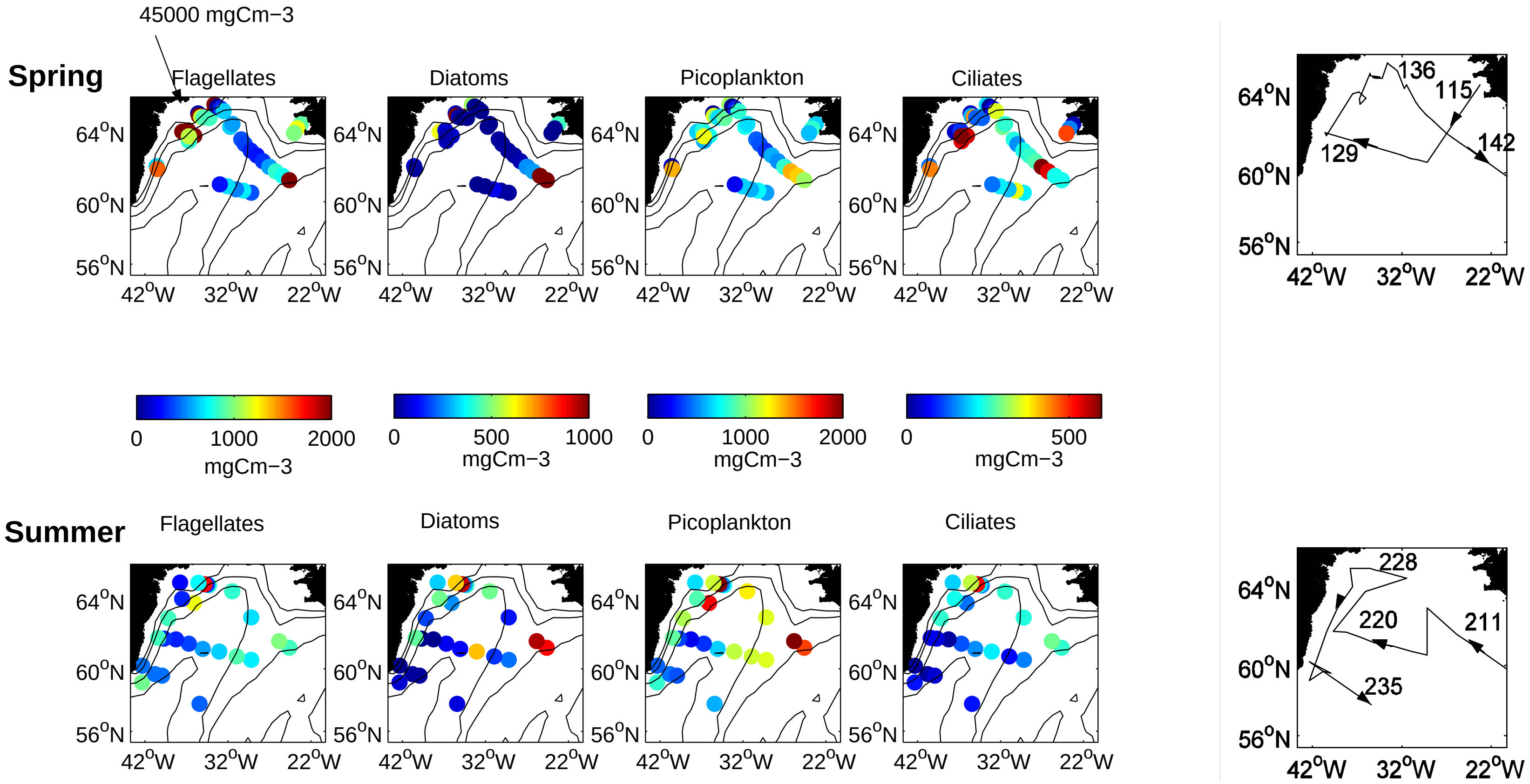

Figure 8.1: Depth-integrated carbon (mgCm^{-3}) within the four principal taxonomic groups. Spring cruise data is on the top row, summer cruise data on the bottom row. Note that the scale is different for each group, but the same for spring and summer within each group. In spring on the East Greenland shelf a dense bloom of *Phaeocystis* sp. is marked with an arrow. The last column shows the cruise track for the spring and summer cruises with arrows marking the direction of the route and numbers marking the day of the year on which the ship passed that point.

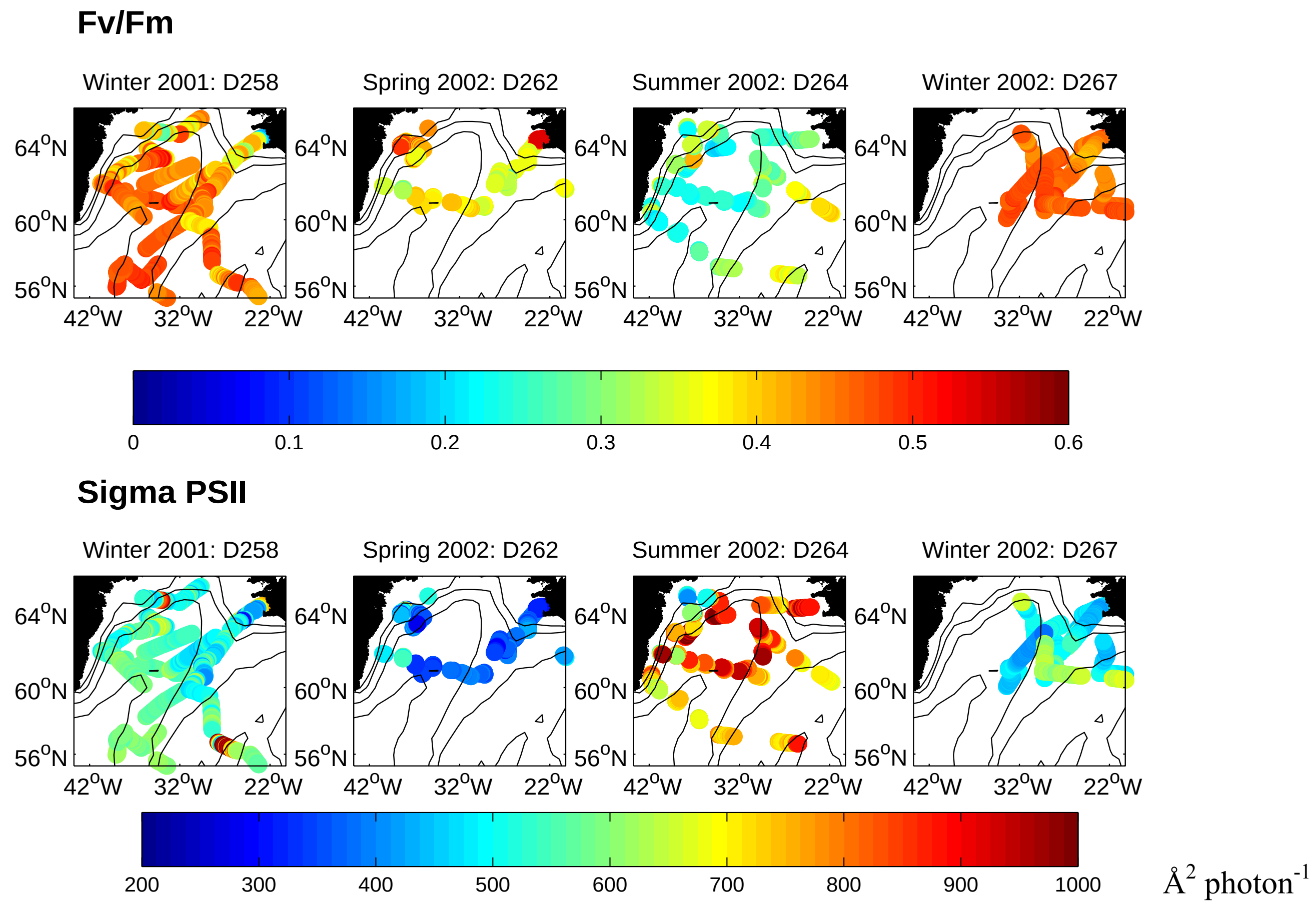

Figure 8.2: Top row F_v/F_m (dimensionless) and bottom row σ_{PSII} (Å^2 photons^{-1}) from the underway surface FRRF measurements for each of the cruises. Data courtesy of Claire Holeton, NOCS.

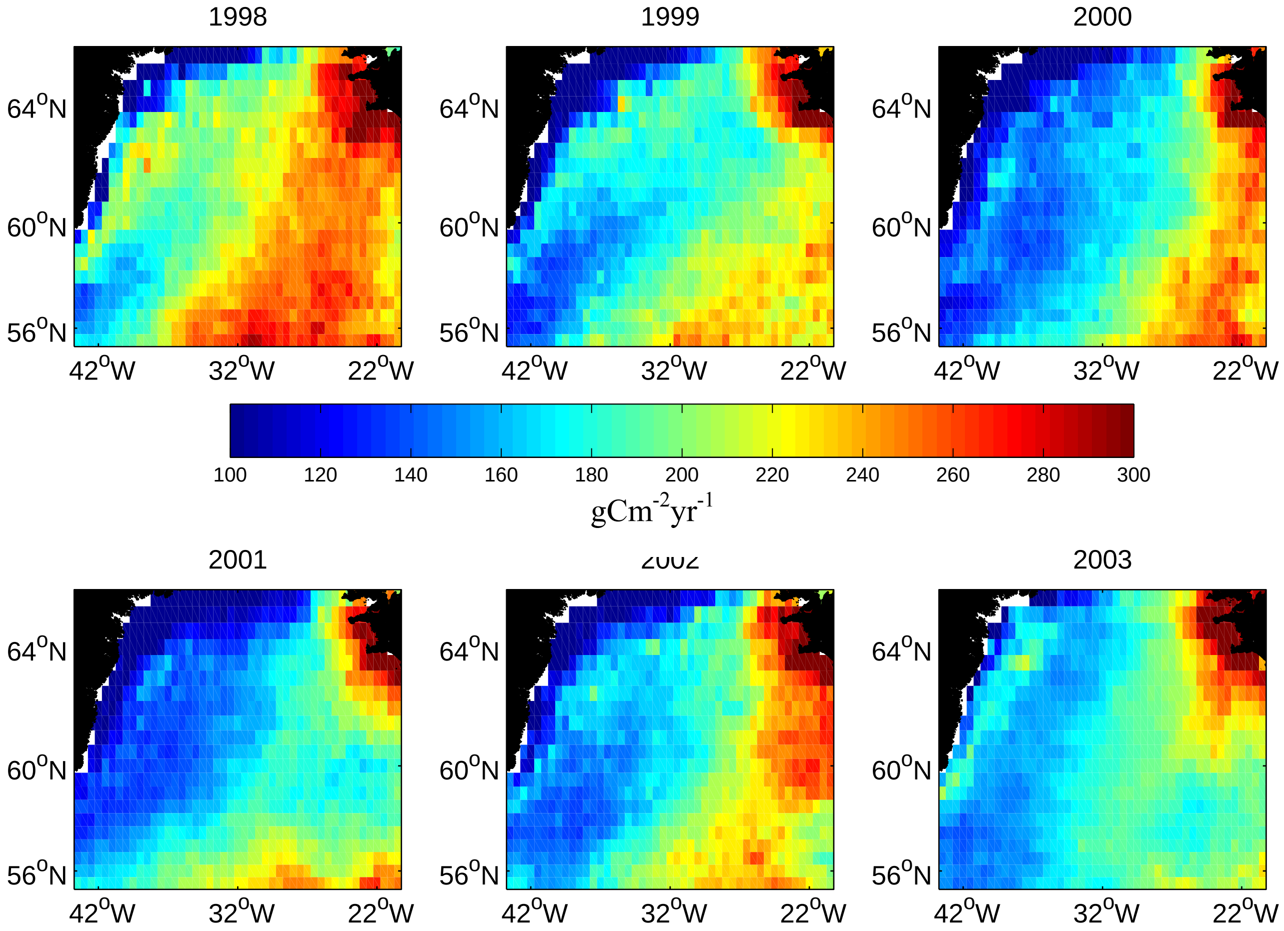

.

Figure 8.3: Total primary production as estimated from the Behrenfeld and Falkowski (1997) algorithm.

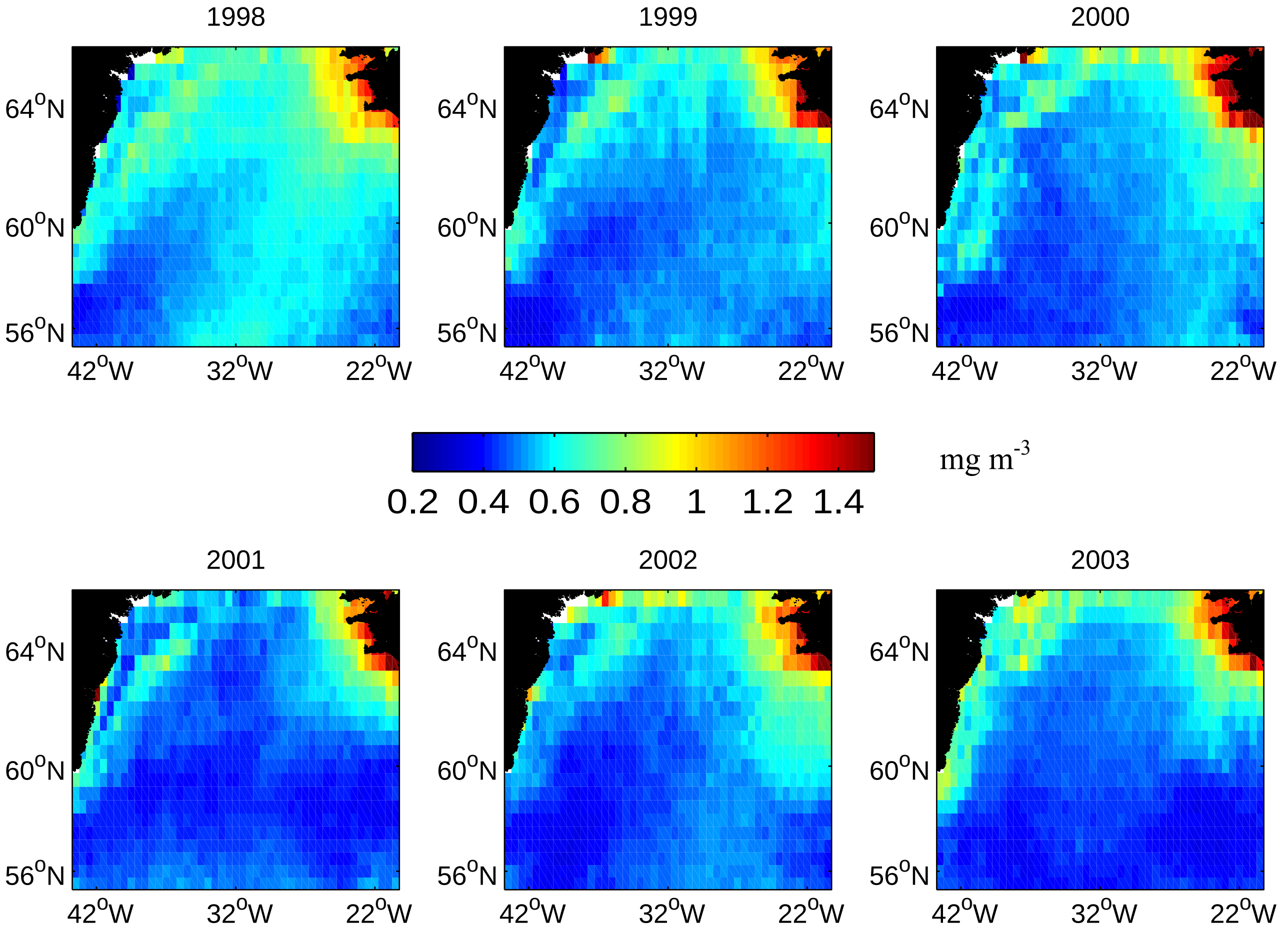

Figure 8.4: Annual mean chl-a concentration for 1998 – 2003.

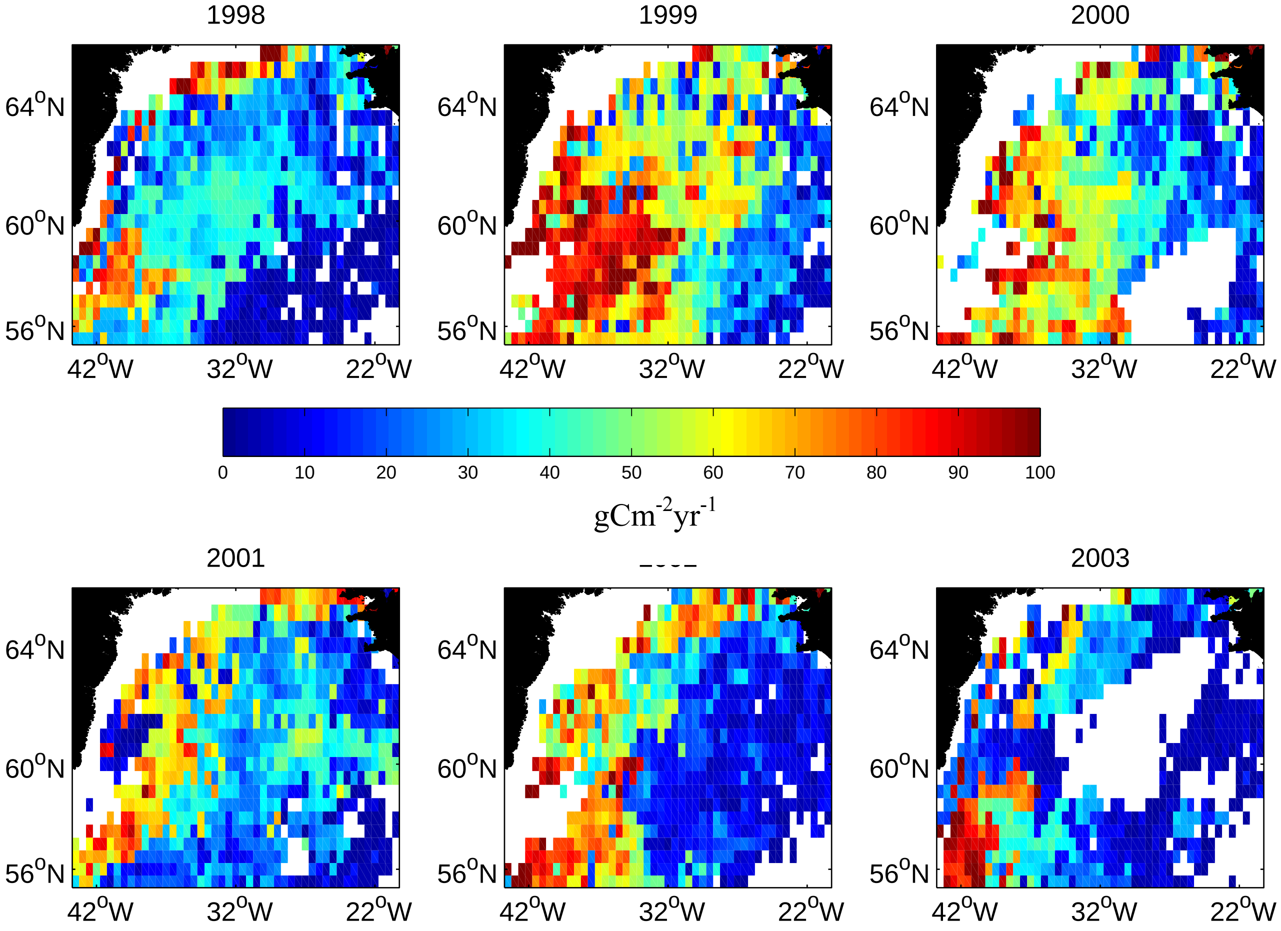

Figure 8.5: Export production estimated as the component of total production between the start of the spring bloom and the day when silica becomes depleted (< 2 μmol l^{-1}).

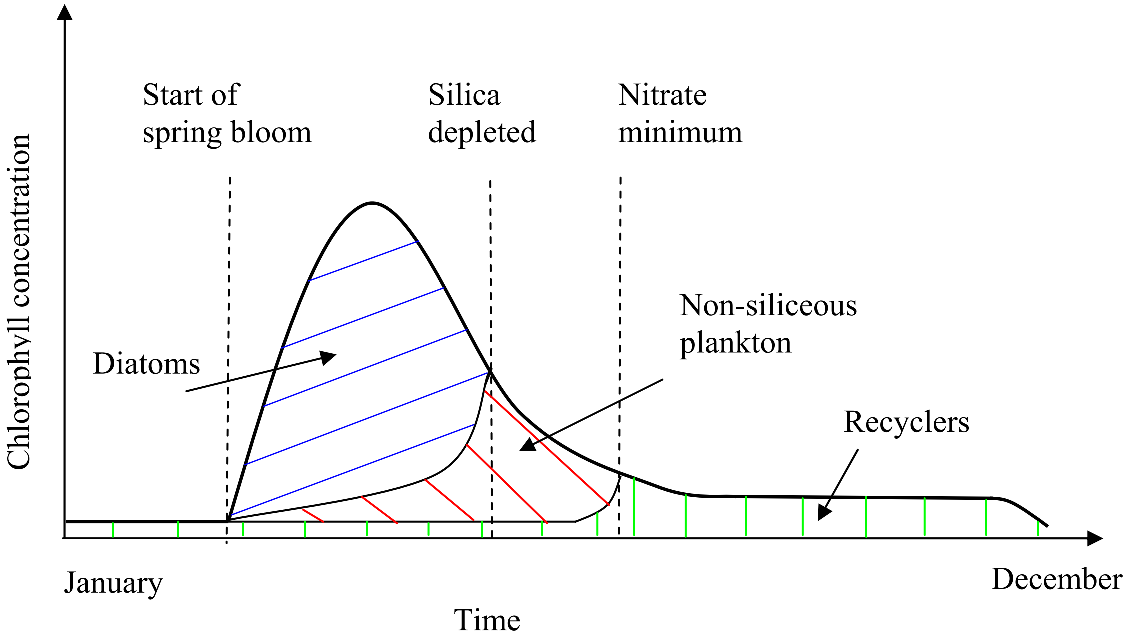

Figure 8.6: Sketch of the expected progression of community composition in relation to nutrient availability in the Irminger Basin.

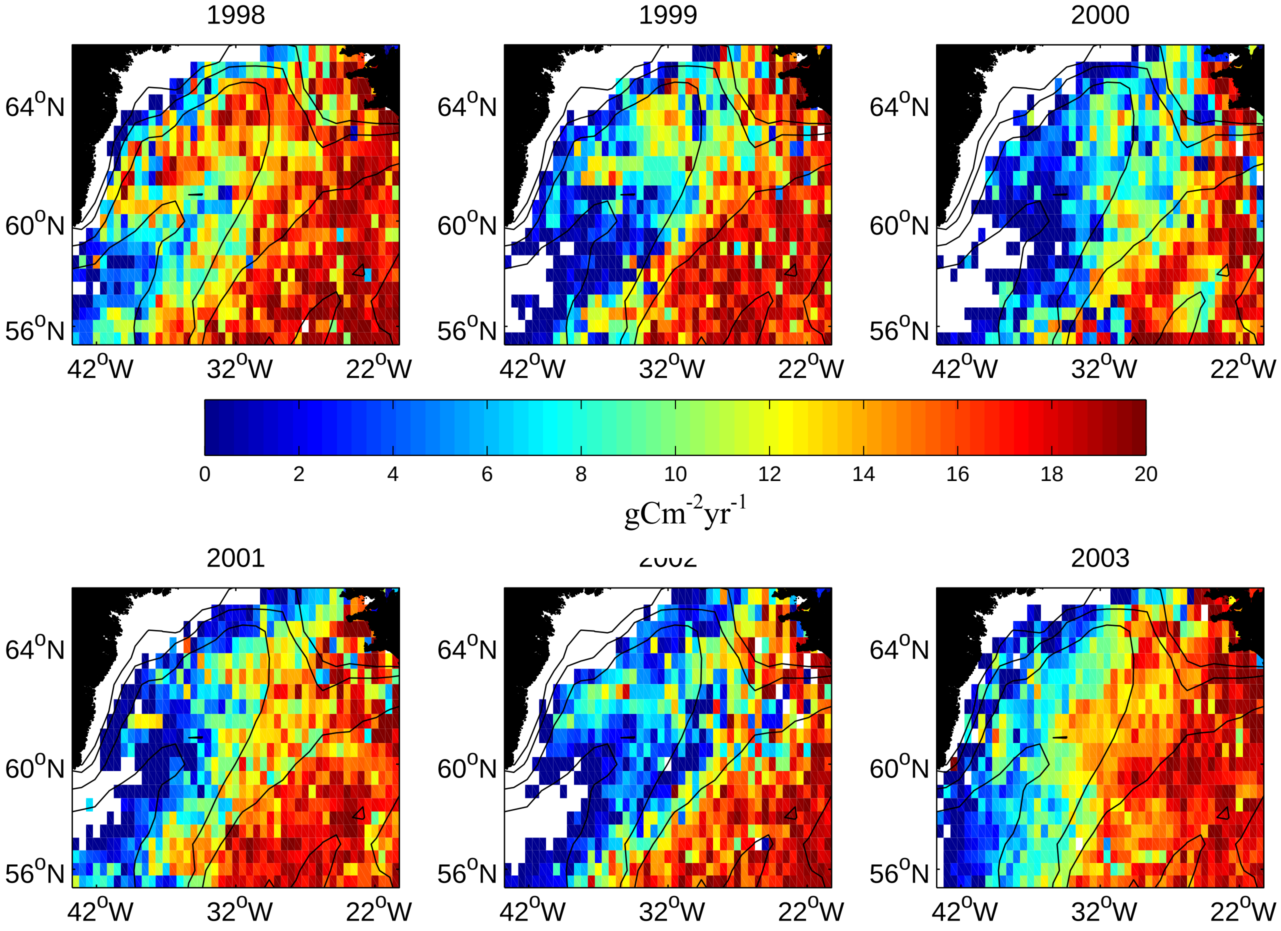

Figure 8.7: Additional production after silica has become depleted and until nitrate has reached its annual minimum concentration. The amount of nitrate consumed is converted into units of carbon using the Redfield ratio (Redfield et al., 1963)

9. SUMMARY:

9.1. SUMMARY OF CONCLUSIONS:

This thesis aimed to characterise the physical controls on spring bloom dynamics in the Irminger Basin. By combining satellite, *in situ* and model data a comprehensive picture of the impact of interannual meteorological variability on the phytoplankton population has been constructed.

The unique seasonally-resolved data from the Marine Productivity cruises has allowed an examination of the temporal variability in temperature-nutrient relationships. They are usually assumed to be linear and interannually invariant, but in this study they were found to have a seasonal dependence. The linear relationship between temperature and nutrient breaks down during spring and summer. This non-linearity can be corrected, however, by including chlorophyll concentration in the regression. These relationships allow nitrate, phosphate and silica to be estimated at high spatial and temporal resolution from satellite SST and chlorophyll-a data.

Satellite chlorophyll concentration was successfully used to divide the study area into four biogeographical provinces. Cluster analysis and Empirical Orthogonal Function analysis produced similar zones – the Central Irminger Sea, Reykjanes Ridge, East Greenland coast and Iceland shelf. Satellite chlorophyll concentration can thus be used to objectively divide a region into provinces which have distinct biological characteristics.

Interannual variability in the chlorophyll concentration throughout the basin was found to be statistically significant. Objective methods for determining the start and end of a spring bloom were developed. The interannual range in the start of the spring bloom could be up to thirty days at any particular location. A later start to the bloom was not reflected in a curtailed bloom, either in magnitude or duration. This suggests a larger than expected (considering the study area's high latitude) ‘window of opportunity’ in which phytoplankton can successfully grow.

The influence of meteorology on chlorophyll concentration was found to differ between the biogeographic provinces and between the pre- and post-bloom periods. The roles of wind speed, net heat flux, PAR and SST were investigated using Generalised Linear Modelling. In the Central Irminger Sea and Reykjanes Ridge regions net heat flux and PAR are influential prior to the bloom and temperature and wind speed are important post-bloom. On the Greenland coast no single meteorological factor dominated the model.

A method of estimating Sverdrup’s critical depth from satellite and Argo float data was developed. The critical depth model was found to work well in the Irminger Basin, with the spring bloom never commencing before the mixed layer depth was shallower than the critical depth. There was however a delay of up to ~20 days before the bloom started, suggesting that the critical depth model is a necessary but not sufficient criterion for the start of the spring bloom.

In addition to the critical depth criterion, net heat flux and PAR were found to be central to the timing of the initiation of the bloom. A positive net heat flux (into the ocean) for at least five consecutive days and PAR > 81 W m^{-2} for at least two consecutive days is required for a bloom to start. These criteria were found to be valid for the entire Irminger Basin, with the exception of the East Greenland coast, where the bloom begins when PAR is only ~30 W m^{-2}. The *in situ* data revealed that an early, dense bloom of *Phaeocystis* sp. was thriving in an area of freshwater stratification.

After the peak of the spring bloom in the Irminger Basin chlorophyll concentrations remain elevated relative to winter throughout the summer. The decline of the peak of the bloom is not likely to be light limited, as mixed layer depth, seen both in Argo float and modelled data, remains shallow. The high temporal and spatial resolution of the nutrient estimates made from remotely sensed SST and chlorophyll allowed nutrient limitation to be examined. Nitrate and phosphate were not found to be limiting at any time. Silica was found to be depleted in most parts of the basin, with the western parts of the basin becoming depleted up to two months before the central basin.

The East Greenland coast was found to have unusual characteristics – the bloom started earliest in this region and was more variable interannually in magnitude and duration than the rest of the basin. Whilst 2001 experienced anomalously high concentrations of chlorophyll, 2002 had exceptionally low concentrations. Satellite derived wind speed and direction data revealed that 2002 experienced anomalously strong easterly winds, associated with greater than average heat losses during the winter. This weather pattern is attributable to the Greenland tip-jet, itself affected by shifts in the North Atlantic Oscillation. The winter of 2001 was warmer than normal with no prevailing wind direction. The Greenland tip-jet thus affects not only the physical oceanography, but also the spring bloom in the Irminger Basin.

Given daily estimates of nutrient concentration the timing of nutrient depletion in relation to phytoplankton community succession could be examined. Silica is essential to diatom growth and so maps of timing of silica depletion also represent the transition from a diatom dominated community composition to non-siliceous species. As diatoms contribute massively to export production in the North Atlantic this also gives an indication of the timing of export production. A method for estimating a lower bound on export production based on satellite derived primary production and timing of silica depletion was developed. Additionally the contributions to export by diatoms and non-diatoms was estimated on the basis of silica to nitrate drawdown ratios. Basin wide mean export production is estimated at ~60 $gCm^{-2}yr^{-1}$, in line with *in situ* estimates, with the contribution by diatoms estimated at ~65 %.

At the end of the growth season nitrate remains above limiting concentrations, contrary to the expected spring bloom progression in the North Atlantic. Chlorophyll concentrations remain high throughout summer, although nitrate is not consumed, suggesting that production is relying on recycled forms of nitrate. Fast Repetition Rate Fluorometer data suggest that the phytoplankton may be iron limited at the end of the bloom.

9.2. REFLECTIONS ON DATA SOURCES:

The Marine Productivity programme collected a unique, seasonally resolved data set in a rarely visited part of the North Atlantic. The series of cruises allowed the seasonal variability in the physical and biological characteristics of the Irminger Basin to be examined. For example, the seasonality in the temperature-nutrient relationships could be considered. The *in situ* data does have its limitations however. CTD stations are a point measurement in space and time and tend to be very widely spaced. Cruise data are also not synoptic – during a several week cruise the data collected effectively make up a single time series. Even when, as in the Marine Productivity programme, a region is visited more than once it can be difficult to determine whether the data are typical of the region.

Satellite data provide the required spatial and temporal context. At a sampling frequency up to daily, 1 km resolution satellite data allow an assessment of the spatial and temporal variability of a region and therefore an understanding of the representativeness of *in situ* point samples. In the case of the Marine Productivity programme both the spring and summer cruises measured somewhat low concentrations of chlorophyll, although higher than measured during the winter cruises. Supplied only with this data one might conclude that the spring bloom in the Irminger Basin was not very pronounced, with a steady concentration of chlorophyll throughout spring and summer. Certainly, one would be unable to define key characteristics of the bloom: its timing, magnitude or duration. In this case the satellite data are essential to fill in the gaps in the *in situ* data and determine the bloom characteristics. As revealed by the satellite data, the Irminger Basin actually experiences a distinct bloom with a peak in late spring and elevated chlorophyll concentrations throughout summer.

How can one be sure that the data collected during a cruise are representative of that region? Climate scale changes, such as an El Niño event or a shift in the North Atlantic Oscillation, can impact on the physical and biological environment. On a smaller scale meteorological conditions are likely to differ interannually and may have a knock-on effect on the ecosystem. To quantify perturbations to the ecosystem one must first have knowledge of the ‘normal’ state of the system. Establishing this baseline requires a long time series of observations – only then can anomalies from the mean be determined. In the case of the Marine Productivity programme, which sampled the Irminger Basin in 2002, can we be sure that the cruises took place in a typical year? The satellite data allow an assessment of the interannual variability over several years. In the Irminger Basin 2002 actually experienced anomalously low chlorophyll concentrations and was not representative of a typical year.

This additional context provided by satellite data is not only useful in its own right, but feeds into modelling studies too. One of the outputs of the Marine Productivity programme will be a food web model based on the data collected during the cruises. However, 2002 was not representative of a normal year in the Irminger Basin and a model initiated with these data may be incorrectly parameterised and unable to accurately reproduce conditions in other years. The satellite data alerts us to the possibility of interannual variability and provides the temporal framework in which to understand the model results.

In all these examples satellite data supply the spatial and temporal context in which the *in situ* data should be considered. However, satellite data also have shortcomings. Of several important biological parameters only chlorophyll-a concentration can be measured directly by satellites. Key biological parameters such as nutrient concentration, community composition, zooplankton grazing and distribution of chlorophyll with depth cannot be observed directly by satellites. Additionally satellites sense only the surface of the sea and cannot detect the vertical distribution of any water property. However, by combining satellite and *in situ* data the capabilities of both can be extended. For example, nutrients can be estimated from SST and chlorophyll concentration, and thus inferences can be drawn about community composition. Models are available which estimate the vertical profile of biomass from surface chlorophyll, and vertical mixing models can estimate mixed layer depth from surface winds and heat flux. All of these applications of satellite data first require good quality *in situ* data. Only by combining the two data sources are the full capabilities of both realised.

Satellite data have inherent inaccuracies – particularly in the retrieval of chlorophyll concentration. These uncertainties are well documented and in some cases are no greater than those associated with *in situ* measurements. Provided the limitations of the satellite data are kept in mind, the advantages – synoptic data at high spatial and temporal resolution – far outweigh the uncertainties. Indeed, the satellite measurements have provided an invaluable addition to the Marine Productivity data set, enriching and extending the potential of the *in situ* data. The satellite data have allowed a more complete picture of the physical controls on primary productivity in the Irminger Basin to be obtained.

9.3. FUTURE WORK:

This study focussed on the Irminger Basin in the sub-polar North Atlantic. The wider applicability of the techniques developed and the conclusions drawn to other regions of the North Atlantic, and indeed other ocean basins, should be investigated. For example, the use of a multiple regression of SST and chlorophyll concentration to derive nitrate, phosphate and silica concentrations from satellite data could be applicable to other, non-oligotrophic regions. The regression equations will be different in different biogeographic provinces, but global databases of nutrient measurements could be exploited to derive the individual relationships. In this way global estimates of nutrient drawdown, and hence new production, could be made. The technique may not be applicable however, in oligotrophic regions, where SST and chlorophyll concentration are relatively constant throughout the year.

The method developed in this study for estimating critical depth from satellite data is also expected to be applicable to other regions. The global coverage of Argo floats makes a broader study feasible and critical depth and mixed layer depth could be estimated within biogeographic provinces. Because an objective method for estimating the start date of the bloom has been devised here, the time when mixed layer depth becomes shallower than critical depth could be compared to bloom timing globally. Perhaps the delay between Sverdrup's critical depth criteria being met and the start of the bloom observed in this study also applies in other ocean basins? With the global coverage of satellite data, criteria for the initiation of a bloom in terms of net heat flux and PAR could be established. Will they be the same as in the Irminger Basin? Or perhaps other factors, such as wind speed, would be found to be the key to bloom timing. Again, these techniques are only likely to be appropriate in regions where a distinct seasonal increase in chlorophyll concentration occurs i.e. not oligotrophic regions.

In the Irminger Basin itself, a topic which could be further developed is a more accurate representation of community composition. Nutrient availability or depletion implies a certain community dominance, but the composition may be better determined from accessory pigment concentrations (e.g. fucoxanthin is an indicator of diatom presence). Pigments were determined on the cruises by HPLC and it may be possible to relate the relative concentrations of these pigments to satellite chlorophyll concentration, SST or nutrient concentration, and hence estimate the community composition. The cruise data are however limited as the community composition was fairly similar in both the spring and summer cruises, so that the two end-members of any relationship may not have been captured.

The parameters relating to the health of the phytoplankton photosynthetic machinery measured by the FRRF may also be related to nutrient concentration, and hence could be estimated from satellite-derived parameters. It may be possible to construct a time series of F_v/F_m and σ_{PSII} and so determine the timing of potential iron limitation.

The potential impact of interannual variability in the strength of the Greenland tip-jet on the spring bloom is also worth investigating further. The wind stress and zonal and meridional components of the wind speed could be studied for interannual variability. In addition, factors such as sea level pressure or air temperature may have an impact on the tip-jet. It may be that the state of the North Atlantic Oscillation, via its influence on winter storm tracks, is impacting on the following spring's biological productivity in the Irminger Basin.

BIBLIOGRAPHY:

Aiken, J., G. F. Moore, C. C. Trees, S. B. Hooker and D. K. Clark (1995), The SeaWiFS CZCS-type algorithm, SeaWiFS Pre-Launch Technical Report Series, Volume 29, pp 37.

Allen, J. T. and Marine Productivity researchers (2004), RRS Discovery cruise 267: Biophysical studies of zooplankton dynamics in the northern North Atlantic: winter, NERC.

Alvarez-Salgado, X. A., S. Beloso, I. Joint, E. Nogueira, L. Chou, F. F. Perez, S. B. Groom, J. M. Cabanas, A. P. Rees and M. Elskens (2002), New production of the NW Iberian shelf during the upwelling season over the period 1982-1999, *Deep Sea Research I*, **49**, 1725-1739.

Anderson, V. and L. Prieur (2000), One-month study in the open NW Mediterranean Sea (DYNAPROC experiment, May 1995): overview of the hydrobiogeochemical structures and effects of wind events, *Deep Sea Research I*, **47**(3), 397-422.

Antoine, D. and A. Morel (1996), Oceanic primary production. 1. Adaptation of a spectral light-photosynthesis model in view of application to satellite chlorophyll observations, *Global Biogeochemical Cycles*, **10**(1), 43-55.

Antonov, J. I., S. Levitus, T. P. Boyer, M. E. Conkright, T. D. O'Brien and C. Stephens (1998), World Ocean Atlas 1998. Volume 1: Temperature of the Atlantic Ocean, NOAA Atlas NESDIS (27), NOAA National Oceanographic Data Center, Silver Spring, MD, pp 166.

Astoreca, R. (2003), Phytoplankton production in the Irminger Basin, NE Atlantic, in summer and winter 2002, MSc Thesis, School of Ocean and Earth Sciences, University of Southampton, pp 53.

Aufdenkampe, A. K., J. J. McCarthy, C. Navarette, M. Rodier, J. Dunne and J. W. Murray (2002), Biogeochemical controls on new production in the tropical Pacific, *Deep Sea Research II*, **49**, 2619-2648.

Azumaya, T., Y. Isoda and S. Noriki (2001), Modeling of the spring bloom in Funka Bay, Japan, *Continental Shelf Research*, **21**, 473-494.

Backhaus, J. O., E. N. Hegseth, H. Wehde, X. Irigoien, K. Hatten and K. Logemann (2003), Convection and primary production in winter, *Marine Ecology Progress Series*, **251**, 1-14.

Bacon, S. (1997), Circulation and fluxes in the North Atlantic between Greenland and Iceland, *Journal of Physical Oceanography*, **27**, 1420-1435.

Bacon, S., L. R. Centurioni and W. J. Gould (2001), The evaluation of salinity measurements from PALACE floats, *Journal of Atmospheric and Oceanic Technology*, **18**(7), 1258-1266.

Bacon, S., W. J. Gould and Y. Jia (2003), Open-ocean convection in the Irminger Sea, *Geophysical Research Letters*, **30**(5), 1246; doi:10.1029/2002GL016271.

Ballestero, D. (1999), Remote sensing of vertically structured phytoplankton pigments, *Topicos Meteorologicos y Oceanograficos*, **6**(1), 14-23.

Barlow, R. G., R. F. C. Mantoura, M. A. Gough and T. W. Fileman (1993), Pigment signatures of the phytoplankton bloom composition in the Northeastern Atlantic during the 1990 spring bloom, *Deep Sea Research II*, **40**(1/2), 459-477.

Behrenfeld, M. J. and P. G. Falkowski (1997), Photosynthetic rates derived from satellite-based chlorophyll concentrations, *Limnology and Oceanography*, **42**(1), 1-20.

Behrenfeld, M. J. and Z. Kolber (1999), Widespread iron limitation of phytoplankton in the South Pacific Ocean, *Science*, **283**(5403), 840-843.

Bianchi, T. S., C. Lambert and D. C. Biggs (1995), Distribution of chlorophyll a and phaeopigments in the northwestern Gulf of Mexico: a comparison between fluorometric and high-performance liquid chromatography measurements, *Bulletin of Marine Science*, **56**(1), 25-32.

Bishop, J. K. B. and W. B. Rossow (1991), Spatial and temporal variability of global surface solar irradiance, *Journal of Geophysical Research*, **96**(C9), 16,839-16,858.

Bishop, J. K. B., W. B. Rossow and E. G. Dutton (1997), Surface solar irradiance from the International Satellite Cloud Climatology Project, 1983-1991, *Journal of Geophysical Research*, **102**(D6), 6883-6910.

Bjornsson, H. and S. A. Venegas (1997), A Manual for EOF and SVD Analyses of Climatic Data, http://www.dcess.ku.dk/~silvia/eofsvd/eofsvd.pdf.

Boyd, P. and E. R. Abraham (2001), Iron-mediated changes in phytoplankton photosynthetic competence during SOIREE, *Deep Sea Research II*, **48**, 2529-2550.

Boyd, P. and P. J. Harrison (1999), Phytoplankton dynamics in the NE subarctic Pacific, *Deep Sea Research II*, **46**(11/12), 2405-2432.

Boyd, P. W. (2002), The role of iron in the biogeochemistry of the Southern Ocean and equatorial Pacific: a comparison of in situ iron enrichments, *Deep Sea Research II*, **49**(9/10), 1803-1821.

Boye, M., A. P. Aldrich, C. M. G. van den Berg, J. T. M. de Jong, M. Veldhuis and H. J. W. de Baar (2003), Horizontal gradient of the chemical speciation of iron in surface waters of the northeast Atlantic Ocean, *Marine Chemistry*, **80**(2/3), 129-143.

Brierley, A. and Marine Productivity researchers (2003), RRS Discovery cruise 264: Biophysical studies of zooplankton dynamics in the northern North Atlantic: summer, 25 July - 28 August 2002, NERC, pp 108.

Brown, L., R. Sanders, G. Savidge and C. H. Lucas (2003), The uptake of silica during the spring bloom in the Northeast Atlantic Ocean, *Limnology and Oceanography*, **48**(5), 1831-1845.

Brzezinski, M. A. (1985), The Si:C:N ratio of marine diatoms. Interspecific variability and the effect of some environmental variables, *Journal of Phycology*, **21**, 347-357.

Brzezinski, M. A., T. A. Villareal and F. Lipschultz (1998), Silica production and the contribution of diatoms to new and primary production in the central North Pacific, *Marine Ecology Progress Series*, **167**, 89-104.

Campbell, J. W. (1995), The lognormal distribution as a model for bio-optical variability in the sea, *Journal of Geophysical Research*, **100**(C7), 13237-13254.

Centurioni, L. R. and W. J. Gould (2004), Winter conditions in the Irminger Sea observed with profiling floats, *Journal of Marine Research*, **62**(3), 313-336.

Chan, A. (1978), Comparative physiological study of marine diatoms and dinoflagellates in relation to irradiance and cell size. 1. Growth under continuous light, *Journal of Phycology*, **14**, 396-402.

Chavez, F. P., S. K. Service and S. E. Buttrey (1996), Temperature-nitrate relationships in the central and eastern tropical Pacific, *Journal of Geophysical Research*, **101**(C9), 20553-20563.

Clark, D. K. (1997), Bio-optical algorithms - Case 1 waters, MODIS: Algorithm theoretical basis document (ATBD-MOD-18), pp 25, http://modis.gsfc.nasa.gov/data/atbd/atbd_mod18.pdf.

Clarke, R. A. and J. Gascard (1983), The formation of the Labrador Sea water. Part I: Large-scale processes, *Journal of Physical Oceanography*, **13**, 1764-1778.

Colebrook, J. M. (1979), Continuous plankton records: Seasonal cycles of phytoplankton and copepods in the North Atlantic Ocean and the North Sea, *Marine Biology*, **51**, 23-32.

Colebrook, J. M. (1982), Continuous plankton records: Seasonal variations in the distribution and abundance of plankton in the North Atlantic Ocean and the North Sea, *Journal of Plankton Research*, **4**, 435-462.

Cota, G. F., W. O. Smith and B. G. Mitchell (1994), Photosynthesis of phaeocystis in the Greenland Sea, *Limnology and Oceanography*, **39**(4), 948-953.

Cota, G. F., W. G. Harrison, T. Platt, S. Sathyendranath and V. Stuart (2003), Bio-optical properties of the Labrador Sea, *Journal of Geophysical Research*, **108**(C7), 3228, doi:10.1029/2000JC000597.

Davies, A. G. and J. A. Sleep (1981), The photosynthetic response of nutrient-depleted dilute cultures of Skeletonema costatum to pulses of ammonium and nitrate: the importance of phosphate, *Journal of Plankton Research*, **11**, 141-164.

Davison, I. R. (1991), Environmental effects on algal photosynthesis: Temperature, *Fisheries Bulletin*, **70**, 1063-1085.

Dawdy, D. R. and N. C. Matalas (1964), Statistical and probability analysis of hydrologic data, part III: Analysis of variance, covariance and time series, in *Handbook of applied hydrology, a compendium of water-resources technology*, edited V. T. Chow. New York, McGraw-Hill, pp 8.69-8.90.

De Baar, H. J. H. (1994), Von Liebig's Law of the Minimum and plankton ecology (1899-1991). *Progress in Oceanography*, **33**, 347-386.

Demmel, J. (1997), Applied Numerical Linear Algebra, Philadelphia, SIAM.

Dickson, R. J. (2003), Stirring times in the Atlantic, *Nature*, **424**(6945), 141-142.

Dickson, R. J., J. R. N. Lazier, J. Meincke, P. Rhines and J. Swift (1996), Long term coordinated changes in the convective activity of the North Atlantic, *Progress in Oceanography*, **38**, 241-295.

Dierssen, H. M. and R. C. Smith (2000), Bio-optical properties and remote sensing ocean color algorithms for Antarctic Peninsula waters, *Journal of Geophysical Research*, **105**(C11), 26,301-26,312.

Dobson, A. J. (1990), An introduction to generalized linear models, 2nd Edition, London, Chapman and Hall, pp 225.

Doyle, J. D. and M. A. Shapiro (1999), Flow response to large-scale topography: the Greenland tip jet, *Tellus*, **51**, 728-748.

Dugdale, R. C., C. O. Davis and F. P. Wilkerson (1997), Assessment of new production at the upwelling center at Point Conception, California, using nitrate estimated from remotely sensed sea surface temperature, *Journal of Geophysical Research*, **102**(C4), 8573-8585.

Dugdale, R. C. and J. J. Goering (1967), Uptake of new and regenerated forms of nitrogen in primary productivity, *Limnology and Oceanography*, **12**, 196-206.

Dugdale, R. C. and F. P. Wilkerson (1998), Silicate regulation of new production in the equatorial Pacific upwelling, *Nature*, **391**(6664), 270-273.

Dugdale, R. C., F. P. Wilkerson and H. J. Minas (1995), The role of a silicate pump in driving new production, *Deep Sea Research I*, **42**(5), 697-719.

Durbin, E. G., R. G. Campbell, M. C. Casas, M. D. Ohman, B. Niehoff, J. Runge and M. Wagner (2003), Interannual variation in phytoplankton blooms and zooplankton productivity and abundance in the Gulf of Maine during winter, *Marine Ecology Progress Series*, **254**, 81-100.

Dutkiewicz, S., M. Follows, J. Marshall and W. W. Gregg (2001), Interannual variability of phytoplankton abundances in the North Atlantic, *Deep Sea Research II*, **48**, 2323-2344.

Duysens, L. N. M. (1956), The flattening of the absorption spectrum of suspensions as compared with that of solutions, *Biochimica et Biophysica Acta*, **19**, 255-261.

Ebert, U., M. Arrayas, N. Temme, B. Sommeijer and J. Huisman (2001), Critical conditions for phytoplankton blooms, *Bulletin of Mathematical Biology*, **63**(6), 1095-1124.

Eden, C. and C. Boning (2002), Sources of eddy kinetic energy in the Labrador Sea, *Journal of Physical Oceanography*, **32**, 3346-3363.

Egge, J. K. and D. L. Aksnes (1992), Silicate as regulating nutrient in phytoplankton competition, *Marine Ecology Progress Series*, **83**, 281-289.

Epperson, J. F. (2002), An introduction to numerical methods and analysis, John Wiley and Sons, pp 576.

Eppley, R. W. (1972), Temperature and phytoplankton growth in the sea, *Fisheries Bulletin*, **70**, 1063-1085.

Eppley, R. W. and B. J. Peterson (1979), Particulate organic matter flux and planktonic new production in the deep ocean, *Nature*, **282**, 677-680.

Eppley, R. W., J. N. Rogers and J. J. McCarthy (1969), Half-saturation constants for uptake of nitrate and ammonium by marine phytoplankton, *Limnology and Oceanography*, **14**(912-920).

Eslinger, D. L. and R. L. Iverson (2001), The effects of convective and wind-driven mixing on spring phytoplankton dynamics in the Southeastern Bering Sea middle shelf domain, *Continental Shelf Research*, **21**(6-7), 627-650.

Falkowski, P. G. (1997), Evolution of the nitrogen cycle and its influence on the biological CO2 pump in the ocean, *Nature*, **387**, 272-275.

Falkowski, P. G. and J. A. Raven (1997), Aquatic photosynthesis, Oxford, Blackwell Science, pp 375.

Falkowski, P. G., R. T. Barber and V. Smetacek (1998), Biogeochemical controls and feedbacks on ocean primary production, *Science*, **281**(5374), 200-206.

Falkowski, P. G., R. M. Greene and R. J. Geider (1992), Physiological limitations on phytoplankton productivity in the ocean, *Oceanography*, **5**, 84-91.

Falkowski, P. G., R. J. Scholes, E. Boyle, J. Canadell and 13 others (2000), The global carbon cycle: a test of our knowledge of earth as a system, *Science*, **290**, 291-296.

Follows, M. and S. Dutkiewicz (2002), Meteorological modulation of the North Atlantic spring bloom, *Deep Sea Research II*, **49**, 321-344.

Forsythe, W. C., E. J. Rykiel, R. S. Stahl, H. Wu and R. M. Schoolfield (1995), A model comparison for daylength as a function of latitude and day of year, *Ecological Modelling*, **80**, 87-95.

Frantantoni, D. M. (2001), North Atlantic surface circulation during the 1990's observed with satellite-tracked drifter, *Journal of Geophysical Research*, **106**, 22067-22094.

Frouin, R., B. A. Franz and P. J. Werdell (2003), The SeaWiFS PAR product, in *SeaWiFS Post-launch Technical Series, Volume 22: Algorithm updates for the fourth SeaWiFS data reprocessing*, pp 46-49.

Furnas, M. J. (1990), In situ growth rates of marine phytoplankton: approaches to measurement, community and species growth rate, *Journal of Plankton Research*, **12**, 1117-1151.

Geider, R. J., R. M. Greene, Z. Kolber, H. MacIntyre and P. G. Falkowski (1993), Fluorescence assessment of the maximum quantum efficiency of photosynthesis in the western North Atlantic, *Deep Sea Research*, **40**, 1205-1224.

Gill, A. E. (1982), Atmosphere-Ocean Dynamics, International Geophysics Series, New York, Academic Press, pp 662.

Gislason, A. and O. S. Astthorsson (2000), Winter distribution, ontogenetic migration, and rates of egg production of *Calanus finmarchicus* southwest of Iceland, *ICES Journal of Marine Science*, **57**, 1727-1739.

Goericke, R. and J. P. Montoya (1998), Estimating the contribution of microalgal taxa to chlorophyll a in the field - variations of pigment ratios under nutrient- and light-limited growth, *Marine Ecology Progress Series*, **169**, 97-112.

Goes, J. I., T. Saino, H. Oaku, J. Ishizaka, C. S. Wong and Y. Nojiri (2000), Basin scale estimates of sea surface nitrate and new production from remotely sensed sea surface temperature and chlorophyll, *Geophysical Research Letters*, **27**(9), 1263-1266.

Goes, J. I., T. Saino, H. Oaku and D. L. Jiang (1999), A method for estimating sea surface nitrate concentrations from remotely sensed SST and chlorophyll a - A case study for the North Pacific Ocean using OCTS/ADEOS data, *IEEE Transactions on Geoscience and Remote Sensing*, **37**(3), 1633-1644.

Gong, G.-C., K.-K. Liu and S.-C. Pai (1995), Prediction of nitrate concentration from two end member mixing in the Southern East China Sea, *Continental Shelf Research*, **15**, 827-842.

Gordon, H. R. and D. K. Clark (1980), Remote sensing optical properties of a stratified ocean: An improved interpretation, *Boundary-Layer Meteorology*, **8**, 300-313.

Gordon, H. R. and W. R. McCluney (1975), Estimation of the depth of sunglint penetration in the sea for remote sensing, *Applied Optics*, **14**, 413-416.

Gran, H. H. and T. Braarud (1935), A quantitative study of the phytoplankton in the Bay of Fundy and the Gulf of Maine, *Journal of the Biological Board of Canada*, **1**(5), 279-467.

Grant, A. B. (1968), Atlas of oceanographic sections, Report 68-5, Bedford Institute, Nova Scotia, pp 80.

Gregg, W. W., P. Ginoux, P. S. Schopf and N. W. Casey (2003), Phytoplankton and iron: validation of a global three-dimensional ocean biogeochemical model, *Deep Sea Research II*, **50**, 3143-3169.

Hastings, D. (2001), Advanced Very High Resolution Radiometer (AVHRR): Overview, http://www.ngdc.noaa.gov/seg/globsys/avhrr.shtml.

Hawkins, D. M., M. W. Muller and J. A. ten Krooden (1982), Cluster Analysis, in *Topics in multivariate analysis*, edited D. M. Hawkins. Cambridge, Cambridge University Press.

Heath, M. R. (1999), The ascent migration of the copepod *Calanus finmarchicus* from overwintering depths in the Faroe-Shetland Channel, *Fisheries Oceanography*, **8**(Supplement 1), 84-99.

Heath, M. R., P. R. Boyle, A. Gislason, W. S. C. Gurney, S. J. Hay, E. J. H. Head, S. Holmes, A. Ingvarsdottir, S. H. Jonasdottir, P. Lindeque, R. T. Pollard, J. Rasmussen, K. Richards, K. Richardson, G. Smerdon and D. Speirs (2004), Comparative ecology of over-wintering *Calanus finmarchicus* in the northern North Atlantic, and implications for life-cycle patterns, *ICES Journal of Marine Science*, **61**, 698-708.

Heath, M. R., J. G. Fraser, A. Gislason, S. J. Hay, S. H. Jonasdottir and K. Richardson (2000), Distribution and abundance of overwintering *Calanus finmarchicus* in the Northeast Atlantic, *ICES Journal of Marine Science*, **57**, 1628-1635.

Heath, M. R., J. Rasmussen, A. Ingvarsdottir and S. J. Hay (2005), Seasonal changes in the vertical distribution of Calanus finmarchicus in the Irminger Sea. Presented at: Biophysical Interactions in High Latitude Oceans, April 2005, BAS, Cambridge, UK.

Hecky, R. E. and P. Kilham (1988), Nutrient limitations of phytoplankton in freshwater and marine environments; a review of recent evidence on the effects of enrichment, *Limnology and Oceanography*, **33**, 796-822.

Henson, S. A., R. Sanders, J. T. Allen, I. S. Robinson and L. Brown (2003), Seasonal constraints on the estimation of new production from space using temperature-nitrate relationships, *Geophysical Research Letters*, **30**(17), 1912; doi:10.1029/2003GL017982.

Hernandez-de-la-Torre, B., G. Gaxiola-Castro, S. Alvarez-Borrego, J. Gomez-Valdes and S. Najera-Martinez (2003), Interannual variability of new production in the southern region of the California Current, *Deep Sea Research II*, **50**, 2423-2430.

Hirche, H. J. (1996), Diapause in the marine copepod, *Calanus finmarchicus*: a review, *Ophelia*, **44**, 129-143.

Hirche, H. J., T. Brey and B. Niehoff (2001), A high frequency time series at Weathership M, Norwegian Sea: population dynamics of *Calanus finmarchicus*, *Marine Ecology Progress Series*, **219**, 205-219.

Hitchcock, G. L. and T. J. Smayde (1977), The importance of light in the initiation of the 1972-1973 winter-spring diatom bloom in Narragansett Bay, *Limnology and Oceanography*, **22**, 126-131.

Holeton, C., L. Brown, R. Sanders and S. A. Henson (2004), Phytoplankton community structure and timing of export production in the Irminger Basin. Challenger Conference for Marine Science, September 2004, Liverpool, UK.

Holliday, N. P., J. J. Waniek, R. Davidson, L. Brown, R. Sanders, S. A. Henson, R. T. Pollard and J. T. Allen (2005), Large-scale physical controls on phytoplankton growth in the Irminger Sea Part I: Observations, *Journal of Marine Systems*, **Submitted**.

Holm-Hansen, O. and B. G. Mitchell (1991), Spatial and temporal distribution of phytoplankton and primary production in the western Bransfield Strait region, *Deep Sea Research, Part A*, **38**(8/9), 961-980.

Hooker, S. B., W. E. Esaias, G. C. Feldman, W. W. Gregg and C. R. McClain (1992), An overview of SeaWiFS: and ocean color, SeaWiFS Pre-Launch Technical Report Series, Volume 1, pp 27.

Horn, H. and L. Paul (1984), Interactions between light situation, depth of mixing and phytoplankton growth during the spring period of full circulation, *Internationale Revue der gesamten Hydrobiologie,* **69**, 507-519.

Houghton, R. and Y. Tourre (1992), Characteristics of low-frequency sea surface fluctuations in the tropical Atlantic, *Journal of Climate*, **5**, 765-771.

Huisman, J., P. Van Oostveen and F. J. Weissing (1999), Critical depth and critical turbulence: two different mechanisms for the development of phytoplankton blooms, *Limnology and Oceanography*, **44**(7), 1781-1787.

Jeffrey, S. W. and G. F. Humphrey (1975), New spectrophotometric equation for determining chlorophyll a, b c1 and c2, *Biochemie und Physiologie der Pflanzen,* **167**, 191-204.

Jeffrey, S. W. and M. Vesk (1997), Introduction to marine phytoplankton and their pigment signatures, in *Phytoplankton pigments in oceanography: guidelines to modern methods,* edited S.W.Jeffrey, UNESCO, pp 37-85.

JGOFS (1991), Core measurement protocols: Report of the Core Measurement Working Groups, SCOR, ICSC.

Jolliffe, I. T. (1989), Rotation of ill-defined principal components, *Applied Statistics*, **38**, 139-147.

Josey, S. A., E. C. Kent and P. K. Taylor (1999), New insights into the ocean heat budget closure problem from analysis of the SOC air-sea flux climatology, *Journal of Climate*, **12**(9), 2856-2880.

Kamykowski, D., S.-J. Zentara, J. M. Morrison and A. C. Switzer (2002), Dynamic global patterns of nitrate, phosphate, silicate and iron availability and phytoplankton community composition from remote sensing data, *Global Biogeochemical Cycles*, **16**(4), 1077, doi:10.1029/2001GB001640.

Kanamitsu, M. (1989), Description of the NMC global data assimilation and forecast system, *Weather and Forecasting*, **4**, 335-342.

Kanamitsu, M., J. C. Alpert, K. A. Campana, P. M. Caplan, D. G. Deaven, M. Iredell, B. Katz, H.-L. Pan, J. Sela and G. H. White (1991), Recent changes implemented into the global forecast system at NMC, *Weather and Forecasting*, **6**, 425-435.

Kirk, J. T. O. (1994), Light and photosynthesis in aquatic ecosystems. 2nd edition, Cambridge University Press, pp 509.

Kirkwood, D. C. (1995), The SanPlus segmented flow Autoanalyser and its applications, Scalar Analytical BV Publications.

Koeve, W. (2001), Wintertime nutrients in the North Atlantic—new approaches and implications for new production estimates, *Marine Chemistry*, **74**, 245-260.

Kolber, Z. and P. G. Falkowski (1993), Use of active fluorescence to estimate phytoplankton photosynthesis in situ, *Limnology and Oceanography*, **38**(8), 1646-1665.

Kolber, Z., O. Prasil and P. G. Falkowski (1998), Measurements of variable chlorophyll fluorescence using fast repetition rate techniques: defining methodology and experimental protocols, *Biochimica et Biophysica Acta*, **1367**, 88-106.

Korb, R. E. and M. Whitehouse (2004), Contrasting primary production regimes around South Georgia, Southern Ocean: large blooms versus high nutrient, low chlorophyll waters, *Deep Sea Research I*, **51**(5), 721-738.

Kovala, P. E. and J. D. Larrance (1966), Comparison of phytoplankton cell numbers, cell volume, cell surface and plasma volume, per metre, from microscopic counts, Special Report No. 36, University of Washington, Seattle.

Kraus, E. B. and J. S. Turner (1967), A one-dimensional model of the seasonal thermocline, *Tellus*, **19**, 98-105.

Krauss, W. (1995), Currents and mixing in the Irminger Sea and in the Iceland Basin, *Journal of Geophysical Research*, **100**(C6), 10851-10871.

Labry, C., A. Herbland, D. Delmas, P. Laborde, P. Lazure, J. M. Froidefond, A. M. Jegou and B. Sautour (2001), Initiation of winter phytoplankton blooms within the Gironde plume waters in the Bay of Biscay, *Marine Ecology Progress Series*, **212**, 117-130.

Lalli, C. M. and T. M. Parsons (1997), Biological oceanography: an introduction, 2nd Edition, Oxford, Butterworth-Heinemann for the Open University, pp 314.

Laney, S. R. (2003), Assessing the error in photosynthetic properties determined by fast repetition rate fluorometry, *Limnology and Oceanography*, **48**, 2234-2242.

Langdon, C. (1988), On the causes of interspecific differences in the growth-irradiance relationship for phytoplankton. II. A general review, *Journal of Plankton Research*, **10**(6), 1291-1312.

Lavender, K. L. (2002), Observations of open-ocean deep convection in the Labrador Sea from subsurface floats, *Journal of Physical Oceanography*, **32**, 511-526.

Lavender, K. L., R. E. Davis and W. B. Owens (2000), Mid-depth recirculation observed in the interior Labrador and Irminger seas by direct velocity measurements, *Nature*, **407**, 66-69.

Laws, E. A., P. G. Falkowski, W. O. Smith Jr., H. Ducklow and J. J. McCarthy (2000), Temperature effects on export production in the open ocean, *Global Biogeochemical Cycles*, **14**(4), 1231-1246.

Le Borgne, R., R. T. Barber, T. Delcroix, H. Y. Inoue, D. J. Mackey and M. Rodier (2002), Pacific warm pool and divergence: temporal and zonal variations on the equator and their effects on the biological pump, *Deep Sea Research II*, **49**(13/14), 2471-2512.

Levitus, S. (1982), Climatological atlas of the world ocean, NOAA Professional Paper 13, U.S. Government Print Office, Washington, DC, pp 173.

Liebig, J. (1840), Die Chemie und ihrer Anwendung auf Agricultur und Physiologie, 4th Edition, London, Taylor and Watson.

Liu, W. T. and W. Tang (1996), Objective interpolation of scatterometer winds, Technical Report 96-19, Jet Propulsion Laboratory, California Institute of Technology.

Longhurst, A. (1998), Ecological Geography of the Sea, San Diego, Academic Press, pp 398.

Longhurst, A., S. Sathyendranath, T. Platt and C. Caverhill (1995), An estimate of global primary production in the ocean from satellite radiometer data, *Journal of Plankton Research*, **17**, 1245-1271.

Mann, K. H. and J. R. N. Lazier (1996), Dynamics of Marine Ecosystems: Biological-Physical Interactions in the Oceans, 2nd Edition, Blackwell Science, pp 394.

Marra, J. (1997), Analysis of diel variability in chlorophyll fluorescence, *Journal of Marine Research*, **55**, 767-784.

Marra, J. (2004), The compensation irradiance for phytoplankton in nature, *Geophysical Research Letters*, **31**, L06305, doi: 10.1029/2003GL018881.

Marshall, J. and F. Schott (1999), Open-ocean convection: Observations, theory and models, *Reviews of Geophysics*, **37**, 1-64.

Martin, J. H., S. E. Fitzwater, R. M. Gordon, C. M. Hunter and S. J. Tanner (1993), Iron, primary production and carbon-nitrogen flux studies during the JGOFS North Atlantic Bloom Experiment, *Deep Sea Research II*, **40**(1/2), 115-134.

Mayor, D., T. Anderson, D. Pond and X. Irigoien (2004), The role of lipids in supporting egg production of *Calanus finmarchicus* in the North Atlantic. Challenger Conference for Marine Science, September 2004, Liverpool, UK.

McClain, C., W. Esaias, S. Hooker and G. Feldman (2000), SeaWiFS Level 1A and Level 2 HDF Dataset Guide Document, http://daac.gsfc.nasa.gov/guides/GSFC/guide/SeaWiFS_L1A2_Guide.gd.html.

McClain, E. P., W. G. Pichel and C. C. Walton (1985), Comparative performance of AVHRR based multichannel sea surface temperatures, *Journal of Geophysical Research*, **90**(C6), 11,587-11,601.

Menden-Deuer, S. and E. J. Lessard (2000), Carbon to volume relationships for dinoflagellates, diatoms, and other protist plankton, Limnology and Oceanography, **45,** 569-579.

Miller, C. B. (2004), Biological Oceanography, Malden, MA, Blackwell Science, pp 402.

Milliff, R. F. and J. Morzel (2001), The global distribution of the time-average wind stress curl from NSCAT, *Journal of Atmospheric Science*, **58**, 109-131.

Minas, H. J. and M. Minas (1992), Net community production in 'High Nutrient-Low Chlorophyll' waters of the tropical and Antarctic oceans: grazing vs iron hypothesis, *Oceanologica Acta*, **15**(2), 145-162.

Mitchell, B. G. (1992), Predictive bio-optical relationships for polar oceans and marginal ice zones, *Journal of Marine Systems*, **3**, 91-105.

Mitchell, B. G. and O. Holm-Hansen (1991), Bio-optical properties of Antarctic Peninsula waters: Differentiation from temperate ocean models, *Deep Sea Research, Part A*, **38**, 1009-1028.

Mitchell, B. G. and D. A. Kiefer (1988), Chlorophyll-a specific absorption and fluorescence excitation spectra for light-limited phytoplankton, *Deep Sea Research, Part A*, **35**(5), 639-663.

Moisan, T. A. and B. G. Mitchell (1999), Photophysiological acclimation of *Phaeocystis antarctica Karsten* under light limitation, *Limnology and Oceanography*, **44**, 247-258.

Moore, C. M., M. I. Lucas, R. Sanders and R. Davidson (2005), Basin-scale variability of phytoplankton bio-optical characteristics in relation to bloom state and community structure in the Northeast Atlantic, *Deep Sea Research I*, **52**, 401-419.

Moore, G. W. K. (2003), Gale force winds over the Irminger Sea to the east of Cape Farewell, Greenland, *Geophysical Research Letters*, **30**(17), 1894; doi:10.1029/2003GL018012.

Moore, J. K., S. C. Doney and K. Lindsay (2004), Upper ocean ecosystem dynamics and iron cycling in a global three-dimensional model, *Global Biogeochemical Cycles*, **18**, GB4028, doi: 10.1029/2004GB002220.

Morel, A. (1988), Optical modeling of the upper ocean in relation to its biogenous matter content (case I waters), *Journal of Geophysical Research*, **93**(C9), 10749-10768.

Morel, A. and J.-F. Berthon (1989), Surface pigments, algal biomass profiles and potential production of the euphotic layer: Relationships reinvestigated in view of remote-sensing applications, *Limnology and Oceanography*, **34**, 1545-1562.

Morel, A. and A. Bricaud (1981), Theoretical results concerning light absorption in a discrete medium and application to specific absorption of phytoplankton, *Deep Sea Research*, **28**, 1375-1393.

Morin, P., P. Lecorre, Y. Marty and S. L'Helguen (1991), Spring evolution of nutrients and phytoplankton on the Armorican shelf (North-West European Shelf), *Oceanologica Acta*, **14**(3), 263-279.

Morin, P., M. V. M. Wafar and P. Le Corre (1993), Estimation of nitrate flux in a tidal front from satellite-derived temperature data, *Journal of Geophysical Research*, **98**(C3), 4689-4695.

Mueller, J. L. (2000), SeaWiFS algorithm for the diffuse attenuation coefficient, K(490), using water-leaving radiances at 490 and 555 nm, in *SeaWiFS Postlaunch Calibration and Validation Analyses, Part 3: SeaWiFS Post-Launch Technical Report Series, Volume 11*, pp 24-28.

Nansen, F. (1912), Das Bodenwasser und die Abkuhlung des Meeres, *Internationale Revue der gesamten Hydrobiologie und Hydrographie*, **V**, 1-42.

Nelson, D. M. and W. O. Smith Jr. (1991), Sverdrup revisited: Critical depths, maximum chlorophyll levels, and the control of Southern Ocean productivity by the irradiance-mixing regime, *Limnology and Oceanography*, **36**(8), 1650-1661.

Newman, M. and P. D. Sardeshmukh (1995), A caveat concerning Singular Value Decomposition, *Journal of Climate*, **8**, 352-360.

Nezlin, N. P. and B.-L. Li (2003), Time-series analysis of remote-sensed chlorophyll and environmental factors in the Santo Monica - San Pedro Basin off Southern California, *Journal of Marine Systems*, **39**, 185-202.

Niehoff, B., U. Klenke, H. J. Hirche, X. Irigoien, R. N. Head and R. P. Harris (1999), A high frequency time series at Weathership M, Norwegian Sea, during the 1997 spring bloom: the reproductive biology of *Calanus finmarchicus*, *Marine Ecology Progress Series*, **176**, 81-92.

North, G. R., T. L. Bell, R. F. Cahalan and F. J. Moeng (1982), Sampling errors in the estimation of empirical orthogonal functions, *Monthly Weather Review*, **110**, 699-706.

Obata, A., I. J. and M. Endoh (1996), Global verification of critical depth theory for phytoplankton bloom with climatological in situ temperature and satellite ocean color data, *Journal of Geophysical Research*, **101**(C9), 20657-20667.

Olafsson, J. (2003), Winter mixed layer nutrients in the Irminger and Iceland Seas, 1990-2000, *ICES Marine Science Symposia*, **219**, 329-332.

O'Reilly, J. E. and 24 Co-Authors (2000), SeaWiFS Postlaunch Calibration and Validation Analyses, Part 3, SeaWiFS Post-Launch Technical Report Series, Volume 11, pp 49.

O'Reilly, J. E., S. Maritorena, B. G. Mitchell, D. A. Siegel, K. L. Carder, S. A. Garver, M. Kahru and C. McClain (1998), Ocean colour chlorophyll algorithms for SeaWiFS, *Journal of Geophysical Research*, **103**(C11), 24,937-24,953.

Orvik, K. A. and P. P. Niiler (2002), Major pathways of Atlantic water in the northern North Atlantic and Nordic seas toward Arctic, *Geophysical Research Letters*, **29**(19), 2.1-2.4, doi: 10.1029/2002GL015002.

Pätsch, J., W. Kuehn, G. Radach, J. M. Santana Casiano, M. Gonzalez Davila, S. Neuer, T. Freudenthal and O. Llinas (2002), Interannual variability of carbon fluxes at the North Atlantic Station ESTOC, *Deep Sea Research II*, **49**, 253-288.

Pastuszak, M., W. R. Wright and D. Patanjo (1982), One year of nutrient distribution in the Georges Bank region in relation to hydrography, 1975-1976, *Journal of Marine Research*, **40**(Supplement), 525-542.

Pickart, R. S., F. Straneo and G. W. K. Moore (2003a), Is Labrador Sea water formed in the Irminger Basin?, *Deep Sea Research I*, **50**, 23-52.

Pickart, R. S., M. A. Spall, M. H. Ribergaard, G. W. K. Moore and R. F. Milliff (2003b), Deep convection in the Irminger Sea forced by the Greenland tip jet, *Nature*, **424**, 152-156.

Pickart, R. S., D. J. Torres and R. A. Clarke (2002), Hydrography of the Labrador Sea during active convection, *Journal of Physical Oceanography*, **32**, 428-457.

Platt, T., C. Caverhill and S. Sathyendranath (1991a), Basin-scale estimates of oceanic primary production by remote sensing: the North Atlantic, *Journal of Geophysical Research*, **96**(C8), 15147-15159.

Platt, T., D. F. Bird and S. Sathyendranath (1991b), Critical depth and marine primary production, *Proceedings of the Royal Society, London (B)*, **246**, 105-217.

Platt, T. and B. Irwin.(1968), Primary production measurements in St Margaret's Bay, 1967, Fisheries Research Board of Canada Technical Report No. 77, Dartmouth, N.S., pp 123.

Platt, T. and S. Sathyendranath (1988), Oceanic primary production: estimation by remote sensing at local and regional scales, *Science*, **241**(4873), 1613-1620.

Pollard, R. T., S. J. Hay and Marine Productivity researchers (2002), RRS Discovery cruise 258: Biophysical studies of zooplankton dynamics in the northern North Atlantic: winter, 1 Nov - 18 Dec 2001, NERC, pp 112.

Pollard, R. T., J. F. Read, N. P. Holliday and H. Leach (2004), Water masses and circulation pathways through the Iceland Basin during Vivaldi 1998, *Journal of Geophysical Research*, **109**(C4), doi: 10.1029/2003JC00267.

Preisendorfer, R. W. (1988), Principal Component Analysis in Meteorology and Oceanography, Amsterdam, Elsevier, pp 425.

Price, J. F., R. A. Weller and R. Pinkel (1986), Diurnal cycling: Observations and models of the upper ocean response to diurnal heating, cooling and wind mixing, *Journal of Geophysical Research*, **91**, 8411-8427.

Rahmstorf, S. (1991), A zonal-averaged model of the ocean's response to climate change, *Journal of Geophysical Research*, **96**(C4), 6951-6963.

Read, J. F. (2001), CONVEX-91: water masses and circulation of the Northeast Atlantic subpolar gyre, *Progress in Oceanography*, **48**, 461-510.

Redfield, A. C., B. H. Ketchum and F. A. Pritchard (1963), The influence of organisms on the composition of seawater, in *The Sea* (2), edited N. Hill. New York, Interscience.

Reverdin, G., P. P. Niiler and H. Valdimarsson (2003), North Atlantic Ocean surface currents, *Journal of Geophysical Research*, **108**(C1), 2.1-2.21, doi: 10.1029/2001JC001020.

Richards, K. and Marine Productivity researchers (2002), RRS Discovery cruise 262: Biophysical studies of zooplankton dynamics in the northern North Atlantic: spring, 18 April - 27 May 2002, NERC, pp 102.

Richman, M. B. (1986), Rotation of principal components, *International Journal of Climatology*, **6**, 293-335.

Riley, G. A. (1957), Phytoplankton of the North Central Sargasso Sea, *Limnology and Oceanography*, **2**, 252-270.

Rochford, P. A., A. B. Kara, A. J. Wallcraft and R. A. Arnone (2001), Importance of solar subsurface heating in ocean general circulation models, *Journal of Geophysical Research*, **106**(C11), 30923-30938.

Roemmich, D., O. Boebel, Y. Desaubies, H. Freeland, K. Kim, B. King, P.-Y. LeTraon, R. Molinari, W. Brechner Owens, S. Riser, U. Send, K. Takeuchi and S. Wijffels (2001), Argo: the global array of profiling floats, in *Observing the oceans in the 21st century*, edited C. J. Koblinsky and N. R. Smith, GODAE Project Office/Bureau of Meteorology, pp 248-258.

Rogers, J. C. (1990), Patterns of low-frequency monthly sea pressure variability (1899-1986) and associated wave cyclonic frequencies, *Journal of Climate*, **3**, 1364-1379.

Sanders, R., L. Brown, S. A. Henson and M. I. Lucas (2005), New production in the Irminger Basin during 2002, *Journal of Marine Systems*, **55**(3/4), 291-310.

Sanders, R. and T. Jickells (2000), Total organic nutrients in Drake Passage, *Deep Sea Research*, **47**(6), 997-1014.

Santoleri, R., V. Banzon, S. Marullo, E. Napolitano, F. D'Ortenzio and R. Evans (2003), Year-to-year variability of the phytoplankton bloom in the southern Adriatic Sea (1998-2000): Sea-Viewing Wide Field-of-view Sensor observations and modeling study, *Journal of Geophysical Research*, **108**(C9), 8122, doi:10.1029/2002JC001636.

Sathyendranath, S. (1986), Remote sensing of phytoplankton: a review, with special reference to picoplankton, *Canadian Bulletin of Fisheries and Aquatic Sciences*, **214**, 561-583.

Sathyendranath, S., L. Lazzara and L. Prieur (1987), Variations in the spectral values of specific absorption of phytoplankton, *Limnology and Oceanography*, **32**(2), 403-415.

Sathyendranath, S., A. Longhurst, C. Caverhill and T. Platt (1995), Regionally and seasonally differentiated primary production in the North Atlantic, *Deep Sea Research I*, **42**(10), 1773-1802.

Sathyendranath, S., T. Platt, E. P. W. Horne, W. G. Harrison, O. Ulloa, R. Outerbridge and N. Hoepffner (1991), Estimation of new production in the ocean by compound remote sensing, *Nature*, **353**, 129-133.

Savidge, G., P. Boyd, A. Pomroy, D. Harbour and I. Joint (1995), Phytoplankton production and biomass estimates in the northeast Atlantic Ocean, May to June 1990, *Deep Sea Research I*, **42**(5), 599-617.

Sedwick, P. N., G. R. DiTullio and D. J. Mackey (2000), Iron and manganese in the Ross Sea, Antarctica, *Journal of Geophysical Research*, **105**(C5), 11321-11336.

Siegel, D. A., S. C. Doney and J. A. Yoder (2002), The North Atlantic spring phytoplankton bloom and Sverdrup's critical depth hypothesis, *Science*, **296**, 730-733.

Sinclair, M., D. V. S. Rao and R. Couture (1981), Phytoplankton distribution in estuaries, *Oceanologica Acta*, **4**(2), 239-246.

Skliris, N., K. Elkalay, A. Goffart, C. Frangoulis and J. H. Hecq (2001), One-dimensional modelling of the plankton ecosystem of the north-western Corsican coastal area in relation to meteorological constraints, *Journal of Marine Systems*, **27,** 337-362.

Smetacek, V. and U. Passow (1990), Spring bloom initiation and Sverdrup's critical-depth model, *Limnology and Oceanography*, **35**(1), 228-234.

Smith, R. C. and A. Morel (1974), Relation between total quanta and total energy for aquatic photosynthesis, *Limnology and Oceanography*, **19**(4), 591-600.

Sokal, R. R. and F. J. Rohlf (1995), Biometry, 3rd Edition, New York, W. H. Freeman and Company, pp 887.

Spall, M. A. and R. S. Pickart (2003), Wind-driven recirculations and exchange in the Labrador and Irminger seas, *Journal of Physical Oceanography*, **33**, 1829-1845.

Stal, L. J. and A. E. Walsby (2000), Photosynthesis and nitrogen fixation in a cyanobacterial bloom in the Baltic Sea, *European Journal of Phycology*, **35**(2), 97-108.

Stramma, L., P. Cornillon, R. A. Weller, J. F. Price and M. G. Briscoe (1986), Large diurnal sea surface temperature variability: Satellite and in situ measurements, *Journal of Physical Oceanography*, **56**, 345-358.

Stramska, M., D. Stramski, R. Hapter, S. Kaczmarek and J. Ston (2003), Bio-optical relationships and ocean color algorithms for the north polar region of the Atlantic, *Journal of Geophysical Research*, **108**(C5), 3143, doi:10.1029/2001JC001195.

Straneo, F., R. S. Pickart and K. L. Lavender (2003), Spreading of Labrador Sea water: an advective-diffusive study based on Lagrangian data, *Deep Sea Research I*, **50**, 701-719.

Strass, V. and J. D. Woods (1988), Horizontal and seasonal variation of density and chlorophyll profiles between the Azores and Greenland, in *Towards a Theory on Biological-Physical Interactions in the World Ocean*, edited B. J. Rothschild. Dordrecht, Kluwer, pp 113-136.

Strass, V. and J. D. Woods (1991), New production in the summer revealed by the meridional slope of the deep chlorophyll maximum, *Deep Sea Research A*, **38**(1), 35-56.

Strathman, R. R. (1967), Estimating the organic carbon content of phytoplankton from cell volume or plasma volume, Limnology and Oceanography **12,** 411-418.

Strom, S. L., C. B. Miller and B. W. Frost (2000), What sets lower limits to phytoplankton stocks in high-nitrate, low-chlorophyll regions of the open ocean?, *Marine Ecology Progress Series*, **193**, 19-31.

Sverdrup, H. U. (1953), On conditions for the vernal blooming of phytoplankton, *Journal du Conseil Permanent International Pour L'Exploration de la Mer*, **18**, 287-295.

Sy, A., M. Rhein, J. R. N. Lazier, K. P. Koltermann, J. Meincke, A. Putzkal and M. Bersch (1997), Surprisingly rapid spreading of newly formed intermediate waters across the North Atlantic Ocean, *Nature*, **386**, 675-579.

Syrett, P. J. (1981), Nitrogen metabolism of microalgae, *Canadian Bulletin of Fisheries and Aquatic Sciences*, **210**, 182-210.

Thomas, A. C., D. W. Townsend and R. Weatherbee (2003), Satellite-measured phytoplankton variability in the Gulf of Maine, *Continental Shelf Research*, **23**, 971-989.

Thomson, R. E. and I. V. Fine (2003), Estimating mixed layer depth from oceanic profile data, *Journal of Atmospheric and Oceanic Technology*, **20**, 319-329.

Townsend, D. W., L. M. Cammen, P. M. Holligan, D. E. Campbell and N. R. Pettigrew (1994), Causes and consequences of variability in the timing of spring phytoplankton blooms, *Deep Sea Research I*, **41**(5/6), 747-765.

Townsend, D. W., M. D. Keller, M. E. Sieracki and S. G. Ackleson (1992), Spring phytoplankton blooms in the absence of vertical water column stratification, *Nature*, **360**(6399), 59-62.

Trees, C. C., J. Aiken, H. J. Hirche and S. B. Groom (1992), Bio-optical variability across the Arctic front, *Polar Biology*, **12**(3/4), 455-461.

Tungaraza, C., V. Rousseau, N. Brion, C. Lancelot, J. Gichucki, W. Baeyens and L. Goeyens (2003), Contrasting nitrogen uptake by diatoms and Phaeocystis-dominated phytoplankton assemblages in the North Sea, *Journal of Experimental Marine Biology and Ecology*, **292**(1), 19-41.

Turton, J (2002), Argo 2002: Progress towards a global array of profiling floats, Oceanology International, London, pp 10.

Tyrell, T. (1999), The relative influences of nitrogen and phosphorus on oceanic primary production, *Nature*, **400**, 525-531.

Vazquez, J. (1999), AVHRR Oceans Pathfinder Sea Surface Temperature Data Sets, http://podaac.jpl.nasa.gov:2031/DATASET_DOCS/avhrr_pathfindr_sst.html.

Venegas, S. A.(2001), Statistical methods for signal detection in climate, Danish Center for Earth System Science, Copenhagen, pp 96, http://www.dcess.ku.dk/~silvia /methods/methods.pdf.

von Storch, H. and A. Navarra, Eds. (1999), Analyses of Climate Variability - Applications of statistical techniques. Berlin, Springer Verlag.

von Storch, H. and F. W. Zwiers (1999), Statistical analysis in climate research, Cambridge, Cambridge University Press, pp 484.

Walsby, A. E., Y. Z. Yacobi and T. Zohary (2003), Annual changes in the mixed depth and critical depth for photosynthesis by *Aphanizomenon ovalisporum* that allow growth of the cyanobacterium in Lake Kinneret, Israel, *Journal of Plankton Research*, **25**(6), 603-619.

Waniek, J. J., A. Iriarte, S. Holley, S. J. Brentnall and D. A. Purdie (2002), About the role of meteorological forcing on spring bloom dynamics in oceanic, coastal and estuarine systems. Challenger Centenary Conference, Plymouth, UK; Book of Abstracts.

Waniek, J. J. (2003), The role of physical forcing in initiation of spring blooms in the northeast Atlantic, *Journal of Marine Systems*, **39**, 57-82.

Waniek, J. J., N. P. Holliday, R. Davidson, L. Brown and S. A. Henson (2005), The importance of freshwater in controlling the onset and species composition of the Greenland Shelf spring bloom, *Marine Ecology Progress Series*, **288**, 45-57.

Waniek, J. J. and N. P. Holliday (2005), The physical and meteorological preconditioning of phytoplankton and zooplankton development in the Irminger Sea Part II: Model study, *Journal of Marine Systems*, **Submitted**.

Wehde, H. (2003), Influence of mixed-layer depth variations on primary production, *ICES Marine Science Symposia*, **219**, 393-395.

Werdell, P. J., S. Bailey, G. Fargion, C. Pietras, K. Knobelspiesse, G. Feldman and C. McClain (2003), Unique data repository facilitates ocean color satellite validation, *EOS Transactions*, **84**(38), 377,387.

Wheeler, P. A. and S. A. Kokkinakis (1990), Ammonium recycling limits nitrate use in the oceanic sub-Arctic Pacific, *Limnology and Oceanography*, **35**(6), 1267-1278.

Wong, A. P. S., G. C. Johnson and W. Brechner Owens (2003), Delayed-Mode Calibration of Autonomous CTD Profiling Float Salinity Data by theta–S Climatology, *Journal of Atmospheric and Oceanic Technology*, **20**(2), 308-318; doi: 10.1175/1520-0426(2003)020<0308:DMCOAC>2.0.CO;2.

Wu, J., W. Sunda, E. A. Boyle and D. M. Karl (2000), Phosphate depletion in the western North Atlantic ocean, *Science*, **289**, 759-762.

Yentsch, C. S. (1960), The influence of phytoplankton pigments on the colour of seawater, *Deep Sea Research*, **7**, 1-9.

Yoder, J. A. (1979), Effect of temperature on light-limited growth and chemical composition of *Skeletonema costatum* (Bacillariophycaea), *Journal of Phycology*, **15**, 362-370.

APPENDIX 1:

Henson, S. A., R. Sanders, J. T. Allen, I. S. Robinson and L. Brown (2003), Seasonal constraints on the estimation of new production from space using temperature-nitrate relationships, *Geophysical Research Letters*, **30**(17), 1912;
doi:10.1029/2003GL017982

GEOPHYSICAL RESEARCH LETTERS, VOL. 30, NO. 17, 1912, doi:10.1029/2003GL017982, 2003

Seasonal constraints on the estimation of new production from space using temperature-nitrate relationships

Stephanie A. Henson,[1] Richard Sanders,[2] John T. Allen,[2] Ian S. Robinson,[1]
and Louise Brown[2]

Received 17 June 2003; accepted 7 August 2003; published 13 September 2003.

[1] Inverse relationships between sea surface temperature and concentrations of the major inorganic nutrients have recently been exploited to estimate new production from remotely sensed data. In situ surface data collected in the Irminger Basin during four successive seasons in 2001/2 allow a robust examination of the conceptual processes behind temperature-nitrate relationships. The data confirm a simple model of the seasonal variation in the temperature-nitrate relationship. A strong inverse correlation between temperature and nitrate is found in both winter data sets, but no correlation is seen in spring or summer. Furthermore, the slope of the temperature-nitrate regression is found to be different for the two winter data sets. The results have implications for using temperature-nitrate relationships to derive new production estimates at high latitudes from satellite sea surface temperature measurements. However, the data allow a simple, lower-bound estimate of the region's new production to be made by exploiting Argo float data. *INDEX TERMS:* 4845 Oceanography: Biological and Chemical: Nutrients and nutrient cycling; 4805 Oceanography: Biological and Chemical: Biogeochemical cycles (1615); 4227 Oceanography: General: Diurnal, seasonal, and annual cycles; 4572 Oceanography: Physical: Upper ocean processes; *KEYWORDS:* temperature-nitrate relationship, seasonal variability, Irminger Basin, new production estimates. **Citation:** Henson, S. A., R. Sanders, J. T. Allen, I. S. Robinson, and L. Brown, Seasonal constraints on the estimation of new production from space using temperature-nitrate relationships, *Geophys. Res. Lett.*, *30*(17), 1912, doi:10.1029/2003GL017982, 2003.

1. Introduction

[2] Export production is the flux of biogenic material from surface waters to the ocean interior and is generally taken to be the fraction of production derived from the new, rather than recycled, input of nutrients to the euphotic zone. Estimating the magnitude and seasonality of this flux is vital to understanding the controls over, and strength of, the biological carbon pump and its impact on atmospheric CO_2 levels [*Eppley and Peterson*, 1979]. Shipbased observations, such as new production measurements and changes in nutrient concentrations, all inevitably suffer from an inability to sample over wide areas or long time periods. For this reason much attention has been focused on using remote sensing techniques to estimate new production. One method is to exploit the widely reported inverse relationships between sea surface temperature (SST) and concentrations of nitrate, phosphate and silicate [e.g., *Sathyendranath et al.*, 1991; *Morin et al.*, 1993; *Minas and Codispoti*, 1993; *Chavez et al.*, 1996; *Goes et al.*, 2000]. The correlation reflects the mixing of cold, nutrient rich water into the euphotic zone, which is subsequently warmed through solar heating and depleted of nutrients following the onset of the phytoplankton growth season. Although the slope of the temperature-nitrate (TN) relationship varies with location and season, the apparent consistency of the correlation has enabled the determination of large-scale estimates of surface nitrate from satellite SST measurements [see *Kamykowski et al.*, 2002 and references therein]. In turn estimates of the *f*-ratio, and hence new production, have been derived [*Sathyendranath et al.*, 1991; *Dugdale et al.*, 1997; *Alvarez-Salgado et al.*, 2002].

[3] Determining the parameters of the TN regression for a particular location necessarily requires a large number of in situ measurements. Previous authors have tended to aggregate all available cruise data from a region, irrespective of season. Although the possible effects of seasonal and interannual variability on the TN relationship have been acknowledged [*Pastuszak et al.*, 1982; *Sathyendranath et al.*, 1991; *Minas and Minas*, 1992; *Gong et al.*, 1995], little attention has been paid to the causes and consequences of such variability. In this study a unique data set from four consecutive cruises to the same region (including a repeat winter survey) is used to explore the seasonal and interannual variability in the TN relationship in a high latitude area of the North Atlantic where export production is thought to be high [e.g., *Laws et al.*, 2000].

2. Measurements

[4] The objective of the Marine Productivity program was to study the physical factors controlling zooplankton distribution (http://www.nerc.ac.uk/marprod). As part of the program four consecutive cruises to the Irminger Basin were undertaken: two early winter cruises (November–December 2001 and 2002), a pre-bloom spring cruise (April–May 2002) and a post-bloom summer cruise (July–August 2002). Figure 1 shows the location of the study region and data points. It should be noted that several data points fall outside the Irminger Basin, defined as west of the Reykjanes Ridge. Removing these data points had little effect on the results and they were therefore included in the analysis. This study uses nutrient data from the surface bottle of each CTD cast and, with the exception of the winter 2001 cruise, surface nutrient samples taken every four hours from the RRS *Discovery*'s

---

[1] School of Ocean and Earth Science, Southampton Oceanography Centre, European Way, Southampton, UK.

[2] George Deacon Division for Ocean Processes, Southampton Oceanography Centre, European Way, Southampton, UK.

0094-8276/03/2003GL017982$05.00

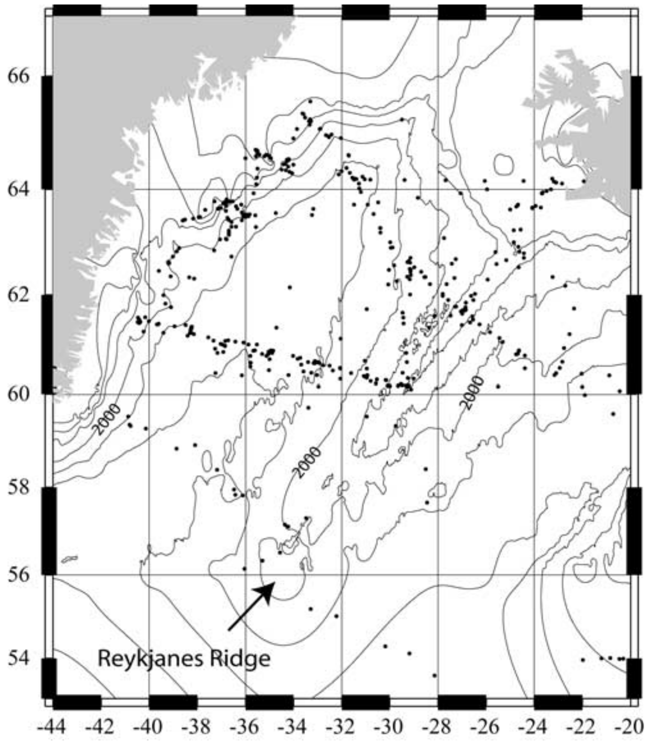

Figure 1. Study area and location of data points.

continuous thermosalinograph outflow at a depth of 5 m. The concentration of nitrate was determined via conventional colorimetric methods (cadmium reduction) using a Skalar San Plus autoanalyser [*Kirkwood*, 1995]. Continuous underway SST data were recorded by the ship's Surfmet system. Protocols for collecting and analyzing samples were the same for all four cruises [*Pollard et al.*, 2002; *Richards et al.*, 2002; *Brierley et al.*, 2003; *Allen et al.*, 2003]. A total of 480 good quality temperature/nitrate pairs were used.

3. Results and Discussion

[5] A linear fit to a TN plot containing data from all four cruises had an r^2 of 0.71; TN relationships reported in the literature typically have $r^2 > 0.85$. In an attempt to understand the reasons for this somewhat disappointing result the biophysical processes underlying the TN relationship were considered.

[6] Although a strong inverse relationship between nitrate and temperature has been observed any correlation between the two properties arises indirectly. Models of the annual cycle in nutrient and chlorophyll concentrations all display a strong seasonality at high latitudes, characterized by a short lived burst of phytoplankton growth during the spring bloom. In the classic model of the annual nutrient cycle winter wind-driven cooling and deep convective mixing results in low surface temperatures but high surface nutrient levels at the end of winter. Biological utilization of nitrate is minimal due to low light levels and continual mixing until, in spring, increasing light levels and re-stratification due to increased surface heating and reduced wind stress result in the onset of renewed biological production and rapid consumption of nutrients. In post-bloom summer nutrients have been stripped by phytoplankton from surface waters and the SST is at its peak. As solar heating declines through autumn and early winter overturning commences and cold nutrient-rich water is brought to the surface but phytoplankton are not able to utilize it. Therefore this is the only time of the year when nitrate and temperature are conserved and a linear TN relationship can be expected. At all other times of the year biological consumption of nutrients invalidates the assumption that SST varies linearly with surface nitrate.

[7] This conceptual model of the annual cycle in the TN relationship is represented in Figure 2 (expanding on *Minas and Minas* [1992]). Point A represents post-bloom summer, with high temperatures and low nitrate concentrations. Point B is the late winter/pre-bloom spring before large-scale nutrient uptake begins and is associated with low temperatures and high nitrate concentrations. Points A and B represent the end-members of the mixing due to convective overturning that takes place during autumn and early winter. The return path from point B to A takes place during the growth season and can follow one of two routes. If biological utilization of nitrate occurs at a faster rate than an increase in SST through solar heating, path 1 is taken. This situation would be typical of a fast-growing spring bloom in high latitudes. Alternatively, if the increase in SST occurs more rapidly than biological uptake of nitrate, path 2 will be followed. This situation could occur in regions of rapid heating, such as the North-west Indian Ocean.

[8] To investigate the seasonality in the data, TN plots were produced for each season and a linear regression was carried out individually on the four data sets (Figure 3). The spring and summer cruise TN plots display almost no correlation, as shown by the r^2 values (0.07 and 0.22 respectively). Both winter data sets however display a strong inverse correlation between temperature and nitrate ($r^2 = 0.82$ and 0.84, for winter 2001 and 2002 respectively). Data from the successive winter 2001, spring 2002 and summer 2002 cruises are displayed together in Figure 4. The solid line AB is the winter mixing line for the winter 2001 cruise data set. The dotted line represents the return path from point B to A. The late summer and early spring data lie around points A and B respectively. The majority of the scatter lies below the winter line suggesting that the spring bloom in 2002 followed path 1. Therefore in the Irminger Basin biological utilization

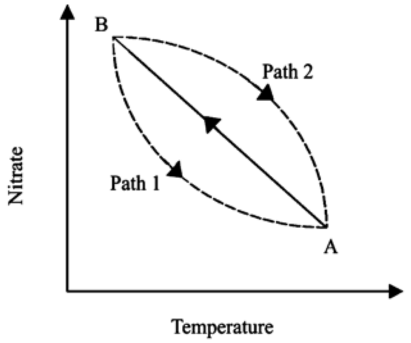

Figure 2. Idealised representation of the annual temperature-nitrate cycle. Point A represents post-bloom summer and Point B pre-bloom spring. Two alternative spring bloom scenarios are represented by Paths 1 and 2. See text for further explanation.

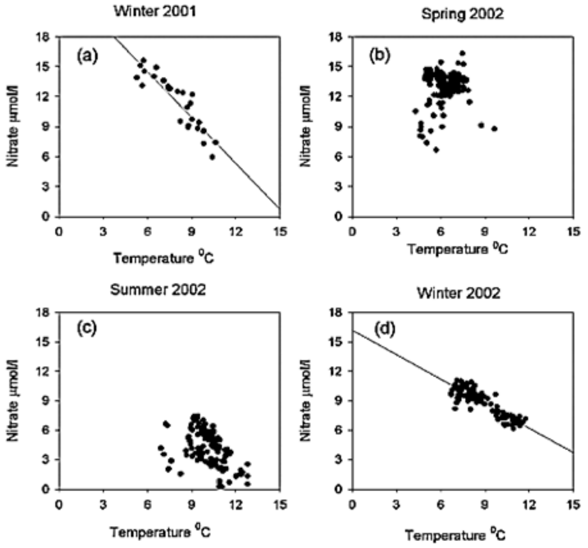

Figure 3. Temperature-nitrate plots for (a) Winter 2001 $N = 23.71 - 1.53(T)$, $r^2 = 0.82$; (b) Spring 2002 and (c) Summer 2002 regression lines not shown because statistically insignificant; and (d) Winter 2002 $N = 16.27 - 0.84(T)$, $r^2 = 0.84$.

occurs at a faster rate than SST increases due to surface heating. It is interesting to speculate that if stratification due to increased solar heating is not prompting the onset of the spring bloom, some other factor may also be responsible. The most likely is increasing day length. Could light, not stratification, be the controlling factor in the timing of the onset of the spring bloom in this region?

[9] Data from the winter 2002 cruise (not shown in Figure 4 for clarity) is consistent with the transition from the high temperature, low nitrate regime in summer 2002 back to the low temperature, high nitrate winter regime. The winter 2002 data has the same nutrient-depleted end-member (point A) as winter 2001 confirming the cyclical nature of the TN relationship. The two winter data sets do however have different slopes (Figure 3). Winter 2002 has a shallower slope than winter 2001 implying that the 2002 early winter mixed layer was shallower and therefore less nitrate was mixed into surface waters. *Waniek* [2003] suggests that wintertime meteorological conditions can affect the depth of the winter mixed layer, and thus end-of-winter nutrient levels. A stormy winter may lead to a deeper mixed layer and an enhanced nutrient supply thereby affecting the magnitude and duration of the spring bloom. Autumn 2002 may have been relatively warm and calm in comparison to 2001, leading to reduced nitrate concentrations in the surface waters during the early winter cruises. *J. Olafsson* [University of Iceland, pers. comm.] reports that the mixed layer depth (MLD) in November in the Irminger Basin was indeed shallower in 2002 than in 2001 and that winter 2002 was particularly mild. However, *Olafsson* [2003] also notes that in the Irminger Basin a shallower (deeper) winter mixed layer did not necessarily coincide with reduced (enhanced) end-of-winter nitrate concentrations. Alternatively the difference in surface nitrate concentrations may reflect changes in the composition of sub-mixed layer water masses.

[10] It may be that the variability in the TN relationship for the Irminger Basin reflects a seasonal cycle that is more pronounced in high latitudes than in the lower latitudes for which TN regressions have generally been performed. The seasonal and interannual variability in the TN relationship in this region sounds a note of caution in aggregating data compiled from several different seasons and years in order to calculate new production estimates from satellite SST. More positively, we have defined the seasonal time range during which a mechanistic link exists between temperature and nitrate and therefore when TN relationships are expected to be linear and can be used with confidence to derive primary production from satellite SST data.

[11] Although the Irminger Basin may not be suitable for estimating seasonal primary production from space using the TN relationship, a lower-bound estimate of the region's new production can still be made. The calculation of new production from changes in nitrate concentration requires an estimate of the total nitrate removed from the water column over one annual cycle. Although satellites are only able to sense the sea surface the MLD can be determined either via regressions with SST [*Goes et al.*, 2000] or via Argo floats. *Goes et al.* [2000] assume that all removal of nitrate in primary production takes place by phytoplankton growth within the mixed layer and that the nitrate consumed is equal to the seasonal change in nitrate multiplied by the depth of the nitracline at the end of summer.

[12] Typically, the MLD in a region will shoal from winter to summer. Thus, calculating new production following *Goes et al.* [2000] using the MLD at the end of summer will leave some of the nitrate utilized in new production unaccounted for. Instead integrating the nitrate concentration difference over the mean MLD for the productive season provides a first order approximation of the nitrate consumed. The nitrate consumed during the growth season is then $\Delta N = [N_B - N_A]\,[(Z_{D(spr)} + Z_{D(sum)})/2]$, where N_B and N_A are the concentrations of nitrate (µmol/l) in winter and at the end of summer respectively and $Z_{D(spr)}$ and $Z_{D(sum)}$ are the MLD in spring at the onset of biological activity and summer respectively. New production can then be calculated as $P_N = R\Delta N$, where R is the Redfield Ratio of carbon to nitrogen in phytoplankton.

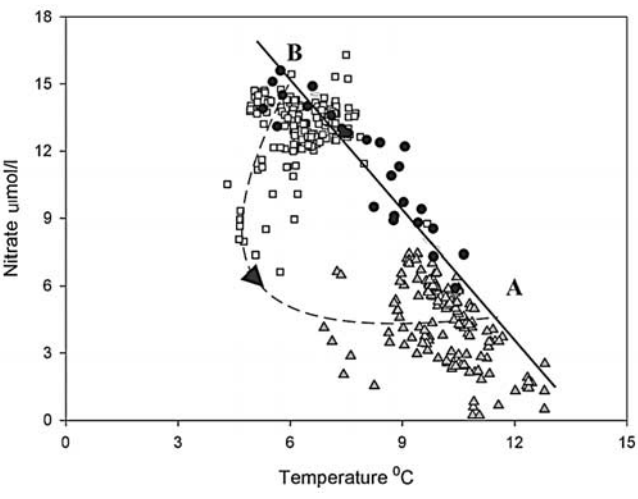

Figure 4. Data from winter 2001 (circles), spring 2002 (squares) and summer 2002 (triangles). The straight line is the winter 2001 mixing line and the dotted line is the return path from point B to A.

[13] From Figure 4 the pre-bloom (N_B) and post-bloom (N_A) nitrate concentrations (points B and A respectively) can be estimated. In this calculation the MLD was retrieved from Argo float data (http://argo.jcommops.org). Comparison of an Argo float temperature time-series in the region with the corresponding satellite chlorophyll images allowed an estimate of the MLD at the beginning and end of the growth season to be made. The mean MLD was 50m and thus the new production in this region is estimated to be $\sim$60 gCm^{-2}yr^{-1}. This is comparable to the $\sim$50 gCm^{-2}yr^{-1} calculated by R. Sanders and L. Brown (manuscript in preparation, 2003) (available at http://www.soc.soton.ac.uk/GDD) from in situ measurements, but somewhat lower than the $\sim$100 gCm^{-2}yr^{-1} estimated by *Laws et al.* [2000] and *Falkowski et al.* [1998] from SeaWiFS and CZCS data respectively. This discrepancy may arise because this approach does not account for any low levels of new production in winter, new production that takes place beneath the mixed layer or associated with transient events such as storms or eddies. Interannual variability is also ignored in this calculation and, as we have demonstrated, this may not be insignificant.

4. Conclusion

[14] Data from four successive seasons (including a repeat winter survey) allow a unique insight into the seasonal and interannual variability in biophysical processes that underlie a relationship between temperature and nitrate in the surface waters of the Irminger Basin. The in situ data confirmed a simple model of the seasonal variability in the TN relationship. Strong linear relationships were found in both winter data sets. In addition the slope of the TN regression was different for the two winters as a consequence of interannual variability in physical forcing. It may be that a TN relationship is valid only for a specific location, season and even year, raising concern over the validity of using this approach for the estimation of new production from satellite data. However, rather than being a hindrance to formulating TN relationships the variability itself contains information on the underlying biological and physical processes. A simple method of estimating a lower bound on new production using mixed layer depth data from Argo floats was introduced.

[15] **Acknowledgments.** Thanks to Christine Lane for help with preparing Figure 1. The authors thank the officers, crew and scientists of all four Marine Productivity cruises. The Marine Productivity program was funded by the Natural Environment Research Council (UK).

References

Allen, J. T., et al., Marine Productivity Cruise Report No. 4. RRS "Discovery" Cruise 267. Biophysical studies of zooplankton dynamics in northern North Atlantic: Winter 2, Univ. of East Anglia, in press, 2003.

Alvarez-Salgado, X. A., S. Beloso, I. Joint, E. Nogueira, L. Chou, F. F. Perez, S. Groom, J. M. Cabanas, A. P. Rees, and M. Elskens, New production of the NW Iberian shelf during the upwelling season over the period 1982–1999, *Deep Sea Res., Part I*, *49*(10), 1725–1739, doi:10.1016/S0967-0637 (02), 00094-8, 2002.

Brierley, A. S., et al., Marine Productivity Cruise Report No. 3. RRS "Discovery" Cruise 264. Biophysical studies of zooplankton dynamics in northern North Atlantic: Summer, Univ. of East Anglia, in press, 2003.

Chavez, F. P., S. K. Service, and S. E. Buttrey, Temperature-nitrate relationships in the central and eastern tropical Pacific, *J. Geophys. Res.*, *101*(C9), 20,553–20,563, 1996.

Dugdale, R. C., C. O. Davis, and F. P. Wilkerson, Assessment of new production at the upwelling center at Point Conception, California, using nitrate estimated from remotely sensed sea surface temperature, *J. Geophys. Res.*, *102*(C4), 8573–8585, 1997.

Eppley, R. W., and B. J. Peterson, Particulate organic matter flux and planktonic new production in the deep ocean, *Nature*, *282*, 677–680, 1979.

Falkowski, P. G., R. T. Barber, and V. Smetacek, Biogeochemical controls and feedbacks on ocean primary production, *Science*, *281*, 200–206, 1998.

Goes, J. I., T. Saino, H. Oaku, J. Ishizaka, C. S. Wong, and Y. Nojiri, Basin scale estimates of Sea Surface Nitrate and New Production from remotely sensed Sea Surface Temperature and Chlorophyll, *Geophys. Res. Lett.*, *27*(9), 1263–1266, 2000.

Gong, G.-C., K.-K. Liu, and S.-C. Pai, Prediction of nitrate concentration from two end member mixing in the Southern East China Sea, *Cont. Shelf Res.*, *15*, 827–842, 1995.

Kamykowski, D., S. J. Zentara, J. M. Morrison, and A. C. Switzer, Dynamic global patterns of nitrate, phosphate, silicate, and iron availability and phytoplankton community composition from remote sensing data, *Global Biogeochem. Cycles*, *16*(4), 1077, doi:10.1029/2001GB001640, 2002.

Kirkwood, D. S., The San Plus segmented flow Autoanalyser and its applications, Skalar Analytical BV Publications, 1995.

Laws, E. A., P. G. Falkowski, W. O. Smith, H. Ducklow, and J. J. McCarthy, Temperature effects on export production in the open ocean, *Global Biogeochem. Cycles*, *14*(4), 1231–1246, 2000.

Minas, H. J., and L. A. Codispoti, Estimation of primary production by observation of changes in the mesoscale nitrate field, *ICES Mar. Sci. Symp.*, *197*, 215–235, 1993.

Minas, H. J., and M. Minas, Net Community Production in High Nutrient-Low Chlorophyll Waters of the Tropical and Antarctic Oceans–Grazing Vs Iron Hypothesis, *Oceanol. Acta*, *15*(2), 145–162, 1992.

Morin, P., M. V. M. Wafar, and P. Le Corre, Estimation of nitrate flux in a tidal front from satellite-derived temperature data, *J. Geophys. Res.*, *98*(C3), 4689–4695, 1993.

Olafsson, J., Winter mixed layer nutrients in the Irminger and Iceland Seas, 1990–2000, *ICES Mar. Sci. Symp.*, Hydrobiological Variability in the ICES Area, 1990–1999, in press, 2003.

Pastuszak, M., W. R. Wright, and D. Patanjo, One year of nutrient distribution in the Georges Bank region in relation to hydrography, 1975–1976, *J. Mar. Res.*, *40*(Supplement), 525–542, 1982.

Pollard, R. T., S. J. Hay, et al., Marine Productivity Cruise Report No. 1. RRS "Discovery" Cruise 258. Biophysical studies of zooplankton dynamics in northern North Atlantic: Winter, 1 Nov–18 Dec 2001, Univ. of East Anglia, 112 pp., 2002.

Richards, K. J., et al., Marine Productivity Cruise Report No. 2. RRS "Discovery" Cruise 262. Biophysical studies of zooplankton dynamics in northern North Atlantic: Spring, 19 April–27 May 2002, British Oceanographic Data Centre, 102 pp., 2002.

Sathyendranath, S., T. Platt, E. P. W. Horne, W. G. Harrison, O. Ulloa, R. Outerbridge, and N. Hoepffner, Estimation of New Production in the Ocean by Compound Remote- Sensing, *Nature*, *353*(6340), 129–133, 1991.

Waniek, J. J., The role of physical forcing in initiation of spring blooms in the northeast Atlantic, *J. Mar. Syst.*, *39*(1–2), 57–82, doi:10.1016/S0924-7963 (02)00248-8, 2003.

S. A. Henson and I. S. Robinson, School of Ocean and Earth Science, Southampton Oceanography Centre, European Way, Southampton, SO14 3ZH, UK. (shen@soc.soton.ac.uk)

R. Sanders, J. T. Allen, and L. Brown, George Deacon Division for Ocean Processes, Southampton Oceanography Centre, European Way, Southampton, SO14 3ZH, UK.